Towards large scale quantum networks

Shaobo Gao

New College

University of Oxford

A thesis submitted for the degree of

Doctor of Philosophy

Trinity 2020

This thesis is dedicated to
my loving parents W.Gao and H.Tian
for their continued guidance and support
as well as for offering me a peaceful and positive upbringing

Acknowledgements

My greatest gratitude and respect go to Dr. Joseph Goodwin, who helped me when I was at the crossroads of my DPhil study. He is patient as a supervisor, generous as a project leader, cheerful as a colleague and supportive as a friend. His practical experience and versatile knowledge always inspire me. His encouragement and support played a key role in the completion of my research.

I am also grateful to Dylan Saunders who supervised me in the first two years of my DPhil study with his great passion for physics; and Patrick Ledingham who supervised me successively, helping me with his great patience and strong sense of responsibility.

I have the greatest respect for David Lucas, Ian Walmsley and Joshua Nunn who are wonderful group leaders as well as eminent physicists. They have always inspired me with their profound understanding of physics and helped me when I was in need.

I am also very thankful to the academic scholars from my funding community Prof. Pingxing Chen, Prof. Weitao Liu for their support, both in academy and personal life. Great gratitude also goes to Prof. Lijian Zhang who encouraged me to pursue my DPhil in Oxford.

My DPhil study wouldn't have been as cheerful or as rich without my great colleagues and friends. Oscar Lazo has been helping me with useful discussions about physics, philosophy and politics throughout my time studying in Oxford. I have also benefited a lot from many in-depth discussions with William Hughes and Dr. Ezra Kassa.

I will always remember the companion from Gla (Sahutchai) Inwongwan who was there with me in all my important moments, dark or proud; David Drahi, a loyal friend who always gives me constructive and honest advice; Margaret Miao, Stefanie Arend, Maggie, Dongyang Xu and Shan Wang who emotionally support me so much; Zhifeng Chen, Reevu Maity

and Ben Logan who inspired me with every insightful discussion either during a long walk or late at night.

I would also like to thank Dr. Zhong Han, Dr. Heng Shen, and Clemens Löschnauer as supportive colleagues and friends; Gang Wang who advised me with almost every dinner and Jack Sparrow who always gives me courage to pursue the life I truly desire.

Abstract

Quantum computing has the potential to solve problems that take current classical computers much longer to solve. The last two decades witnessed a substantial development of various physical platforms, most of which have shown a "Proof of principle" demonstration for quantum computing. We are now in a critical stage where the goal is to develop the system to a large scale so that we can make quantum computing useful for real world applications. However, the question of which physical platform shows most promise remains uncertain. In this thesis, I examine two mainstream platforms: linear optics and trapped ions, from the point of view of scalability. For each platform, my own work has focused particularly on how to model and engineer the temporal properties of single photons.

For linear optical quantum computing, I propose to use an off-resonant cascaded absorption (ORCA) buffer to purify and unify the single-photons from different noisy sources. A proof of principle experiment is demonstrated to show that the ORCA buffer is in principle, noise-free. Simulation suggests that with the current ORCA buffer, we can purify the single-photon source better than with ideal intensity filtering. Meanwhile, it can unify different sources and increase the *inter-indistinguishability* from 60% to 96%.

For the trapped ion system, one promising scalable approach is to use photons to mediate entanglement between ions in remote traps. To achieve this, ion-photon entanglement must first be generated. We propose to use a cavity-enhanced Raman transition on the $D_{3/2} \rightarrow P_{3/2} \rightarrow D_{5/2}$ 'λ-system' in a strontium ion level scheme for ion-photon entanglement generation. A full mathematical description is constructed to describe the entanglement dynamics considering the Rayleigh-scattering-induced temporal mixing noise. With this theory, simulation shows that we expect to achieve ion-ion remote entanglement rate of more than 75KHz with

negligible infidelity from temporal mixing noise. Both proposals, if fully demonstrated experimentally, will be powerful tools to solve the scalability challenge for their respective systems, paving the way towards large scale realistic quantum computing.

Contents

List of Figures

Publications

S. Gao, W. Hughes, D.M. Lucas, T. G. Ballance, and J. F. Goodwin. An optically-heated atomic source for compact ion trap vacuum systems. *in preparation*, 2020.

S. Gao, O. Lazo-Arjona, B. Brecht, K. T. Kaczmarek, S. E. Thomas, J. Nunn, P. M. Ledingham, D. J. Saunders, and I. A. Walmsley. Optimal coherent filtering for single noisy photons. *Phys. Rev. Lett.*, 123:213604, Nov 2019.

E. Kassa, W. Hughes, S. Gao, and J. F. Goodwin. Effects of cavity birefringence on remote entanglement generation. 2020. arXiv,2008.11712.

D. Main, T. M. Hird, S. Gao, E. Oguz, D. J. Saunders, I. A. Walmsley, and P. M. Ledingham. Preparing narrow velocity distributions for quantum memories in room-temperature alkali vapours. *Phys. Rev. A, under review*, 2020.

D. Main, T. M. Hird, S. Gao, I. A. Walmsley, and P. M. Ledingham. Room temperature atomic frequency comb memory for light. *Phys. Rev. Lett. under review*, 2020.

Chapter 1

Introduction

I believe that two factors drive the development of human civilization: the rapid accustomization to new luxury and the selfless trust in the possibilities for the future.

Think of a middle class businessman back in late 1800s, he might have a big house to live in and maybe a butler to take care of the his property. Every week he can go to the other side of the town to attend a concert or visit a friend. Life is decent and maybe satisfying. If he time travels to 2020, he would suddenly find out that he can travel to the other side of the world within a day or do business with the whole world without even stepping out of his room. He would definitely be shocked and very excited to embrace all the luxury and convenience that modern technology brings to him. But for how long? Several months? A year? After that, he will find out that he still needs to spend most of his time working and travelling. The internet is no longer an excitement to him but more like a necessity for his business. He uses his smartphone for contacting different business partners and reading disturbing news around the world. The internet and the smartphone are as shiny as he first saw them, but he has now become accustomed to them. The roar of the flight taking off doesn't spark any electric signal in his neurons. The amazing luxury soon becomes part of his life and doesn't excite him anymore, just like all of us. Pessimistic as it sounds, this adaptation of luxury is written in our genes so deeply that very few people can fight against it or even realise it.

But why are we still so passionate about new technology if it never really brings us persistent happiness? Think of the gentleman again. He has just earned 10 million by successfully organising an auction selling his rare, antique furniture from 1900. He could use the money to relax with his family on an island in the Caribbean sea for the rest of his life. But he instead decides to invest the money on 5G infrastructure construction. Why? Because he thinks that the new technology enables all kinds of possibilities for his business, and also to human society. What comes with the

investment are human resources. Thousands of technicians and programmers are employed to work on 5G technology. They commute to work everyday, work hard, hoping to make a better life in the yet-to-come 5G era.

Most people believe that new technologies will bring the possibility of new convenience and comfort to themselves or their loved ones. With this hope, we work, we create and we develop. We attach so much important to the future in modern life; on one hand because we trust much and invest so much in this future that our belief in the future becomes our main source of motivation; and on the other hand because modern science offers, as never before in human history, such a powerful platform for human imagination. A good example is that if you were to ask a person 120 years ago whether he believed that a human could travel around the world in one day, he would probably shake his head and says it was not possible. But if you ask a person in 2020 whether he believes we can build a quantum computer (if he ever heard of it), he would most probably smile and say it's just a matter of time. In fact we are much less close to a realistic quantum computer nowadays than we were to an airplane 120 years ago.

This is how science really benefits us, not a more convenient life, not more money, but a platform for imagination, a hope of human future.

Few things in the history of science stimulated human imagination more than quantum mechanics. Many proof of principle quantum experiments have shown a spectacular view of the physical world, with many of the concepts emerging from it seeming too odd to be true. Knowing quantum mechanics has never boosted my confidence about how much I know about the world. Instead, it keeps reminding me how ignorant humans can be. Even with just our very limited knowledge about quantum world, we have started to think of using it as a tool to change our life. Quantum engines, quantum materials, quantum AI... We will be more and more capable of many revolutionary technologies while remaining ignorant about the most important questions about the universe, and about humans ourselves. I am passionately excited about the possibilities science and technology bring to us. But at the same time, I am deeply concerned about what these possibilities are. Prosperity or self-destruction? Harmony or exploitation?

I raise these concerns in the beginning of the thesis because they are more important than the academic purpose of my DPhil journey in Oxford, which tries to apply the principles of quantum mechanics to the development of a realistic working quantum computer. When I arrived in Oxford, I joined the group of Prof Ian Walmsley, and the first year of my DPhil witnessed the success of the first working quantum

memory in the group. I spent a whole year trying to improve the storage time of the memory until Dylan, one of my supervisors, realised that, with some simple modifications, it could potentially be interfaced with the broadband single-photon sources. I later found that it could not only store single-photons but also improve the quality of them. This is a critical technique for large scale linear optical quantum computing. This research led to the publication [44]. The experimental implementation of this work continued beyond the time when my supervisor Ian Walmsley decided to pursue his career in Imperial College London at the end of my second year. With the Walmsley group moving to Imperial, I thought it would be interesting to apply my knowledge of single photon quantum optics to a new problem and arranged to move to David Lucas's group investigating their new research project: ion-ion remote entanglement with integrated optical cavities. The motivation of this project clearly overlapped with my previous work: building a large scale quantum computer. It is also a happy coincident that both research projects required detailed examination of the temporal properties of single photons. I spent most of my time in the third year developing a novel theoretical framework to better understand these properties and constructing a simulation toolbox to help guide the design of future experiments. In the mean time, I participated in many projects aiming at improving the scalability of ion traps, including testing an optically heated atomic oven for ion loading [43], testing an integrated vacuum system, designing a trap substrate with integrated optical cavities, developing a testing system for monolithic cavities, and exploring a method for the passive cavity alignment of cavity component using liquid surface tension which I am very much passionate with. These projects involved many eye-opening technologies and I truly enjoyed them. Therefore I was very sad when all the laboratories had to shut down due to the pandemic throughout the year of 2020. Of course this was nothing compared with all the suffering around the world due to COVID-19. It is a very complicated feeling when I think of those who are dying because of lack of medical resources while I am worrying about my DPhil degree. All I hope is that some day a quantum computer can be used for inventing medicines that are made accessible to the poor.

Before I navigate into the details of my research, I would like to highlight a field of quantum optics that has just started showing its importance in the application of quantum computing. This is the temporal mode control of single photons. The quantum properties of single photons play key roles in many quantum computing platforms, for example, trapped ions and cold atom arrays for inter-module connection, let alone the linear optics quantum computing systems which mainly use

single photons to perform quantum operations. The main effort of the single-photon community has been focused on its statistical purity (having only one photon in the wavepacket). However, for most applications, having a statistically pure single photon is not enough. We will see from the thesis that the temporal properties of the single photons are crucial for networked quantum computing in both platforms. I believe that future networked quantum technologies will require a very clear understanding, detailed framework and precise experimental control of the temporal properties of single photons. I hope that this thesis, although not solely dedicated to, can provoke wider interest in this topic.

This thesis is divided into three parts. In Chapter 2, I will try to convince the reader that a quantum computer has the potential to outperform a classical computer. I discuss in more detail about two promising physical platforms for quantum computing: linear optics and trapped ions, both as examples of showing how a quantum computing can physically work and as an introduction to the next two chapters where I discuss two proposals to move towards realistic large-scale quantum computing. In Chapter 3, I focus on solving the problem of single-photon source scalability using quantum buffers. In Chapter 4, I construct a full description of using optical cavities to entangle trapped ions more efficiently. Chapter 5 provides a summary and an extended outlook of future work.

Chapter 2

Realization of practical quantum computing

2.1 Quantum computing

It has been several decades since the idea of building a quantum computer was first proposed. At the very beginning, people had very little idea of what a quantum computer might be able to do and even less of how to build one. It is still very much the same to the public, even nowadays. When I talk to my non-physicist friends, quantum computers are no more than a science fiction idea which can solve everything. I am not surprised by that at all, because for a long time, it has been very unclear, even to physicists, what a quantum computer will physically look like. Even today, quantum computing is still one of those ideas which cannot be explained in a simple and precise way. The reason, partially, is that "quantum" itself is not an easy concept. We are building a quantum machine to process information without a good understanding of what quantum is. The other reason, in my opinion, is that we have not identified a single physical platform upon which to build a quantum computer. Each platform has its own advantages and disadvantages and the physical platform almost determines which information processing protocols people can use.

In this section, I will try to explain, as simply as possible while not distorting the science, what a quantum computer is and how it could outperform a classical computer. With this explanation, we can start to discuss how to build a practical quantum computer.

But let us begin from the beginning.

2.1.1 Classical computing

We are all familiar with classical computers, they are the laptop you use to write thesis; the mobile with which you send messages; the chip inserted in the air-conditioner that controls the temperature of your offices; the servers that connect your personal devices and millions of others' around the world. But regardless of all these diversities, a classical computer is just a way of encoding and processing information plus the physical carrier of such information.

All information can be presented by numbers. In classical computation we choose to use binary numbers to encode information as a sequence of "bits" (0 or 1). The reason for this choice is rather simply that it is easier to build a physical carrier with only two states. The processing of information with binary numbers is based upon systems of connected "logic gates". All "logic gates" can be built up by a single type of "universal gate": the NAND gate (or,alternatively, the NOR gate).

Two tasks are left in producing the computer: First, constructing algorithms that translate real-life information processing task into logic gates; and second, finding a physical system that can reliably achieve an universal gate operation in a fast, scalable and cheap way.

The first part of this work is done by computer scientists. They find out that some problems may be fundamentally harder than other, "harder" here meaning that the required computational steps (logic gates) scales more dramatically with the size of the problem. Some problems are so hard that it requires millions of years for a classical computer to solve the problem. However, it remains a mystery whether this is because there is no simpler way or whether it is just because we haven't yet find one. This is a very hand-wavy way of explaining the *"P versus NP problem"*. From a very practical point of view, there are some difficult problems that cannot be efficiently solved by computers, at least for now. A good example is factoring large numbers: finding two prime numbers whose product is a given large number. This problem is so difficult for computers that we can use this problem to securely encrypt information. We believe that no hackers can solve this problem so that our money in the bank is safe. There are other difficult problems that we really want to solve efficiently, but for which we haven't yet found a way.

The second part is done by physicists. They choose to use high and low voltages in a circuit to represent bits (0 and 1), with the NAND gate is implemented by using two (or more) transistors. A transistor is a semiconducting device that has three terminals which serve as electric switch. After decades of fabrication technology development, transistors nowadays are vary mature and can be produced in very small size in a

very cheap way. Many billions of micro transistors are fabricated on the silicon chips inserted on our daily-used devices. Every time I type a word, there are millions of transistors switching on and off at a time scale of nanoseconds. However, fabulous as it is, there is limit. In 1965, Gordon Moore, then the CEO of Intel, observed that the number of components (transistors) per integrated circuit doubled every two year. This observation, later referred to as "Moore's Law", on one hand shows how fast technology is developing while on the other hand, predicts that we will reach the physical limit of transistor size within the next ten years (before 2030). The transistor will then be at the scale of molecules, where quantum effects dominate. They will then no longer operate reliably, which represents a fundamental bottle neck to the development of information technology.

It seems that the traditional computers are facing problems in both directions: algorithm and hardware. Richard Feynman proposed in 1983 the idea of building a new type of computer which itself use the law of quantum mechanics to process information in a fundamentally different way. In this way, Moore's law would no longer be a constraint. This was still just a concept until two years later David Deutsch came up with a quantum algorithm [29] which shows that the quantum computing can be implemented through a universal set of logic gate. More importantly, it shows a higher efficiency in terms of gates scaling compared with classical computing [107]. Deutsch's algorithm was later joined by Shor's algorithm [129] for factoring large numbers, Grover's algorithm [54] for unsorted search, and many more since then. The quantum computer then, for the first time, demonstrated its computational power for real world problems, and then onwards, the word "quantum computer" start drawing public attentions.

2.1.2 Quantum computing

It may be too optimistic to say that quantum computers are the key to break Moore's Law because we have absolutely no idea how the size of quantum computer will change over time. However, we have some confidence in the claim that a quantum computer has the potential for computational power beyond what is possible with classical computers. To draw a comparison with classical computers, we shall understand quantum computing via the same three aspects: information encoding, algorithms, and physical platforms.

2.1.2.1 Quantum bits - qubits

A classical bit has two discrete states: 0 and 1. This is represented by the voltage of an electric circuit. The voltage is either high or low - there is no middle ground. It is this very attribute that makes classical bits very robust against environment fluctuation. The voltage has to fluctuate more than half of the voltage difference to create a bit error.

For a quantum computer, the 0 and 1 is no longer carried by voltage, which is a classical variable. They are carried by a quantum object, for example, an electron. The two electron spin states represent 0 and 1 respectively. If we create an electron with spin state "1", put it though a classical logic gate as we did with the classical computer, and observe the output spin state to get the output bit, it would be no different from a classical computer apart from the fact that the new computer is more expensive and fragile. So a computer with quantum object as a bit-carrier should, in theory, be able to do everything a classical computer can do. A quantum object, however, can do something a classical object cannot do. It can be in a superposition of the two states. Therefore the bit it carries is also in a state between the "0" and the "1":

$$|\phi\rangle = \alpha|0\rangle + \beta|1\rangle \tag{2.1}$$

where $|\alpha|^2 + |\beta|^2 = 1$. We use ket "$|\rangle$" to show that the bit is carried by quantum object. This bit is called a *"qubit"*.

A qubit carries information for both "0" and "1". If a qubit is sent into a reversible logic gate U (it can be easily shown that a reversible logic gate can be expressed by a unitary matrix), the gate output is:

$$U|\phi\rangle = \alpha U|0\rangle + \beta U|1\rangle \tag{2.2}$$

We can see that the output contains the information of $U|0\rangle$, which is the gate output of classical bit "0", and $U|1\rangle$, which is the gate output of classical bit "1". So one step of qubit operation contains the information of two steps by a classical bit operation. If the input is not a single bit but a sequence of N bits, one step of qubit operation contains the information of 2^N steps with classical bits.

This would be all an irresponsible physicist might tell you about quantum computing if he only had three minutes to explain. This is not wrong and it does show the parallel processing power a quantum computing has. But it is far from the whole picture. What would be the use of the information if we cannot read it? In the above case, only one of the results can be read out because a measure of the output

would destroy the output state. You can not measure $U|0\rangle$ and $U|1\rangle$ at the same time because the state only collapses to one of them. All this example really tells us is that the operation and measurement of qubit(s) follows different rule from that of a classical computer. If we cleverly design the algorithm, we might be able to achieve something a classical computer cannot offer.

2.1.2.2 Quantum algorithms

A quantum algorithm is an algorithm which runs on a quantum computation model. The most common model is the quantum circuit model which is schematically very similar to classical computation. Input sequences of qubits go through a sequence of quantum gates one after another until the final step, where a state measurement is implemented to read-out the result. To see how a quantum algorithm can enable a quantum computer to outperform a classical computer, we take the simplest example proposed by David Deustch in 1985. It is called the Deutsch algorithm.

Before we introduce the algorithm, we should discuss a little bit more about the difference between the classical logic gate and the quantum logic gate. This gives some insight about the difference between the two type of computers and we need it to explain Deustch-Jozsa algorithm.

A classical logic gate implements a Boolean function. As we mentioned before, it has single or multiple binary inputs, and all Boolean functions can be decomposed into simple Boolean functions with single outputs, for example, OR, AND or NAND. Most of these simple functions are irreversible, which means that the input cannot be inferred from the output. Most modern classical computers use these logic gates as their basic computational units because they are simple. However, a complicated logic gate can also be decomposed in a different way into a different set of simple, reversible logic gates, for example, NOT, CNOT or TOFFOLI. The advantage of reversible logic gates is that they do not dissipate energy, which is a major concern for classical supercomputers (and my smartphone...!).

A quantum logic gate, however, is usually constructed in a reversible way. Any non-unitary operation on an isolated system is forbidden by quantum mechanics, therefore a quantum logic gate implemented by an isolated physical system should be an unitary transformation of the input, and is thus reversible. We should also be aware that the set of quantum logic gates is larger than the set of reversible classical logic gates because there are some quantum logic gates that do not make sense for classical logic gates, for example, the Hadamard gate, or the phase gate.

We can now introduce the Deutsch algorithm. Imagine we have a simple Boolean function f that takes one bit as input. There are two kinds of single bit Boolean functions, one of which has constant output regardless of the input, which we call constant function. The other type either keep the output the same as the input or flip the input. We call these balanced functions because they have a balanced probability of having "0" and "1" as output (see Fig.2.1a). The problem addressed by the Deutsch algorithm is to determine whether a given function is constant, or balanced.

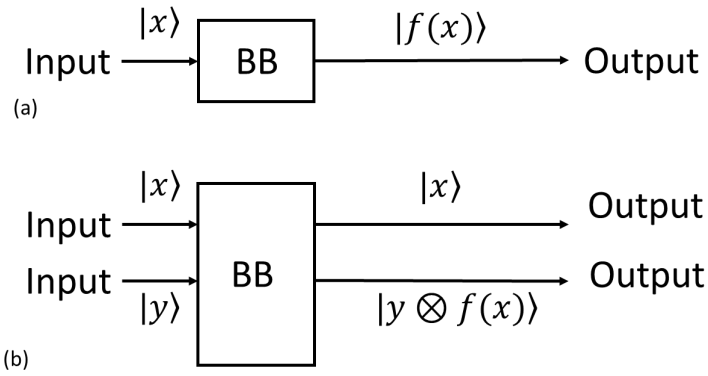

Figure 2.1: Deutsch algorithm.

If we use a classical computer, we will need two steps to solve the problem. The first step is to send in bit "0" and measure the output. The second step is to send in "1" and measure. But we will soon see that if we use a quantum computer, we only need one step.

First we need to design the logic gate that carries the function to be a reversible gate U_f. In figure 2.1b, the input now has two bits $|x\rangle$ and $|y\rangle$. The outputs are $|x\rangle$ and $|y \oplus f(x)\rangle$, where $\oplus$ is addition modulo 2 which is implemented as a CNOT gate. The algorithm has three steps. First we prepare the state $|01\rangle$ and apply a Hadamard gate to each qubit, to give the input qubits state:

$$|xy\rangle = \frac{1}{2}(|0\rangle + |1\rangle)(|0\rangle - |1\rangle) \tag{2.3}$$

The second step is the send the qubits through the reversible logic gate U_f:

$$\begin{aligned} |\phi\rangle =& \frac{1}{2}(|0\rangle(|0 \oplus f(0)\rangle - |1 \oplus f(0)\rangle) + |1\rangle(|0 \oplus f(1)\rangle - |1 \oplus f(1)\rangle)) \\ =& \frac{1}{2}((-1)^{f(0)}|0\rangle(|0\rangle - |1\rangle) + (-1)^{f(1)}|1\rangle(|0\rangle - |1\rangle)) \\ =& (-1)^{f(0)}\frac{1}{2}(|0\rangle + (-1)^{f(0)\oplus f(1)}|1\rangle)(|0\rangle - |1\rangle) \end{aligned} \tag{2.4}$$

We can ignore the global phase $(-1)^{f(0)}$. The third step is to implement another Hadamard gate to each qubit. We then have:

$$|\phi\rangle = \frac{1}{2}((1+(-1)^{f(0)\oplus f(1)})|0\rangle + (1-(-1)^{f(0)\oplus f(1)})|1\rangle)|1\rangle \tag{2.5}$$

We then measure the output qubits. The qubits are $|01\rangle$ if and only if $f(0)\oplus f(1)=0$ and the qubits are $|11\rangle$ if and only if $f(0)\oplus f(1)=1$. The two outcomes correspond to f being a constant function and a balanced function respectively.

We have shown, by a simple algorithm, that a quantum computer can achieve speed up (less queries of the function f) compared with a classical computer. This algorithm can be generalised to Deutsch-Jozsa algorithm which deals with more bits and solves the problem in a deterministic way. The numbers of queries of function f for a classical computer to solve the problem increases exponentially, while a quantum computer only requires two queries of f (instead of one query for simple Deutsch algorithm). Even though of little use in real life, this algorithm demonstrates the exponential speed up of quantum computers in a simple way. It still remains a question what attributes of the quantum computer enables the computational power, but it seems that if there is a true speed up, the algorithm must make use of some quantum phenomenon which classical bits doesn't have, for example, superposition and entanglement.

There is superposition but no entanglement in the Deutsch algorithm-this is because the problem only involves a single qubit. However, for more complicated problems which involve more qubits, multi-party superposition is required. Entanglement as a natural result of multi-particle superposition becomes essential for those algorithms [92].

Quantum algorithms are an important and thriving field, but beyond the scope of this thesis. There are many review articles explaining the foundation and state of the art [101]. We should be aware that algorithms are designed to run on a certain computation model, and there are different quantum computation models, including the quantum circuit model [97], one-way quantum computation [16], adiabatic quantum computing [27], topological quantum computing [106], Boson sampling and so on. Some of them are universal while some only deal with certain types of problems.

2.1.2.3 Physical platforms for quantum computing

One complication about quantum computing is that there are many physical platforms as candidates to implement quantum algorithms. Some algorithms are designed only for a certain type of physical platform and hence not suitable for others. Some

platforms are only practical for certain types of computational model while not for others. Even for the same computational model, different physical systems show distinctive advantages and disadvantages. To avoid overly complicating the discussion, I will focus on the lowest layer of quantum computation - the physical platform and only mention the computational model when necessary.

Superconducting quantum computing Superconducting circuits are currently the most commercialised platform for quantum computing, and it achieved *quantum supremacy* [115] by Google in 2019 [5]. Micro electric circuits are cooled down to 100mK in a dilution refrigerator, placing the circuits in a superconducting state. Cooper pairs are now the charge carriers instead of single electrons. As bosons, cooper pairs are described by condensate wave functions, which allows macroscopic quantum effects to occur. Different electric circuits are weakly coupled by Josephson junctions through a quantum tunnelling effect. The Josephson Junction creates nonlinear inductance which results in an anharmonic potential in each electric circuit. Different types of qubit have been designed for superconducting quantum computers: qubits can be carried by the circuit charge, magnetic flux, wavefunction phase or hybrids combinations of these properties. Single qubit gates are induced by microwave pulses on resonance (or off resonance) with the energy gap between the designed qubit states. There are different ways of implementing two qubit gates. Most common is to connect them to an intermediate electrical circuit, although this constrains the connectivity to nearest-neighbour couplings only. Another approach is to couple different circuits into a microwave cavity, which eliminates the nearest-neighbor constraint. In both methods, the qubits can be coupled into and out of the coupler by tuning the qubit energy gap on and off resonance. This can be done easily by adjusting the circuit capacitance and inductance. The superconducting circuit is fabricated on chips so it is ready to scale and an universal quantum logic gate-set has been demonstrated experimentally [20] so it is suitable for universal quantum computing through the quantum circuit model. Other computation models are also feasible, for example, the quantum annealing model [19]. In fact, the first commercial quantum computer was built, controversially, using such a model on a superconducting platform by D-Wave System [75]. The main challenges of superconducting quantum computation are microwave engineering and limited coherence time.

Quantum computing with neutral atoms It is a natural choice to use atoms to encode qubits. They have a range of levels with naturally unequal energy difference.

They are simple isolated systems so their dynamics are well-described by quantum mechanics. Atoms are usually laser-cooled and are trapped by optical[117] or magnetic [86] lattices, which trap an array of atoms in 1D, 2D, or 3D configurations. The qubits are usually encoded in the Zeeman or hyperfine levels of each atom (or an atom ensemble[94]). The qubit state is initialised by optical pumping and measured via state-dependent fluorescence detection. Single qubit operations are usually implemented by microwaves or a two-frequency Raman optical field and a operation fidelity of $> 99\%$ has been demonstrated [148]. There are many approaches for two- or multiple-qubit gates. One of the most commonly used is the Rydberg interaction. The best fidelity so far is 97% [87]. One advantage of a neutral atom array is that it is suitable for multi-qubit gates operation due to the long range Rydberg interaction [73]. Furthermore, the fact that a lattice can easily trap thousands of atoms makes neutral atoms a promising platform for scalable quantum computing and quantum simulation. For more details, see review paper [122]

Quantum computing with Nitrogen-vacancy (NV) centers in diamond NV centers in diamond consist of a nearest-neighbor pair of a nitrogen atom, which substitutes for a carbon atom, and a lattice vacancy. It creates a local potential that generates atom-like energy levels for an electron. Qubits are encoded on these energy levels. Microwaves can be delivered by on-chip wires or waveguides to the NV center to manipulate the qubits, so the fabrication is easy to scale. Single qubit operations are performed in the same way as with normal atoms. Multiple qubit gates can be achieved using coherent magnetic dipole-dipole interactions but only for qubits separated by distances on the nanometer scale. Larger scale NV-centre-based quantum computing will have to use photonic channels, with entanglement of pairs of separated qubits mediated by entangled photons. However, as with all solid state quantum devices, it is very challenging to generate stable and identical qubits. This will make the entanglement swapping using photons very difficult.

Linear optical quantum computing (LOQC) LOQC uses photons as information carriers, mainly uses linear optical elements, or optical instruments (including reciprocal mirrors and waveplates) to process quantum information, and uses photon detectors and quantum memories to detect and store quantum information. One clear advantage of LOQC is that photons travel fast, so it is a natural candidate for a long distance quantum network. Another advantage is that photons do not easily interact with environment, so the quantum state can be stable. However, one critical

disadvantage is that photons as bosons can be easily lost, making LOQC probabilistic and hence difficult to scale. We will discuss this in more detail in Chapter 2.2.

Ion trap quantum computing Charged atoms can be easily trapped by electric or magnetic potentials. The qubit is encoded in the Zeeman or hyperfine levels just as with neutral atoms. Single qubit gates are implemented by optical fields or microwaves with very high fidelity (for example, single qubit gate with fidelity 0.999999 [56]). Two-qubit gates are typically achieved via the Coulomb interaction between ions. Gates can be implemented between any two (or more) ions in a trap because of the long range of the Coulomb force. The highest fidelities of both single and two qubit gates are achieved using this platform. Quantum supremacy was also achieved in ion trap system [153] (but less advertised than superconducting platform). Operating with large number of ions in one trap is difficult because of the inhomogeneity of the trap potential and spectral crowding of the vibrational modes used to mediate the gate operations, but several approaches are being explored to tackle the scaling problem. We will discuss this in more detail in Chapter 2.3.

There are several other platforms suitable for quantum computing. The ones I listed above are just so far the most developed platforms. However, there isn't a single platform that clearly outperforms others in all criteria. It is always worth exploring new options.

2.1.3 Quantum networking

In the previous three sections, we have learnt the difference of encoding bits between classical and quantum computers. We have shown that through careful design of algorithms, a quantum computer can achieve speed-up compared with a classical computer. Different physical platforms to implement quantum algorithms were introduced briefly. Hopefully by now I have convinced you that it is in principle possible to build a quantum machine to outperform classical computer in solving some problems. However, to show that something works in principle is very different from making it practical in real life. To see this, let us examine what is required for a practical quantum computer.

An algorithm solving a real-life problem using circuit model gives the number of logic qubits and the number of qubit gates (circuit depth) needed. When such qubit operations are implemented on a quantum platform (e.g. superconducting circuits, trapped ions), errors can occur, with much larger probability than classical gates, with each qubit gate. Some types of the error accumulate with the circuit and eventually

wash out the useful information. For example, a design of chemicals for increasing the yield of fertilizers for crop production, requires a few hundreds of qubits, and a sequence of more than 10^{10} operations should be reliably implemented [119]. It is almost inconceivable that a quantum computer could exhibit error rates low enough to achieve such circuit depth without any errors occurring. Therefore, a useful quantum computer has to be *fault-tolerant* using quantum error correction (QEC) codes.

For classical computers, error correction is implemented with almost no further physical cost. Hamming codes detect and correct errors while only requiring roughly 10% overhead in the number of physical bits versus logic bits. However, for quantum error correction, the overhead is much higher and very much dependent on various issues, for example, the raw gate fidelity, the physical platform, the types of gates, the circuit depth and type of the QEC code. For the example given above, with the state of art gate fidelity of 0.999, tens to hundreds of thousands of physical qubits are required for one logical qubit [119]. Hundreds of millions of physical qubits are required in total. Another example of factoring large numbers using Shor's algorithm requires a similar amount of resources [49]. There are, however, other problems that are simpler but still useful which are less resource-consuming. For example, it is believed that Digital Quantum Simulation [47] on a circuit-based quantum computer could be the first useful quantum computing application to be achieved. Simulating particles interacting through a pairwise potential requires more than 100 logical qubits with a few hundred thousand qubit gates [72] to outperform classical computers. A few hundred thousand physical qubits are thus required.

All the above quantum computations assume nearest-neighbouring qubit connectivity. It has been shown that a full qubit connectivity can reduce the resources needed [89]. A better gate fidelity can also greatly reduced the physical qubits overhead. New error correction codes and algorithms will be proposed. So it is a bit early to say with confidence how may physical qubits we definitely need to achieve practical fault-tolerant quantum computing. But, as a minimum, tens of thousands of physical qubits seems necessary and more qubits are always helpful in solving more problems. None of the physical platforms so far is anywhere close to such a goal. So scalability is a big challenge for all platforms, and it is something we have to tackle. It is fairly clear that in all the platforms it is difficult to achieve a million well-behaved qubits in one single module (or computational unit). Therefore, as well as the efforts towards scaling the number of qubits in a single computational site, physicists are starting to try to connect different modules in a fast and reliable way. It's like connecting together the different processors in a massive multi-CPU supercomputer. This is called

a networked quantum computation. Each module in the network should be able to be independently built and tested, and its performance should not be degraded when connected to other modules.

The way to achieve large scale quantum networks is platform dependent. Different platforms may have very distinctive approaches. In this thesis, I will focus on two examples of the most well developed physical platforms and discuss the obstacles on their way to scalable quantum computing. They are the photonic system and the ion trap system.

2.2 Linear optical quantum computing (LOQC)

2.2.1 Quantum computing with photonic qubits

2.2.1.1 Light quantum as quantum bits

Using photons as carriers of qubits is a promising approach to quantum networking because they naturally combine quantum computing and quantum communication which distributes quantum information across different computational modules. Another important advantage of photonic qubits is that photons interact very little with the environment so the photonic quantum state is in principle free from decoherence.

A photon has multiple degrees of freedom (commonly referred to as "modes"). Two of them are widely used in photonic quantum computing: the polarisation modes and the spatial modes. If the qubit $|0\rangle$ and $|1\rangle$ are represented by photon polarisation H and V, we call this qubit a polarisation qubit. If the logic qubit (L) is represented by the choice of two different spatial rails $|0\rangle_L = |0,1\rangle_r$, $|1\rangle_L = |1,0\rangle_r$, where $|0\rangle$ and $|1\rangle$ are the photon occupation number of each rail, we call this type of qubit a dual-rail qubit. The advantage and disadvantage of these two kinds of qubit is dependent on the quantum gate implemented and they can be transformed to each other very easily by a polarised beamsplitter.

There are other kind of qubits, for example, time bin qubits. These qubits are encoded on the arrival time of the photon as "early" or "late". But it is difficult to implement any single-qubit operation with it. Compared with dual-rail qubits, single-rail qubits use vacuum and single-photon states on the optical path to encode quantum information. Quantum information can also be processed using weak coherent states $|\alpha\rangle$. This model is called optical continuous variable quantum computing.

In this thesis I will only focus on polarisation qubits and dual-rail qubits.

One major concern about photonic qubits is that photons do not tend to interact with each other. The non-linear effect at single-photon level is so weak that it is not straightforward to implement two-qubit gates. Therefore different approaches have been proposed to use only linear optics for multi-qubit gates.

2.2.1.2 Linear optics and non-deterministic quantum gates

Linear optics are the most common, simple and economical optics. They are called linear optics because their Hamiltonian is independent of the intensity of the input light. Thus the output of the device is linearly dependent upon the input. The main linear optics used for quantum computing are phase shifters, beamsplitters (polarised or non-polarised) and wave plates.

A phase shifter changes the phase of the electromagnetic field in a given mode:

$$\hat{a}_{out} = e^{i\phi}\hat{a}_{in} \tag{2.6}$$

with the Hamiltonian $H = \phi\hbar\omega\hat{a}^{+}\hat{a}$. Experimentally, a phase shifter is just a slice of a material transparent to the photon with a refractive index different from that of air.

A beamsplitter is a semi-reflective mirror which splits a input photon into a transmission port and a reflected port. If the probability amplitude of transmission and reflection is $\sin\theta$ and $\cos\theta$ and the relative phase is ϕ, the field operators evolution are then:

$$\begin{aligned} \hat{a}^{+}_{\text{out}} =& \cos\theta\hat{a}^{+}_{\text{in}} + ie^{-i\phi}\sin\theta\hat{b}^{+}_{\text{in}}, \\ \hat{b}^{+}_{\text{out}} =& ie^{-i\phi}\sin\theta\hat{a}^{+}_{\text{in}} + \cos\theta\hat{b}^{+}_{\text{in}}, \end{aligned} \tag{2.7}$$

where $\hat{a}_{\text{in}}$ and $\hat{b}_{\text{in}}$ are the annihilation operators of the field at the beamsplitter input ports.

Wave plates have the same Hamiltonian as that of a beamsplitter, only that $\hat{a}_{\text{in}}$ and $\hat{b}_{\text{in}}$ now represent the annihilation operators of the two orthogonal polarisation modes.

The above devices are sufficient to implement any single-qubit rotation [130].

In the polarisation and dual-rail representations, single-qubit operations can be implemented deterministically. However, for an entangling gates for example:

$$|HH\rangle \rightarrow \frac{1}{\sqrt{2}}(|HV\rangle + |VH\rangle), \tag{2.8}$$

A two-qubit gate is required. Linear optics operate on each qubit independently of the other, so the output qubit is a separable state, therefore it is impossible to achieve such a two-qubit gate in a deterministic way using only linear optics.

In the single-rail representation, the entangling gate is straightforward:

$$|01\rangle \rightarrow |01\rangle + |10\rangle. \tag{2.9}$$

This is just a beamsplitter. However, it is impossible to implement single-qubit operations deterministically because such operations do not preserve photon number.

The arguments above suggest that we cannot perform single-qubit and two-qubit operations deterministically at the same time with linear optics. It has to be a probabilistic process. If the success probability of one two-qubit gate is p, the success probability of N gates is p^N, which exponentially decreases to 0. This is the major concern of optical quantum computing and it is only until the proposal of KLM protocol (explained briefly later) when it became a candidates for realistic quantum networking. In this protocol, operation probabilities can be increased to near unity by making a projective measurements on a large number of physical qubits for one logical qubit. This measurement based scheme (KLM scheme) inspired many protocols, which focus on reducing the large physical qubit overhead.

2.2.1.3 Near-deterministic quantum gate protocol

To understand how to construct a near-deterministic quantum circuit from non-deterministic gates, we should first understand quantum teleportation:

A. Quantum teleportation

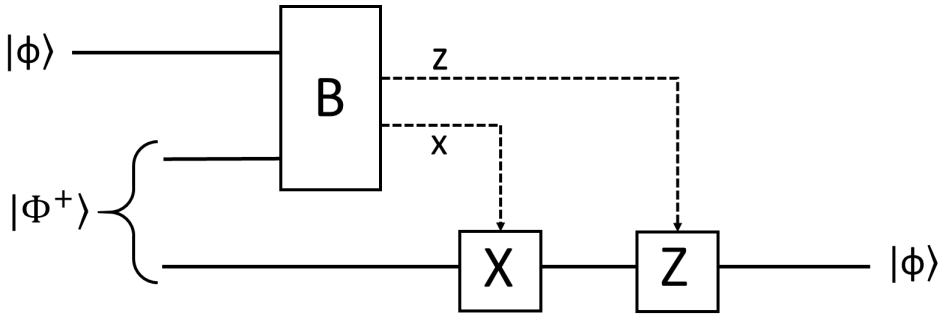

Figure 2.2: Quantum teleportation. $|\Phi^+\rangle$ is the Bell state $|00\rangle + |11\rangle$, $|\phi\rangle$ is the qubit to be teleported. B box is a Bell state measurement, with x, z $\in \{0, 1\}$ the binary representation of the measurement outcome. X, Z are single qubit Pauli operations.

Quantum teleportation transports an unknown qubit $|\phi\rangle$ from one carrier (Alice) to another (Bob). Before the teleportation, Alice and Bob share a pair of maximally entangled qubits, for example, Bell pair $|\Phi^+\rangle$. Alice then implements a Bell measurement on the the qubit $|\phi\rangle$ and one of the Bell qubits. The Bell measurement has two outputs $x, z = 0, 1$. Alice sends the value of x and z to Bob. Depending on the value of x and z, Bob implements (or not) a Pauli X gate and Pauli Z gate on the Bell qubit on his side. The output qubit is $|\phi\rangle$.

B. Teleportation trick and KLM protocol

In 1999, Gottesman and Chuang [53] proposed to use teleportation to remove the probabilistic gate off-line. The idea is to implement a two-qubit quantum gate on prepared Bell states multiple times off-line until it succeeds, before teleporting the result up to the quantum circuit.

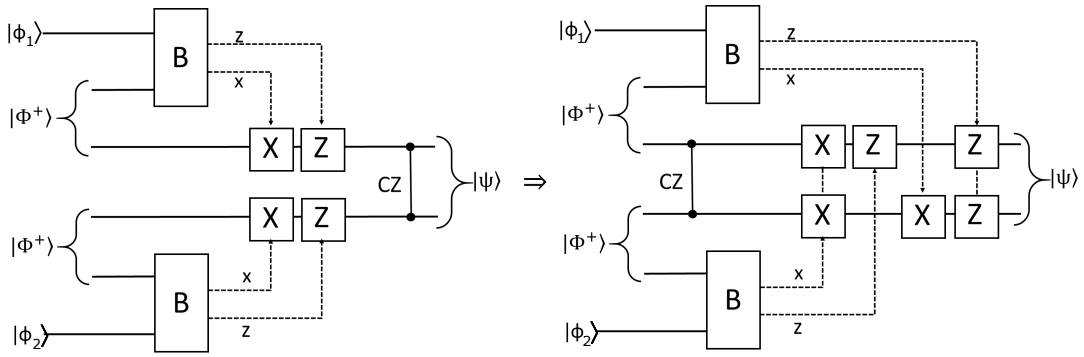

Figure 2.3: Teleportation trick. When we apply two CZ gates to two teleportation qubits, it is equivalent to applying the CZ gate on the Bell states with added single-qubit gates.

The left diagram of Fig.2.3 is applying control Z (CZ) gate to the transported qubit $|\phi_1\rangle$ and $|\phi_2\rangle$. In principle it can be any gate, and we are just using a CZ gate as an example. We can commute the CZ gate with X, Z gate with added single-qubit gates. The probabilistic CZ gate is moved before X, Z gates and therefore can be implemented offline with the two Bell states. However, the Bell measurement itself is a probabilistic measurement with linear optics. So we just move the probability from the circuit to the Bell measurement. We seemed to to be back where we were until near deterministic teleportation was proposed by Knill, Laflamme and Milburn in 2001 [78].

KLM protocol uses $2n$ entangled qubits as ancillas, instead of two Bell states. A quantum Fourier transform followed by measurement of the output is implemented instead of Bell measurement. The success probability of two qubits teleportation is $n^2/(n+1)^2$, which asymptotically converges to 1. We now have a near deterministic teleportation and thus deterministic two-qubit gate with only linear optics with the cost of large number of ancilla entangled qubits. The problem now is more technical: how to efficiently generate this large number of single-photons at the same time. This can be a problem as difficult.

2.2.1.4 Boson sampling

A universal linear optical quantum computing is possible as we have shown in previous section. However, it is experimentally very challenging. First we need to prepare and synchronize a large number of entangled single-photons for just one logic gate. Then we need to store them in a quantum memory until they are called by the quantum circuit. We also need tunable beamsplitters and phase shifters with precise control. After we implement quantum Fourier transform and the measurement, we need to control and implement the single-qubit gate according to the measurement result very fast before the photon qubit is lost. Finally we need to make the measurement with very high efficiency. There is still a long way to go before we tackle all the technical problems for optical quantum computing.

However, if we compromise the universality of the quantum computing, we can solve certain problems more efficiently than classical computer with modest experimental challenges. A popular example is Boson sampling where only single-photon sources, passive linear optics and photon detection (which doesn't need to be perfect) are required. Boson sampling (Fig. 2.4) is a problem designed to be easy for optical quantum computing but difficult for classical computer.

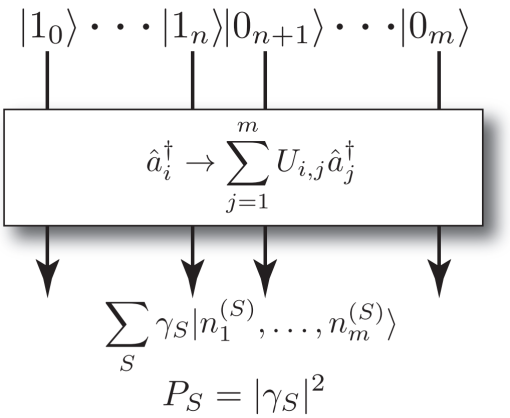

Figure 2.4: Boson sampling [45].

Imagine a black box with m inputs and m outputs. Each of the first $n(< m)$ inputs has one single-photon while the rest has vacuum as input. The Black box is made of linear optics potentially interconnecting all m channels. The ith$(< n)$ input photon is represented by a creation operator on the ith$(< n)$ mode: $\hat{a}_i^+$, its corresponding output is an unitary transformation of the creation operator:

$$\hat{U}\hat{a}_i^+\hat{U}^+ = \sum_j U_{ji}\hat{a}_j^+ \tag{2.10}$$

The Unitary transformation $\hat{U}$ is determined by the linear optics network black box. The output of an input state $|\psi\rangle_{in}$ is represented by the tensor product of all n single-photons. We end up in:

$$|\psi\rangle_{\text{out}} = \sum_S \gamma_S |n_1^S n_2^S, ..., n_m^S\rangle \tag{2.11}$$

where S stands for an output configuration. For example, if the last n output ports each has one photon while the rest have vacuum, this is an output configuration and γ_S is its probability amplitude. The question now is to calculate this probability amplitude γ_S. It is shown by Scheer [123] that γ_S are related to matrix permanents $\text{Per}(U_S)$, where U_S is an $n * n$ matrix with elements defined by U_{ij}. This problem is known to be $\#P$-complete problem which is even harder than NP-complete problem. The best algorithm requires $2^n n^2$ step to solve by classical computer. However, This distribution can be estimated by repeating the experiment multiple times. The goal is to sample the distribution with finite measurements.

The experimental implementation of Boson sampling is much easier than universal optical quantum circuit with KLM protocol. It only consists of three components: single-photon sources, passive linear optics and photon detectors. Linear optics are

very simple optics that can be integrated as waveguides on a chip to achieve a stable, scalable linear optics network. Bucket single-photon detectors are also very efficient in IR wavelength. The most challenging component so far is good quality single-photon source, which is a booming field in quantum technology.

2.2.2 Scalability of Single-photon source (SPS) for LOQC

We have, quantitatively, introduced the main protocols for linear optical quantum computing. Regardless of the probabilistic nature of photonic qubit, the KLM scheme enables a near deterministic, thus scalable, quantum circuit. Boson sampling is an classically hard problem but can be estimated efficiently by photonic quantum network. Compared with universal linear optical quantum computing like KLM scheme, Boson sampling has much less requirement of resources.

Both the KLM scheme and Boson sampling require synchronized single-photons to start with. It is the first, and probably the most important technical challenge for a scalable photonic quantum network. In this section, I will explain what is a single-photon source and how to characterize the quality of it. Then I will briefly introduce different types of single-photon sources with a critical point of view and finally highlight a promising candidate for scalable single-photon source - quantum dots.

2.2.2.1 Characterising an SPS

We borrow the definition of a single-photon source from Mark Oxborrow [111]:

A device for ensuring that one or several spatial-temporal modes will, after the source has acted on them, contain precisely one photon, where the spatial-temporal modes in receipt of the photon can be selected by, or are at least known to, the experimenter in advance of the said photon's detection.

This definition focuses on two points, firstly "*one photon*", secondly "pre-known spatial-temporal mode(s)", which help to characterise and to categorise an SPS.

The concept of an ideal SPS varies depending on the application of it. However, according to the definition, an SPS should have at least the following two features:

(1). Single-photon statistics. When the user of an ideal SPS is expecting a photon to be emitted, there should be zero probability of having more than 1 photon. This is described by zero-time second-order correlation function $g^{(2)}(\tau = 0)$ which is measured by Hanbury Brown and Twiss experiment [55]. The light field is sent to a 50:50 beamsplitter and two single-photon detectors D_1 and D_2 are on the two

output ports of the beamsplitter. The measurement of the two detectors are sent to electronics to record the delay time between the two clicks of the detectors. The zero-time second-order correlation function is given by:

$$g^{(2)}(0) = \frac{\langle a^+ a^+ aa \rangle}{\langle n \rangle^2} = \frac{N_{coin}}{N_1 * N_2} \tag{2.12}$$

where N_{coin} is the coincident counts (probability) when the delay time is 0, N_1 and N_2 are the detection counts (probability) of the detectors D_1 and D_2. $g^{(2)}(0)$ is related to the two photon probability p_2 by:

$$g^{(2)}(0) = \frac{2p_2}{p_1^2} \tag{2.13}$$

assuming that the probability of having more than two photons is negligible.

(2). Deterministic emission. This echos with the "pre-known spatial-temporal mode(s)" in the definition. An SPS user should know exactly when the photon is coming in order to trigger the next quantum operations. This "pre-knowledge" can be a fixed time sequence, which makes the SPS a "*deterministic source*", or can be heralded, which is called a "*probabilistic source*". Ideally, we should aim at "*deterministic source*" because the pre-programmed time sequence makes single-photons multiplexing very efficient, which is important for large scale quantum information processing. However, "*deterministic source*" is very challenging and still far from practical, even though tremendous progress has been made in the last decade.

The figure of merit to characterise a "*deterministic source*" is the source Brightness defined as:

the probability of having one or more than one photon per trial.

The reason for including "more than one photon" is due to the fact that it is very difficult (or impossible for now) to efficiently resolve photon number.

For some applications like short distance quantum communication, $g^{(2)}(0)$ and Brightness (B) are sufficient to characterise. Whether the photon is in single or multiple temporal modes is irrelevant. This is because the qubit for quantum communication is usually in a Hilbert space orthogonal to temporal mode Hilbert space. Also, there is no quantum interference involved in these applications like quantum communication. So any difference or mixture of the temporal mode wouldn't make a difference. However, for most other applications which require photon indistinguishability, any mixture or uncertainty of the photon temporal modes result in a degradation of operational fidelity. Examples include quantum repeater for long distance quantum communication or photonic quantum computing. Indistinguishability

is defined by the wavepacket overlap M measured by the Hong-Ou-Mandel (HOM) visibility V_{HOM}. Here we define two different kinds of indistinguishability to characterise the source devices:

a). *self-indistinguishability* $I^{(1)}$, the V_{HOM} of single-photons coming from the same source generated at different time

b). *inter-indistinguishability* $I^{(2)}$, the V_{HOM} of single-photons coming from different sources.

The reason of distinguishing these two figures of merit is that, in practice, for many SPS, it is different level of challenge to fabricate separate sources emitting indistinguishable photons. Increasing the quality ($I^{(1)}$) of a single SPS doesn't always mean the improvement of unification ($I^{(2)}$) of different sources.

We should point out here that $V_{HOM} = 1$ is a strong condition. It requires the photons to be the identical in all degrees of freedom, both polarisation and temporal mode. The interfered quantum field should also be in single-photon state, meaning $g^{(2)}(0) = 0$. For the rest of this Chapter, I will assume that the two photon has exactly the same polarisation. We will deal with SPS with very low $g^{(2)}(0)$, and we have already demonstrated that ORCA protocol is noise free so there is no change in $g^{(2)}(0)$ when photon pass through the atomic ensemble. So the indistinguishalibility is a figure of merit for the temporal mode degree of freedom.

2.2.2.2 Single-photon source (SPS)

Probabilistic sources

A truly deterministic SPS has been widely investigated in the last decade because many quantum information applications require it. However, different approaches have also been explored. These are called "non-deterministic sources" but can be heralded, which means that although we cannot be sure when does a single photon arrive, we will still be able to know the arrival of a photon when there is one. This is usually done by generating a pair of "correlated photons" at the same time and use one of them to herald the other. One mature, popular method involves a laser excitation of a nonlinear optical material. However, since the photon pairs are generated probabilistically and independently, more pair of photons might be generated together at the same time. When a heralded event occurs, there will be multiple photons in the heralded channel. One has to decrease the probability of generating photon pairs so that the probability of generating more than one pair of photons is much lower. These disadvantages set a fundamental limit of trading-off between

$g^{(2)}$ and *brightness* [21]. It is also very difficult to synchronize different probabilistic sources since the multi-photon probability scales exponentially with photon number.

1.Parametric downconversion The first effort of generating photon pair as light sources used atomic cascade scheme [41]. But spontaneous parametric downconversion (PDC) has been the most mature and mostly used scheme for creating correlated photon pairs during the last two decades. This scheme was first proposed by Zeldovich and Klyshko in 1969 [152] with pair correlations first observed in 1970 [139].

In a PDC process, a pump laser illuminates a material with a $\chi^{(2)}$ optical nonlinearity, creating two photons with energy and momentum conservation. This determines the possible wavevector relations between the two output photons. This is also called the phase-matching condition because the photons generated at different position of the material with the mentioned constraint are phase matched in certain direction so they constructively interfere and produce an output. There are different types of polarisation phase matching possible for parametric downconversion: type-I, where the two photons have the same polarisation, and type-II, where the two photons have orthogonal polarisation. There are many properties of the down-converted photon pairs that can be correlated, including time, energy, momentum, polarisation, and angular momentum for use in making a heralded single-photon source.

The $\chi^{(2)}$ nonlinearity can occurs in many different inorganic crystals, including, for example, KDP (potassium dideuterium phosphate, KD2PO4), BBO (beta barium borate, BaB2O4), LiNbO3 (lithium niobate), and LiIO3 (lithium iodate).

PDC sources can be engineered to the desired output wavelength and momentum. These techniques also help improve the degree of factorability of the states produced. Factorable state means that the two photons are not frequency correlated. So the detection of the heralding photon will not project the heralded photon to a mixed state.

For more details about PDC source, please refer to [26]

2. Four-wave mixing (FWM) Four-wave mixing is a $\chi^{(3)}$ nonlinear process in which two pump photons are converted into two correlated photons. It is the dominant nonlinear process in centro-symmetric materials such as glass that do not allow $\chi^{(2)}$ nonlinearity. Optical fibre with its long interaction length can be used to enhance the $\chi^{(3)}$ nonlinearity. To date, many experiments have demonstrated generation of correlated photon pairs in a single spatial mode using four-wave mixing in single-mode optical fibers [88, 36], with recent results demonstrating heralded single-photon

sources using dispersion shifted fibre (DSF), photonic crystal fibre (PCF), birefringent single-mode fibre (BSMF), and Silicon-on-insulator (SOI) waveguides. However, one issue with pair sources based on FWM is that Raman scattering produces a single-photon background that contaminates the photon statistic purity.

Deterministic sources

Most of the deterministic sources are "single emitter". It is ideally a two-level quantum system consisting of a ground stable state and an excited state. An excitation is created on-demand with certainty. A single-photon is generated when the system falls back to the ground state through relaxation or coherent transportation. A cavity is often used to direct and engineer the single-photon.

1. Single neutral atoms Single-atom emitters are designed to work in the strong-coupling regime of cavity QED. To date, alkali atoms such as Cs and Rb have been used [3, 28]. Atoms are first captured and cooled inside a magneto-optical trap (MOT). After the MOT is turned off, the atoms fall freely under the pull of gravity. When atoms pass through a high-finesse optical cavity, an optical trap is turned on to trap the atom. For a single-atom emitter, it is important to have only one atom trapped inside the cavity. The atom has a Λ-type energy level system (or similar), consisting of two stable ground states $|g\rangle$ and $|u\rangle$ and one excited state $|e\rangle$. The resonance of the optical cavity is made close to the transition of $|g\rangle$ to $|e\rangle$ and the transition of $|u\rangle$ to $|e\rangle$ is on-resonance with the pump laser pulse a STIRAP scheme is usually applied to avoid population on the excited state. Stimulated Raman adiabatic passage (STIRAP) [46] is an adiabatic population transforming protocol to optimise the photon extraction probability. Since it is a coherent process, it is reversible and the source can work both as a single-photon emitter and receiver and, because atoms are all identical, atom-based sources could be produced in quantity for a scalable system. Despite these advantages, single-atom emitters are compromised by a limited trapping time [95], fluctuating atom-cavity mode coupling [32] that can yield decoherence effects (although these effects can be made small), and possible multi-atom effects. All of these issues need to be resolved before single atoms can be used as true on-demand sources of single-photons and nodes in quantum networks.

2. Single ions Ions are atoms with positive charges. They can be used as single-photon emitters [8, 30] in a very similar way. Both neutral atoms and ions use the Λ energy level configuration which requires an initial state, an excited state, and a final

state which is another stable or meta-stable state. A pumping laser is off detuned to the transition between the initial state and the excited state while an optical cavity is off detuned to the final state and the excited state by the same amount. A single photon is generated when the ion population is transfer from the ground state to the final state adiabatically. The main difference between ion and neutral atom system is the way they are captured and stabilised. Trapped ions can be stably localized at the center of the optical cavity with the capability of confining the ion's motional wavepacket to a region much smaller than the optical wavelength and fixing the wavepacket position with a precision of a few nanometers. However, because the ground-state dipole transitions of ions are typically in the ultraviolet region, the excited states have strong spontaneous decay rates that compete with the emission of radiation into the cavity mode. This factor can seriously reduce the probability of emitting a single-photon during each pumping cycle. As with single neutral atoms, single ions as the basis of a single-photon source have the advantage that they are all identical, and thus indistinguishability between different sources and different pulses from the same source is not an big issue. In addition, achieving low levels of multi-photon emission and low decoherence does not seem to be inherent problems with ion-based systems. However, as we will show in Chapter 4, spontaneous process can introduce temporal mode mixing which may decrease the indistinguishability depending on the ion level choice and cavity parameter. Furthermore, it is difficult to push ion-cavity system into strong coupling regime because aligning the cavity too close to the trap area will introduce disturbance to the trap potential [113]. Strong coupling has been achieved recently but in a non-scalable end-cap trap [140].

3. Single molecules The photon anti-bunching in a single-molecule system was first observed in 1998 [17, 77]. Single molecules in solid and liquid host as single-photon source has been studied intensively since then. The molecular transition, same as many other deterministic SPS, involves two approximate 2-level system, a singlet ground state $|S_0\rangle$ and a singlet excited state $|S_1\rangle$. Each state represents a set of vibrational energy levels. An electron in the ground state is optically pumped to the excited state and them de-excited to the ground state, emitting a single photon. One can either use a short pulsed laser [91] for the excitation or use a cw pump laser to the molecule, while sweeping an external electric field to shift the molecule's absorption line on and off the laser frequency through the Stark effect, a periodical single-photon emission is thus achieved. A molecule can be put in a cavity to manipulate the emission [136]. So far single-molecule-based sources have only demonstrated

relatively poor $g^{(2)}(0)$ values and photon indistinguishability between photons of the same molecule [76].

4. Solid-state single-photon emitters Solid-state single-photon emitters use defects in the material to create a localized two-level system. It mainly includes fluorescent atomic defects and quantum dots (QDs). But the complex mesoscopic environment of the solid-state also introduce numerous challenges, including inhomogeneous distributions of defects causing variability between photons from different emitters, homogeneous linewidth broadening increasing photon distinguishability from the same emitter. In addition, the extraction of photons, particularly from emitters in host materials with high a refractive index, for example, diamond, is challenging.

Different kinds of material have been explored. The most studied are colour centres in crystals such as nitrogen-vacancy (NV) and silicon-vacancy (SiV) defects in diamond, the self-indistinguishability is rather low with HOM visibility of $\approx 70\%$ [131, 132]. Another candidate for solid-state single-photon emitter is two-dimensional materials, for example, transition metal dichal-cogenides (TMDCs) [57] in which the quantum defects are ascribed to localized, weakly bound excitons, and hexagonal boron nitride (hBN) [142] in which single-photon emitters have been associated with defects within the bandgap. Carbon nanotubes (CNT) [68] have been shown to host single-photon emitter which supports telecom wavelength emission.

2.2.2.3 Quantum dots as an SPS

Perhaps semiconducting quantum dots (QDs) are the most promising deterministic SPS so far, among which InAs/GaAs QD has the best overall performance.

QDs are local "defects" on semiconductor materials, with a local bandgap smaller than the surrounding semiconductor, creating a localized two-level system. We take InAs based QDs as an example, InAs and GaAs are covalently bonded direct-bandgap semiconductors, where the bandgap energies are $E_g(\text{InAs}) = 0.43eV$ and $E_g(\text{GaAs}) = 1.52eV$ at $4K$. The 7% lattice-constant mismatch between GaAs and InAs precludes the typical epitaxial planar-crystal growth process. When more than 1.7 monolayers of InAs is deposited on GaAs, a planar layer forms—called the wetting layer which is biaxially compressed to the GaAs lattice. As crystal growth proceeds, the accumulated strain energy increases, a transition occurs and the total energy is minimized by creating InAs islands as shown in Fig 2.5a. By stopping the growth right after this transition, the islands are typically 10–30 nm lateral size in the in-plane

directions and 2–5 nm out of plane [133]. When further covered with epitaxial GaAs, three-dimensional quantum confinement shifts the lowest optical transitions in the 900–1,000 nm wave-length range at 4 K [35]. The transitions can be brought to $1.3\mu m$ for large QDs covered in InGaAs. InGaAs QDs naturally have a slight asymmetry in their in-plane shape. Other QD growth techniques, such as droplet epitaxy [149], can be used to obtain higher symmetry QDs[81].

Apart from QDs InGaAs for near-infrared emission, other materials have also been widely investigated in the past decade, such as GaAs for emission in the red spectral range [42], and II–VI telluride or selenide-based QDs [25], as well as nitride based III–V QDs [59], for emission in the green to ultraviolet spectral range. Depending on the band-gap, single-photon emission is achieved at temperatures ranging from cryogenic to room temperature.

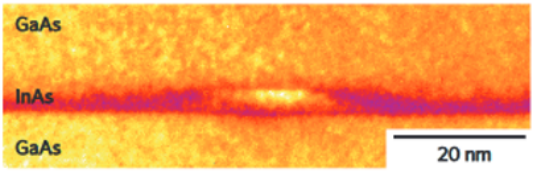

(a) Transmission electron microscopy of a single self-assembled InGaAs quantum dot

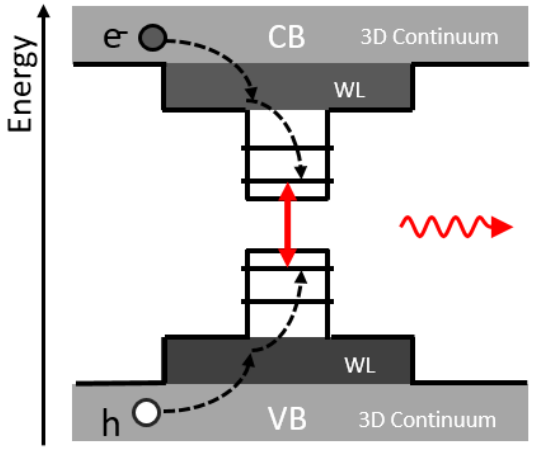

(b) Energy level of QD

Figure 2.5: The image of a quantum dot and its energy level.

The strong quantum confinement in QDs leads to discrete energy levels for both electrons and holes. Carrier localization and Coulomb and exchange interactions lead to excitonic many-body states. Pauli exclusion leads to a ground-state manifold (Fig.2.5b) consisting of: two optically bright excitons $|X\rangle$: one electron and one hole with projection of the total angular momentum along the growth axis $J_z = \pm 1$; a single bright biexciton, $|XX\rangle$: two electrons and two holes; and two charged excitons

known as trions: single excitons containing either an excess electron $|X^-\rangle$ or hole $|X^+\rangle$.

In weak excitation, only one exciton $|X\rangle$ is generated and single-photon is emitted when the QD decays back to the ground state. Single epitaxial QD was first produced in 1994 [35] and single-photon emission was demonstrated in 2000 [96]. There are two pumping scheme of QD. Non-resonance pumping will excite the electron into the wetting layer. The the carriers diffuse to the QD states through carrier collisions and optical phonon emission. A single-photon is thus generated.

The initial carriers have a decay time, which are required to be much shorter than the exciton recombination time to retain the quantum coherence of the emitted photon [39]. This is very challenging so another approach is being explored, the electron can be directly excited into an excited state of the QD. Under strictly resonant excitation, such considerations no longer apply and values of $g^{(2)}(0)$ below 1% have been reported [31, 144]. However, direct excitation scheme is generally less bright because it is difficult to filter the pumping laser from the single-photon.

QDs are so far the system closest to a deterministic SPS. However, QDs (as well as other solid-state sources [1]) suffer from fast local environmental fluctuations that contribute to pure dephasing of the QD. Furthermore, electron-phonon interactions will also result in the decoherence of each emitted photon, which limits the indistinguishability, $I^{(1)} < 1$ even at 0 K and in the weak excitation regime [70, 65]. To suppress these dynamics as well as to direct emission, QDs are typically embedded in waveguides [24, 4] or micro cavities [134, 90, 31, 48]. However, there remains a trade-off between brightness and indistinguishability, as explored in [66].

To achieve scalable photonic quantum network, universal or not, we need to indistinguishable (both $I^{(1)}$ and $I^{(2)}$) multiple single-photons. Even the most promising single-photon source platform is far from this goal. Maybe it is time to think about a compromised approach which, instead of improving the fabrication of single-photon source itself, utilizes an external buffer to purify and unify different sources. This idea will be discussed in detail in Chapter 3.

2.3 Ion trap quantum computing

Using trapped ions for quantum computing was first proposed by Cirac and Zoller [22]. It is one of the most promising platforms because of the long trapping lifetime, long coherence time, strong ion-ion interaction and compatibility with room temperature operation. Single qubit operations [15], two-qubit operations[9], qubit

state preparation and measurement [104] have all been experimentally achieved with fidelities exceeding the threshold for fault-tolerant quantum computing [52]. In this section, I will introduce the basic trap design, qubit encoding and implementation of qubit operations. With this knowledge, we will discuss the approaches and challenges of scaling the qubit number. The second part of this section focuses on one of the scaling approaches in detail.

2.3.1 Trapped ions as quantum bits

2.3.1.1 Trapping the ions

Producing a static, three-dimensional potential minimum for charged particles is not possible because the divergence of static electric field in vacuum is zero. However, it is possible to use either a combination of a static electric field and a magnetic field or a dynamic electric field to achieve time-average localized trapping potential. The exact trapping dynamics and ion equations of motion is well developed and details can be reviewed in many papers and textbooks[85]. In this thesis, I will only give a summary and focus on the physical interpretation and the trap designs.

There are two commonly-used types of ion trap: the Penning trap, and the Paul trap. A penning trap uses a static electric field to confine the ions in one spatial axis, while a homogeneous magnetic field is applied along the axis to impose radial confinement. Penning traps have the ability to maintain large, two-dimensional ion crystals. However, these ions rotate at a constant angular velocity and it is therefore not easy to address only one ion at a time. Another type of ion trap is the Paul trap, where an oscillating electric field is applied to form a pseudopotential confinement in two or three dimensions. In the two-dimensional case where the potential is cylindrically symmetric, an additional static electric field is applied to achieve confinement along the axis. In a Paul trap, the ions are stable apart from small local motions. So it is more straightforward to address single ions and implement qubit operations. Indeed, most state of art ion trap quantum computing is achieved in Paul traps. In the rest of the section, I will only focus on Paul trap design and its variations.

As illustrated in Fig.2.6(a), the RF electric field forms an anti-confinement potential in at least one spatial dimension at any instant in time - the ion is not stable in this dimension and tends to escape. However, in the next half of the RF period, the confinement configuration changes sign and the previous anti-confinement direction becomes confining. When the ion mass, RF frequency and other trap parameters are within certain ranges, a time-averaged confinement in all directions is formed. The

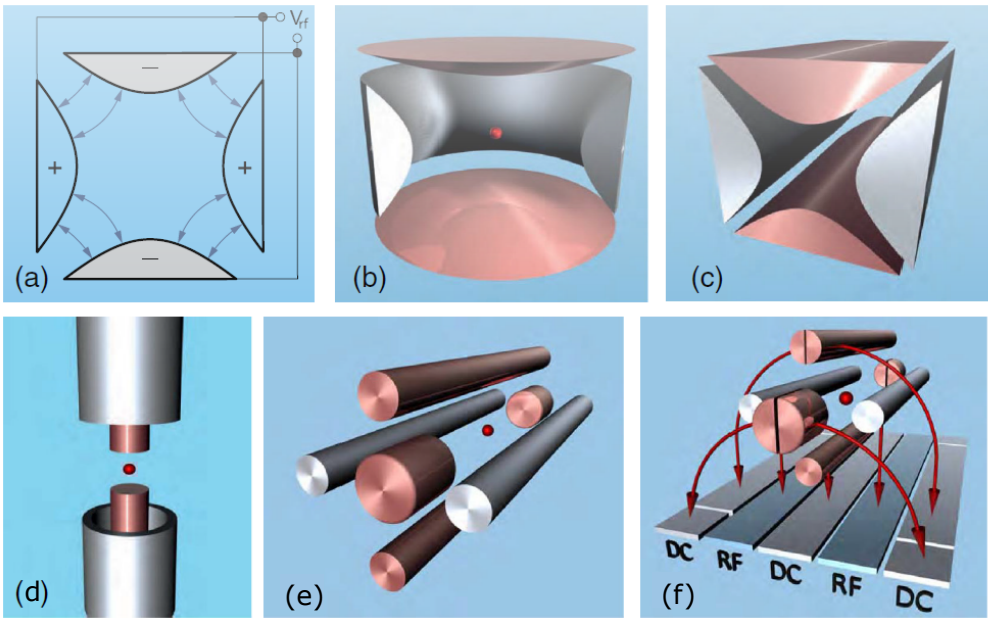

Figure 2.6: (Reproduced from [18].) RF Paul trap design. (a). The basic concept of RF Paul trap. Quadrupolar electrodes produce RF field oscillation. (b). The ideal point trap with hyperbolic electrodes. (c). Linear Paul trap with hyperbolic electrodes. (d). a variation of point trap with concentric RF electrodes. (e). a variation of 3D linear Paul trap where RF electrodes are four symmetrical rods with two cap electrodes at both end of the cylindrical axis.(f). surface trap design.

motion of the ion in a Paul trap satisfies the Mathieu equations [151]. The solution to the Mathieu equation depends on the exact geometry of the trap. For the sake of understanding the basic physics, we take the rod Paul trap shown in Fig.2.6e as an example. The resulting equations of motion in r_i axis are as follows: [23]:

$$\begin{aligned} r_i =& x_0 \cos(At + \phi_i)(1 + B\cos\Omega t) \\ A =& \frac{eV_0}{\sqrt{2}\Omega M r_0^2} \\ B =& -\frac{eV_0}{M\Omega^2 r_0^2} \end{aligned} \tag{2.14}$$

where V_0 is the peak RF voltage, Ω is the RF frequency, M is ion mass, r_0 is the distance between the electrode and the ion. When the solution is stable, the ion motion can be decomposed into two motions. One called "secular motion" is a bounded harmonic motion with frequency A. The other motion is imposed upon the secular motion with frequency the same as the RF. The trap is stable only when this motion is much smaller than the secular motion ($B << 1$) and thus it is called the "micromotion".

There are two main configurations of Paul trap. The first one is called the point trap. The area where electric field is zero is only one spatial point. The ideal electrode configuration matches the potential surfaces, and such an arrangement is shown in Fig.2.6b. But in real experiments, different forms of electrodes are used to make the fabrication simpler and, more importantly, offer more optical access to the trap region for qubit operation. A popular deformed electrode for point trap is called the "endcap" trap Fig.2.6(d), where RF potential is applied between two rings and two cylindrical electrodes placed concentrically along its line of cylindrical symmetry.

The second type is called the linear trap. It removes the third dimension of RF-pseudopotential confinement by making four hyperbolic electrodes with cylindrical symmetry (Fig. 2.6(c)). The RF field is zero along the cylindrical axis. To achieve a confinement along this direction, a static electric field is applied by adding two endcap D.C. electrodes at the two ends of the axis. A harmonic potential is formed along the axis. This configuration can trap an ion chain along the axis with the positions of the ions set by the equalization between the harmonic trap force and the Coulomb repulsion between the trapped ions. There are various forms of Paul trap. The four electrodes can be replaced by four rods or blades (Fig.2.6e). The 3D electrode can even be deformed onto a 2D surface. This is known as the "Surface trap"(Fig.2.6f), which benefits from standard lithography fabrication technology and larger optical access, at the expense of trap depth and increased anharmonicity.

Another important technical problem is ion loading. In most ion trapping experiments, ions are loaded from an atomic oven either through resistive heating [6], pulsed laser ablation [128] and optical heating [43] which is more efficient and amenable to miniaturisation and cryogenic operations. An optically heated atomic oven has very low heat dissipation and it can keep running for thousands of years once integrated into the vacuum chamber. Ionization is achieved by two-stage photo-ionisation [93]. Alternative photoionization pathways that use a larger number of lower energy photons have been explored to reduce the stray fields due to charging [153].

Ions need to be initialized before any qubit operation. The initialization is typically accomplished by laser cooling of the ions towards the motional ground state, followed by optical pumping of the system to one of the internal qubit states. To understand these process, we need to start with an introduction to the ion internal and external states.

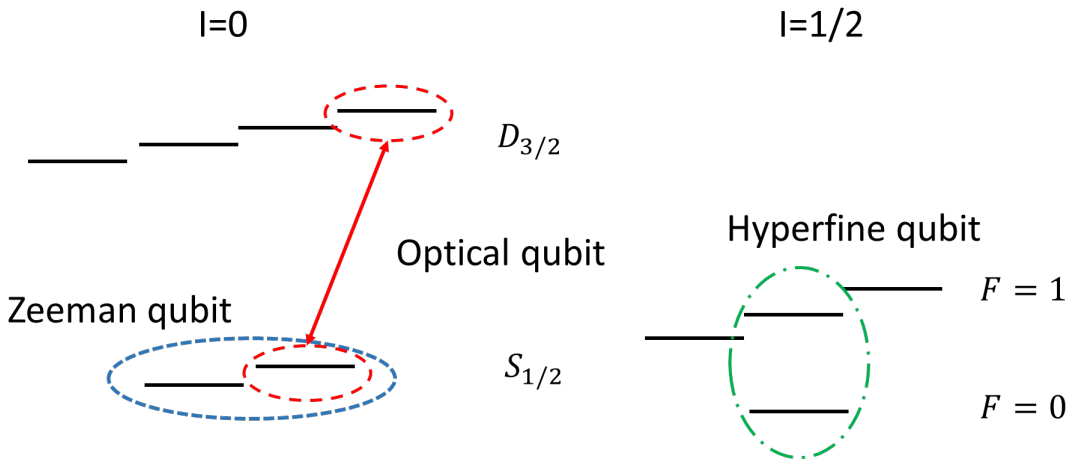

Figure 2.7: Ion level schemes in the presence of magnetic field. I is the nuclear spin

2.3.1.2 Ion states as qubits

A. Qubit state

It is natural to choose Group-II or Group-II-like atoms for quantum computing. There are two valence electrons for this sort of atom, one of which is left after the atom is ionized, leading to an electronic energy level structure that is simple compared with other groups. The choice of qubit levels can be any combination of two long-lived or metastable ion internal states. These internal states could be the ground state hyperfine levels coming from coupling between electron and nuclear spins, which have near-infinite lifetime. Alternatively, low-lying D or F levels are metastable states that have a life time in the time scale of seconds or longer. Another choice of qubit levels are the Zeeman sublevels in the presence of an external magnetic field. Fig.2.7 shows the ion levels that can be used for encoding qubits.

Zeeman qubits Zeeman qubits are qubits encoded on the Zeeman sublevels of the same orbital, and are generally used in even-isotope ions, without hyperfine structure. The qubit frequency splitting depends upon the applied field and g-factor, but is typically in the 10-500MHz range. The advantage of the Zeeman qubit is that the level structure is very simple and the state preparation is straightforward. The disadvantage of Zeeman qubit is that it is sensitive to magnetic field fluctuation. Magnetic field fluctuation leads to qubit dephasing and thus a hit in coherence time. Great efforts have been made to stabilize the magnetic field and a coherence time of 300ms has been achieved by using a magnetic shield and permanent magnets for field production [120]. The coherence is limited by residual thermal fluctuations affecting

both the shielding metal and the magnetic moment of the permanent magnets, so significant improvement may require better temperature control and/or new materials with better magnetic properties. Another disadvantage is that state discrimination is not straightforward because the Zeeman energy splitting is often too small for frequency-selective direct excitation.

Hyperfine qubits For odd-isotope ions, electron angular momentum is coupled with nuclear spin, forming hyperfine levels with gigahertz energy separation between the electronic ground states. The biggest advantage of using a hyperfine qubit is the existence of "clock transitions". The simplest of these lie between the $m_F = 0$ states of two hyperfine manifolds, the frequency splitting of which is insensitive to magnetic field fluctuations when B=0. Even better performance can be found using high-field clock-transitions, such as the $\{F = 4, m_F = 0\} \rightarrow \{F = 3, m_F = +1\}$ transition in $^{43}Ca^{+}$, which has a vanishing first-order field dependence for fluctuations at about B=146G, where the frequency separation of the two qubit states is at a minimum. The use of such field-insensitive states reduces the necessity for the extreme field stabilisation measures for high-quality Zeeman qubits, although a well-controlled field (whether small B=0G or, e.g., B=146G) must still be applied to ensure the clock-transition condition is maintained and a stable quantization axis is defined. "Clock-qubits" of this sort are often so insensitive to magnetic field fluctuations that phase noise on the microwave oscillator becomes the limiting factor [126], and coherence times of up to 1hr have been recorded when using dynamical decoupling techniques to suppress slow drifts [147]. State discrimination is straightforward for hyperfine qubits because of the relatively large energy splitting between two qubit states. The disadvantage is that "clock-state" initialization is more complicated because of the existence of the other Zeeman levels other than $m_F = 0$. The existence of hyperfine structures in the P and D state also means that we need more laser frequencies for state preparation and measurement.

Optical qubits Optical qubits, as the name suggests, are qubits encoded on ion levels separated by the energy of an optical frequency photon. They consist of one ground state and one metastable state in a low-lying D level. Optical qubits benefit from near-unit detection efficiency based on electron shelving [105]. The drawback is that qubit operations rely on narrow-linewidth optical fields and are typically limited to 1s coherence time due to the natural decay of the metastable state. An important advantage of optical qubits in terms of scalability is that the optical fields used for

qubit operations are red or near IR for most ion species of interest. This is favourable for any on chip fabrication for optical delivery.

B. Motional state

One important feature of trapped ion qubits is the ease with which their internal, electronic states can be coupled to their motional states, which are harmonic oscillations in the trap potential. The trap potential frequency is usually in the megahertz range, which sets the energy splitting between the motional states.An optical field blue (red) detuned from the qubit frequency by an amount equal to the trap frequency will periodically create (annihilate) single motional quanta - phonons - in this way, lasers can be used to excite the internal electronic levels dependent upon the ions' external motional states, and conversely, a phonon can be excited dependent upon the ion's internal state. With multiple ions in the same trap, the motion is shared with all the ions, forming phonon modes within an ion crystal. This is the main component for multiple qubit gate operations.

2.3.1.3 Qubit state operations

A. State preparation

State initialization is done by optical pumping. The exact pumping scheme is dependent on the species and qubit level choice, but all generally use photon absorption and emission cycle with selection rules. Emissions to unwanted initial state will be repumped until the quantum state is sequestered to the desired state with large probability. State initialization errors of 10^{-4} can be achieved [56].

The motional state of the ions should also be initialized to near-ground state. This is done by Doppler cooling and then sideband cooling [99] or by EIT cooling [83].

B. Qubit gates

The way single qubit gates are implemented is determined by the type of qubit used. Optical qubits can be driven directly by a narrow-linewidth laser resonant with the qubit frequency splitting. The small splitting of a Zeeman qubit can either be driven directly by radio frequency fields, or indirectly via an optical Raman transition. For a hyperfine qubit, which is usually separated by gigahertz, we can use either Raman driving or microwaves for single-qubit operations. For details about single qubit gate dynamics, see review paper [85]

Multi-qubit gates, regardless of the gate type, are generally achieved by selectively exciting the motional modes of the ion crystal dependent upon the electronic state of the ions involved [67]. Different qubits use the shared ion motional modes as a quantum bus to transfer quantum information between them. A different approach is based on ion remote entanglement between different ion trap modules. This approach will be introduced in Chapter 4.1.1.

C. State measurement

The most common approach for state measurement is state-dependent fluorescence [11]. The qubit to be measured is first transferred (via Raman, microwave or RF pulses appropriately) to either the "bright" state or the "dark" state (if it is not already in one). The bright state will scatter light if it is illuminated while the dark state does not. The light is then captured and detected for some exposure time. This approach is most suitable for optical qubit but also works for hyperfine qubits and Zeeman qubits with an increased error of off-resonance scattering because of the relatively smaller frequency difference between the two qubit states.

2.3.2 Scalability of trapped ions for quantum computing

As has been discussed in section 2.1.3, we are very motivated to scale the qubit number up to a million while keeping the gate error less than 10^{-3}. This is very challenging in any physical platform including trapped ions. Ion numbers of more than a hundred can be achieved in 2D Penning trap but they are not particularly suitable for quantum computing because of the difficulty of individually addressing the qubits. In Paul trap, a fully controlled chain of 20 ions represents the state of art [40]. Beyond this is possible with better fabrication and electronic stability but performing high fidelity operations on a register of more than 100 qubits in a single harmonic potential of a Paul trap is really difficult with current trapping and qubit gate approaches.

There are multiple reasons for the scalability challenge. The first reason is the background gas collision. Undesired collisions between background gas molecules in the vacuum chamber and the ions can cause heating of the ion crystal and scramble the quantum information. The longer the ion string is, the shorter the time between such collisions.

The second reason is spectral crowding of motional states. When there are multiple ions in the trap, their vibrational motion is shared by all ions. There are 3N

vibrational modes of motions for N ions, each with a different phonon energy.When the number of ions in the trap grows, the separation between phonon energies becomes very small, and it becomes ever harder to achieve two-qubit gate operations with high fidelity.

The third reason is the spacing problem. An increase of ion number will decrease the ion spacing. This increases the cross talk between ion when addressing each ion individually. More importantly, the spacing is not equal between the ions. This will lead to all sorts of inhomogeneity across the ion register. For example, different ions will have different coupling to the motional modes. It is very difficult to implement gate operations while ensuring all ions at different positions maintain a closed phase loop.

The fourth reason is rather technical. Most ion trap experiments so far use bulk optics to deliver lasers and collect fluorescence. It is not realistic to address each of the many ions with traditional experiment layout.

All these problems suggest that we should look for other approaches for scaling other than squeezing all the ions into one trap. One way is to integrate many surface traps within one mesoscopic chip with only a small number of ions are trapped in each trap. To implement multi-qubit gates, the corresponding ions are shuttled to the interaction region by carefully changing the voltage on the electrode to alter the trapping potential. This is called the "Quantum CCD" architecture [74]. The difficulty of this approach is how to achieve fast ion transport without "heating up" the ion. In Ref. [13], the transport speed of 50 m/s was demonstrated with only 0.1 quanta of motional excitation.

Another approach is to distribute entanglement between trap modules using photons. Ion-photon entanglement is first implemented on two physically separated modules between the ion's electronic states and the photon states. The photons are then overlapped on a $50:50$ beamsplitter to erase the "which-path" information and then detected on each output port of the beamsplitter. If the two photons are indistinguishable they will bunch to the same output port of the beamsplitter and no coincident detection occurs. If the two photons are of different state, coincident detection will happen half of the time, in which case the entanglement swapping protocol [64] succeeds and the ions in the two separate modules are projected into a Bell state, with the state produced heralded by the combination of detector clicks observed [98]. The entanglement rate is limited by the probabilistic photon collection. The rate can be doubled by discriminating the photon states during detection. This can be easily done by encoding the information on photon polarisation [100]. We will discuss this

scheme in detail Chapter 4.1. To solve the problem of low photon collection probability, a high-finesse optical cavity can be used to confine the photon mode into a Gaussian-like beam as the output of the cavity. This will be discussed in Chapter 4.2.

Apart from scaling protocols to entangle ions in different trap modules. Advances in trap fabrication are equally important. It is necessary to miniaturize each module as well as the electronic control and field delivery system.

Chapter 3

ORCA protocol for LOQC

As has been discussed in Chapter 2.2.2, multiple synchronised single-photons are essential for scalable photonic quantum network in both universal and non-universal scenarios. These photons should be pure ($g^{(2)}(0) = 0$), the source generating these photons should be indistinguishable ($I^{(1)} = 1, I^{(2)} = 1$) and bright. Non of the state of art single-photon source on any platform is close to the criteria. In this chapter, we propose a compromised approach. Instead of improve the single-photon source itself, we use a quantum buffer to purify and unify different sources. In this way, scalable single-photon sources may become achievable.

The idea is inspired by our newly demonstrated noise-free quantum memory: ORCA memory.

3.1 ORCA memory

The off-resonant cascaded absorption (ORCA) protocol [69] is a photon-atomic-ensemble interaction scheme that is used as a quantum memory (see Fig. 3.1). It has three key advantages compared to other schemes: (1) room temperature, (2) broadband, and (3) noise-free operation. The atomic level is a three-level ladder system comprising a ground state, an intermediate state and an excited storage state. The atomic ensemble is prepared in the ground state. A signal field (single-photon) is directed into the ensemble while a strong control field counter-propagates to the signal. The two fields overlap in the ensemble, satisfying a two-photon resonance between the ground state and the storage state. One atom is excited to the storage state, creating coherence between the ground state and the storage state. Characteristic of all atomic ensemble based quantum memories, the excitation is in a superposition of all the atoms in the overlapping region. The coherence is across the ensemble, carrying the temporal mode information of both the signal and the control field. This collective coherence

is called an orbital wave. Since the storage state is a non-stable state, ORCA utilized as a memory has a very short lifetime. However, lifetime is a relative concept depending on the application. Since the ORCA memory supports broad-band signals, the time-bandwidth product can still be large enough for photon synchronization protocols [109]. A big advantage of ORCA is that it's inherently noise free. The counter-propagation feature makes it very simple to filter the stray light. The ladder structure makes sure that there is no four wave mixing noise induced by the control pulse [141].

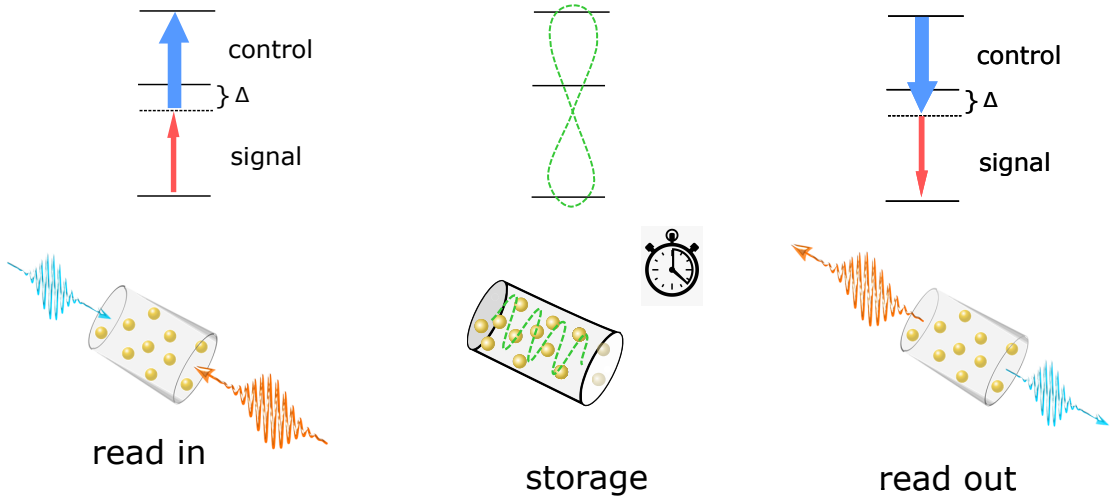

Figure 3.1: The ORCA memory. Blue arrows are the control field. Red arrows are the signal field. They form a two-photon resonance with the atom "ladder shape" energy levels. An atom is excited into the top level and the signal energy is stored in the coherence between top level and bottom level (green curve), before it is retrieved in the read out process.

In the original proposal of the ORCA memory, the signal field is on the bottom step of the ladder while the control is on the top to to avoid inadvertently driving population to the intermediate level with the control pulse. However this limits the choice of the signal frequency. If we invert the roles of the control and signal and keep the detuning larger than the signal bandwidth, we can have a larger choice of storage level and therefore signal wavelength while remaining all the advantages of the original ORCA proposal. The increase of frequency availability opens up more applications towards a hybrid system, which is important for large scale quantum networks. For the rest of this chapter, I will introduce the theory and the experiment of ORCA protocol, focusing on the new proposal.

3.1.1 ORCA theory

The ORCA system has two subsystems: the atomic ensemble and the single-photon. The control field can be seen as independent of the interacting dynamics because it is very strong and the absorption and scattering are negligible when the field is far detuned from the intermediate state.

In this section, I will fully derive the theory of ORCA protocol following five steps:

(1). Derive the Hamiltonian of ORCA system

(2). Establish the time evolution of a single atom.

(3). Establish the time evolution of the signal field (photon) temporal mode

(4). sum the contribution of all the atoms in the interaction region to get the macroscopic variables of the ensemble.

(5). verify approximation.

3.1.1.1 Hamiltonian

The interaction between a light beam with an atom is described by the electric dipole Hamiltonian $H_{\text{int}} = -\mathbf{E} \cdot \mathbf{d}$, where $\mathbf{E}$ is the electric field from the light beam at the atom position and $\mathbf{d}$ is the electron dipole moment in the atom.

The electric field $\mathbf{E} = \mathbf{E_c}(t, z, r) + \mathbf{E_s}(t, z, r)$ consists of two parts: the strong control field $\mathbf{E_c}(t, z, r)$ and the signal field $\mathbf{E_s}(t, z, r)$ which is weak and in general non-classical (e.g. a photon). We can ignore r which is the transverse position vector for both field. This is because in real experiment, we keep the control field wider in waist than the signal in order to make sure that the control field covers all signal field. Therefore, we assume that the control field is constant transversely. For the signal field, we will see soon that ORCA dynamics is linear so the field amplitude does not change the dynamics. We then have:

$$\begin{aligned} \mathbf{E_c}(t, z) &= \mathbf{v_c} \frac{E_c(t, z)}{2} e^{i\omega_c(t+z/c)} + c.c. \\ \hat{\mathbf{E}}_\mathbf{s}(t, z) &= i\mathbf{v_s} g_s A(t, z) e^{-i\omega_s(t-z/c)} + h.c. \end{aligned} \tag{3.1}$$

where $\mathbf{v_c}$ and $\mathbf{v_s}$ are the polarizations of the control field and the signal field. ω_c and ω_s are the optical frequencies of the control field and the signal field. Here we consider the situation where the signal field is a single-photon. $A(t, z)$ is the photon slow-varying temporal mode annihilation operator in the Heisenberg picture derived as follows:

The electric field of a single-photon beam is:

$$\hat{\mathbf{E}}(t, z) = i\mathbf{v_s} \int g(\omega) \hat{a}(\omega) e^{i\omega(t-z/c)} \mathrm{d}\omega + h.c. \tag{3.2}$$

where $g(\omega) = \sqrt{\hbar\omega/4\pi\epsilon_0 V}$ is the mode amplitude and $a(\omega)$ is the annihilation operator. Knowing that the central frequency of the field is ω_s and that the bandwidth of the photon spectrum is much smaller than ω_s, we can extract the optical frequency $e^{i\omega_s(t-z/c)}$ out of the expression:

$$\hat{\mathbf{E}}(t,z) = i\mathbf{v_s}\sqrt{2\pi}g(\omega_s)\left(e^{-i\omega_s(t-z/c)}\frac{1}{\sqrt{2\pi}}\int \hat{a}(\omega)e^{-i\omega z/c}e^{i\omega t}\mathrm{d}\omega\right)e^{i\omega_s(t-z/c)} + h.c. \quad (3.3)$$

The bracket in the middle is then slow-varying temporal mode annihilation operator:

$$A(t,z) = e^{-i\omega_s(t-z/c)}\frac{1}{\sqrt{2\pi}}\int \hat{a}(\omega)e^{-i\omega z/c}e^{i\omega t}\mathrm{d}\omega \quad (3.4)$$

We can get expression (3.1) by defining $g_s = \sqrt{2\pi}g(\omega_s)$.

The interaction between light and the atom mainly involve three levels, the ground state level $|1\rangle$, the intermediate state level $|2\rangle$ and the excited state level $|3\rangle$. The laser is far detuned from other atomic levels so we can ignore them. Of course, the manifold of each level will affect the interaction but we will consider this later. For simplicity, we only consider the Hilbert space expanded by these three states. These three states form a complete orthonormal basis so any operator in this space can be expressed by the "flip operators", including the electric dipole operator:

$$\hat{\mathbf{d}} = \sum_{i,j}\mathbf{d}_{ij}\sigma_{ij} \quad (3.5)$$

where we term $\sigma_{ij} = |i\rangle\langle j|$ the *flip operators*, $\mathbf{d}_{ij} = \langle i|\hat{\mathbf{d}}|j\rangle$ are the matrix elements. The dipole operator has an odd parity [108] so the $\mathbf{d}_{ii} = 0$. Further more, for ladder system, transition between $|1\rangle$ and $|3\rangle$ is first-order forbidden, so we have $\mathbf{d}_{13} = \mathbf{d}_{31} = 0$. The electric dipole operator becomes:

$$\hat{\mathbf{d}} = \mathbf{d}_{12}\sigma_{12} + \mathbf{d}_{23}\sigma_{23} + h.c. \quad (3.6)$$

The Hamiltonian of the light atom system is

$$H = H_L + H_A + H_{\text{int}} \quad (3.7)$$

where $H_L = \int \hbar\omega a^+(\omega)a(\omega)\mathrm{d}\omega$ is the Hamiltonian of the quantum light field, $H_A = \sum_i \hbar\omega_i\sigma_{ii}$ is the Hamiltonian of the bare atom and H_{int} is the interaction Hamiltonian.

3.1.1.2 Equations of motion

The atomic part is described by the time evolution of "flip operators". Here we write it as the Heisenberg equation:

$$\partial_t \sigma_{ij} = -\frac{i}{\hbar}[\sigma_{ij}, H], \tag{3.8}$$

where $H = H_A + H_{\text{int}}$, ignoring H_L as it commutes with "flip operators".

Expanding the equation (3.8) we get

$$\begin{aligned}
\partial_t \sigma_{12} &= -\frac{i}{\hbar}(\hbar\omega_{21}\sigma_{12} - \mathbf{E}\cdot[\mathbf{d}_{12}^*(\sigma_{11}-\sigma_{22}) + \mathbf{d}_{23}\sigma_{13}]),\\
\partial_t \sigma_{13} &= -\frac{i}{\hbar}(\hbar\omega_{31}\sigma_{13} - \mathbf{E}\cdot[\mathbf{d}_{23}^*\sigma_{12} + \mathbf{d}_{12}^*\sigma_{23}]),\\
\partial_t \sigma_{23} &= -\frac{i}{\hbar}(\hbar\omega_{32}\sigma_{23} - \mathbf{E}\cdot[\mathbf{d}_{23}^*(\sigma_{22}-\sigma_{33}) + \mathbf{d}_{12}\sigma_{13}]),
\end{aligned} \tag{3.9}$$

where $\omega_{ij} = \omega_i - \omega_j$ is the transition frequency between atom energy level i and j.

The first linear approximation we make is the population approximation:

$$\sigma_{11} = I, \sigma_{22} = 0, \sigma_{33} = 0. \tag{3.10}$$

Then we can eliminate the optical oscillation of these "flip operators" by transforming into rotating frame using:

$$\begin{aligned}
\tilde{\sigma}_{12} &= \sigma_{12} e^{i\omega_c(t+z/c)},\\
\tilde{\sigma}_{23} &= \sigma_{23} e^{i\omega_s(t-z/c)},\\
\tilde{\sigma}_{13} &= \sigma_{13} e^{i(\omega_c+\omega_s)t} e^{i(\omega_c-\omega_s)z/c}.
\end{aligned} \tag{3.11}$$

Applying the Rotating Wave Approximation (RWA) to neglect fast oscillating terms $e^{i(\omega_{ij(i>j)}+\omega_{s(c)})t}$, $e^{i(\omega_{12}-\omega_s)t}$ and $e^{i(\omega_{23}-\omega_c)t}$, equation (3.9) becomes:

$$\begin{aligned}
\partial_t \tilde{\sigma}_{12} &= -i\delta_1\tilde{\sigma}_{12} + i\frac{\Omega_c}{2} + g_s\frac{\hat{A}^+}{\hbar}d_{23}\tilde{\sigma}_{13},\\
\partial_t \tilde{\sigma}_{23} &= -i\delta_2\tilde{\sigma}_{23} + i\frac{\Omega_c}{2}\tilde{\sigma}_{13},\\
\partial_t \tilde{\sigma}_{13} &= -i(\delta_1+\delta_2)\tilde{\sigma}_{13} + i\frac{\Omega_c}{2}\tilde{\sigma}_{23} - g_s\frac{\hat{A}}{\hbar}d_{23}^*\tilde{\sigma}_{12},
\end{aligned} \tag{3.12}$$

where $\delta_1 = \omega_{21} - \omega_c, \delta_2 = \omega_{32} - \omega_s$ is the detuning of control field and signal field respectively. Ω_c is the Rabi frequency of control field: $\Omega_c^* = \mathbf{E}_c * \mathbf{d}_{12}^*/\hbar$. $d_{23}^* = \mathbf{v}_s * \mathbf{d}_{23}^*$ is the projection of dipole matrix element on the direction of the signal optical polarization. $\hat{A}^{(+)}$ is the photon slow-varying temporal mode operator defined in

Eq.3.4. We now have the equations of motion for single atoms, which is spacial-dependent Maxwell-Bloch equations.

The Maxwell equations describe the optical dynamics. We start with classical treatment. Assuming the polarization density of atomic vapour is isotropic:

$$\Delta \mathbf{E_s} - \frac{1}{c^2}\partial_t^2 \mathbf{E_s} = \mu_0 \partial_t^2 \mathbf{P_s} \tag{3.13}$$

where $\mathbf{P_s}$ is the polarization density vector of the atomic vapour. Since the signal field has the central frequency of ω_s and the bandwidth is small compared with ω_s, we can extract the central frequency $e^{i\omega_s(t-z/c)}$ and define $\alpha(t,z)$ as the positive frequency part of the signal temporal mode as we did in Eq.3.4, but classical. The result is:

$$\mathbf{E_s}(t,z) = i\mathbf{v_s} g_s \alpha(t,z) e^{-i\omega_s(t-z/c)} + c.c. \tag{3.14}$$

We also factorize out the signal frequency from the atomic polarization density vector $\mathbf{P}_s = \tilde{\mathbf{P}}_s e^{-i\omega_s(t-z/c)} + c.c.$. The positive frequency part of the signal propagation equation (3.13) can then be rewritten as:

$$(\Delta - \frac{1}{c^2}\partial_t^2)[i\mathbf{v_s} g_s \alpha e^{-i\omega_s(t-z/c)}] = \mu_0 \partial_t^2 [\tilde{\mathbf{P}}_s e^{-i\omega_s(t-z/c)}]. \tag{3.15}$$

We have assumed that the optical field has no transverse dynamics so that we can ignore transverse derivative. We also assume $\alpha(z,t)$ varies slowly compared with the optical oscillation so that we can implement slow-varying envelop approximation [108] to get rid of second order derivative. The envelope of temporal mode with positive frequency $\alpha(z,t)$ follows:

$$(\partial_z + \frac{1}{c}\partial_t)\alpha = -\frac{i\mu_0 \omega_s c}{2g_s} \mathbf{v}_s^* \cdot \tilde{\mathbf{P}}_\mathbf{s}. \tag{3.16}$$

This equation links the signal temporal mode envelope to the atomic macroscopic polarization density, which is a collective variable of every single atoms in the pixel region *voxel* defined by J.Nunn [108].

$$\mathbf{P}_s = \frac{1}{\delta V} \sum_\beta \mathbf{d}^\beta \tag{3.17}$$

where β runs over all the atoms in δV. $\mathbf{d}$ is the dipole moment of a single atom in Eq. (3.6). Quantum mechanically, atomic dipole moment is described by "flip operator" as in Eq. (3.6). Note that the signal field is mainly interacting with atomic polarization with the resonant frequency so we can ignore the term with σ_{12}. We can

borrow the definition of macroscopic atomic polarization operator $\hat{P}_s$ which works as an annihilation operator:

$$P_{23} = \frac{1}{\sqrt{n}\delta V}\sum_{\beta}\tilde{\sigma}_{23}^{\beta} \tag{3.18}$$

where n is the number density of atomic vapour. The advantage of this definition is that the macroscopic atomic polarization operator $\hat{P}_{23}$ is that its commutation are normalized the same way as the photonic field creation and annihilation operator $[\hat{P}_{23}, \hat{P}_{23}^{+}] = 1$.

It is related with the actual atomic polarization by:

$$\hat{\tilde{\mathbf{P}}}_s = \sqrt{n}\mathbf{d}_{23}P_{23}. \tag{3.19}$$

Tidying up these definitions. We would now like to replace the semi-classical treatment of the propagating signal field by a quantised treatment. This can be done by replacing α in the right hand side of Eq. 3.16 by A defined in 3.4, replacing $\tilde{\mathbf{P}}_\mathbf{s}$ in the left hand side of Eq.3.16 by Eq.3.19. Eq.3.16 then becomes:

$$(\partial_z + \frac{1}{c}\partial_t)A = -\frac{i\mu_0\omega_s c\sqrt{n}}{2g_s}d_{23}P_{23}. \tag{3.20}$$

We then define P_{12} and B in the same vein as P_{23} to be the annihilation operator of macroscopic auxiliary polarization density and orbital wave:

$$\begin{aligned} P_{12} &= \frac{1}{\sqrt{n}\delta V}\sum_{\beta}\tilde{\sigma}_{12}^{\beta}, \\ B &= \frac{1}{\sqrt{n}\delta V}\sum_{\beta}\tilde{\sigma}_{13}^{\beta}. \end{aligned} \tag{3.21}$$

Now we can add in the spontaneous decay non-Hermition terms. Equation (3.12) can then be written as the following:

$$\begin{aligned} \partial_t P_{12} &= i\frac{\Omega_c^*}{2}\sqrt{n} + \frac{g_s}{\hbar}d_{23}A^{+}B - \Gamma_1 P_{12}, \\ \partial_t P_{23} &= i\frac{\Omega_c}{2}B - \Gamma_2 P_{23}, \\ \partial_t B &= i\frac{\Omega_c^*}{2}P_{23} - \frac{g_s}{\hbar}d_{23}^* A P_{12} - i(\delta_1+\delta_2)B - \gamma_3 B, \end{aligned} \tag{3.22}$$

where $\Gamma_1 = \gamma_{12} + i\delta_1, \Gamma_2 = \gamma_{23} + i\delta_2, \gamma_{12}$ andγ_{23} are the spontaneous decay rates of coherence between states $|2\rangle, |1\rangle$ and states $|3\rangle, |2\rangle$, γ_3 is the spontaneous decay rate of storage state $|3\rangle$.

We then examine the relative magnitude of all the terms in the $\partial_t P_{12}$ of the equations Eq. (3.22) and neglect the small ones. $B^{+}B$ is the orbital wave density

operator of atomic vapour. There will be no more than one orbital wave excitation in the atomic ensemble but there are many more atoms that comprise the ensemble, so $\langle B^+B\rangle \ll n$. $\langle A^+A\rangle$ is the photon number of signal field and $\langle A^+A\rangle|g_s * d_{23}|^2/\hbar^2$ is the modulus squared of Rabi frequency of signal field, which is much smaller than that of the control field Ω_c. So $\frac{g_s}{\hbar}A^+Bd_{23} \ll i\frac{\Omega_c^*}{2}\sqrt{n}$ and we should be able to neglect the term $\frac{g_s}{\hbar}A^+Bd_{23}$ in the equation.

We then apply the adiabatic limit approximation to solve two of the equations algebraically by making $\partial_t P_{12} = \partial_t P_{23} = 0$. This is called Adiabatic Following (see appendix A for details), which happens when the time scales of interest, in this case, the time scale of P changing with Rabi frequency, is much larger than the time scale of the natural dynamics given by $\Gamma = \gamma - i\delta$, where γ is the spontaneous decay rate. This adiabatic condition comes down to the following:

$$(\delta_c, \Omega) \ll |\delta_i|, (i = 1, 2) \tag{3.23}$$

where δ_c is the bandwidth of the control field. Solving the macroscopic polarization density algebraically in equation (3.22), we get:

$$\begin{aligned} P_{12} &= \frac{i\Omega_c^*\sqrt{n}}{2\Gamma_1}, P_{23} = \frac{i\Omega_c B}{2\Gamma_2}, \\ \partial_t B &= -\frac{|\Omega_c|^2}{4\Gamma_2}B - i\kappa\frac{\Omega_c^*}{2\Gamma_1}A - i(\delta_1+\delta_2)B - \gamma_{23}B, \end{aligned} \tag{3.24}$$

where $\kappa = \frac{\sqrt{n}g_s}{\hbar}\mathbf{v_s}\cdot\mathbf{d_{23}^*}$.

Equations (3.20) and (3.24) give us the linear equations of motion of ORCA memory:

$$\begin{aligned} \partial_t B &= -\frac{|\Omega|^2}{4\Gamma_2}B - i\kappa\frac{\Omega^*}{2\Gamma_1}A - i(\delta_1+\delta_2)B - \gamma_{23}B, \\ (\partial_z + \frac{1}{c}\partial_t)A &= -\frac{i\kappa^*\Omega}{2\Gamma_2}B. \end{aligned} \tag{3.25}$$

This result could be further simplified if we neglect the spontaneous decay of the spin wave (because it is relatively long lived for the application of ORCA buffer which we will introduce soon) and if the signal and control field is under two photon resonance condition: $\delta_1 + \delta_2 = 0$.

$$\begin{aligned} \partial_t B(z,t) &= -\frac{|\Omega_c|^2}{4\Gamma_2}B(z,t) - i\kappa\frac{\Omega_c^*}{2\Gamma_1}A(z,t), \\ (\partial_z + \frac{1}{c}\partial_t)A(z,t) &= -\frac{i\kappa^*\Omega_c}{2\Gamma_2}B(z,t). \end{aligned} \tag{3.26}$$

Eq.3.26 are the equations of motion for the modified ORCA system. They are first-order derivative linear equations describing the coupling between atomic orbital wave $B(z,t)$ and single photon temporal mode $A(z,t)$ with the presence of the control field $\Omega_c(z,t)$. These equations are used in simulations to predict and to fit the experiment results.

It should be pointed out here that the original ORCA protocol is intrinsically free of four wave mixing noise as explained in section 3.1. However, in this modified ORCA scheme where the frequency of the strong control field is at the transition involving the populated ground state, the intermediate state $|2\rangle$ will be populated even though the control field is not on resonance. It is not obvious yet how will this make a difference to the performance of the protocol. We will now remove the assumption $\sigma_{22} = 0$ and see under what condition the linear equations of motion (3.26) still hold true.

Considering now only $\sigma_{33} = 0$, and adding $\tilde{\sigma}_{22} = \sigma_{22}$ in to Rotating frame transformation (3.11), with adiabatic following approximation, equations of motion (3.9) become:

$$\begin{aligned}
\tilde{\sigma}_{12} &= -\frac{i\Omega_c^*(1-2\tilde{\sigma}_{22})}{2\Gamma_1}, \\
\tilde{\sigma}_{23} &= \frac{i\frac{\Omega_c}{2}\tilde{\sigma}_{13} - \frac{g_s}{\hbar}Ad_{23}^*\tilde{\sigma}_{22}}{\Gamma_2}, \\
\partial_t\tilde{\sigma}_{13} &= -\frac{|\Omega_c|^2}{4\Gamma_2}\tilde{\sigma}_{13} - \frac{ig_sd_{23}^*\Omega_c^*A}{2\hbar\Gamma_1} + \frac{ig_sd_{23}^*\Omega_c^*A}{\hbar}\tilde{\sigma}_{22}(\frac{1}{\Gamma_1} - \frac{1}{2\Gamma_2}), \\
\partial_t\tilde{\sigma}_{22} &= i\frac{E_c}{2\hbar}(d_{12}^*\tilde{\sigma}_{12}^* - d_{12}\tilde{\sigma}_{12}).
\end{aligned} \tag{3.27}$$

The first two terms of the third equation are the same as that in linear equations of motion. The removal of the population approximation contributes to the third term. Now we compare its magnitude with that of the second term by taking the ratio with the assumption that $\delta_1 = -\delta_2$ and that $|\delta_1| >> \gamma_{1,2}$. The ratio becomes $3\tilde{\sigma}_{22}$, and so the equations of motion become:

$$\begin{aligned}
\partial_tB(z,t) &= -\frac{|\Omega_c|^2}{4\Gamma_2}B(z,t) - i\kappa\frac{\Omega_c^*}{2\Gamma_1}(1-3\tilde{\sigma}_{22})A(z,t), \\
(\partial_z + \frac{1}{c}\partial_t)A(z,t) &= -\frac{i\kappa^*\Omega_c}{2\Gamma_2}B(z,t) + \frac{|\kappa|^2}{\Gamma_2}\tilde{\sigma}_{22}A(z,t) \\
\partial_t\tilde{\sigma}_{22} &= -\frac{\Omega_c^2\gamma_{12}}{2\Delta^2}(1-2\tilde{\sigma}_{22}).
\end{aligned} \tag{3.28}$$

From the first two equations we can see that the population in the intermediate state will enable a linear absorption of the signal and also weaken the coupling strength linearly.

We can also examine the condition when the intermediate population is small by assuming that the control field is square shaped and solve the third equation in (3.28):

$$\tilde{\sigma}_{22} = \frac{1}{2}(1 - e^{-\frac{\Omega_c^2 \gamma_{12}}{\Delta^2}(t+z/c)}) \tag{3.29}$$

where $0 < t < T$ and T is the pulse duration. This leads to the condition of low intermediate population is:

$$\Omega_c^2 \gamma_{12} T \ll \Delta^2. \tag{3.30}$$

For our experiment, $T \approx 10^{-9}, \gamma_{12} \approx 10^6$, and $\Omega_c^2 \ll \Delta^2$ is the adiabatic condition which is satisfied for the far-off resonance condition. So the intermediate state has a very low level of population ($\ll 10^{-3}$), making the population approximation (3.10) quite robust.

3.1.2 Experiment

3.1.2.1 Experiment setup

For an experimental realisation we consider ORCA with caesium-133 (see fig 3.2a) because, among all alkali atoms, caesium has the largest number density and dipole moments at room temperature. The disadvantage of Caesium is that the memory will have short lifetime due to dipole beating and Doppler dephasing [154]. However, for the application of ORCA buffer, short lifetime is not a critical problem because we don't need the buffer time to be much longer than the single photon duration, which, for solid state SPS, is usually less than 1ns. Here, we apply the control field off-resonantly to the D2-line ($S_{1/2} \rightarrow P_{3/2}$) resonance, counter-propagating with the signal which is applied to the $P_{3/2} \rightarrow D_{5/2}$ (Fig. 3.2b). This signal transition (917 nm) is of particular interest as it is well-matched to many state-of-the-art quantum dots (QDs) single-photon sources, e.g. [125]. To pinpoint the exact frequency, we can adjust the detuning of the control field, such that the two-photon resonance condition matches the source emission. In this experiment, we use attenuated coherent light for the signal. Furthermore, the bandwidth of the ORCA buffer is set by that of the control field, and can easily accommodate the GHz-band of many single-photon sources [125].

The experiment consists of four parts: the control preparation, signal preparation, the cell and the detection system.

The control field is produced from mode-locked titanium sapphire (Ti:Sapphire) laser (Spectra-Physics Tsunami) with an intracavity Gires-Tournois interferometer (GTI). The wavelength is tuned by calibrating to a CW diode laser locked to the

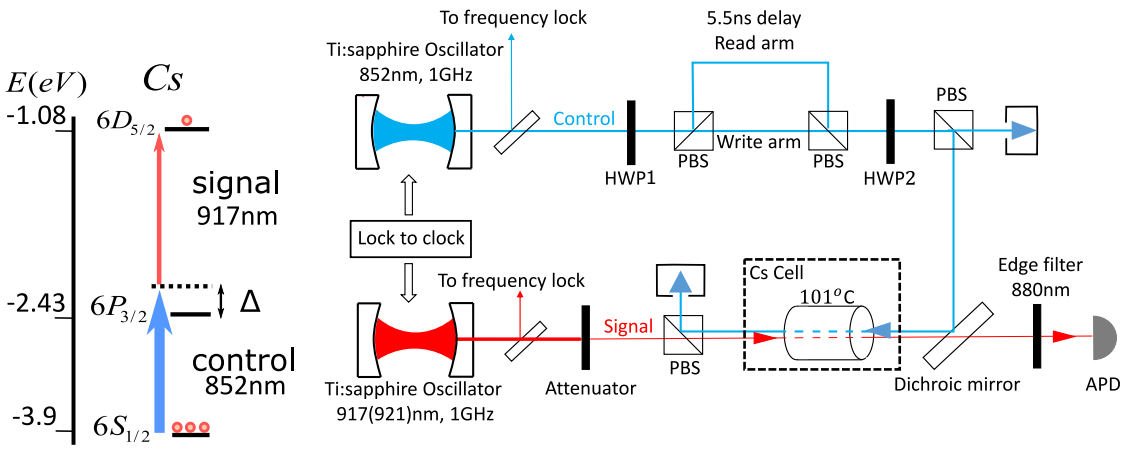

Figure 3.2: (a) Atomic transitions of the ORCA buffer. Δ is the frequency detuning from single-photon resonance. (b) Experimental setup of ORCA buffer

852 nm D2-line of Caesium. The following steps are implemented to achieve such laser frequency locking: 1. A CW diode laser is locked to a hyperfine transition between Cesium $6^2S_{1/2}$ and $6^2P_{3/2}$ through saturated absorption spectroscopy. 2. Send the frequency locked diode laser though a spectrometer together with the mode-locked pulsed Ti:Sapphire laser. Adjust the Ti:Sapphire laser by tuning the integrated grating in the Ti:Sapphire laser so that the pulsed spectrum overlaps with the diode laser. This is a very coarse tuning because the spectrometer has limited resolution of down to 2 GHz minimum. 3. Send the Ti:Sapphire laser through a Caesium vapour cell. Adjust the Ti:Sapphire laser frequency by manually changing the lasing cavity piezo voltage. We can easily detect strong fluorescence when the Ti:Sapphire laser is on resonance with the D2 line. 4. Send both the diode laser and the Ti:Sapphire laser into a scanning Fabry-Perot interferometer and capture the transmission line for both lasers. The two frequencies of the two lasers should very close to each other in frequency now, surely within one FSR. Computer should be able to find the central peak of both lasers and lock the Ti:Sapphire frequency by locking the distance between the two laser transmission peaks.

The control laser is then split by a PBS after a half wave plate (HWP). One of the arms is called the "*read-in*" arm while the other is called "*read-out*" arm which is delayed from the "*read-in*" arm for 5.5ns. They are combined by another PBS. At this point, the read-in control pulse and the read-out control pulse are orthogonally polarised. We use another HWP and a PBS to project the polarisation onto a common axis. The control fields are then coupled to an SM fibre to clean-up the spatial mode.

The power of the two arms is adjusted by the two HWPs.

The signal field is an attenuated coherent light from another (≈ 0.9) GHz bandwidth mode-locked Ti:Sapphire laser. The wavelength is locked and tuned by a wavemeter to 917nm. Both of the control and the signal has 80MHz repentant rate and the pulses from two Ti:Sapphire are synchronised by Lock-to-Clock® electronics. The signal is also coupled to an SM fibre after attenuation.

Filtering of ORCA is extremely simple. The signal and the control after the SM fibre counter propagate with each other and the pulses overlap in the cell region. The signal and the control have opposite polarizations so that a PBS on the signal side can prevent the strong control field propagate into the signal laser. The signal mode after the cell goes through a dichroic mirror which prevents any control mode back reflection propagating. A long pass edge filter at 880nm is placed right in front of the fibre coupler to filter room light and control light scattering before it is coupled to a single-mode fibre which leads to the avalanche photodiode detector (APD). The transmission efficiency of signal from inside the cell to the detector is 21% and the APD efficiency is $\approx 50\%$.

The ORCA memory is a standard caesium vapour cell with 7cm in length and 1 inch in diameter. It is wrapped in an oven heated up to $\sim$100 Celsius degree to increase the number density. The temperature is measured by vapour's optical depth, which is determined by the transmission of a CW laser through the cell when scanning the frequency of the laser around the caesium transition. Two lenses were used (not shown in the diagram) to focus both the signal and control beam at the centre of the cell. The signal is measured to be $170\mu m$ while the control is around $210\mu m$.

Other auxiliary devices includes: a power pick-off in the control beam before it is reflected by the dichroic mirror and was directed to a powermeter (ThorlabsPM100D). Mechanical shutters (Pololu robotic and electronics®) are placed on the light beams to automatically switch between different measuring configurations. Step motors are used to control the rotation of the HWPs.

3.1.2.2 Measurement configuration and data taking

To measure the efficiency and noise of ORCA protocol, the experiment is done in four measurement configurations: noise, signal and memory.

The *noise* configuration is when the signal is turned off while control is on. Any detection should be noise coming from the dark count of the detector, room light, control field leakage or unwanted noise process happens in the cell. The *signal* configuration is when the signal is on but both control fields are off. The *memory* configuration is

when signal and both control fields are on and the signal is read-in and then read-out within 5.5ns in each repetition time (12.5ns). The time trace is shown in Fig. 3.3. It is a real time detection of the signal. The signal is a pulsed weak coherent state with 80MHz repetition rate. The *signal* configuration corresponds to the "control off" track. The *memory* configuration corresponds to the "control on" track. The reduction of the signal from "control off" to "control on" is used the calculate the read-in efficiency. The weaker pulse 5.5ns away from the main peak indicates a signal read-out and is used to calculate the read-out (total) efficiency.

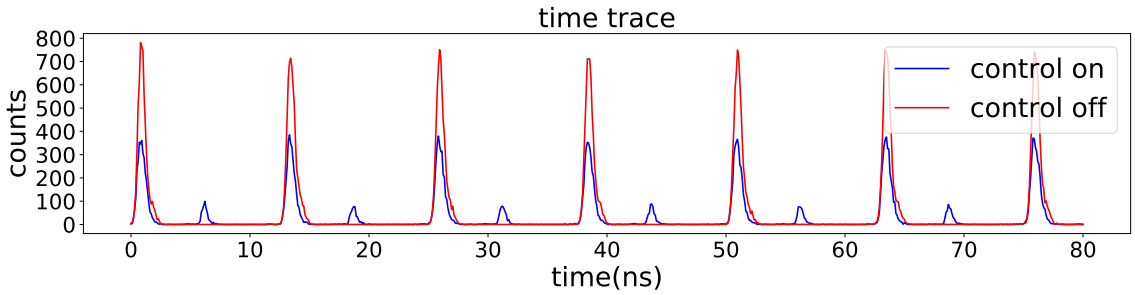

Figure 3.3: Time trace of ORCA buffer experiment. Counts arriving on the detector in different configurations: *"control off"* is the signal configuration. *"control on"* is the memory configuration where there is a read-out pulse 5.5 ns after the read-in time.

Data is taken by a Swabian Timetagger 20 operating in the "histogram" mode. The read-in efficiency is calculated by:

$$\eta_{in} = \frac{N_{sig}^{(s)} - N_{sig}^{(m)}}{N_{sig}^{(s)} - N_{noise}} \tag{3.31}$$

where $N_{sig}^{(m)}$ is the signal count in the *memory* configuration and $N_{sig}^{(s)}$ is the signal count in the *signal* configuration. The read-out/memory efficiency is:

$$\eta_{out} = \frac{N_{out}^{(m)} - N_{noise}}{N_{sig}^{(s)} - N_{noise}} \tag{3.32}$$

where $N_{out}^{(m)}$ is the output count in the *memory* configuration. To characterise the noise of the ORCA memory, we use the definition $\mu_1 = N_{noise}/\eta_{out}$ which describes the noise-output ratio when the input is a single-photon *Fock state*. N_{noise} is the noise count in *noise* configuration.

3.1.3 Result and data analysis

We choose a buffer time of 5.5 ns. We would like the buffer time to be short to maintain high efficiency but not too short so that the read-in and read-out are well resolved by a photodiode. We also optimised the detuning to be 7.6GHz for best read-out efficiency. We observe a total efficiencies η_{out} >10%, and noise-free performance with $\mu_1 < (1 \pm 0.06) \times 10^{-4}$. A natural question to ask is how does this influence the photon statistic, for example the second order correlation functions $g^{(2)}$. We now try to build a relation between μ_1 and $g^{(2)}$.

Following Goldschmidt [50], for two incoherent fields the combined $g^{(2)}$ is:

$$g^{(2)}_{out} = \frac{p_s^2 g_s^{(2)} + 2p_s p_n + p_n^2 g_n^{(2)}}{(p_s + p_n)^2}. \tag{3.33}$$

Here p_s is the probabilities of the signal at the output of our memory. p_n is the probability for the undesired background process, which can be regarded as a form of noise. This expression is valid for a quantum memory because there is no coherent interaction between the noise field and the signal field during memory operation. We Taylor expand around $p_n = 0$, as $p_n \ll 1$, and take the first order,

$$g^{(2)}_{out} \sim g^{(2)}_s - \frac{2(g^{(2)}_s - 1)p_n}{p_s}. \tag{3.34}$$

For our system, $p_s = B_0\eta$, where B_0 is the brightness (the probability of emitting a photon on demand) of the source, and η is the memory efficiency, and $\mu_1 = p_n\eta$, then

$$g^{(2)}_{out} \sim g^{(2)}_s - \frac{2(g^{(2)}_s - 1)\mu_1}{B_0} = g^{(2)}_s + \frac{2\mu_1}{B_0} - \frac{2g^{(2)}_s\mu_1}{B_0} \tag{3.35}$$

For an input state with $g^{(2)}_s \sim 0$, and $B_0 \sim 1$, $g^{(2)}$ after the memory is $g^{(2)}_{out} \sim 2\mu_1$, which is negligible given our measured μ_1. Furthermore, this small amount of noise is comparable with observed detector dark count rates.

Apart from the noise-free demonstration, it is also important to verify the theoretical model can properly capture the behaviour of the ORCA protocol. To do this, we scan the two control fields power and fit it with simulation using equations of motion Eq. (3.26).

There are four parameters in the equation that can be used as fitting parameters:

1. The decay time. The decay time is determined by two factors: the Doppler dephasing,which is determined by temperature, and the hyperfine beating which is highly dependent on polarization of the signal and control. A hyperfine beating

happens when there are multiple excited levels. Each level has its own speed of phase evolving time. So the total orbital wave sees a dephasing and rephasing with a pattern dependent on the polarization of the signal and control.

2. The dipole moment of $6S_{1/2} \rightarrow 6P_{3/2}$. The dipole moments should be calculated by the Wigner-Eckart theorem as a product of reduced matrix element and Clebsch-Gordan coefficient

$$\langle F, m_F|er_q|F', m'_F\rangle = \langle F||er||F'\rangle\langle F, m_F|F', 1, m'_F, q\rangle. \tag{3.36}$$

In principle, we need to have a full set of equations of motion that describe the interaction between different polarisation components of optical field with all the $|F, m_F\rangle$ levels with the coupling given by the dipole moments above. However, it is complicated and difficult to track. Instead, we model F levels but not the m_F levels. It is an effective 1D treatment of the 3D problem. So the dipole moments in the equations are "effective dipole moments". It is necessary to adjust the "effective dipole moment" to fit and verify our model. Specifically, we calculate the reduced matrix element $\langle F||er||F'\rangle$ and multiply it by a fitting parameter.

It can be seen from the equations of motion (3.26) that the dipole moments of $r1(6S_{1/2} \rightarrow 6P_{3/2})$ and $r2(6P_{3/2} \rightarrow 6D_{5/2})$ always appear in the the multiplication form $r1 * r2$ because of the two photon resonance dynamic. This allows us to adjust the product by only varying $r1$.

3.The overlap position of the signal and the control field. To understand this, we should first understand the long cell limit and the short cell limit.

Long cell limit means that the signal and the control can fully overlap with each other within the cell.

$$L > \frac{l_{sig} + l_{ctrl}}{2}. \tag{3.37}$$

One important feature of this is that the orbital wave will be symmetric. Another feature is that the efficiency will be optimised because the cell is long enough to cover the whole region of the signal-control overlapping.

The short cell limit means that the cell is much shorter than the spatial overlap dimension between signal and control such that there is no envelope variation of the two fields within the cell.

$$L \ll \frac{l_{sig} + l_{ctrl}}{2}. \tag{3.38}$$

When the cell is in this regime, the atoms have no information of the envelope propagation, so in this case counter- and co-propagating signal/control fields are equivalent.

Therefore the ORCA behaves as a short cell Raman memory. Another feature of this regime is that the orbital wave is also symmetric.

For both cases, it is possible to find analytical solutions for the equations of motion. Its discussion is beyond the scope of this thesis. When the cell length is neither much shorter nor longer than the optical pulses, the interaction is not spatially symmetric. The position of the overlap of the signal and control in the cell is crucial. We fit this parameter by changing the delay between signal and control.

4. The temperature. The number density of the Alkali vapour is very sensitive to temperature. Experimentally we measure the temperature in the cell by measuring the D2 absorption line. A fitting of this parameters can be used as a verification of the model if the fitted temperature agrees with the measured temperature.

Results are shown in Fig. (3.4), numerical solutions of both groups agree decently with the experiment. The blue line is with read-in control energy of 700pJ, fitting parameters were calculated from this data set. The same fitting parameters were used to predict total efficiency with read-in control energy of 1310pJ (red line) and it agrees well with the experiment data. The main point of this result is that our theory model is feasibly and thus can be reliably used for ORCA simulation as quantum buffer.

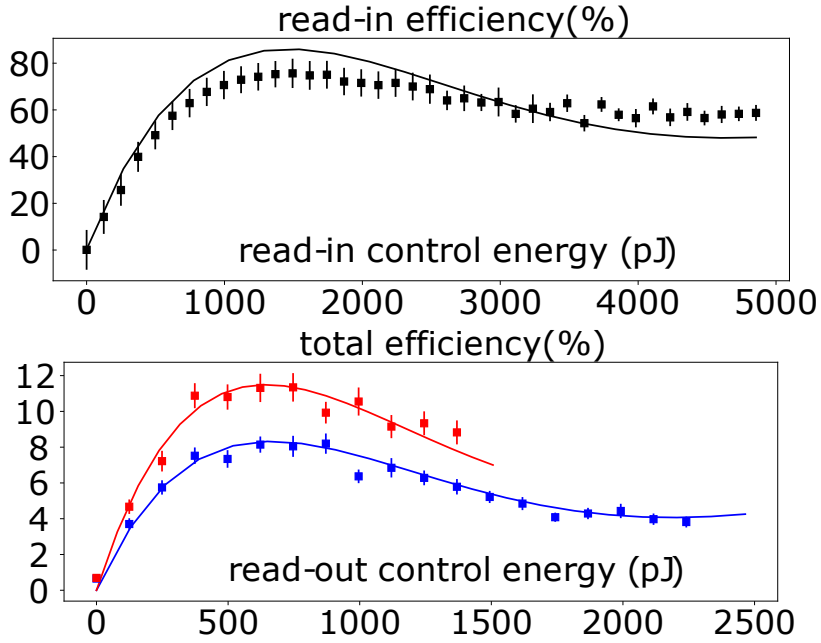

Figure 3.4: Memory efficiency for different read-in and read-out control pulse power. Square dots with error bars are experimental data. We show total efficiency for different read-in control powers in the lower figure: blue for 700pJ and red for 1310pJ.

The table 3.1 below gives the parameters we use in the experiment and the fitted parameters we get from the simulation. The measured efficiency of 10% at 5.5ns and

experiment		simulation	
parameter	value	parameter	value
$cell\,length$	$7.2cm$	η_{decay}	0.223
$temperature$	$101°C$	d_1	8.222×10^{-30}
$bandwidth(control)$	1.48GHz	d_2	1.43×10^{-29}
$bandwidth(signal)$	1.1GHz	$temperature$	$99.6°C$
T_{setup}	21%		
τ_σ	$10.3ns$		
τ_γ	$86ns$		
T_{buff}	$5.5ns$		
$detuning$	7.6GHz		

Table 3.1: T_{setup} is the signal transmission from after the cell to single-photon detector; τ_σ is the lifetime according to Doppler dephasing; τ_γ is the natural life time of storage state; T_{mem} is the memory time. η_{decay} is the fitted decay magnitude which is defined as: $\eta_{tot} = \eta_0\eta_{decay}$, where η_{tot} is the total memory efficiency at time T_{mem}, η_0 is the *short-time efficiency*. η_{decay} is determined by τ_σ, τ_γ and the hyperfine beating pattern since we didn't pump the population to a certain m_F state. d_1 and d_2 are the dipole moments of the two transitions in Cs ladder system: $6S_{1/2} \rightarrow 6P_{3/2} \rightarrow 6D_{5/2}$.

the fitted $\eta_{decay} = 0.223$ gives a "*zero storage time efficiency*" $\eta_0 = 34\%$. The fitted temperature is almost the same as the measured temperature.

3.2 ORCA as quantum buffer for single-photon source

It has been pointed out in Chapter 2.2.2 that single-photon source (SPS) is essential for photonic quantum information processing. In this section, we propose "*ORCA buffer*" as a new technique to improve the performance of noisy single-photon source.

3.2.1 ORCA quantum buffer

In this section, we introduce the idea of using a quantum buffer to optimally improve the performance of a noisy single-photon from a deterministic SPS. We discuss how the ORCA protocol meets the requirement of a quantum buffer and then compare ORCA buffer with normal intensity filtering using QDs as an example.

3.2.1.1 Quantum buffer for single-photon source

Recently, steady progress has been made for single-photon sources with near-ideal single-photon statistics[125, 124]. The brightness is also improving substantially into the regime where it can be called a "deterministic source". Recent studies also show a high self-indistinguishability ($I^{(1)}$) in QDs embedded in microcavity. However, it still remains a challenge to increase the indistinguishability higher while keeping the brightness high. Furthermore, it is even more challenging to build different sources emitting indistinguishable photons ($I^{(2)}$), especially for solid-state SPS because the fabrication environment of each source is hard to control.

Degradation of indistinguishability comes from all degrees of freedom, including photon statistics, polarization and temporal mode. Frequency also matters but in principle it can be described by the temporal mode. Since photon statistics and polarization is near the ideal, the main challenge of improving indistinguishability relies on better controlling of the temporal mode. The critical remaining factor that limits this is the mixing of temporal optical modes due to numerous additional undesired physical processes (see review [34]) in most single-photon emitters [1]. To circumvent this issue, it is common to filter the photons after emission. However, passive intensity filtering only achieves at best $I^{(1)}, I^{(2)} \to 1$ in the limit of $B \to 0$ [102]. To understand this and to illustrate how we overcome this problem, we consider the normalized density matrix ρ which represents the temporal-spectral degrees of freedom of the photon. The single-photon coming out of a noisy SPS is a mixed state $\rho = \sum \alpha_k |\psi_k\rangle\langle\psi_k|$, where $|\psi_k\rangle$ are single-photon excitations of the respective temporal eigenmodes $\psi_k(t)$. The indistinguishability of the photon is unity when ρ has only one non-zero eigenvalue i.e. is in a single temporal-spectral mode [14]. Self-indistinguishability of the emission is the overlap between the excitations described by the density matrix:

$$\text{Ind.} = \text{Tr}[\rho^2] = \sum |\alpha_k|^2 = 1/K \tag{3.39}$$

where K is the mode capacity, meaning how many modes does the state have.

A mixed state has $I^{(1)} < 1$ and comprises multiple orthogonal eigenmodes. Therefore, an intensity (temporal or spectral) filter can not select only one mode within a mixed state unless it is in the limit of infinitesimally narrow bandpass, which necessarily reduces the brightness of the selected mode to zero. Here, we propose a coherent filter – a quantum buffer – which can remove higher order temporal modes of a single-photon without detriment to the main eigenmode, increasing indistinguishability to

unity whilst minimizing the reduction in brightness. Furthermore, it can manipulate the selected mode into a user-defined one thereby unifying temporal-spectral modes from disparate photon sources increasing inter-indistinguishability ($I^{(2)}$) also to unity.

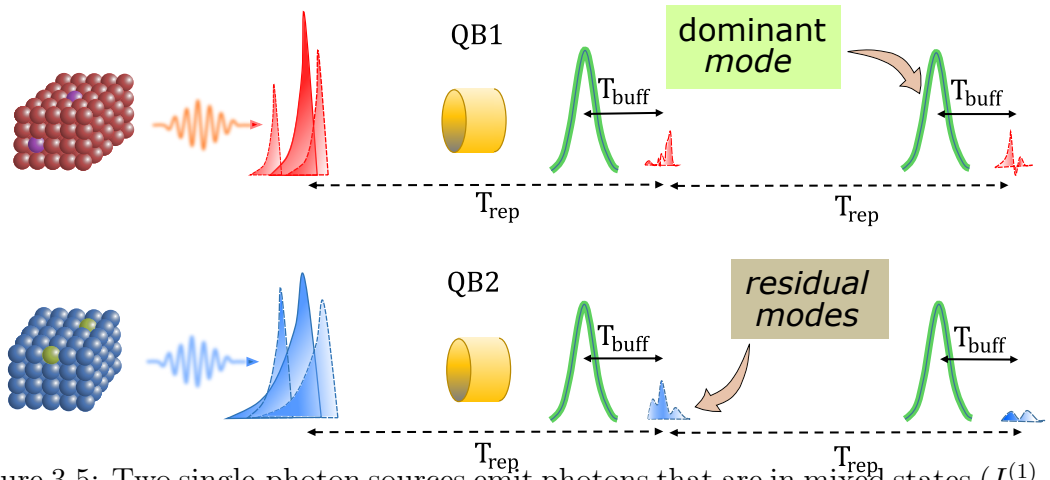

Figure 3.5: Two single-photon sources emit photons that are in mixed states ($I^{(1)} < 1$) and in different sets of temporal-spectral modes ($I^{(2)} < 1$). After filtering with the quantum buffers (QB), the dominant mode and the residual modes are separated by a short programmable delay T_{buff}, pure ($I^{(1)} = 1$) and identical photons ($I^{(2)} = 1$) are recalled by filtering out the residual noisy modes.

The basic operating principle of a quantum buffer is shown in Fig. 3.5. A buffer is placed after each single-photon source to delay a user-specified temporal-spectral wave packet, or a temporal mode. In practise this should be the dominant ($k = 0$) eigenmode $|\psi_0\rangle$ with the largest eigenvalue α_0. All other modes ($k \geq 1$) are transmitted and time separated from the buffered mode ($k = 0$) with a buffer time T_{buff}, so can be removed. A readout of the stored photon should retain the temporal purity. As a result, the output of our quantum buffer will be in a pure state. All the other degrees of freedom of the emission are identical and the second-order correlation function $g^{(2)}(0)$ of the buffered photons remains at zero, $I^{(1)} = 1$ would be achieved. An ideal quantum buffer selects the dominant eigenmode with unit efficiency, and therefore the brightness will decrease proportionally to the largest eigenvalue, $B_{\text{out}} = \alpha_0 B_0$, where B_0 is the brightness of the single-photon source before the quantum buffer. Since different sources may have different dominant temporal modes $|\psi_0\rangle$, the filtered mode will differ from source to source. An ideal quantum buffer will unify these modes, producing the same output temporal mode $|\phi\rangle$ for every single-photon source, making both $I^{(1)}$ and $I^{(2)}$ unity.

Devices that can select particular temporal modes have been demonstrated previously [33, 2, 118, 116, 127], however, careful engineering of the underlying nonlinear operation is required to suppress spurious noise processes and render noise levels

quantum compatible. Furthermore, phase-matching constraints make the operational bandwidth too large for the GHz bandwidths of leading photon sources [124, 134]. Here we propose to use ORCA protocol as a quantum buffer for the following reasons:

1). Noise-free. As has been demonstrated experimentally, the total noise level of ORCA is smaller than dark counts of the detector. This is important because the noise will not only contribute to an increase in single-photon purity (Eq. 2.13), but also degrade the indistinguishability.

2). Broad bandwidth. The bandwidth of signal of ORCA protocol is in GHZ level which matches with many solid-state SPS. It is also fairly flexible (up to $\approx 10^2$ GHz) by changing the bandwidth of the control field.

3). Flexible single frequency. The rough wavelength is determined by the transition of the atom, However, the exact signal frequency is adjustable (also up to $\approx 10^2$ GHz) by changing the detuning of the control. Of course, the efficiency is different with different detuning but it can be compensated by stronger control field power and/or atomic density.

4). High end-to-end efficiency. The ORCA protocol is simple and doesn't need complicated filtering because the signal and control counter propagate with each other. Therefore the loss of signal after the buffer is minimal.

3.2.1.2 Singlemodeness of ORCA buffer

With all the advantages of the ORCA protocol being said, there is one more feature of a quantum buffer "*singlemodeness*". This describes how mode-selective a buffer can be. Ideally, we want a quantum buffer with perfect *singlemodeness* to select only one temporal mode to store and retrieve it completely. It can be proved that ORCA buffer can achieve singlemode operation with unit efficiency provided one has good control of the cell length matching with each signal and a very large control field power (see outlook for detail). However, in practice, a limited choice of cell length and limited control field power will change the situation. In this section, we will first introduce theoretically how an ORCA buffer can selectively interact with a photon with a mixed temporal mode optical field. Then we will simulate for the given limited control field power and devices, how well the ORCA buffer can perform.

We first recall the ORCA equations of motion:

$$\begin{aligned} \partial_t B(z,t) &= -\frac{|\Omega_c|^2}{4\Gamma_2} B(z,t) - i\kappa \frac{\Omega_c^*}{2\Gamma_1} A(z,t), \\ (\partial_z + \frac{1}{c}\partial_t) A(z,t) &= -\frac{i\kappa^* \Omega_c}{2\Gamma_2} B(z,t). \end{aligned} \tag{3.40}$$

This is a linear interaction, therefore the mapping of light, $S_{\text{in}}(t)$, to atoms, $B(z)$, and then atoms, $B(z)$, back to light $S_{\text{out}}(t)$ can be described via the Green's functions:

$$\begin{aligned} B(z) &= \int G_{\text{in}}(z,t) S_{\text{in}}(t) dt, \\ S_{\text{out}}(t) &= \int G_{\text{out}}(t,z) B(z) dz. \end{aligned} \tag{3.41}$$

The Green's functions can either be numerically calculated (see chapter 3.3 for details) or tomographically measured [103]. A singular value decomposition (SVD) of the input Green's function:

$$G_{\text{in}}(z,t) = \sum_k \lambda_k^{\text{in}} b_k(z)\, u_k^*(t) \tag{3.42}$$

will give a series of orthogonal input signal modes $u_k(t)$ mapping to orthogonal atomic coherence modes $b_k(z)$ (orbital wave) with a read-in efficiency equal to the square of the corresponding singular value λ_k^{in}. A *single-mode* interaction has a Green's function with only one non-zero singular value λ_0^{in}, meaning that there is only one input mode $u_0(t)$ that interacts with the ORCA buffer. Since the Green's function G_{in} is determined by the temporal-spectral mode of the control field $\Omega^{\text{in}}(t)$, we can engineer the ORCA buffer by pulse-shaping the control field such that $u_0(t)$ matches the dominant mode $\psi_0(t)$ of a QD single-photon source emission. In practice, the required control field pulse shape is found numerically by an optimization algorithm. If the ORCA buffer is not perfectly *single-mode*, there will be other signal modes being read into the buffer, which could be read-out and contaminate the output.

In the same way, we can manipulate G_{out} such that the output mode of the ORCA buffer is a user-defined one to match emissions from different single-photon sources.

In the general case, the output of an ORCA buffer is not ideal single mode so can be a mixture of different modes described by the density matrix

$$\rho_{\text{out}} = \frac{1}{W} \sum_k \xi_k \alpha_k |v_k\rangle\langle v_k|, \tag{3.43}$$

where ξ_k is the buffer efficiency for the quantum state $|\psi_k\rangle \to |v_k\rangle$ with $W = \sum_k \xi_k \alpha_k$ (normalization constant). The brightness after the buffer is $B = W$; the indistinguishability of the output photon will be $I_{\text{out}} = 1/K_{\text{out}}$ (refer to Eq.(3.39)) where K is the mode capacity.

To see how a real ORCA performs, we simulate the buffer process using QDs and caesium ORCA as an example. We start by modelling a single-photon emitted by a QD.

The mixture of temporal-spectrum mode results from two dynamics. Firstly the pure dephasing and electron-phonon interaction during the photon generation process which limits the temporal mode purity of every single-photon. Secondly the uncertainty of central frequency and arrival time of different photons. The second mixture is introduced externally when considering the interference (e.g.HOM interference) between different photons. Both dynamics contribute to the decrease of indistinguishability $I^{(1)}$ and $I^{(2)}$.

Our approach is to first build the two-colour spectrum $C(\omega,\mu) = \langle \hat{E}^+(\omega)\hat{E}(\mu)\rangle$ (or two-time correlation function $C(t,t')$) of the single-photon electric field. For QDs, this two-colour spectrum is well explored in [66], where they discussed the ultimate trade off between indistinguishability and brightness. It can be easily proved that $C(\omega,\mu) = C^*(\mu,\omega)$ as follows:

$$\begin{aligned} C(\omega,\mu) &= \langle \hat{E}^+(\omega)\hat{E}(\mu)\rangle \\ &= \langle [\hat{E}^+(\mu)\hat{E}(\omega)]^+\rangle \\ &= [\langle \hat{E}^+(\mu)\hat{E}(\omega)\rangle]^* \\ &= C^*(\mu,\omega). \end{aligned} \tag{3.44}$$

$C(\omega,\mu)$ is Hermition and thus eigenvalue decomposable and therefore the single-photon with electric field $C(\omega,\mu)$ is in the state described by intrinsic density matrix $\rho^{\omega\mu}_{itr}(\omega_0,t_0) = C(\omega,\mu)/M$, where $M = \int C(\omega,\omega)d\omega$ is the normalization factor, ω_0, t_0 are the central frequency and emission time of the photon.

We can then directly use $\tilde{\rho}_{\omega\mu}(\omega_0,t_0)$ to further construct our density matrix which includes external uncertainty, namely, spectral diffusion and time jitter. Spectral diffusion happens when the fluctuation of the local environment changes the central frequencies of the two different photons. Time jitter occurs when the QD is pumped off-resonantly. This can be tackled by pumping resonantly but the brightness is limited due to the emission filtering from the pump field.

The spectral diffusion [80, 12, 37, 112] and time jitter is described by central frequency and emission time distribution $p(\omega_0,t_0)$:

$$p(t_0,\omega_0) \propto e^{-\frac{t_0^2}{2\sigma_{t_0}}} * e^{-\frac{\omega_0^2}{2\sigma_{\omega_0}}}. \tag{3.45}$$

The overall density matrix of the photon from QD is then:

$$\rho^{\omega\mu} = \int p(t_0,\omega_0)\rho^{\omega\mu}_{itr}(\omega_0,t_0)dt_0 d\omega_0. \tag{3.46}$$

An eigenvalue decomposition of the density matrix is:

$$\rho = \sum \alpha_k |\psi_k\rangle\langle\psi_k| \tag{3.47}$$

which gives all the temporal eigenmodes. The Fourier transform of the spectral correlation function is the two-time correlation function which, in practice, can be measured without any detailed knowledge about the noise dynamics of the source.

In our simulation specifically, we produce such eigenmodes for a state-of-the-art off-resonantly excited QD with a self-indistinguishability of $I^{(1)} \approx 0.7$ (similar to QD3 in Ref. [134]). Here the distinguishability of the QD is mainly caused by timing jitter induced by the off-resonant pumping scheme.

The ORCA buffer is already modeled and verified experimentally in Chapter 3.1. To test the *singlemodeness*, we simulate our ORCA buffer using the same parameters we fitted from the experiment and use the first several main eigenmodes of the QDs as the input signal. Different eigenmodes have different storage efficiency. Fig.(3.6) shows the simulation results. The QDs start with a $I^{(1)} = 1/K = 0.75$, after quantum buffer the indistinguishability is substantially improved ($I^{(1)} = 1/K = 0.98$). This is because the $k = 0$ mode is delivered with high efficiency while the $k \geq 1$ modes are highly suppressed, indicating that the ORCA buffer is very near a single-mode-operation. The Brightness is reduced to 40%, $B_{\text{out}} = 0.4B_0 \approx 0.29$, where $B_0 = 0.72$ is the initial brightness of the actual QD. This predicted performance already matches the leading resonantly pumped QDs (e.g. QD4 in reference [134]). Note that this ORCA buffer is using Gaussian shaped control pulse as we did in the experiment. It is not optimal for the given dominant eigenmode. To improve performance even further, we numerically optimize the shape and energy of both the read-in and read-out control pulse. The brightness and self-indistinguishability after buffering then is: $I^{(1)}_{\text{out}} \approx 0.98$, $B_{\text{out}} \approx 0.61B_0 \approx 0.43$ (blue bars in Figure 3.6).

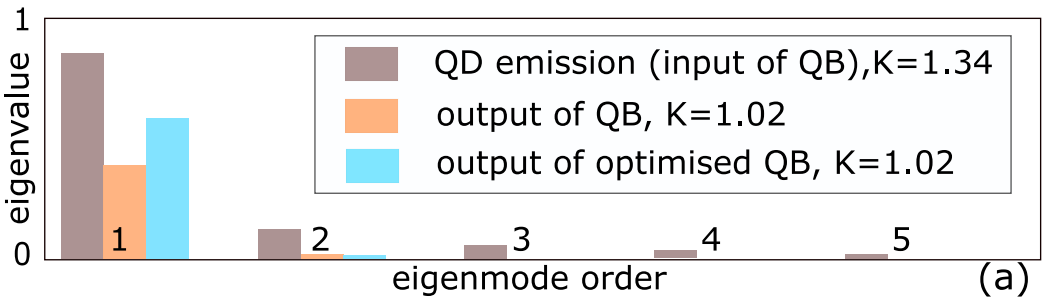

Figure 3.6: Simulation of singlemodeness of an ORCA buffer based on the demonstrated experimental performance in Fig. 3.2. We show the first 5 eigenvalues/modes before (brown) and after (orange and blue) the ORCA buffer. K is the mode capacity.

The dynamics in this simulation is more like a black box, we put in the QD emission and blindly optimize the control field shape. We will give a more complete picture in Green's function point of view later in Chapter 3.3.

3.2.1.3 Comparison to intensity filtering

An important property of the buffer is its ability to outperform passive filtering (i.e. a time-stationary linear filter) when delivering pure single-photon states. Therefore we compare our predicted ORCA temporal-spectral filtering against this conventional passive intensity filtering approach [58, 150] for QD emission as the input.

We first model a passive spectrum intensity filter (e.g. cavity) which defines an intensity transmission window for light $F(\omega)$. Light field $|\psi(\omega)\rangle$(normalized) will be filtered into $|\Psi(\omega)\rangle = \sqrt{F(\omega)}|\psi(\omega)\rangle$(not normalized), therefore, photon in the form of equation (3.47) will become

$$\rho' = \sum \alpha_k |\Psi_k\rangle\langle\Psi_k|. \tag{3.48}$$

The brightness of the state ρ' is

$$B = \mathrm{Tr}[\rho']/\mathrm{Tr}[\rho]. \tag{3.49}$$

The filtered state ρ' can be eigenvalue decomposed

$$\rho' = \sum \alpha'_k |\psi'_k\rangle\langle\psi'_k|. \tag{3.50}$$

Similarly with equation (3.47), the indistinguishability after intensity filter is

$$\text{Ind.} = \mathrm{Tr}[\rho'^2]/\mathrm{Tr}[\rho']^2 = \sum |\alpha'_k|^2/(\sum |\alpha'_k|)^2. \tag{3.51}$$

A time gate is a temporal intensity filter which defines an intensity transmission window $F(t)$. The brightness and the indistinguishability is calculated in the same way.

We then simulate 100 QDs with various noise dynamics. In our simulation of different QDs, we make spectral diffusion to be the same and small since it has a similar effect to density matrix as time jitter. We vary the time jitter of $\sigma_{t_0} \in [0.02, 0.6] * (1/\gamma)$ where γ is the linewidth of photon spectrum without spectrum diffusion. and cavity Q factor of $Q \in [10^2, 10^4]$ (with coupling constant $\hbar g = 50\mu eV$). The performance of intensity filter is found to be within the grey area of Fig. (3.7). Unit indistinguishability can only be achieved in the limit that the brightness goes to zero.

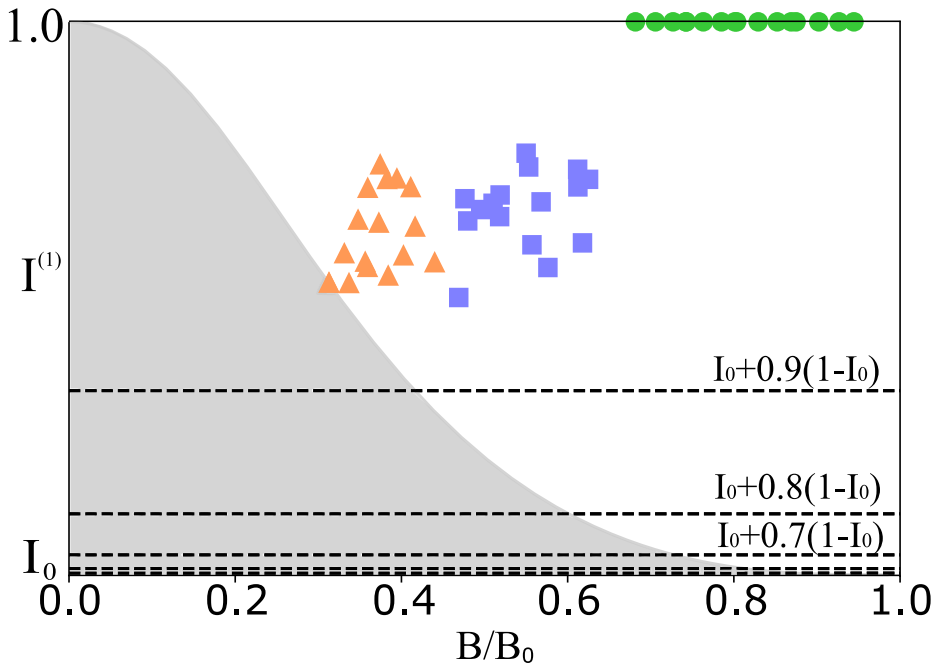

Figure 3.7: ORCA buffer compared with intensity filter. The shaded area indicates the simulated intensity filtering. We plot the self-indistinguishability $I^{(1)}$, against the brightness B normalized by the initial brightness B_0. I_0 is the initial self-indistinguishability. The dashed-lines indicate $I^{(1)} = I_0 + q(1 - I_0)$ with q being a fraction indicating the improvement of $I^{(1)}$. The triangles indicate ORCA buffer filtering with Gaussian temporal-mode control pulse for 16 random samples. The squares are ORCA buffer filtering with optimized control pulse shape and energy for the same set. The circles show the performance of an ideal quantum buffer.

We also plot the predicted performance of our experimental demonstration of the ORCA buffer system, both without (orange triangle) and with (blue square) control-pulse shape optimization, for 16 QD within the same noise variation range. They both outperform passive filtering. An ideal filter would have $I^{(1)} = 1$, and $B = B_0\alpha_0$ (green circle).

3.2.1.4 Unifying different SPSs

Besides improving the self-indistinguishability $I^{(1)}$, perhaps a more exciting application is unifying different sources to increase $I^{(2)}$. This is because it is far more challenging to build different source generating indistinguishable photons than increasing the $I^{(1)}$ of each single source. Our quantum buffer can convert the input temporal-spectral mode to an arbitrary output mode via reshaping of the read-out control field, thereby mode-matching emission from disparate QDs. We demonstrate this capability numerically by modelling two distinct QD emissions with the same

central frequency with an inter-indistinguishability of $I^{(2)} = 0.62$, as in Fig. 3.8. We then simulate two ORCA buffers, one interacting with each QD. By selecting the largest eigenmode of each QD in their respective ORCA buffers using necessarily different read-in fields, and then recall them with the same appropriately adjusted read-out control field shapes, the inter-indistinguishability would be $I^{(2)} = 0.96$ since the stored excitations are read out into nearly identical modes.

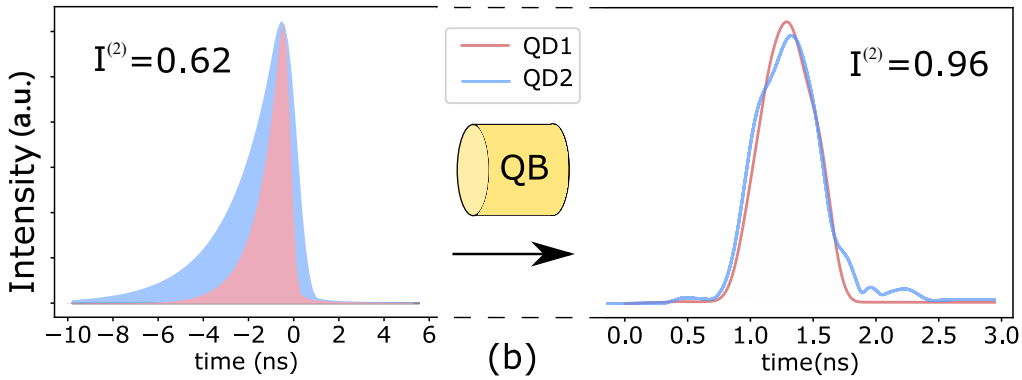

Figure 3.8: Mode unification by an ORCA buffer. Emission from two distinct QDs ($I^{(2)} = 0.62$) with different decay times (left figure) are actively unified by an ORCA buffer into two nearly identical photons (right figure, $I^{(2)} = 0.96$).

In the typical case where the different QD outputs are also distinguishable in their central emission frequency, it is possible using the ORCA protocol to adjust the readout frequency of the stored excitation as compared to the input.

Frequency conversion is achieved by changing the detuning of the two photon resonance configuration. Both control photon and signal photon will blue detuned and red detuned from resonance by the same frequency "detuning".(Shown in Fig). After read in signal with a certain detuning Δ_1, by reading out with a different detuning Δ_2, the read-out signal is shifted by $\Delta = \Delta_2 - \Delta_1$.

However, the efficiency will be decreased when either Δ_1 or Δ_2 is large. Here we explore the efficiency decrease when we increase the detuning. The simulation shows that we can still get 25% of short time read-out efficiency with 200GHz($\approx$ 1nm) detuning, as shown in Fig 3.9a.

Another effect that may also influence the buffer efficiency is the phase mismatch. The photon is stored as an orbital wave in the atomic ensemble, as is described in supplementary II, with a momentum of $\overrightarrow{k}_{ow} = (|\overrightarrow{k}_c| - |\overrightarrow{k}_s|)\overrightarrow{e}$, where $\overrightarrow{e}$ is the unit vector in the propagation direction. The phase-matching condition is that $\overrightarrow{k}_{ow} = \overrightarrow{k}'_c + \overrightarrow{k}'_s$. Meanwhile, the energy conservation should always be fulfilled:

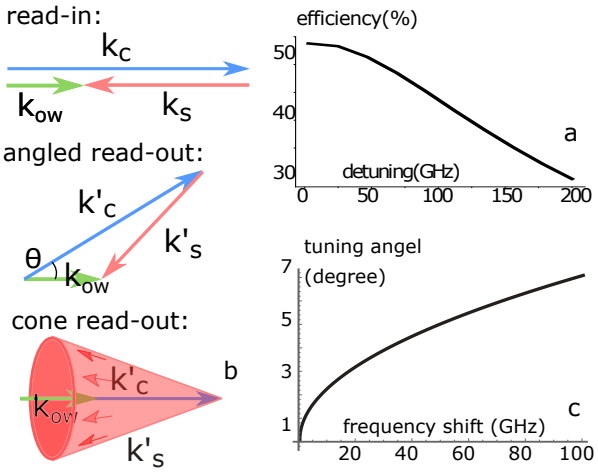

Figure 3.9: ORCA buffer efficiency with different detuning

$\hbar\Delta\omega_s = -\hbar\Delta\omega_c$, where $\Delta\omega_c$ and $\Delta\omega_s$ are the frequency shift of read-out control and output signal respectively.

If we keep the direction of read-out control and output signal collection to be in direction of $\overrightarrow{e}$, we will have a phase mismatch given by ΔkL,, where $\Delta k = |\overrightarrow{k}_{ow}| - |k'_c + \overrightarrow{k}'_s| = 2\Delta\omega/c$ is the wave vector mismatch and L is the length of the interaction area. The converted output as a spacial mode shown in fig 3.9b. The conversion efficiency hence drop by a factor of $\text{sinc}^2(\Delta kL/2)$. For example, with our vapour cell length 7 cm, the conversion efficiency is 50% when the frequency shift is 12 GHz and 10% when the frequency shift is 20 GHz.

However, this decrease in efficiency can be tackled by changing the angle of the read-out control field, shown in fig 3.9. The tuning angel is shown in fig 3.9.

$$\cos\theta = \frac{\omega_c^2 - \omega_c\omega_s - \Delta\omega(\omega_c + \omega_s)}{\omega_c^2 - \omega_c\omega_s - \Delta\omega(\omega_c - \omega_s)}. \tag{3.52}$$

By combining coherent temporal mode filtering and frequency conversion in a single device, this approach would overcome a key barrier to scaling photonic quantum technologies demanding many identical pure state single-photons.

3.3 Mode overlapping

We have introduce the dynamics and performance of ORCA buffer both theoretically and experimentally. One central attribution of ORCA buffer is the singlemodeness. In this section, we will analyse the mode capacity and mode selectivity from the point of view of the Green's function of ORCA. We start with calculating the Green's function.

3.3.1 Calculating the Green's function

As we have mentioned in Chapter 3.2.1.2, Green's function of ORCA buffer (memory) can be calculated theoretically. There are two ways to find a Green's function.

1). The equations of motion (3.26) is a linear map from the input signal ψ_{in} to output signal ψ_{out}:

$$\psi_{out}(t) = \int G(t,t')\psi_{in}(t')dt' \tag{3.53}$$

where $G(t,t')$ is the Green's function.

Writing the signal in retarded time $\tau = t - z/c$, with the following derivative transformation

$$\partial_z + \frac{1}{c}\partial_t \to \partial_z, \partial_t \to \partial_\tau, \tag{3.54}$$

we now rewrite the equations of motion as

$$\begin{aligned} \partial_t B(z,\tau) &= -\frac{|\Omega(z,\tau)|^2}{4\Gamma_2}B(z,\tau) - i\kappa\frac{\Omega^*(z,\tau)}{2\Gamma_1}A(z,\tau), \\ \partial_z A(z,\tau) &= -\frac{i\kappa^*\Omega(z,\tau)}{2\Gamma_2}B(z,\tau), \end{aligned} \tag{3.55}$$

and applying the unilateral Fourier Transformation over z:

$$\begin{aligned} \tilde{A}(k,\tau) &= \frac{1}{\sqrt{2\pi}}\int_0^\infty A(z,\tau)e^{ikz}dz, \\ \tilde{B}(k,\tau) &= \frac{1}{\sqrt{2\pi}}\int_0^\infty B(z,\tau)e^{ikz}dz, \\ \tilde{\kappa}(k) = \frac{1}{\sqrt{2\pi}}\int_0^L \kappa e^{ikz}dz &= \frac{\kappa}{ik\sqrt{2\pi}}(e^{ikL}-1), \end{aligned} \tag{3.56}$$

and the k- space equations of motion are

$$\begin{aligned} \partial_t\tilde{B} &= -\frac{|\tilde{\Omega}|^2}{4\Gamma_2}(*)\tilde{B} - i\tilde{\kappa}(*)\frac{\tilde{\Omega}^*}{2\Gamma_1}(*)\tilde{A}, \\ -ik\tilde{A} - \frac{1}{\sqrt{2\pi}}A_{in} &= -\frac{i\tilde{\kappa^*}(*)\tilde{\Omega}}{2\Gamma_2}(*)\tilde{B}, \end{aligned} \tag{3.57}$$

where $(*)$ indicates a convolution. Solving the second of these equations and substituting into the first we get:

$$\begin{aligned} \partial_\tau\tilde{B} &= \Theta(*)\tilde{B} + \frac{\tilde{\kappa}(*)\tilde{\Omega}^*}{2\sqrt{2\pi}\Gamma_1 k}A_{in}, \\ \Theta &= -\frac{|\tilde{\Omega}|^2}{4\Gamma_2} - \frac{i|\tilde{\kappa}|^2(*)|\tilde{\Omega}|^2}{4\Gamma_1\Gamma_2 k}, \end{aligned} \tag{3.58}$$

If we consider $\tilde{B}$ to be a vector with continuous element k, then equation (3.58) can be written as

$$\begin{aligned} \partial_\tau \tilde{B} &= -iM\tilde{B} + \Phi(\tau)A_{in}, \\ \Phi(\tau) &= \frac{\tilde{\kappa}(*)\tilde{\Omega}^*}{2\sqrt{2\pi}\Gamma_1 k}, \end{aligned} \tag{3.59}$$

where M is defined as $-iM = \Theta$.

Suppose we define a propagation operator V such that $\partial_\tau V = iVM$, then we conveniently have: $\partial_\tau(V\tilde{B}) = V\Phi(\tau)A_{in}$. Integration of this equation gives:

$$\tilde{B}(\tau) = V^{-1}V_{\tau=0}\tilde{B}_0 + V(\tau)^{-1}\int_{-\infty}^{\tau} V(\tau')\Phi(\tau')A_{in}(\tau')d\tau'. \tag{3.60}$$

Since there is no spin wave at the beginning of the interaction, $\tilde{B}_0 = 0$. To examine the stored spin wave after the interaction, we take $\tau \to \infty$

$$\tilde{B}_{out} = \int_{-\infty}^{\infty} V_{out}^{-1}V(\tau)\Phi(\tau)A_{in}(\tau)d\tau. \tag{3.61}$$

It is important to note that $A_{in}(\tau)$ is a scalar,while V is a matrix and $\Phi(\tau)$ a vector. The read-in Green's function is then:

$$G_{A\to B}(k,\tau) = V_{out}^{-1}V(\tau)\Phi(\tau). \tag{3.62}$$

With this in mind, we can write $\tilde{B}(k)$ as being linearly dependent on $A_{in}(\tau)$

$$\tilde{B}_{out}(k) = \int_{-\infty}^{\infty} G_{A\to B}(k,\tau)A_{in}(\tau)d\tau. \tag{3.63}$$

With the same method we can get

$$A_{out}(\tau) = \int_{-\infty}^{\infty} G_{B\to A}(\tau,k)B_{in}(k)dk. \tag{3.64}$$

Combining these two linear maps will give a total linear map from input signal to output signal

$$A_{out}(\tau) = \int_{-\infty}^{\infty} G(\tau,\tau')A_{in}(\tau')d\tau' \tag{3.65}$$

with the overall Green's function:

$$G(\tau,\tau') = G_{B\to A}(\tau,k)G_{A\to B}(k,\tau'). \tag{3.66}$$

2) The second way is to construct a Green's function numerically by calculating the transmission of a complete signal basis (in this thesis, we use Hermite-Gaussian basis).

$$G(t,t') = \sum_i \lambda_i S_i(t') h_i^*(t) \tag{3.67}$$

where $h_i(t)$ is the Hermit-Gaussian function in order i. $S_i(t)$ is obtained by calculating (through equations (3.26)) the output signal of ORCA buffer when the input signal is $h_i(t)$, λ_i is the square root of the corresponding buffer efficiency.

3.3.2 Mode overlap between SPS and ORCA buffer

We find out that the optimised ORCA buffer has a Green's function not necessarily *single mode*. However, it still behaves like a near single-mode quantum buffer. To explain this, we have to look at how the Green's function's input singular vectors overlap with the QD eigenmodes.

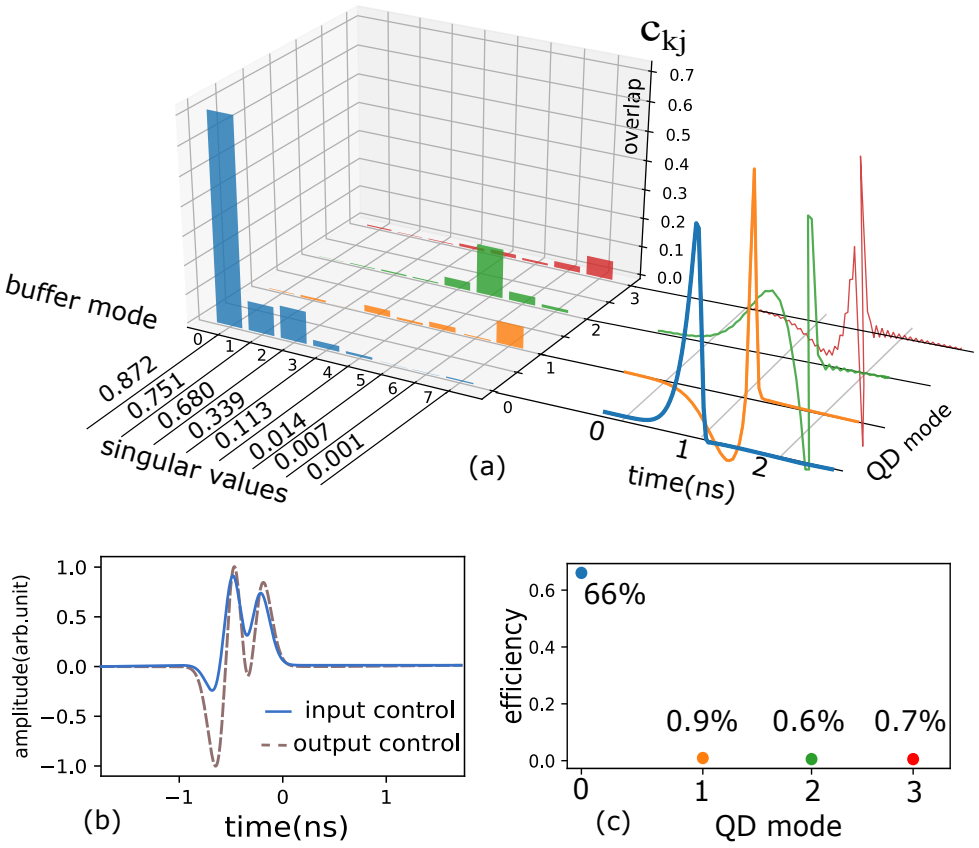

Figure 3.10: (a) shows the first four modes of the emission of a QD example(in four different colors). It also lists the singular values of the Green's function with the control fields given by (b). The bars in (a) give the overlaps c_{kj} between the kth left singular mode of the Green's function and the ith QD mode. Mode selectivity of this ORCA buffer is justified by (c) which shows that only the dominant QD mode has non-zero buffer efficiency.

A singular value decomposition of the Green's function $G_{\text{in}}(t', t) = \sum_k \lambda_k \beta_k(t')\, u_k^*(t)$ will give a sequence of input singular mode $u_k^*(t)$ with singular value λ_k. The output signal of the ith single-photon source mode (equation (3.65)) is:

$$\begin{aligned} S_i^{out}(t') &= \int_{-\infty}^{\infty} G(t', t) S_i^{in}(t) dt \\ &= \int_{-\infty}^{\infty} \sum_k \lambda_k \beta_k(t')\, u_k^*(t) S_i^{in}(t) dt \\ &= \sum_k \lambda_k \beta_k(t') \int_{-\infty}^{\infty} u_k^*(t) S_i^{in}(t) \\ &= \sum_k \lambda_k c_{ki} \beta_k(t') \end{aligned} \tag{3.68}$$

where $c_{ki} = \int_{-\infty}^{\infty} u_k^*(t) S_i^{in}(t)$ is the overlap between ORCA buffer modes and QD modes. The buffer efficiency of the ith QD mode is:

$$\eta_i = \sum_k (\lambda_k c_{ki})^2 \tag{3.69}$$

Here we give an example of the Green's function optimized to buffer a certain QD emission. We show the singular values λ_k, the QD-ORCA overlap c_{ki} and the QD mode buffer efficiency η_i in Fig.3.10.

Ideally, we would like the Green's function to have only one non-zero singular value λ_0 and the dominant QD mode S_0^{in} only overlapping with that singular mode $u_0(t)$. As we can tell from the singular values, the ORCA buffer is close to single mode but there are still some fraction on the second, third and fourth modes. However, this is not a problem because higher QD modes do not overlap with the first four buffer modes ($c_{ki} \approx 0$). Fig. 3.10c demonstrates the singlemodeness of ORCA buffer. Only the dominant QD mode has a non-zero buffer efficiency.

In other words, the *singlemodeness* of the SPS-ORCA system is determined by η_i, instead of λ_k. The ORCA system itself can afford to be multimode as long as c_{ki} pairs with λ_k in a favourable way.

3.4 Conclusion

In this chapter, ORCA buffer is proposed to purify and unify single photon temporal modes. A proof of principle experiment demonstrated the validity of the theory model as well as the lower-than-dark-count noise. Simulations based on the theory model and the experiment parameters have shown that ORCA buffer can outperform ideal traditional filters in terms of inner-indistinguishability and increase the

inter-indistinguishability significantly. A Green's function analysis was performed to understand how to construct a single mode buffer from a multi mode ORCA. Since fabricating high-quality, indistinguishable SPS is still challenging, the ORCA buffer protocol offers an alternative way to tackle the problem and pave the way towards large scale LOQC.

Chapter 4

Ion-ion remote entanglement

4.1 Polarisation encoded ion-ion remote entanglement (RE)

As as been discussed in Chapter 2.1.3, quantum computing is only useful when we can scale the physical qubits to a large number while keeping a fairly high gate fidelity. Ion traps, like other physical platforms for quantum computing, face many challenges in terms of scalability. Using photons to entangle different ion trap modules is one way to mitigate the difficulty. To entangle two ions remotely, each ion is first entangled with a certain DoF of its emitted photon. One straightforward choice is the photon polarisation. Several experiments have demonstrated such remote entanglement but with very low rate and compromised fidelity. Before we explore methods to improve the photon collection rate and fidelity, we should first perform a more careful analysis of the entanglement scheme, considering different error sources in a more general point of view.

4.1.1 Entanglement scheme

To entangle two ions remotely, each ion is first entangled with the polarisation of its emitted photon. The two photons generated by Alice and Bob are mixed on the beamsplitter to erase the which-way information followed by polarisation-sensitive detection on the two output ports. Coincident detection of one H photon and one V photon projects the remaining ionic parts of the wavefunction into an entangled Bell state. This remote entanglement scheme was proposed and demonstrated with direct excitation configuration in Ref.[98, 61], where the ion-photon entanglement is generated by atom spontaneous decay. Each ion is excited to a short lived state (P state), followed by spontaneous decay to its two ground qubit states (Zeeman qubit).

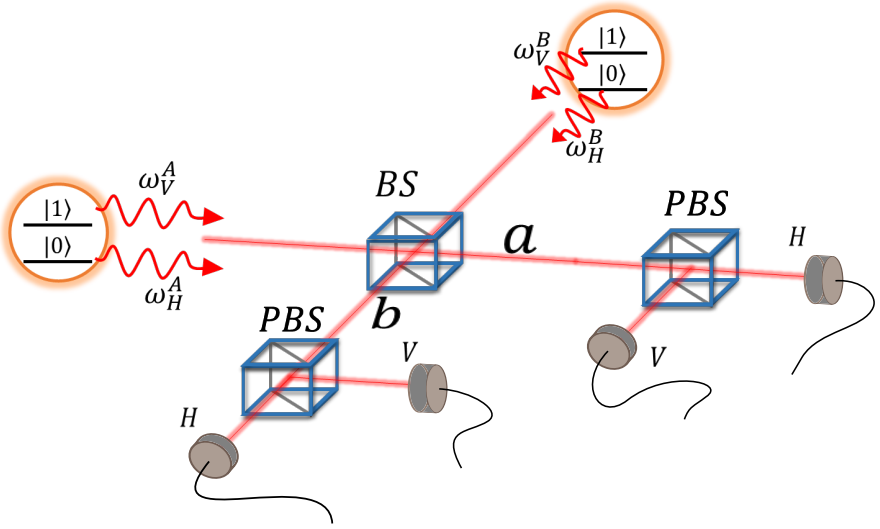

Figure 4.1: Remote entanglement scheme.one photon is generated in each site of the entanglement, the polarisation of the photon is entangled with inner state $|0\rangle$ and $|1\rangle$ of the ion. the two photon are then mixed in a 50:50 beamsplitter and detected by four time-resolved detector. a and b indicate the two port after beamsplitter. Any H-V coincidence detection will herald an ion-ion Bell state $|01\rangle + |10\rangle$

The ion qubit is then entangled with the angular momentum of the photon because of angular momentum conservation. The angular momentum is projected to be the polarisation of the photon, which is used for heralding ion-ion entanglement.

In the direct excitation ion-photon entanglement configuration, only two internal states of the ion are involved. However, if we want to explore other level choices, for example, using D metastable level for entanglement generation [138], there can be three Zeeman levels involved corresponding to three transitions σ^+, σ^-, π. In this case, the polarisation detection (two degrees of freedom) cannot discriminate all three situations so an apparently heralded state may not always correspond to the target Bell state. In order to make the analysis more general, we take into account three ion levels from the beginning.

In the following notation of cavity-ion state, we use two symbols in the bra-ket with the first indicating the ion system and the second indicating the photonic system, for example, $|0\sigma^+\rangle$. The first symbol 0 refers to the ion state and the second symbol σ^+ refers to the cavity photon polarisation. As we mentioned above, we will examine three ion levels with three photon polarisations associated with them. These system states are $|0\sigma^+\rangle$, $|1\pi\rangle$ and $|2\sigma^-\rangle$. If we think of ion state $|0\rangle$ and $|1\rangle$ as the qubit states, we will see soon that state $|2\sigma^-\rangle$ will herald a wrong ion-ion state and thus reduce the entanglement fidelity. This error can be corrected to some extent after heralding

but we still want to minimize this error. This hasn't been formally introduced yet but it is useful to keep this in mind from now on.

Assuming no dispersion in path before the photons interfere on the beamsplitter, the photon wavepacket does not change while the photon is travelling. We can easily write down the state of Alice ion-photon system:

$$\begin{aligned} & e^{i\omega_0^A(t-t_A)} f_{\sigma^+}^A[t-t_A-Z^A/c] e^{i\omega_{\sigma^+}^A(t-t_A)-ik_{\sigma^+}^A Z^A}|0\sigma^+\rangle \\ & +e^{i\omega_1^A(t-t_A)} f_{\pi}^A[t-t_A-Z^A/c] e^{i\omega_{\pi}^A(t-t_A)-ik_{\pi}^A Z^A}|1\pi\rangle \\ & +e^{i\omega_2^A(t-t_A)} f_{\sigma^-}^A[t-t_A-Z^A/c] e^{i\omega_{\sigma^-}^A(t-t_A)-ik_{\sigma^-}^A Z^A}|2\sigma^-\rangle \end{aligned} \tag{4.1}$$

where f is the non-normalised wavepacket of the photon. The subscript on f indicates the polarisation of the wavepacket. The superscript on f indicates the site the photon came from, Alice or Bob. t_A is the excitation time of Alice. ω_0^A is the Alice ion frequency of the ion level $|0\rangle$. Exponential terms are the phase evolution. In the phase evolution terms, ion phase only evolves only in time, for example, $e^{i\omega_0^A(t-t_A)}$ in the first phase term of $|0\sigma^+\rangle$. However, the photon phase evolves in both time and space, for example, $e^{i\omega_{\sigma^+}^A(t-t_A)-ik_{\sigma^+}^A Z^A}$, where $k_{\sigma^+}^A$ is the wave vector of σ^+ photon from Alice, and Z^A is the distance Alice's photon travels.

There are two ways of collecting the photon. One is to collect using an imaging system with its optical axis aligned with the magnetic field axis so that only σ^+ or σ^- photons are collected. After a $\lambda/4$ waveplate, these are transformed, respectively, to H or V polarised photons. This method is only valid when there are three, rather than two Zeeman states involved. The advantage of this photon collection configuration is that there is no erroneous heralding because π photons do not propagate along the B field direction. However, depending on whether an optical cavity is used, it can be very technically challenging to generate stable σ photons in the presence of birefringence. This problem is discussed in Ref. [71] and will be summarized in section 4.1.2. The other possible photon collection configuration is perpendicular to the magnetic field axis, where π photons are projected to be V polarized and both σ photons are projected to be H polarized. Since both σ are projected to look the same and herald an entanglement event, a loss (error) state is generated. Luckily, this error can be fully corrected if we have the exact detection time information. This will also be discussed in section 4.1.2. An advantage of this approach is that birefringence can be efficiently suppressed [71], which is almost impossible for the former configuration.

To construct our theoretical analysis, we choose the latter (H/V) configuration because the treatment will automatically include the first, It is obvious how to apply this analysis to the first configuration but not the other way around. Furthermore,

for any system where birefringence cannot be sufficiently suppressed, it is preferable to use the latter configuration.

Collecting light perpendicular to the magnetic field, after the projection of σ^+, σ^- and π photons, the system state is then:

$$\begin{aligned} & e^{i\omega_0^A(t-t_A)} f_H^A[t-t_A-Z^A/c] e^{i\omega_H^A(t-t_A)-ik_H^A Z^A}|0H\rangle \\ +& e^{i\omega_1^A(t-t_A)} f_V^A[t-t_A-Z^A/c] e^{i\omega_V^A(t-t_A)-ik_V^A Z^A}|1V\rangle \\ +& e^{i\omega_2^A(t-t_A)} n^A[t-t_A-Z^A/c] e^{i\omega_n^A(t-t_A)-ik_n^A Z^A}|2H\rangle \end{aligned} \tag{4.2}$$

Several notes should be made here:

(1) This is assuming the ion-photon system is a pure state, which is not necessarily true. We will deal with mixed states in section 4.3.

(2) This state is a function of time t and photon position of interest Z. So it doesn't make sense to ask what the state of the system is without knowing both the time and the position (of the photon) you are considering.

(3) f or n is normalised to the probability of that photon being emitted, as opposed to being normalised to 1, meaning it already has the correct amplitude. It is useful to keep track of the photon amplitude because it is crucial for entanglement rate.

(4) Although σ^+ and σ^- are both projected to H, their temporal wavepackets are different. The desired photon is labeled as f_H^A while photon associated with the decay to state $|2\rangle$ is labeled as n^A to highlight the difference. we will call the state $|2\rangle$ as *error state* because it generate loss error for the final entanglement state.

(5) The excitation time t_A is only physical for the wavepacket, not for the phase. We keep it here as a mathematical offset of the system's phase.

We write down the state of Bob in the same way:

$$\begin{aligned} & e^{i\omega_0^B(t-t_B)} f_H^B[t-t_B-Z^B/c] e^{i\omega_H^B(t-t_B)-ik_H^B Z^B}|0H\rangle \\ +& e^{i\omega_1^B(t-t_B)} f_V^B[t-t_B-Z^B/c] e^{i\omega_V^B(t-t_B)-ik_V^B Z^B}|1V\rangle \\ +& e^{i\omega_2^B(t-t_B)} n^B[t-t_B-Z^B/c] e^{i\omega_n^B(t-t_B)-ik_n^B Z^B}|2H_n\rangle \end{aligned} \tag{4.3}$$

Then we can take Alice to be: $c_0^A|0_A H_A\rangle + c_1^A|1_A V_A\rangle + c_2^A|2_A H_A\rangle$, and Bob to be $c_0^B|0_B H_B\rangle + c_1^B|1_B V_B\rangle + c_2^B|2_B H_B\rangle$. After the 50:50 beamsplitter, $|H_A\rangle \to (|H_A^a\rangle + |H_A^b\rangle)/\sqrt{2}$, $|H_B\rangle \to (|H_B^a\rangle - |H_B^b\rangle)/\sqrt{2}$, where a, b label the two output ports of the beamsplitter. For coincidence detection of H and V photons on different output ports of the beamsplitter, the Alice-Bob system is projected onto an ion state $c_1|1_A 0_B\rangle - c_2|0_A 1_B\rangle + c_3|1_A 2_B\rangle - c_4|2_A 1_B\rangle$, where $c_{1,2}$ is a ideally to be $\sqrt{1/2}$ so that the state is a Bell state. For coincidence detection of H and V photons on the same output

port of beamsplitter, the Alice-Bob system is projected onto an orthogonal ion-ion system $c_1|0_A1_B\rangle + c_2|1_A0_B\rangle + c_3|2_A1_B\rangle + c_4|1_A2_B\rangle$. In real life, these coefficients are highly dependent on $c^{A,B}_{0,1,2}$ and the exact detection time. This will be one of the main focuses of the remaining parts of this section.

To analyse the amplitude and phase of the four terms after detection, we take $c_1|1_A0_B\rangle - c_2|0_A1_B\rangle + c_3|1_A2_B\rangle - c_4|2_A1_B\rangle$ as an example and write down the full form of the state before the photons are detected.

$$\begin{aligned}
&\frac{1}{2}\Big[e^{i\omega_1^A(t-t_A)}e^{i\omega_0^B(t-t_B)}f_V^A[t-t_A-Z_b^A/c]e^{i\omega_V^A(t-t_A)-ik_V^AZ_b^A}\\
&\qquad\times f_H^B[t-t_B-Z_a^B/c]e^{i\omega_H^B(t-t_B)-ik_H^BZ_a^B}|1_A0_BV_b^AH_a^B\rangle\Big]\\
-&\frac{1}{2}\Big[e^{i\omega_0^A(t-t_A)}e^{i\omega_1^B(t-t_B)}f_H^A[t-t_A-Z_a^A/c]e^{i\omega_H^A(t-t_A)-ik_H^AZ_a^A}\\
&\qquad\times f_V^B[t-t_B-Z_b^B/c]e^{i\omega_V^B(t-t_B)-ik_V^BZ_b^B}|0_A1_BH_a^AV_b^B\rangle\Big]\\
+&\frac{1}{2}\Big[e^{i\omega_1^A(t-t_A)}e^{i\omega_2^B(t-t_B)}f_V^A[t-t_A-Z_b^A/c]e^{i\omega_V^A(t-t_A)-ik_V^AZ_b^A}\\
&\qquad\times n^B[t-t_B-Z_a^B/c]e^{i\omega_n^B(t-t_B)-ik_n^BZ_a^B}|1_A2_BV_b^AH_a^{Bn}\rangle\Big]\\
-&\frac{1}{2}\Big[e^{i\omega_2^A(t-t_A)}e^{i\omega_1^B(t-t_B)}n^A[t-t_A-Z_a^A/c]e^{i\omega_n^A(t-t_A)-ik_n^AZ_a^A}\\
&\qquad\times f_V^B[t-t_B-Z_b^B/c]e^{i\omega_V^B(t-t_B)-ik_V^BZ_b^B}|2_A1_BH_a^{An}V_b^B\rangle\Big]
\end{aligned} \tag{4.4}$$

We make the assumption that the detector is frequency insensitive, so there is, in principle no difference in the detection between $|V_b^A\rangle$ and $|V_b^B\rangle$ or between $|H_b^{An}\rangle$ and $|H_b^B\rangle$ even if they have different frequencies. So after detection, $|V_b^AH_a^B\rangle$ and $|H_a^AV_b^B\rangle$ are not distinguished by detectors and thus can be taken out of the bracket, implicating that the ion system is separable from the photon system. With detection time of t_H at port a and t_V at port b, L being the designed path length and Δx being

the path difference between Alice and Bob, we come to an ion-ion state:

$$\begin{aligned}
&\frac{1}{2}\Big[e^{i\omega_1^A(t-t_A)}e^{i\omega_0^B(t-t_B)}f_V^A[t_V-t_A-(L+\Delta x)/c]e^{i\omega_V^A(t_V-t_A)-ik_V^A(L+\Delta x)}\\
&\qquad\times f_H^B[t_H-t_B-L/c]e^{i\omega_H^B(t_H-t_B)-ik_H^BL}|1_A0_B\rangle\Big]\\
&-\frac{1}{2}\Big[e^{i\omega_0^A(t-t_A)}e^{i\omega_1^B(t-t_B)}f_H^A[t_H-t_A-(L+\Delta x)/c]e^{i\omega_H^A(t_H-t_A)-ik_H^A(L+\Delta x)}\\
&\qquad\times f_V^B[t_V-t_B-L/c]e^{i\omega_V^B(t_V-t_B)-ik_V^BL}|0_A1_B\rangle\Big]\\
&+\frac{1}{2}\Big[e^{i\omega_1^A(t-t_A)}e^{i\omega_2^B(t-t_B)}f_V^A[t_V-t_A-(L+\Delta x)/c]e^{i\omega_V^A(t_V-t_A)-ik_V^A(L+\Delta x)}\\
&\qquad\times n^B[t_H-t_B-L/c]e^{i\omega_n^B(t_H-t_B)-ik_n^BL}|1_A2_B\rangle\Big]\\
&-\frac{1}{2}\Big[e^{i\omega_2^A(t-t_A)}e^{i\omega_1^B(t-t_B)}n^A[t_H-t_A-(L+\Delta x)/c]e^{i\omega_n^A(t_H-t_A)-ik_n^A(L+\Delta x)}\\
&\qquad\times f_V^B[t_V-t_B-L/c]e^{i\omega_V^B(t_V-t_B)-ik_V^BL}|2_A1_B\rangle\Big]
\end{aligned} \tag{4.5}$$

We can than rewrite the state in a more concise form with each coefficient in the form of oscillation term $e^{i\alpha_i}$ and slow varying amplitude h_i:

$$\begin{aligned}
\Phi(t,t_H,t_V) =&h_1e^{i\alpha_1}|10\rangle+h_2e^{i\alpha_2}|01\rangle+h_3e^{i\alpha_3}|12\rangle+h_4e^{i\alpha_4}|21\rangle\\
=&e^{i\alpha_1}(h_1|10\rangle+h_2e^{i\phi}|01\rangle+h_3e^{i\theta_3}|12\rangle+h_4e^{i\theta_4}|21\rangle),\\
h_1 =&\frac{1}{2}f_V^A[t_V-t_A-(L+\Delta x)/c]f_H^B[t_H-t_B-L/c]\\
h_2 =&\frac{1}{2}f_H^A[t_H-t_A-(L+\Delta x)/c]f_V^B[t_V-t_B-L/c]\\
h_3 =&\frac{1}{2}f_V^A[t_V-t_A-(L+\Delta x)/c]n^B[t_H-t_B-L/c]\\
h_4 =&\frac{1}{2}n^A[t_H-t_A-(L+\Delta x)/c]f_V^B[t_V-t_B-L/c]
\end{aligned} \tag{4.6}$$

where we can remove a global phase $e^{i\alpha_1}$ and left with qubit *entanglement phase* (relative phase between the terms associated with qubit states) $\phi=\alpha_2-\alpha_1$ and two error channel phase $\theta_{3,4}=\alpha_{3,4}-\alpha_1$ as shown in Eq.4.6. These phases are:

$$\begin{aligned}
\phi =&\Delta\omega_{ion}^A(t-t_A)-\Delta\omega_{ion}^B(t-t_B)+\Delta\omega_H^{AB}t_H-\Delta\omega_V^{AB}t_V+\Delta\omega_{VH}^At_A\\
&-\Delta\omega_{VH}^Bt_B+(\Delta\omega_{VH}^A-\Delta\omega_{VH}^B)L/c+\Delta\omega_{VH}^A\Delta x/c\\
\theta_3 =&(\omega_2^B-\omega_0^B)(t-t_B)+(\omega_n^B-\omega_H^B)(t_H-t_B-L/c)\\
\theta_4 =&(\omega_2^A-\omega_0^A)(t-t_A)+(\omega_n^A-\omega_H^A)(t_H-t_A-(L+\Delta x)/c)+\phi
\end{aligned} \tag{4.7}$$

where $\Delta\omega_{ion}^{A(B)} = \omega_0^{A(B)} - \omega_1^{A(B)}$ is the Alice (Bob) ion qubit frequency splitting. $\Delta\omega_{H(V)}^{AB} = \omega_{H(V)}^{A} - \omega_{H(V)}^{B}$ is the H(V) photon frequency difference between Alice and Bob, and $\Delta\omega_{VH}^{A(B)} = \omega_V^{A(B)} - \omega_H^{A(B)}$ is the frequency difference between V and H photon from Alice(Bob). We have also used the assumption that the light path is non-dispersive so that $k = \omega/c$. If we choose $t_A = t_B = 0$, the phases become:

$$\begin{aligned}
\phi =& \Delta\omega_{ion}^{AB} t + \Delta\omega_H^{AB} t_H - \Delta\omega_V^{AB} t_V \\
&+ (\Delta\omega_{VH}^{A} - \Delta\omega_{VH}^{B}) L/c + \Delta k_{VH}^{A} \Delta x \\
\theta_3 =& (\omega_2^B - \omega_0^B) t + (\omega_n^B - \omega_H^B)(t_H - L/c) \\
\theta_4 =& (\omega_2^A - \omega_0^A) t + (\omega_n^A - \omega_H^A)(t_H - (L + \Delta x)/c) + \phi
\end{aligned} \tag{4.8}$$

where we have assumed small Zeeman splitting so that $\omega_2 - \omega_1 = \omega_1 - \omega_0$, and $\Delta\omega_{ion}^{AB} = \Delta\omega_{ion}^{A} - \Delta\omega_{ion}^{B}$. From this formula, we can easily see that

(1) The phase evolves because of the spin state difference between Alice and Bob.

(2) The phase between the terms of the Bell state will be determined by the detection time. If one can subtract this phase, entanglement can be achieved with distinguishable photons ($\Delta\omega_H^{AB} \neq 0$).

(3) The fluctuation of photon frequency will result in a phase fluctuation and this fluctuation is scaled up by the absolute path length L.

(4) Path length fluctuation will contribute to the phase fluctuation even if Alice and Bob's systems are the same, unless the frequencies of H and V photons are the same.

One should also bear in mind that:

(1) $h_i$is an non-normalized complex function that are products of single-photon temporal modes from both nodes with extra phases thrown in.

(2) The choice of $t_A = t_B = 0$ is only valid for phase analysis. For wavepacket (with mode f_i), $t_{A/B}$ is physical and not free to choose.

For Eq.4.8, different choice of t_A and t_B would give different results. The relative phase of the Bell state is dependent on a mathematical choice. It seems wrong but this actually makes sense. It is meaningless to talk about the relative phase of a Bell state without giving a reference. It is all about what you define as the standard Bell state which has relative phase 0. What Eq.4.8 really means is: When someone presses the start button of the experiment, if the detectors fire at that moment, that ion-ion entanglement state is defined to be the reference state with relative phase 0. For other events, the entanglement relative phase is different from that of the reference state by ϕ.

4.1.2 Experimental errors

A. Error channel

For some choices of ion entanglement levels and photon collection configuration, there are three Zeeman states involved in the dynamics, with two of the states entangled with the same polarized photon. This error process is included in the analysis in the previous section. If we do not post-correct this error, the entanglement fidelity can be greatly degraded. However, since the process is coherent, we can fully correct the error state $|2\rangle$ back to entanglement state $|0\rangle$ by an unitary transformation.

From Eq.(4.6), we can rewrite the ion-ion state as:

$$\Phi(t_H, t_V) = h_1|1_A\tilde{0}_B\rangle + h_2 e^{i\phi}|\tilde{0}_A 1_B\rangle \tag{4.9}$$

where :

$$\begin{aligned} |\tilde{0}\rangle_B =& |0\rangle_B + \frac{n^B(t_H - t_B - L/c)}{f_H^B(t_H - t_B - L/c)} e^{i[(\omega_2^B - \omega_0^B)t + (\omega_n^B - \omega_H^B)(t_H - L/c)]}|2_B\rangle \\ |\tilde{0}\rangle_A =& |0\rangle_A + \frac{n^A(t_H - t_A - (L+\Delta x)/c)}{f_H^A(t_H - t_A - (L+\Delta x)/c)} e^{i[(\omega_2^A - \omega_0^A)t + (\omega_n^A - \omega_H^A)(t_H - (L+\Delta x)/c)]}|2_A\rangle \end{aligned} \tag{4.10}$$

If we apply a correction operation to rotate $|\tilde{0}\rangle$ to $M|0\rangle$, where M is a normalization factor, then the error state $|2\rangle$ is fully corrected. Such state correction should be performed for each heralded event. Precise information of the detection time is also necessary.

B. Phase fluctuation

The ion-ion entanglement phase can be disturbed by different noise processes.

(1). *Magnetic field fluctuation.* An external magnetic bias field is used to generate Zeeman level splitting. Fluctuations in the strength of this field will lead to a Zeeman level fluctuation, and therefore a spectral diffusion of the generated photon. If the fluctuations between different ion traps are not synchronised, the frequency fluctuation difference will lead to an uncertainty of the ion-ion entanglement phase. The phase diffusion can be derived from Eq.4.8. For experiments with light paths on the scale of metres or less, the dominant term in Eq.4.8 is the time related terms. We can estimate the phase diffusion to be in the scale of:

$$\Delta\phi = \Delta_B\omega \cdot \tau \tag{4.11}$$

where $\Delta_B\omega$ is the spectral diffusion of the generated photon (caused by ion level fluctuation), τ is the photon pulse duration. For photons of sub-microsecond duration,

this should be negligible since the Zeeman level fluctuation can be easily stabilised to below KHz. However, if the photon is much longer, this phase diffusion can be an issue. For long light path experiment ($L > 100$km), the spatial term (with L) is dominant and can be a big problem if the Zeeman level fluctuations cannot be stabilised to Hz level.

(2). *Detection time-resolution.* Often referred to as detection jitter, the time-resolution gives the uncertainty of detection times t_H and t_V. It will lead to an uncertainty of the ion-ion entanglement phase similar to that associated with magnetic field fluctuation, so its effect can be estimated from Eq.4.8. An Avalanche photodiode (APD) usually has a time-resolution of ns. A superconducting nanowire single-photon detector (SNSPD) has better time-resolution of less than 10 ps [79]. In both cases, the entanglement phase uncertainty is negligible. However, detection jitter can be a problem if we want to implement state correction, as defined in Eq. 4.10. Nanosecond detection jitter allows a 10 MHz state frequency splitting with negligible phase uncertainty ($\Delta\phi < 10^{-2}$). But if we use SNSPD, the phase uncertainty is negligible with less than 1 GHz qubit state splitting.

There are also other noise mechanisms that can result in phase uncertainty, for example, excessive laser linewidth and fluctuations in the path length of the photon, but these are expected to be small.

C. polarisation oscillation

Some devices (such as cavities, fibres, windows, mirrors or lenses) introduced to the system might have birefringence effects. These devices will cause a polarisation rotations which, if not corrected, can greatly reduce the fidelity of the ion-ion entanglement process. If the rotation is orthogonal and static, the correction can be implemented by waveplates directly on the generated photon. However, if the birefringent device affects the photon generation dynamics, the polarisation rotation is then time-dependent, known as polarisation oscillation. An example is an elliptical optical cavity. Even if the oscillation is fully characterised, current state of the art polarisation manipulation technology is far from being capable of applying the arbitrary sub-microsecond polarisation modulations necessary to reverse the effects of the birefringence. Ref.[71] shows that there is some fundamental non-correctable infidelity caused by cavity birefringence and the correctable infidelity still requires very complicated state correction after each entanglement heralding.

D. Beamsplitter misalignment

The asymmetry of beamsplitter between transmission and reflection can be easily added to the coefficient $h_{1,2,3,4}$ defined in Eq.4.6 by replacing h_1 by $h_1(1+\epsilon_{bs})$, replacing h_2 by $h_2(1-\epsilon_{bs})$, replacing h_3 by $h_3(1-\epsilon_{bs})$, replacing h_4 by $h_4(1+\epsilon_{bs})$, where ϵ_{bs} is the error of in transmission of the beamsplitter.

F. Temporal mixing

All of the analysis above assumes that the photon has a pure temporal mode. However, depending on the entanglement scheme used, this is not always a safe assumption to make. If the temporal mode of the photon electric field is mixed, there will be a phase uncertainty of the ion-ion entanglement dependent on the detection time, which leads to unrecoverable loss of fidelity. We will address this problem in detail in the section 4.3.

All of the formulation above assumes an ion-photon entanglement to begin with. Traditionally, as has been briefly mentioned, such entanglement is generated through spontaneous decay from an excited state into two distinguishable manifolds of the ground state (Fig.4.2). However, since the spontaneous decay is to a 4π space around the ion, the photon collection efficiency is very low (even a powerful NA=0.6 lens can collect less than 10% of the light). A natural idea to increase the collection rate is to add an optical cavity around the ion to confine the photon emission into the cavity mode. However, there are many technical challenges and limitations associated with the introduction of an optical and the entanglement scheme typically used, involving a vacuum stimulated Raman transition (Fig.4.4), is quite different. In the rest of this chapter, I will first (section 4.2) compare the advantage and the disadvantage of the "direct excitation" scheme and the "cavity-enhanced (vacuum stimulated) Raman transition" scheme (we use *Raman scheme* for short). I then (section 4.3) construct a mathematical framework for some of the main noise processes in the Raman scheme. Finally (section 4.4) we show parameter optimisation and fabrication tolerance of the Raman scheme. An analytical solution will also be given in the discussion section 4.5.

4.2 Ion-photon entanglement generation

The technical requirements for cavity and photon behaviour are highly dependent on the entanglement generation scheme. Here I introduce and compare the traditional direct excitation scheme with the preferable Raman transition scheme.

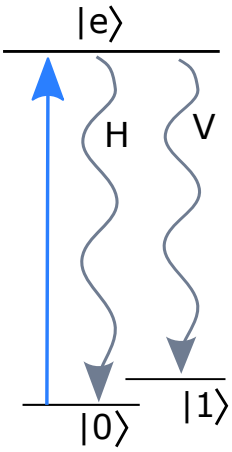

Figure 4.2: Direct excitation scheme. An ion is prepared in a excited state $|e\rangle$, followed by a spontaneous decay down to qubit state $|0\rangle$ and $|1\rangle$. A photon is emitted with its polarisation entangled with the qubit state.

4.2.1 Direct excitation

The most straightforward ion-photon entanglement generation scheme is through direct excitation (Fig.4.2). In one experiment using this scheme without cavity [61], an $^{40}Ca^{+}$ is prepared into one of the $4S$ states which are split by an external magnetic field. The ion is excited into a excited state $4P_{1/2}$ with a picoseconds optical pulse before it spontaneously decays back to the S states. A photon is generated during the decay with its polarisation entangled with the final ion state because of angular momentum conservation.

$$|\Psi\rangle = |S_{1/2}\rangle|\pi\rangle + |S_{-1/2}\rangle|\sigma^{-}\rangle \tag{4.12}$$

An optical cavity can be placed around the ion to enhance the spontaneous decay into the cavity mode. The cavity axis is orthogonal to the magnetic field, so that the π and σ fluorescence are projected to H and V polarisation as seen from the cavity axis. If we define the two ion spin state to be the qubit, we than generate an ion-photon entanglement:

$$|\Psi\rangle = |0H\rangle + |1V\rangle \tag{4.13}$$

The advantage of this "direct excitation" scheme is that it is easy and, in theory, the ion-photon entanglement generated is a temporally pure state.

Regardless of the temporal purity of the direct excitation scheme, in practice, there are several disadvantages to be considered:

(1) For commonly used alkaline earth metal ions (Ca^{+}, Sr^{+}, Ba^{+}), the spontaneous decay is deep blue in color ($< 500nm$). The scattering losses

on both the cavity mirror surface and within the optical fibre are relatively high, limiting the entanglement rate.

(2) The photon wavepacket is altered by cavity parameters, any difference of cavity fabrication between Alice and Bob will lead to distinguishability between two photons, degrading the ion-ion entanglement. To see this more quantitatively, we take the bad cavity regime (where coupling is weak compared with cavity decay and ion decay) as a example. In this regime, the photon wavepacket is simply altered by multiplying the Purcell factor:

$$F_P = \frac{3\lambda^3}{4\pi^2}\frac{Q}{V} = \frac{3\lambda^3\epsilon_0\hbar L}{2\pi^2 d^2 c}\frac{g_0^2}{-\ln R} \approx \frac{3\lambda^3\epsilon_0\hbar L}{2\pi^2 d^2 c}\frac{g_0^2}{1-R} \tag{4.14}$$

where L is the cavity length, d is the dipole moment, g_0 is the cavity coupling constant and R is the round-trip reflectivity. For a micro-cavity, the mode volume is very small. Any misalignment between the cavity and the ion position will introduce in the variation of the coupling g_0. Meanwhile, for a typical micro-cavity, the transmission is as low as down to several hundreds ppm or even lower. It is very challenging to coat two pairs (Alice and Bob) of cavity mirrors with the same round-trip loss. Furthermore, any misalignment of the cavity mirrors will significantly change the cavity mirror clipping loss. All the above issues make it very technically challenging to generate photons with similar wavepacket from two remote sites. To have an idea of how having different waveforms influence the ion-ion entanglement state, we specify the waveform in Eq.4.6. For direct excitation, h_3, h_4 and ϕ are 0. The inequality of h_1 and h_2 decreases the entanglement between the two ions. If we simplify the problem such that Alice and Bob are the same apart from the Purcell factors, Fig.4.3 visualises how a mismatch between Purcell factor can contribute to reduction in entanglement fidelity.

(3) Spontaneous decay into free space limits the photon collection fraction. To see this, we need to write down the time evolution of the system and get the solution at infinite time. The system interaction Hamiltonian is:

$$H_{int} = \hbar g_0(|1\rangle\langle 0| + |0\rangle\langle 1|) \tag{4.15}$$

where $|0\rangle = |g1\rangle$ means the ion is in the ground state with a photon in the cavity mode and $|1\rangle = |e0\rangle$ means the ion is in the excited state with

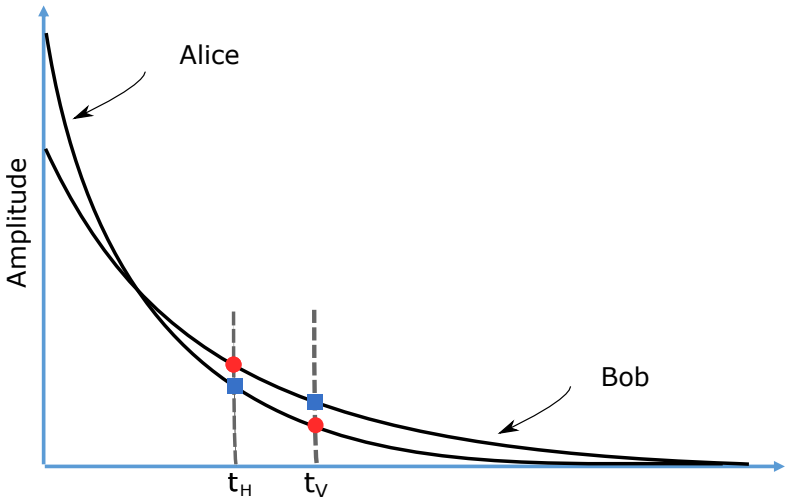

Figure 4.3: Waveform mismatch. the Purcell factors are 20% different, leading to a 20% difference in waveform. h_1 is the product of the two red circles while h_2 is the product of the two blue squares, making the ion-ion state differ from the maximally entangled Bell state $(|01\rangle + |10\rangle)/\sqrt{2}$.

no cavity photon. If we are in the rotating frame of the atom two-level transition, the total Hamiltonian is:

$$H = H_{int} + H_{photon} \tag{4.16}$$

Using the Heisenberg equation for the evolution of the density matrix:

$$i\hbar \frac{\partial}{\partial t}\rho = [H, \rho], \tag{4.17}$$

we get the density matrix elements' equations of motion:

$$\begin{aligned}
\frac{\partial}{\partial t}\rho_{00} &= -ig(\rho_{10} - \rho_{01}) - 2\kappa\rho_{00} \\
\frac{\partial}{\partial t}\rho_{11} &= ig(\rho_{10} - \rho_{01}) - 2\gamma\rho_{00} \\
\frac{\partial}{\partial t}\rho_{01} &= -ig(\rho_{11} - \rho_{00}) - (\kappa + \gamma)\rho_{01} \\
\frac{\partial}{\partial t}\rho_{10} &= ig(\rho_{11} - \rho_{00}) - (\kappa + \gamma)\rho_{10}
\end{aligned} \tag{4.18}$$

where κ is the cavity coherence loss rate and γ is the spontaneous decay rate of the excited state. We then integrate these equations from time 0

to time T. We get:

$$\begin{aligned}
\rho_{00}(T) - \rho_{00}(0) =& ig \int_0^T (\rho_{01} - \rho_{10}) \mathrm{d}t - P_R(T) \\
\rho_{11}(T) - \rho_{11}(0) =& -ig \int_0^T (\rho_{01} - \rho_{10}) \mathrm{d}t - P_S(T) \\
\int_0^T \rho_{01} \mathrm{d}t =& -[\rho_{01}(T) + ig(\frac{P_S(T)}{2\gamma} - \frac{P_R(T)}{2\kappa})] \frac{1}{\kappa + \gamma} \\
\int_0^T \rho_{10} \mathrm{d}t =& -[\rho_{10}(T) - ig(\frac{P_S(T)}{2\gamma} - \frac{P_R(T)}{2\kappa})] \frac{1}{\kappa + \gamma}
\end{aligned} \tag{4.19}$$

Where P_S is the probability of spontaneous emission into free space and P_R is the probability of extracting the photon from the cavity (assuming no extra loss):

$$\begin{aligned}
P_S(T) &= \int_0^T 2\gamma \rho_{11} \mathrm{d}t \\
P_R(T) &= \int_0^T 2\kappa \rho_{00} \mathrm{d}t
\end{aligned} \tag{4.20}$$

The initial condition is $\rho_{00}(0) = \rho_{10}(0) = \rho_{01}(0) = 0$, $\rho_{11}(0) = 1$. The maximum photon extraction is at infinite time $T \to \infty$ when $\rho_{00}(\infty) = \rho_{11}(\infty) = \rho_{10}(\infty) = \rho_{01}(\infty) = 0$. At infinite time, we get the solution for Eq.(4.19):

$$P_R = \frac{C_{de}}{C_{de} + 1} \tag{4.21}$$

where C_{de} is the ratio of the probability of photon extraction from the cavity to the probability of spontaneous emission:

$$C_{de} = \frac{P_R}{P_S} = \frac{g^2 \kappa}{g^2 \gamma + \kappa(\kappa + \gamma)\gamma} \tag{4.22}$$

We should notice that when κ is large, the cooperativity becomes the Purcell factor, as expected.

We have introduced the advantages and disadvantages of the "direct excitation" scheme. These will be compared with the "Raman scheme" in the next section 4.2.2.

4.2.2 Raman transition entanglement excitation

The introducing of an optical cavity around the ions not only increases the photon collection probability via the direct excitation scheme, but also enable another

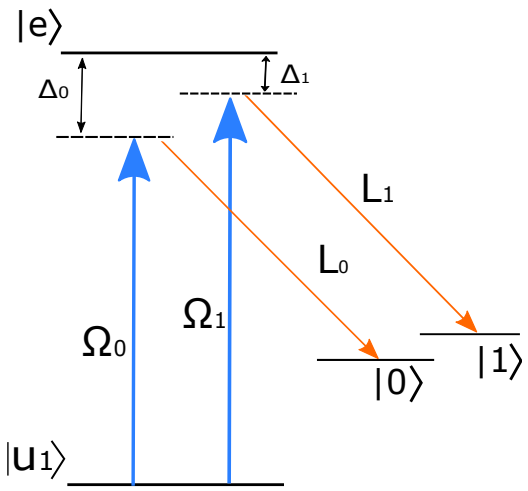

Figure 4.4: Raman transition excitation: The bichromatic Raman driving pulse has time dependent Rabi frequencies Ω_0 and Ω_1 with detunings Δ_0 and Δ_1. Population in the ground state $|u_1\rangle$ is then transferred to the qubit state $|0\rangle$ and $|1\rangle$ via an optical cavity resonance on the Raman transition with the same frequency detuning as the Raman driving field. A photon is generated into the cavity mode with its angular momentum entangled with the final ion qubit state.

richer excitation scheme that generate ion-photon entanglement: Raman transition entanglement generation. This scheme was first proposed in [138]. The scheme is illustrated in Fig.4.4. In an ideal case, an ion is prepared in a single ground state $|u_1\rangle$, The population is transformed to two qubit states $|0\rangle$ and $|1\rangle$ through two off-resonant Raman paths, created by two Raman driving pulses with different frequencies. The two Raman processes are stimulated by an optical cavity. Since the Raman drivings are turned on adiabatically, one can coherently transform the population from the initial state to the qubit state, creating a Raman photon in the cavity mode rather than into free space.

Compared with "direct excitation", it has several advantages:

(1). The choice of the colour of the cavity photon is more flexible. Many available options are close to telecom-band for commonly used alkaline earth metal ions, making the cavity scattering and fibre loss much lower.

(2). A relatively low intensity Raman driving field is required, instead of a picosecond pulsed laser, making the system more reliable, cheaper and more scalable.

(3). The photon generation is a coherent process, so the wavepacket can be controlled. Any difference in cavity loss between Alice and Bob can be

compensated by adjusting the process parameters (to some extent), such as Raman driving power and shape.

(4). The adiabaticity of the process leaves the excited state less populated than direct excitation, so the photon extraction probability is higher. To see this, we compare the two cooperativities of the two schemes. For Raman scheme, the upper bound of extraction probability is determined by the cooperativity $C_{Raman} = g^2/2\kappa\gamma$ [51]:

$$P_R^{Raman} = \frac{2C_{Raman}}{2C_{Raman} + 1} \tag{4.23}$$

The ratio between the two cooperativities is:

$$\frac{C_{de}}{2C_{Raman}} = \frac{\kappa^2}{\kappa^2 + \kappa\gamma + g^2} < 1 \tag{4.24}$$

So the photon extraction upper bound of the Raman scheme is always larger than that of direct excitation.

There are also disadvantages of the cavity-enhanced Raman scheme:

(1). Any population in the excited state can potentially spontaneous decay back to the initial state. This decay will restart the Raman process, generating a photon that is temporally distinguishable from a photon that hasn't undergone spontaneous decay. So the statistical average of the photon temporal state is a mixed state. This can be a serious problem depending on the cavity quality, ion level choice and Raman driving pulse shape. Work has been done to battle this process by cleverly choosing energy levels such that the spontaneous decay rate to the initial state is low compared with other spontaneous decay [146].

(2). Although the extraction probability limit is looser than direct excitation, it is still limited by practical issues like detection windows and driving pulse shape, and the dynamics are generally more complicated.

(3). For some schemes, there are more than two dark states. The third dark state is a noise channel ($h_{3,4}$) which can only be suppressed by large energy splitting between the dark states. This requires a high magnetic field which may limit the application. As has been discussed in Chapter 4.1.1, one can use unitary transformation to rotate the ion population from the superposition of qubit channel and noise channel to pure qubit

channel. However, In Chapter 4.1.1, we only give state rotation for temporally pure entangled state. However, because of the spontaneous decay mentioned in point (1), the entanglement state can be a temporally mixed state. It is not straightforward on how to correct such mixed state. We will discuss this in section 4.3.3

We have introduced a potentially preferable ion-photon generation scheme: "Raman scheme". We have also discussed the advantages and disadvantages of this scheme in comparison with the traditional "direct excitation scheme". To understand the dynamics of "Raman scheme", one has to investigate more carefully the ion-cavity system. We start with building and solving the master equation of the system.

4.2.3 Time evolution of "Raman scheme" ion-photon entanglement

To have a systematic understanding of the Raman scheme, we need to generalise the system considering the spontaneous decay and all of the atomic levels involved (Fig.4.5).

The system has two subsystems: the ion and the photon. The ion has six levels: two ground states $|u_1\rangle$ and $|u_2\rangle$, one of which u_1 is the initial state; one excited state $|e\rangle$; and three memory states, two of which are the qubit states $|0\rangle$ and $|1\rangle$ while the third one $|2\rangle$ is an inevitable error state as we defined in section 4.1.1. The photon has eight states: the vacuum state $|O\rangle$, the emission into unbounded states not localised in cavity $|F\rangle$, three cavity photon states with their angular momentum associated with three ion memory states, to be more specific, $|\sigma^+\rangle$, $|\sigma^-\rangle$ and $|\pi\rangle$, three cavity retrieved photon states $|\sigma_R^+\rangle$, $|\sigma_R^-\rangle$ and $|\pi^R\rangle$. So in principle, there are $6 \times 8 = 48$ possible states for the ion-photon system. However, most of these do not obey energy conservation or angular momentum conservation given the initial conditions and driving field, and thus do not participate and can be ignored. The remaining states are relabeled by numbers as follows:

$|0\rangle := |u_2 F\rangle$

$|1\rangle := |u_1 O\rangle$ is the initial state

$|2\rangle := |eO\rangle$ is the excited state, also the intermediate state.

$|3\rangle := |0\sigma^-\rangle$ represents the ion being in $|0\rangle$ state with a σ^- photon in the cavity.

$|4\rangle := |0\sigma_R^-\rangle$ represents the ion being in $|0\rangle$ state with an extracted σ^- photon out of cavity.

$|5\rangle := |1\pi\rangle$ represents the ion being in $|1\rangle$ state with a π photon in the cavity.

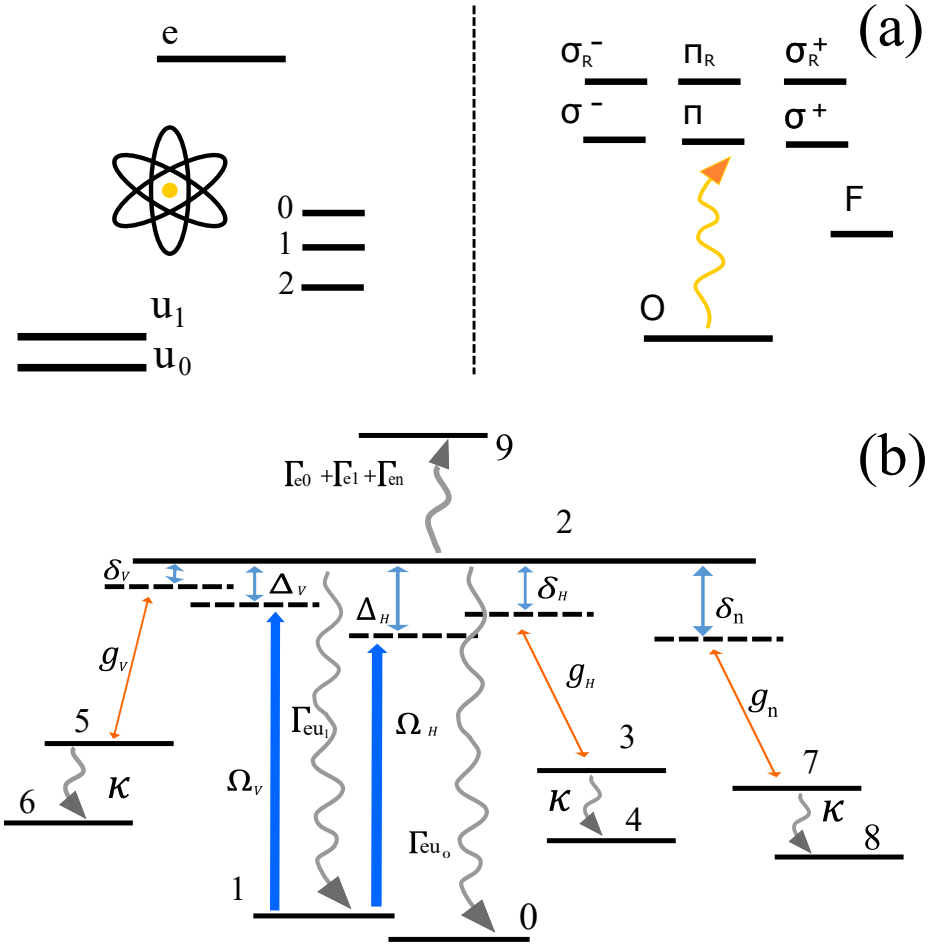

Figure 4.5: Ion-cavity system levels.(a).Two subsystems:ion with two ground state $|u_1\rangle$ and $|u_0\rangle$, one excited state $|e\rangle$ and three memory levels $|0, 1, 2\rangle$; photon with one vacuum state $|O\rangle$, three cavity photons $|\sigma^+, \sigma^-, \pi\rangle$, three retrieved photon states $|\sigma_R^+, \sigma_R^-, \pi_R\rangle$ and one free space emission state $|F\rangle$. (b) The reduced states for the ion-cavity system. $|1\rangle$ is the initial state. $|3, 5, 7\rangle$ are the cavity photon states where ion is in a memory state while a cavity photon is generated. $|4, 6, 8\rangle$ are the retrieved states where ion is in a memory state while a photon is retrieved from the cavity. $|0, 9\rangle$ represent the photon loss into free space.

$|6\rangle := |1\pi_R\rangle$ represents the ion being in $|1\rangle$ state with an extracted π photon out of the cavity.

$|7\rangle := |2\sigma^+\rangle$ represents the ion being in $|2\rangle$ state with a σ^+ photon in the cavity.

$|8\rangle := |2\sigma_R^+\rangle$ represents the ion being in $|2\rangle$ state with an extracted σ^+ photon out pf cavity.

$|9\rangle := |0F, 1F, 2F\rangle$ is a collection of three states. The excited state will spontaneously decay to five of the states pictured in Fig.4.5, in which $|0F\rangle, |1F\rangle, |2F\rangle$ are not to our interest. We don't need to distinguish them because they would not be detected or herald a entanglement.

It has been discussed in Chapter 4.1.1 that σ^- and π cavity photons are projected to H and V polarised photons and σ^+ photons are also projected to H polarisation and will trigger loss error if not corrected. So from here we will relabel σ^- as H, π as V and σ^+ as n.

The interaction Hamiltonian of the atom-cavity system is then (for details, see Appendix C):

$$\begin{aligned} H_{int} =& \hbar g_H(e^{i\delta_H t}\sigma_{e0}a_H^+ + e^{-i\delta_H t}\sigma_{e0}^+ a_H) + \hbar\frac{\Omega_H}{2}(e^{-i\Delta_H t}\sigma_{u_1e} + e^{i\Delta_H t}\sigma_{u_1e}^+) \\ &+ \hbar g_V(e^{i\delta_V t}\sigma_{e1}a_V^+ + e^{-i\delta_V t}\sigma_{e1}^+ a_V) + \hbar\frac{\Omega_V}{2}(e^{-i\Delta_V t}\sigma_{u_1e} + e^{i\Delta_V t}\sigma_{u_1e}^+) \\ &+ \hbar g_n(e^{i\delta_n t}\sigma_{e2}a_n^+ + e^{-i\delta_n t}\sigma_{e2}^+ a_n) \end{aligned} \tag{4.25}$$

where σ_{ij} is the ion transition operator $|j\rangle\langle i|$. This Hamiltonian is with the rotation-wave-approximation in atomic transition rotating frame, so $H_{atom} = 0$.

The master equation is then:

$$\begin{aligned} \frac{\mathrm{d}}{\mathrm{d}t}\rho =& \frac{1}{i\hbar}[H_{int}, \rho] + \Gamma_{eu_1}D[J_{21}]\rho + \Gamma_{eu_0}D[J_{20}]\rho \\ &+ KD[J_{34}]\rho + KD[J_{56}]\rho + KD[J_{78}]\rho + (\Gamma_{e0} + \Gamma_{e1} + \Gamma_{en})D[J_{29}]\rho \end{aligned} \tag{4.26}$$

where $\Gamma = 2\gamma$ is the spontaneous decay rate, $K = 2\kappa$ is the cavity decay rate. J_{ij} is the system transition operator $|j\rangle\langle i|$ and D[] is the Lindblad super operator.

A simulation of this master equation will give the time evolution of the system and the intensity of the retrieved photon: $\rho_{44}(t)$ is the non-normalised σ_- photon wavepacket modulus, $\rho_{66}(t)$ is the non-normalised π photon wavepacket and $\rho_{88}(t)$ is the non-normalised σ_+ photon wavepacket.

To visualise the time evolution of the system, we take $^{88}Sr^+$ as an example. We choose $5S_{1/2}, m_J = -1/2$ as initial ion state $|u_1\rangle$, $5P_{1/2}, m_J = 1/2$ as the excited state

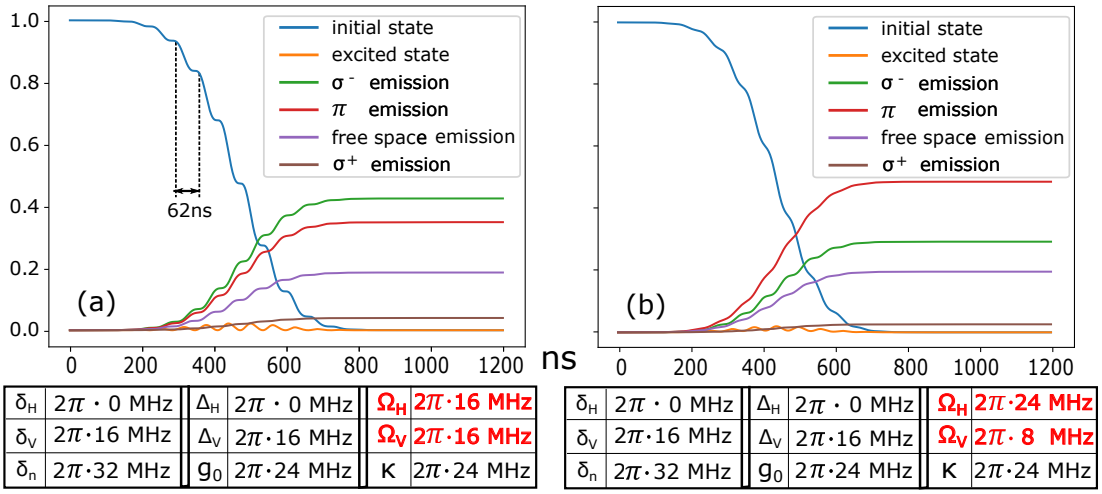

Figure 4.6: Time evolution of bi-chromatic Raman scheme in separable regime. $\delta_{H/V/n}$ is the cavity detuning from excited state for $\sigma^-/\pi/\sigma^+$ polarisation. $\Delta_{H/V}$ is the driving field detuning from excited state. $\Omega_{H/V}$ is the Rabi frequency of the bi-chromatic driving field, g_0 is the cavity coupling constant and K is the cavity loss rate. (a) and (b) has different drive Rabi frequencies (highlighted by red colour in the parameter tables)

and $4D_{3/2}, m_J = 3/2, 1/2, -1/2$ as the memory states $|0\rangle, |1\rangle, |2\rangle$. Fig.(4.6→4.8) show the system dynamics with different parameters.

For the regime where cavity linewidth is smaller than or comparable with the cavity detuning difference $\delta_H - \delta_V$, there is not too much cross coupling between the two Raman processes. This means that the driving field which is on resonance with the qubit state $|1\rangle$ is not strongly coupled with qubit state $|0\rangle$. We call this the separable regime. In this regime, the amplitude of the H and V emissions can be adjusted by changing the driving field intensities. We can see from Fig.4.6 that the H and V polarised photon have different amplitude which is not ideal for maximising the entanglement generation rate. However, by adjusting the driving field intensity, we can swap the amplitude of H (green line) and V (red line) photons. We observe the periodical wiggling of system dynamics. This is due to the frequency beating of the bi-chromatic field. The $62ns$ period corresponds to the 16MHz frequency difference of the driving fields.

In some situations when the separable regime is not an option, there will be very limited adjustment. In this regime, the bi-chromatic field is working not very different from an achromatic field (See Fig.4.7). We should point out that even though the relative amplitude between H and V is not adjustable in this regime, the absolute amplitude is still adjustable to compensate for the fabrication difference between

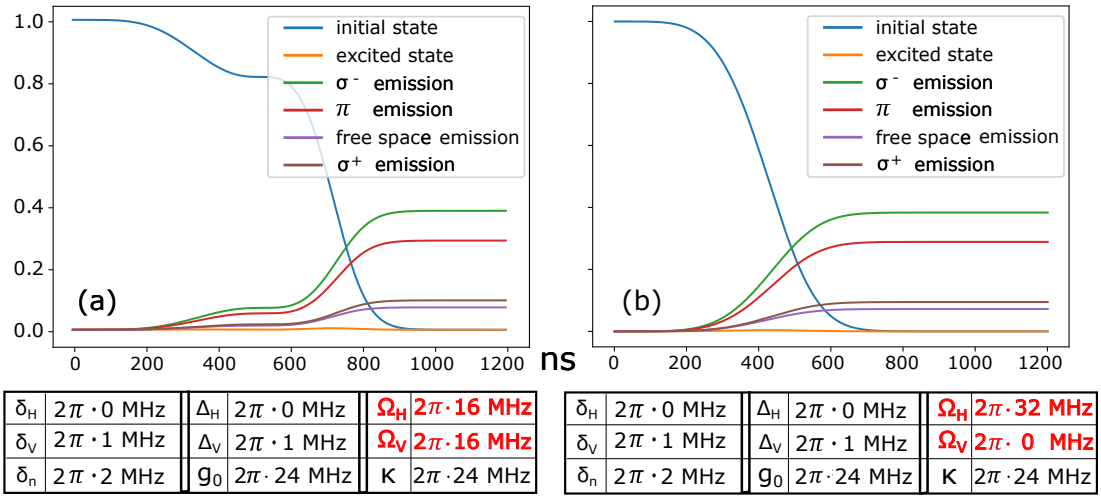

δ_H	$2\pi \cdot 0$ MHz	Δ_H	$2\pi \cdot 0$ MHz	Ω_H	$2\pi \cdot 16$ MHz
δ_V	$2\pi \cdot 1$ MHz	Δ_V	$2\pi \cdot 1$ MHz	Ω_V	$2\pi \cdot 16$ MHz
δ_n	$2\pi \cdot 2$ MHz	g_0	$2\pi \cdot 24$ MHz	K	$2\pi \cdot 24$ MHz

δ_H	$2\pi \cdot 0$ MHz	Δ_H	$2\pi \cdot 0$ MHz	Ω_H	$2\pi \cdot 32$ MHz
δ_V	$2\pi \cdot 1$ MHz	Δ_V	$2\pi \cdot 1$ MHz	Ω_V	$2\pi \cdot 0$ MHz
δ_n	$2\pi \cdot 2$ MHz	g_0	$2\pi \cdot 24$ MHz	K	$2\pi \cdot 24$ MHz

Figure 4.7: Time evolution of bi-chromatic Raman scheme not in separable regime.

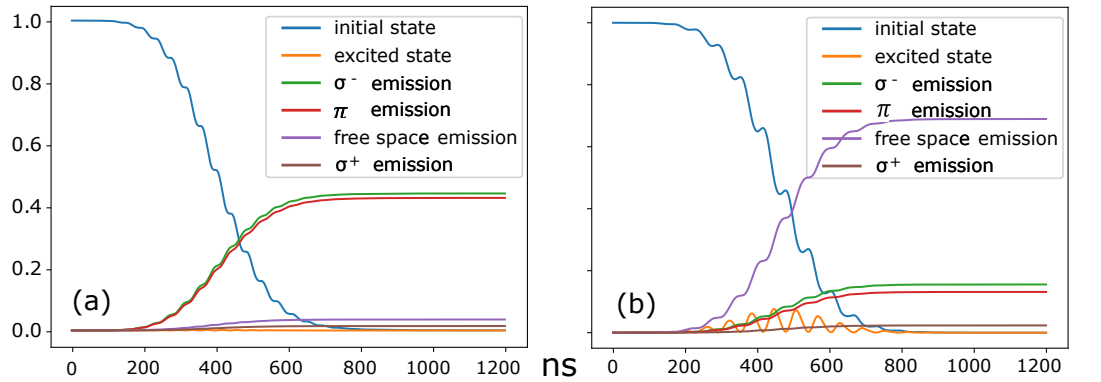

δ_H	$2\pi \cdot 0$ MHz	Δ_H	$2\pi \cdot 0$ MHz	Ω_H	$2\pi \cdot 16$ MHz
δ_V	$2\pi \cdot 16$ MHz	Δ_V	$2\pi \cdot 16$ MHz	Ω_V	$2\pi \cdot 16$ MHz
δ_n	$2\pi \cdot 32$ MHz	g_0	$2\pi \cdot 48$ MHz	K	$2\pi \cdot 10$ MHz

δ_H	$2\pi \cdot 0$ MHz	Δ_H	$2\pi \cdot 0$ MHz	Ω_H	$2\pi \cdot 16$ MHz
δ_V	$2\pi \cdot 16$ MHz	Δ_V	$2\pi \cdot 16$ MHz	Ω_V	$2\pi \cdot 16$ MHz
δ_n	$2\pi \cdot 32$ MHz	g_0	$2\pi \cdot 10$ MHz	K	$2\pi \cdot 48$ MHz

Figure 4.8: Time evolution of bi-chromatic Raman scheme with different cavity quality

different ion sites.

The performance of the system can be quite different with different cavity parameters. The thorough discussion on this will be established later in Chapter 4.3 and Chapter 4.4. Here in Fig.(4.8), we take examples of a good cavity and a bad cavity and show the different dynamics of the system. We can use the cooperativity to estimate the quality of the ion-cavity system. The spontaneous decay rate of $88Sr^+5P_{1/2}$ is $\gamma = 2\pi * 12\text{s}^{-1}$. The cooperativity of the good cavity shown in Fig.4.8(a) is $C = 10$, while the cooperativity of the bad cavity shown in Fig.4.8(b) is $C = 0.084$.

In Fig.4.8(b), we can retrieve total photon of more than 35%. However, if we calculate from cooperativity, the photon extraction probability is upper bounded by

$P = 2C/(2C+1) = 14.4\%$. Is this contradictory? The reason is that the upper bound $P = 2C/(2C+1)$ is true if not considering the contribution from recycled Raman process. "recycled Raman process" means that the ion population which decays from the excited state back to the initial state $|u_1\rangle$ will be driven again through Raman process. Although these photons are not coherent with the ideal photon ("ideal photon" meaning photons which were not produced after a spontaneous decay), it still contributes to the photon extraction probability. So $P = 2C/(2C+1)$ can be interpreted as the upper bound of "ideal photon". As has been mentioned earlier in this section, the photon generated after spontaneous decay will degrade the temporal purity of the photon and lead to entanglement infidelity. This is the main non-technical infidelity of the Raman scheme. There is no full mathematical treatment of this problem apart from simulating the spontaneous process via the Quantum Monte Carlo method. In the next section, we will construct an approach that allows us to directly predict the ion-ion entanglement infidelity by calculating the statistical observables of the system.

4.3 Temporal mode of ion-ion entanglement

"Recycled Raman process" will lead to temporal mixing of the retrieved photon. In this section, we will introduce a novel systematical approach to understand and calculate the nature of this temporally mixed state.

4.3.1 Photon temporal mixing

During the Raman process, every spontaneous decay back to the initial state will generate a different photon wavepacket because (Fig. 4.9):

> (1) The photon wavepacket is time-shifted by the time interval before the decay happens.
>
> (2) The driving is not constant so the photon will not be driven by the same driving pulse. So the temporal shape will not be the same as the "ideal photon".

A statistical average of all events will mix the photon temporal modes corresponding to different decay time with different probabilities. The cavity output is a mixed temporal state, specifically a mixture of modes sampled from an infinite sequence of temporal modes $\{[f_H^{A(i)}(t), f_V^{A(i)}(t), n^{A(i)}(t)]\}$ for Alice and $\{[f_H^{B(j)}(t), f_V^{B(j)}(t), n^{B(j)}(t)]\}$

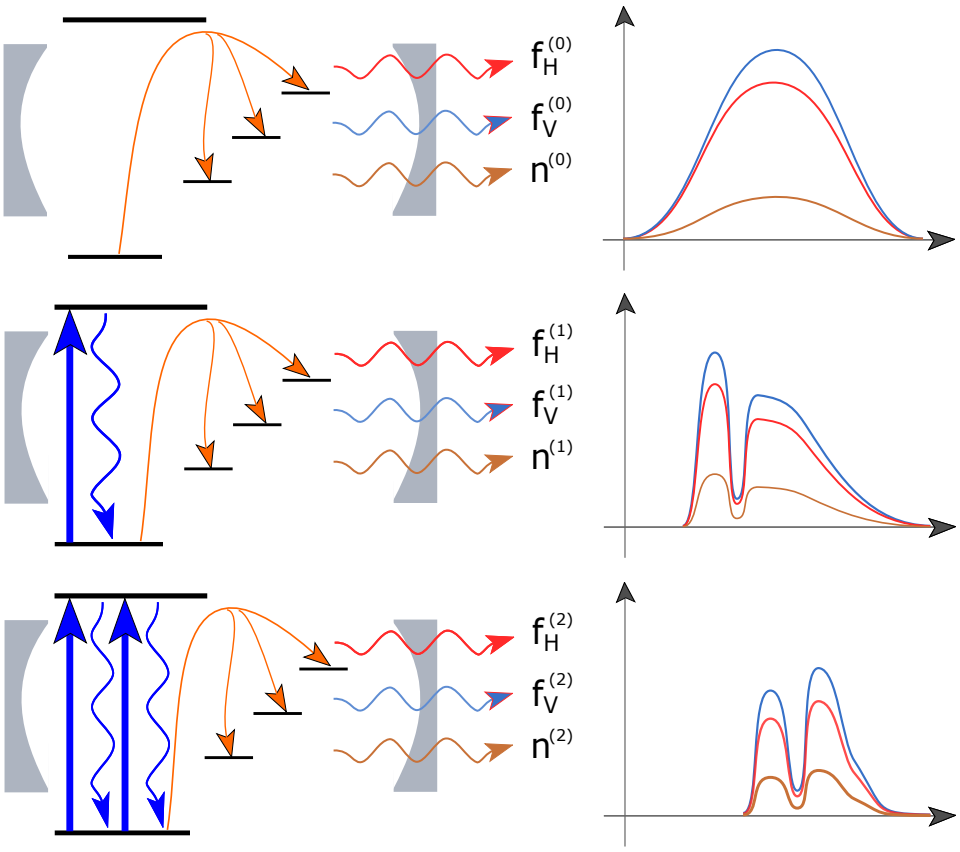

Figure 4.9: Temporal mixing. The top diagram is the situation without a spontaneous scattering process. A schematic representation of the temporal mode is shown in the right column. The middle diagram shows the situation when the ion has gone through one spontaneous scattering process before emitting a photon in to the cavity mode. The temporal mode is different from the top diagram, starting from a later time. The bottom diagram is the situation with two spontaneous scattering processes. The actual photon temporal mode is a mixture of all the situations including all the processes involving one or more spontaneous scattering events.

for Bob, where i and j are continuous indices indicating the time when the last spontaneous decay occurs (i.e. where the final, successful Raman transfer starts). Just as in Chapter 4.1.1, all these temporal modes are non-normalised and their squared modulae are the probabilities of such a photon being generated. An ion-ion entanglement heralding event implies the mixed sum of all the possible combinations of Alice modes and Bob modes $[i, j]$

For a combination of $[i, j]$, we can write down the ion-ion entangled state in matrix form following Eq.(4.6)

$$|\psi^{ij}(t, t_H, t_V)\rangle = \frac{1}{2}\begin{bmatrix} f_V^{A(i)}(t_V^A) f_H^{B(j)}(t_H^B) \\ f_H^{A(i)}(t_H^A) f_V^{B(j)}(t_V^B) e^{\mathrm{i}\phi} \\ f_V^{A(i)}(t_V^A) n^{B(j)}(t_H^B) e^{\mathrm{i}\theta_3} \\ n^{A(i)}(t_H^A) f_V^{B(j)}(t_V^B) e^{\mathrm{i}\theta_4} \end{bmatrix} \tag{4.27}$$

where $t_H^A = t_H - t_A - (L + \Delta x)/c$, $t_V^A = t_V - t_A - (L + \Delta x)/c$, $t_H^B = t_H - t_B - L/c$, $t_V^B = t_V - t_B - L/c$, are the clicking times relative to the photon envelopes, and $\phi, \theta_{3,4}$ are the phases which are independent of temporal mode $[i, j]$. It should be pointed out that this state is not normalised and it contains the actual probability amplitude. The non-normalised density matrix of the ion-ion system after herald detection events at times t_H and t_V is the statistical average of all possible temporal modes from Alice (indexed by i) and Bob (indexed by j):

$$\begin{aligned} \rho_{ion-ion}^{sd}(t, t_H, t_V) &= \sum_{ij} |\psi^{ij}(t, t_H, t_V)\rangle\langle\psi^{ij}(t, t_H, t_V)| \\ &= \begin{bmatrix} \rho_{11}^{sd} & \rho_{12}^{sd} & \rho_{13}^{sd} & \rho_{14}^{sd} \\ \rho_{12}^{sd*} & \rho_{22}^{sd} & \rho_{23}^{sd} & \rho_{24}^{sd} \\ \rho_{13}^{sd*} & \rho_{23}^{sd*} & \rho_{33}^{sd} & \rho_{34}^{sd} \\ \rho_{14}^{sd*} & \rho_{24}^{sd*} & \rho_{34}^{sd*} & \rho_{44}^{sd} \end{bmatrix} \end{aligned} \tag{4.28}$$

where

$$
\begin{aligned}
\rho_{11}^{sd} =& \frac{1}{4}\sum_{ij}|f_V^{A(i)}(t_V^A)|^2|f_H^{B(j)}(t_H^B)|^2 = \frac{1}{4}I_V^A(t_V^A)I_H^B(t_H^B)\\
\rho_{22}^{sd} =& \frac{1}{4}\sum_{ij}|f_H^{A(i)}(t_H^A)|^2|f_V^{B(j)}(t_V^B)|^2 = \frac{1}{4}I_H^A(t_H^A)I_V^B(t_V^B)\\
\rho_{33}^{sd} =& \frac{1}{4}\sum_{ij}|f_V^{A(i)}(t_V^A)|^2|n^{B(j)}(t_H^B)|^2 = \frac{1}{4}I_V^A(t_V^A)I_n^B(t_H^B)\\
\rho_{44}^{sd} =& \frac{1}{4}\sum_{ij}|n^{A(i)}(t_H^A)|^2|f_V^{B(j)}(t_V^B)|^2 = \frac{1}{4}I_n^A(t_H^A)I_V^B(t_V^B)\\
\rho_{12}^{sd} =& \frac{1}{4}\sum_{ij}f_V^{A(i)}(t_V^A)f_H^{B(j)}(t_H^B)f_H^{A(i)*}(t_H^A)f_V^{B(j)*}(t_V^B)e^{-\mathrm{i}\phi}\\
=& \frac{1}{4}C_{HV}^{A*}(t_H^A,t_V^A)*C_{HV}^{B}(t_H^B,t_V^B)*e^{-\mathrm{i}\phi}\\
\rho_{23}^{sd} =& \frac{1}{4}\sum_{ij}f_H^{A(i)}(t_H^A)f_V^{B(j)}(t_V^B)f_V^{A(i)*}(t_V^A)n^{B(j)*}(t_H^B)e^{\mathrm{i}(\phi-\theta_3)}\\
=& \frac{1}{4}C_{HV}^{A}(t_H^A,t_V^A)*C_{nV}^{B*}(t_H^B,t_V^B)*e^{\mathrm{i}(\phi-\theta_3)}\\
\rho_{34}^{sd} =& \frac{1}{4}\sum_{ij}f_V^{A(i)}(t_V^A)n^{B(j)}(t_H^B)n^{A(i)*}(t_H^A)f_V^{B(j)*}(t_V^B)e^{\mathrm{i}(\theta_3-\theta_4)}\\
=& \frac{1}{4}C_{nV}^{A*}(t_H^A,t_V^A)*C_{nV}^{B}(t_H^B,t_V^B)*e^{\mathrm{i}(\theta_3-\theta_4)}\\
\rho_{13}^{sd} =& \frac{1}{4}\sum_{ij}f_V^{A(i)}(t_V^A)f_H^{B(j)}(t_H^B)f_V^{A(i)*}(t_V^A)n^{B(j)*}(t_H^B)e^{\mathrm{i}(-\theta_3)}\\
=& \frac{1}{4}I_V^{A}(t_V^A)*C_{Hn}^{B}(t_H^B,t_H^B)*e^{\mathrm{i}(-\theta_3)}\\
\rho_{24}^{sd} =& \frac{1}{4}\sum_{ij}f_H^{A(i)}(t_H^A)f_V^{B(j)}(t_V^B)n^{A(i)*}(t_H^A)f_V^{B(j)*}(t_V^B)e^{\mathrm{i}(\phi-\theta_4)}\\
=& \frac{1}{4}C_{Hn}^{A}(t_H^A,t_H^A)*I_V^{B}(t_V^B)*e^{\mathrm{i}(\phi-\theta_4)}\\
\rho_{14}^{sd} =& \frac{1}{4}\sum_{ij}f_V^{A(i)}(t_V^A)f_H^{B(j)}(t_H^B)n^{A(i)*}(t_H^A)f_V^{B(j)*}(t_V^B)e^{\mathrm{i}(-\theta_4)}\\
=& \frac{1}{4}C_{nV}^{A*}(t_H^A,t_V^A)*C_{HV}^{B}(t_H^B,t_V^B)*e^{\mathrm{i}(-\theta_4)}
\end{aligned}
\tag{4.29}
$$

where $I_V^A(t_V^A) = \sum_i |f_V^{A(i)}(t_V^A)|^2$ is the detection probability of Alice V polarised

photon at time t_V^A. And

$$\begin{aligned} C_{XY}^{Z}(t_H^Z, t_V^Z) =& \sum_i f_X^{Z(i)}(t_X^Z) f_Y^{Z(i)*}(t_Y^Z), \\ X, Y \in& \{H, V, n\}, \\ Z \in& \{A, B\} \end{aligned} \tag{4.30}$$

is defined to be the Envelope Cross Correlation Function (ECCF).This function is closely related to the non-normalised Cross Correlation Function (CCF) defined by:

$$\begin{aligned} G_{XY}^{Z}(t_X^Z, t_Y^Z) =& \langle b_X^+(t_X^Z) b_Y^-(t_Y^Z) \rangle, \\ X, Y \in& \{H, V, n\}, \\ Z \in& \{A, B\}, \end{aligned} \tag{4.31}$$

where $b_{X/Y}^{+/-}$ are the output temporal mode annihilation operators, whose relations with the electric field operators are given by:

$$E_{X/Y}^{+/-} = \sqrt{\frac{\hbar \omega_{X/Y}}{2\epsilon_0 V}} b_{X/Y}^{-/+}(t_{X/Y}) \tag{4.32}$$

note:

The Cross Correlation Function (CCF) is a photon field function. Its physical meaning is the field correlation between $\{H, n\}$ polarised photon at time t_H and V polarised photon at time t_V. One might be more familiar with the two-time correlation function (we take V polarisation as an example):

$$g_V(t, t') = \frac{\langle b_V^+(t) b_V^-(t') \rangle}{|\langle b_V^+(t) b_V^-(t) \rangle|^2}, \tag{4.33}$$

which is widely used to evaluate the coherence property of a light source. If the source emits a temporally pure light field, the field at time t is always coherent with the field at t', and the correlation function $g_V(t, t')$ will be constant 1. If the field has some amount of phase uncertainty, the coherence between two different times t and t' will be disturbed and the correlation function $g_V(t, t')$ will be less than 1. The CCF has very similar physical meanings and mathematical properties. Two differences between the CCF and the correlation function are that:

(1). Instead of being a correlation with itself at different times, the CCF is the correlation between two distinct fields, $\{H, n\}$ and V.

(2). The CCF is not normalised in order to keep track of the photon probability.

Just like the correlation function, the CCF is decreased if the phase between X

and Y is uncertain. In other words, the CCF contains all the information we need to understand how temporally mixed the fields are.

Mathematically speaking, it is the expectation value of the photon field operators: $b_X^+(t_H)b_Y^-(t_V)$. We will see soon that the field operator is related to the ion-cavity operator and hence can be calculated through the system master equation and quantum regression theory.

The CCF and the ECCF are related by:

$$\begin{aligned} C_{XY}^Z(t_X^Z, t_Y^Z) &= \sum_i f_X^{Z(i)}(t_X^Z) f_Y^{Z(i)*}(t_Y^Z) \\ &= \frac{2\epsilon_0 V}{\hbar\sqrt{\omega_X^Z \omega_X^Z}} [\sum_i E_X^{Z(i)}(t_X^Z) E_Y^{Z(i)*}(t_Y^Z)] e^{\mathrm{i}\omega_X^Z t_X^Z} e^{-\mathrm{i}\omega_Y^Z t_Y^Z} \\ &= \frac{2\epsilon_0 V}{\hbar\sqrt{\omega_X^Z \omega_X^Z}} \langle E_X^{Z-}(t_X^Z) E_Y^{Z+}(t_Y^Z)\rangle e^{\mathrm{i}\omega_X^Z t_X^Z} e^{-\mathrm{i}\omega_Y^Z t_Y^Z} \\ &= \langle b_X^+(t_X^Z) b_Y^-(t_Y^Z)\rangle e^{\mathrm{i}\omega_X^Z t_X^Z} e^{-\mathrm{i}\omega_Y^Z t_Y^Z} \\ &= G_{XY}^Z(t_X^Z, t_Y^Z) e^{\mathrm{i}(\omega_X^Z t_X^Z - \omega_Y^Z t_Y^Z)} \end{aligned} \tag{4.34}$$

We have reached something important here. The ion-ion density matrix with detection time t_H and t_V is determined by three factors:

(1): The photon temporal probability (field intensity) I_X^Z which can be calculated by solving the master equation Eq.4.26.

(2): The time dependent phase $\{\phi, \theta_3, \theta_4\}$ which are independent of photon temporal mode.

(3): The Cross Correlation Function (CCF) in Eq.4.31 which is defined as the expectation value of field operators at two time t_H and t_V. The calculation of the CCF will be introduced in the following section 4.3.2.

Although we construct the ion-ion density matrix starting from an infinite continuum of temporal modes $f_X^{Z(i)}(t)$, the final density matrix doesn't need to be dependent on the exact form of those mode functions. We can calculate just the CCF instead of all the complicated photon temporal modes.

Having calculated the ion-ion density matrix, one can then calculate the state correction and then the fidelity is easily predicted from the corrected density matrix.

4.3.2 Calculating the Cross Correlation Function (CCF)

The calculation of the CCF is done by generalising the Quantum Regression Theorem (QRT). QRT was originally used to deal with noise process in open quantum

system [82]. It has since been widely used to calculate correlation functions of system variables, for example, $\langle A(t)B(t')\rangle$. The standard calculation of the correlation function deals with time-independent master equations [135]. However, in our Raman Scheme, the driving field is a pulse - luckily the QRT can be easily generalised to time-dependent systems [38]. Following this generalisation, we now introduce the calculation of the CCF.

Firstly, we relate the CCF, which is a field function, to the ion-cavity system operators.

4.3.2.1 CCF as an ion-cavity system function

Following the definition of CCF in Eq.4.31, we take one of the sites as an example and remove the site index Z:

$$G_{XY}(t_H, t_V) = \langle b_X^+(t_H) b_Y^-(t_V)\rangle,\ \{X, Y\} = \{H, V, n\} \tag{4.35}$$

Since $b_{X/Y}^{+/-}$ is a output temporal mode operator, its dynamics are not captured by the system master equation. However, we can connect the output field with the system field operator by the cavity Input-Output Relation [135]:

$$b_{\text{out}}(t) - b_{\text{in}}(t) = \sqrt{K}a(t) \tag{4.36}$$

where b stands for bath, meaning the single-photon optical mode outside the cavity, K is the cavity loss, a is the optical mode in the cavity. For the cavity-ion system, the initial bath mode is vacuum, so we have $b_{\text{in}}(t) = 0$. The Input-Output relation becomes the Output-System Relation:

$$b_{\text{out}}(t) = \sqrt{K}a(t) \tag{4.37}$$

Now we can build the connection between the output CCF and the system temporal mode operator:

$$G_{XY}(t_H, t_V) = K\langle a_X^+(t_H) a_Y^-(t_V)\rangle,\ \{X, Y\} = \{H, V, n\} \tag{4.38}$$

It is necessary to make some clarification here. The photon creation and annihilation operators in Eq.4.38 will give non-negative CCF only if the corresponding photonic field have the same polarisation. To make this point clearer, we temporally rewrite the field operators a_X as $a_X \boldsymbol{\epsilon}_Y$ to highlight the polarisation of the field. X indicates the temporal mode of the photon while Y indicates the actual polarisation.

The last step before we calculate the CCF is to understand how does the field operator $a_{X/Y}^{+/-}$ act upon our system in Fig.4.4. An field annihilation operator annihilates a cavity photon and leaves the ion unchanged. So intuitively, the only possible choices are:

$$\begin{aligned} a_H\boldsymbol{\epsilon}_H =&|4\rangle\langle 3| \text{ takes state } |3\rangle \text{ to } |4\rangle. \\ a_V\boldsymbol{\epsilon}_V =&|6\rangle\langle 5| \text{ takes state } |5\rangle \text{ to } |6\rangle. \\ a_n\boldsymbol{\epsilon}_H =&|8\rangle\langle 7| \text{ takes state } |7\rangle \text{ to } |8\rangle. \end{aligned} \tag{4.39}$$

The polarisation information is embedded in the ion final state. Now we are only one step from specifying a_H, a_V and a_n. A system field operator should always have both waveform information and polarisation information just as the operators on the left hand side of Eq.4.39. Any correlation function between these operators will be zero because their polarisations are orthogonal. In order to examine only the waveform correlation while keeping the operator as system operator, we need to construct operators describing the concerning waveforms but with the same polarisation. Such operators may look like: $a_H\boldsymbol{\epsilon}_H$, $a_V\boldsymbol{\epsilon}_H$ and $a_n\boldsymbol{\epsilon}_H$. We can specify these operators by imagine a process: before the cavity decay from $|3,5,7\rangle$ to $|4,6,8\rangle$, the cavity photon and the atom exchanges angular momentum such that all cavity photons have polarisation corresponding to angular momentum σ^-. This process together with the cavity decay afterwards will leave the system in state $|4\rangle$ only. It should be pointed out here that such process is only useful in the rotation frame when all the atomic states are degenerate (in our case, they all have energy 0) so that such process doesn't involve any energy exchanging. With this process, we construct system operators:

$$\begin{aligned} a_H\boldsymbol{\epsilon}_H =&|4\rangle\langle 3| \text{ takes state } |3\rangle \text{ to } |4\rangle \\ a_V\boldsymbol{\epsilon}_H =&|4\rangle\langle 5| \text{ takes state } |5\rangle \text{ to } |4\rangle. \\ a_n\boldsymbol{\epsilon}_H =&|4\rangle\langle 7| \text{ takes state } |7\rangle \text{ to } |4\rangle. \end{aligned} \tag{4.40}$$

We are now ready to use QRT for CCF calculation.

4.3.2.2 Quantum regression theory (QRT)

Eq.4.38 and Eq.4.40 re-express the CCF as the expectation value of ion-cavity system operator. With the system master equation, the generalised QRT can solve CCF easily. We start by introducing the generalized QRT method.

The system master equation is first written with a time-dependent Liouvillian operator $\mathcal{L}(t)$:

$$\mathrm{d}_t\rho(t) = \mathcal{L}(t)\rho(t) \tag{4.41}$$

Imagine the system (S) and the reservoir (R) are coupled to form a closed system, so the system's evolution can be described by a unitary transformation U. Then the system's density matrix can be written as:

$$\rho_S(t') = \mathrm{Tr}_R[U(t',t)\rho_{SR}(t)U^+(t',t)], \quad (t' > t) \tag{4.42}$$

This equation can be interpreted as:

For any SR space matrix which follows the unitary transformation of U, its projection on the system (S) subspace follows the Liouvillian equation Eq.4.41.

The system correlation function is:

$$\begin{aligned}
\langle A(t)B(t')\rangle =& \mathrm{Tr}[A(t)B(t')\rho_{SR}] \\
=& \mathrm{Tr}[U^+(t,0)AU(t,0)U^+(t',0)BU(t',0)\rho_{SR}] \\
=& \mathrm{Tr}[U^+(t,0)AU^+(t',t)BU(t',0)\rho_{SR}] \\
=& \mathrm{Tr}[AU^+(t',t)BU(t',t)U(t,0)\rho_{SR}U^+(t,0)] \\
=& \mathrm{Tr}[BU(t',t)\rho_{SR}(t)AU^+(t',t)] \\
=& \mathrm{Tr}_S[B\mathrm{Tr}_R[U(t',t)\rho_{SR}(t)AU^+(t',t)]] \\
=& \mathrm{Tr}_S[B\Lambda(t',t)]
\end{aligned} \tag{4.43}$$

where:

$$\Lambda(t',t) = \mathrm{Tr}_R[U(t',t)\rho_{SR}(t)AU^+(t',t)], \quad (t' > t) \tag{4.44}$$

follows Liouvillian equation 4.41:

$$\mathrm{d}_{t'}\Lambda(t',t) = \mathcal{L}(t')\Lambda(t',t) \tag{4.45}$$

with the initial condition:

$$\Lambda(t,t) = \mathrm{Tr}_R[\rho_{SR}(t)A] = \rho_S(t)A \tag{4.46}$$

To calculate the case when $t' < t$, following the same procedure in Eq.4.43, we have:

$$\langle A(t)B(t')\rangle = \mathrm{Tr}_S[A\Lambda'(t',t)], \quad (t > t') \tag{4.47}$$

where

$$\Lambda'(t',t) = \mathrm{Tr}_R[U(t,t')B\rho_{SR}(t')U^+(t,t')] \tag{4.48}$$

following Liouvillian equation:

$$\mathrm{d}_t\Lambda(t,t') = \mathcal{L}(t)\Lambda(t,t') \tag{4.49}$$

with initial condition:

$$\Lambda(t', t') = B\rho_S(t') \tag{4.50}$$

For the CCF calculation, $A = a_X^+$, $B = a_V^-$, $t = t_H$, $t' = t_V$. A summary of the calculation steps are:

(1). Using the master equation Eq.4.26 to calculate ion-cavity system density matrix $\rho_S(t)$ on each site.

(2). Using the ion-cavity system density matrix $\rho_S(t)$ and $A = a_X^+$ to calculate the initial condition of $\Lambda(t_H, t_H)$ for every t_H by Eq.4.46.

(3). With the initial condition, calculating $\Lambda(t_V, t_H)$ using Eq.4.45.

(4). Using $\Lambda(t_V, t_H)$ and $B = a_Y^-$ to calculate the system correlation function $\langle a_X^+(t_H) a_Y^-(t_V)\rangle$ by Eq.4.43.

(5). Finally, we get the output field CCF from system correlation function by Eq.4.38.

4.3.3 State correction

With the photon temporal probability (field intensity) calculated from the master equation, phase calculated from Eq.4.8 and ECCF calculated by extended QRT from the last section, we can fully calculate the ion-ion state density matrix after a heralding detection event (Eq.4.28). In this section, we will implement a state correction on this density matrix so that the ion-ion density matrix after each heralding event is optimally close to a Bell state.

Before we implement the state correction, we should understand what factors cause a deviation from Bell state:

(1). When Alice and Bob have different set-up parameters or their light path length are different, the phase of the ion-ion entanglement (Eq.4.29) will be dependent on the clicking time. Furthermore, the phase will also continue to evolve in the time after heralding. A direct integration will lose the phase information and degrade the entanglement. This is inevitable if the site difference is random error, so a good stability of cavity transition and megnatic field on each site is crucial to the experiment. If the differences between Alice and Bob are systematic, the entanglement phase is no different from pure state entanglement and can be corrected by choosing the correct measurement time so that the phase shift due to

herald detection times t_H and t_V is compensated by the phase accumulated after heralding. This has been discussed in more details in Chapter 4.1.1 for pure state entanglement and the same treatment applies to mixed states.

(2) A more complicated state error is the loss channel, which gives non-zero diagonal elements ρ_{33}^{sd} and ρ_{44}^{sd} in the ion-ion entanglement density matrix in Eq.4.29. We have discussed about eliminating this error by applying a unitary operation to move the system from the error state to the qubit state after each heralded event (Eq.4.10). However, the method is for a well-defined pure state. It is not obvious how to implement this method to a mixed state. In the following section, we will introduce the optimal method to correct a mixed state which has more than one temporal mode.

4.3.3.1 Dominant temporal modes (DTM)

The raw density matrix after each heralded event is detection-time dependent and different from the Bell state. We need to implement a state correction to optimally rotate the state. To find such rotation, we propose to use the *dominant temporal modes (DTM)* as the pure temporal mode to implement the unitary transformation Eq.4.10. The idea is that since we cannot fully correct a mixed state to a pure state, we will try to find the dominant pure state in the mixed state and implement an optimal correction.

The DTM is defined as a set of three pure temporal modes on site $Z \in \{A, B\}$ for H polarised photon $D_H^Z(t)$, V polarised photon $D_V^Z(t)$ and noise channel photon $D_n^Z(t)$. They are the first eigenmodes of the field non-normalized two-time correlation functions $g_H^Z(t_H^Z, t_H^{Z\prime})$, $g_V^Z(t_V^Z, t_V^{Z\prime})$ and $g_n(t_H^Z, t_H^{Z\prime})$ each multiplied with an complex amplitude. The field non-normalized two-time correlation functions are defined as follow:

$$g_X^Z(t_X^Z, t_X^{Z\prime}) = \langle a_X^+(t_X^Z) a_X^-(t_X^{Z\prime}) \rangle,\ X = \{H, V, n\},\ Z = \{A, B\} \tag{4.51}$$

The complex amplitude is the square root of the biggest eigenvalue multiplied by a phase factor, which defines the relative phase between the three temporal modes D_H^Z, D_V^Z, D_n^Z.

This definition may sound complicated. We may understand it better by looking at its two main attributes:

(1). It represents the first eigenvector of the non-normalised two-time correlation function. for example, if the first eigenvector of $g_V^A(t_V^A, t_V^{A\prime})$ is $E_V^A(t_V)$, then: $D_V^A \propto E_V^A(t_V^A)$.

(2). It is normalized to the probability (eigenvalue). If the first eigenvalue of $g_V^A(t_V^A, t_V^{A\prime})$ is $\lambda^{(0)}$, then $\int D_V^A(t_V^A) D_V^{A*}(t_V^A) \mathrm{d}t_V^A = \lambda^{(0)}$.

Before we step into mathematical detail, we should make the physical meaning of this method clearer:

The state correction we implement on the ion-ion state is an unitary operation, which cannot change the degree of temporal purity of the density matrix. It is also not possible to implement an arbitrary unitary operation on the density matrix because we can only implement local operations to each local ion. We have learnt from section 4.1.2 that we can fully correct the state from error channel if the photon is temporally pure. Inspired by that, we try to find the dominant temporally pure part of the ion-ion state by finding the dominant temporally pure photon state, which is the first eigenmode of the photon two-time correlation function.

The DTM method is based on the following mathematical claim:

There exists an infinite set of orthogonal temporal modes

$$\{[\mathcal{E}_H^{Z(i)}(t), \mathcal{E}_V^{Z(i)}, \mathcal{E}_n^{Z(i)}(t)]\},$$

which gives the same ion-ion entanglement density matrix as the set of continuous photon emission temporal modes

$$\{[f_H^{Z(i)}(t), f_V^{Z(i)}(t), f_n^{Z(i)}(t)]\}.$$

These orthogonal temporal modes are the eigenmodes of the field two-time correlation functions (Eq.4.51) re-normalised to the corresponding eigenvalue:

$$\int \mathcal{E}_X^{Z(i)}(t) \mathcal{E}_X^{Z(i)*}(t) dt = \lambda_X^{Z(i)}$$

If there is any set of temporal modes that give the same ion-ion entanglement state, it must gives the same CCF and photon temporal probability (field intensity) I_X^Z since these two variables fully determines the density matrix in Eq.4.28. If such a set of modes exist, they should also give the same field two-time correlation function. So mathematically, such modes are a decomposition of the two-time correlation function. Among all the decompositions, eigenvalue decomposition gives the dominant mode the biggest possibility because eigenmodes are orthogonal. So the dominant mode of

the eigenmodes is the maximum pure mode in the mixed state. To have a visual idea of what these orthogonal modes look like, we first take a simpler system with only one Raman process as an example. In this simple example, there is only one final state and the drive field is monochromatic. The drive field is a sin^2 shape with a period of 1 μs. Fig.4.10 shows the eigenmodes of the two-time correlation function of the photon field. The eigenvalues represent the probability of corresponding eigenmode in the temporally mixed photon pulse. This is the photon field generated from the simplest Raman process. In real life when there are $|1\rangle$ and $|2\rangle$, we sometimes use bi-chromatic driving for optimal population transfer. This will cause a beating of the driving field and thus dips on the photon waveform, as can be seen from Fig.4.11 which represents the situation with bi-chromatic driving and three final states. With the given cavity parameter, we can see that the first eigenmode dominants the mixture with 95% probability.

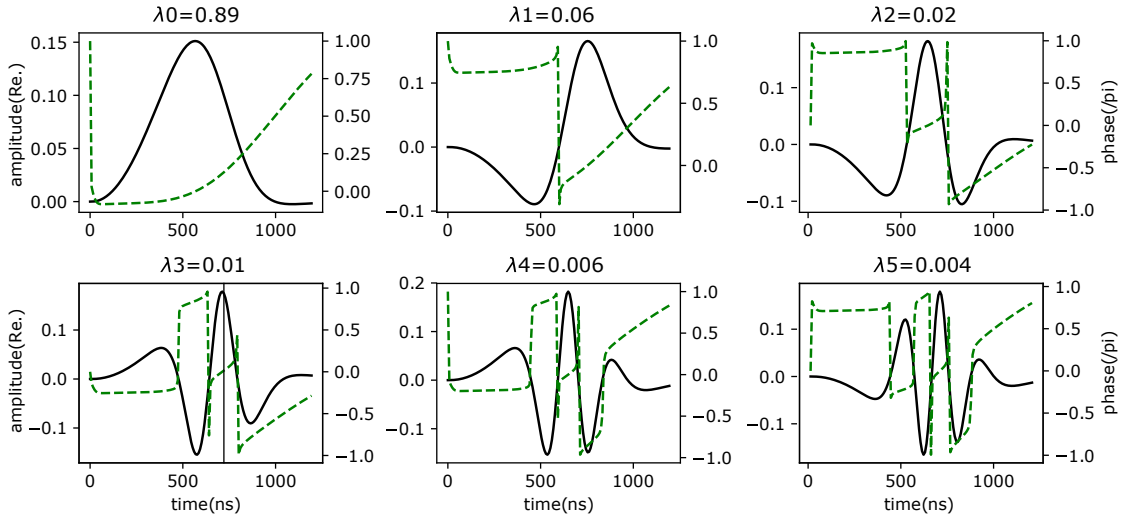

Figure 4.10: Simplest example of temporal eigenmode. The six subplots are the first six eigenmodes of the H correlation function. Black lines are the real part of the amplitude of the modes. Dashed lines are the phase of the mode. The titles of each plot are the corresponding eigenvalues λ_i. The cavity parameters for this example are $\Delta_H = \delta_H = 110$MHz, $\Omega_H = 100$MHz, $g_0 = 2\pi \times 32$MHz, $K = 2\pi \times 24$MHz, where Δ_H is the detuning of the driving field, δ_H is the detuning of the cavity, Ω_H is the maximum Rabi frequency of the driving field, the driving field has the envelope of a $\sin^2$ shape, g_0 is the cavity coupling constant, and K is the cavity loss rate.

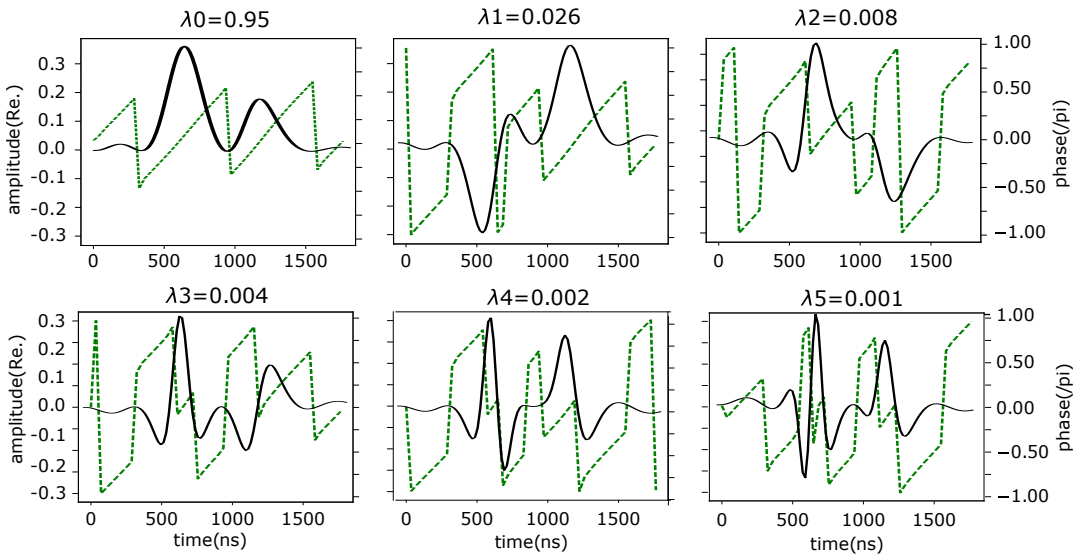

Figure 4.11: Example of temporal eigenmode. The cavity parameters for this example are $\Delta_H = \delta_H = 110\text{MHz}$, $\Delta_V = \delta_V = 120\text{MHz}$, $\delta_n = 130\text{MHz}$, $\Omega_H = 50\text{MHz}$, $\Omega_V = 50\text{MHz}$, $g_0 = 2\pi \times 32\text{MHz}$, $K = 2\pi \times 24\text{MHz}$, where $\Delta_{H/V}$ is the detuning of the driving field, $\delta_{H/V/n}$ is the detuning of the cavity, $\Omega_{H/V}$ is the maximum Rabi frequency of the driving field, the driving field has the envelope of a $\sin^2$ shape, g_0 is the cavity coupling constant, and K is the cavity loss rate.

However, rigorously speaking, this claim is based on the fact that such modes exist. The tool box below gives the proof.

proof:

the density matrix of the ion-ion entanglement is given by the ECCF $C^Z_{XY}(X \neq Y)$ and the detection probability I^Z_X, I^Z_Y. So if we can find a set of temporal mode $\{[\mathcal{E}^{Z(i)}_H(t), \mathcal{E}^{Z(i)}_V(t), \mathcal{E}^{Z(i)}_n(t)]\}$ that gives the same ECCF and $I^Z_X(X = H, V, n)$, the proof is done.

Firstly, we can simplify the three-mode problem to a two-mode problem. If we can prove that there exists a set of temporal mode $\{[\mathcal{E}^{Z(i)}_X(t), \mathcal{E}^{Z(i)}_Y(t)], (X \neq Y)\}$ that gives the same ECCF C^Z_{XY} and the detection probability I^Z_X, I^Z_Y, and that $\mathcal{E}^{Z(i)}_{X/Y}(t)$ is the re-normalized eigenvector of two-time correlation function $g^Z_{X/Y}(t^Z, t^{Z\prime})$, then the proof is done.

Before we start the proof, let us review what we mathematically need. We have a set of non-orthogonal paired functions $\{[f^{Z(i)}_X(t), f^{Z(i)}_Y(t)], (X \neq Y)\}$ that give one two-time function ECCF C^Z_{XY} and two single-time functions I^Z_X and I^Z_Y. We need to find a set of orthogonal paired functions $\{[\mathcal{E}^{Z(i)}_X(t), \mathcal{E}^{Z(i)}_Y(t)], (X \neq Y)\}$ that give the same three functions. We will see that we can easily find such paired functions that satisfies two of the three requirements. The main effort of the proof is to demonstrate that such set can also fulfills the third requirement.

The proof has two steps:

(1). Find a set of orthogonal temporal modes that gives the same ECCF C^Z_{XY} and I^Z_X as photon emission temporal modes $\{[f_X^{Z(i)}(t), f_Y^{Z(i)}(t)]\}$.

(2). Prove that these orthogonal temporal modes also gives the same I^Z_Y as the photon emission temporal modes.

Let's take Alice as an example and drop the superscript Z. ECCF is a function of two-time variables. If we take it as a matrix indexed by the two times t and t', then a singular value decomposition (SVD) of ECCF gives a series of orthonormal left-singular vectors $\{N^i_X(t)\}$ and right-singular vectors $\{N^i_Y(t')\}$ with their singular value $\{\sigma^i\}$:

$$C_{XY}(t,t') := \sum_i f^i_X(t) f^{i*}_Y(t') = \sum_i \sigma_i N^i_X(t) N^{i*}_Y(t') \tag{4.52}$$

We then choose a series of temporal modes $\{[\mathcal{E}^i_X, \mathcal{E}^i_Y]\}$ that are proportional to the singular vectors such that:

$$\sigma_i N^i_X(t) N^{i*}_Y(t') = \mathcal{E}^i_X(t) \mathcal{E}^{i*}_Y(t') \tag{4.53}$$

where $\mathcal{E}^i_X$ and $\mathcal{E}^i_Y$ remain two complete orthogonal bases. f^i_X and f^i_Y can be expanded in the two bases:

$$\begin{aligned} f^i_X &= \sum_j p_{ij} \mathcal{E}^j_X \\ f^i_Y &= \sum_k q_{ik} \mathcal{E}^k_Y \end{aligned} \tag{4.54}$$

Eq.4.52 and Eq.4.53 give:

$$\sum_i f^i_X(t) f^{i*}_Y(t') = \sum_i \mathcal{E}^i_X(t) \mathcal{E}^{i*}_Y(t') \tag{4.55}$$

which, in the bases of $\mathcal{E}^i_X$ and $\mathcal{E}^i_Y$, is:

$$\sum_{jk} (\sum_i p_{ij} q^*_{ik}) \mathcal{E}^j_X(t) \mathcal{E}^{k*}_Y(t') = \sum_i \mathcal{E}^i_X(t) \mathcal{E}^{i*}_Y(t') \tag{4.56}$$

It can be easily proved that $\{\mathcal{E}^j_X(t) \mathcal{E}^{k*}_Y(t')\}$ are linearly independent. So we have:

$$\begin{aligned} &\forall \alpha, \quad \sum_i p_{i\alpha} q^*_{i\alpha} = 1; \\ &\forall j \neq k, \ \sum_i p_{ij} q^*_{ik} = 0 \end{aligned} \tag{4.57}$$

There are infinite choices of $[\mathcal{E}^i_X, \mathcal{E}^i_Y]$ that satisfy Eq.4.53. We now introduce in the second requirement: The two sets should have the same I_X. We expand this to a stronger requirement: The two sets should have the same two-time

correlation function $g_X(t_X, t'_X)$. This is a stronger requirement because I_X is just its diagonal terms. Such modes $\{\mathcal{E}_X^i\}$ should satisfy:

$$\sum_i f_X^i(t) f_X^i(t') = \sum_i \mathcal{E}_X^i(t) \mathcal{E}_X^{i*}(t') \tag{4.58}$$

Again, we expand f_X^i in the basis of $\{\mathcal{E}_X^i\}$.

$$\sum_i f_X^i(t) f_X^i(t') = \sum_{jk} (\sum_i p_{ij} p_{ik}^*) \mathcal{E}_X^j(t) \mathcal{E}_X^{k*}(t') \tag{4.59}$$

To fulfill Eq.4.58, one should have:

$$\begin{aligned} &\forall \alpha, \qquad \sum_i |p_{i\alpha}|^2 = 1; \\ &\forall j \neq k, \ \sum_i p_{ij} p_{ik}^* = 0 \end{aligned} \tag{4.60}$$

Up to this point, we have shown that in order for the orthogonal modes $\{[\mathcal{E}_X(t), \mathcal{E}_Y(t)]\}$ to have the same ECCF, the conditions given in Eq. 4.57 must be satisfied. In order for the modes to have the same I_X, the conditions given in Eq.4.60 must be satisfied. For any choice of $\{p_{ij}\}$ satisfying both Eq.4.60, Eq.4.57 can also be satisfied by a corresponding choice of $\{q_{ij}\}$. The first step of the proof is done. We now prove that such $\{q_{ij}\}$ gives the same I_Y.

If we think of $\{p_{ij}\}$ as a sequence of vectors $\{\mathrm{p}_j\}$, Eq.4.60 sets a strong constraint on $\{\mathrm{p}_j\}$:

$\{\mathrm{p}_j\}$ *are orthonormal vectors.*

The fact that $\{q_{ij}\}$ comes in pair with $\{p_{ij}\}$ shows that $\{\mathrm{q}_j\}$ are vectors having the same dimensions as $\{\mathrm{p}_j\}$. Consider constraint Eq.4.57, The second line, $\forall j \neq k$, $\sum_i p_{ij} p_{ik}^* = 0$, suggests that the vector q_k is either 0 or orthogonal to all p_j for $j \neq k$. So it has to be either 0 or along the axis of p_k. The first line suggests that, by having $\alpha = k$, q_k cannot be 0 and it has to be a normalised vector. We can reach the conclusion that $\{\mathrm{p}_j\} = \{\mathrm{q}_j\}$. So we have:

$$p_{ij} = q_{ij} \tag{4.61}$$

We now express the two-time correlation function $g_Y(t, t')$ in the basis of $\{\mathcal{E}_Y^i\}$

with the constraint Eq.4.60:

$$\begin{aligned} g_Y(t,t') &= \sum_i f_Y^i(t) f_Y^i(t') \\ &= \sum_{jk} (\sum_i q_{ij} q_{ik}^*) \mathcal{E}_Y^j(t) \mathcal{E}_Y^{k*}(t') \\ &= \sum_{jk} (\sum_i p_{ij} p_{ik}^*) \mathcal{E}_Y^j(t) \mathcal{E}_Y^{k*}(t') \\ &= \sum_i \mathcal{E}_X^i(t) \mathcal{E}_X^{i*}(t') \end{aligned} \tag{4.62}$$

So we conclude that with $\{[\mathcal{E}_X^i, \mathcal{E}_Y^i]\}$ and $\{[p_{ij}, q_{ij}]\}$ we specified, we can get the same C_{XY}, I_X, I_Y as we do by $\{[f_X^i, f_Y^i]\}$. From Eq.4.58 and Eq.4.62, we can see that these modes are the re-normalised eigenvectors of the two-time correlation function $g_{X/Y}(t,t')$

To calculate the DTM, we first need to calculate any one of the three two-time correlation functions (e.g., for Alice $g_H^A(t_H^A, t_H^{A\prime})$) by the QRT. Then the eigenvalue decomposition of the two-time correlation function gives the eigenvectors $\{N_H^{A(i)}\}$ and the eigenvalues $\{\lambda_H^{A(i)}\}$. We then get the horizontally polarised dominant temporal mode D_H^A:

$$D_H^A = \sqrt{\lambda_H^{A(0)}} N_H^{A(0)}. \tag{4.63}$$

In principle, there should also be a phase associated with this mode, however, since only the relative phase between D_H^A, D_V^A, D_n^A matters, we choose the phase for D_H^A to be 0.

A singular value decomposition (SVD) of ECCF C_{HV}^A gives a series of orthonormal left-singular vectors $\{N_H^{A(i)}\}$ and right-singular vectors $\{N_V^{A(i)}\}$ with their singular values $\{\sigma_{HV}^{A(i)}\}$ as in Eq.4.52 projected to H and V polarisation. We then get the vertically polarised dominant temporal mode D_V^A:

$$D_V^{A*} = \frac{\sigma_{HV}^{A(0)} N_H^{A(0)} N_V^{A(0)}}{D_H^A} \tag{4.64}$$

In the same way, we can get D_n^A, the dominant temporal mode for the 'loss' channel, via the singular value decomposition C_{Hn}^A:

$$D_n^{A*} = \frac{\sigma_{Hn}^{A(0)} N_H^{A(0)} N_n^{A(0)}}{D_H^A} \tag{4.65}$$

We have now found the DTM $\{D_H^B, D_V^B, D_n^B\}$ for Bob in the same way as we did for Alice. They are the maximal temporally pure part of the photons generated by

Raman scheme. We can see that they are almost the same as the biggest eigenvectors of the two-time correlation functions, with the difference of just a relative constant phase.

4.3.3.2 State correction by DTM

We can now implement optimal state correction with the method first mentioned in Chapter 4.1.1 but with the DTM $\{D_H, D_V, D_n\}$ from Eq.4.63, Eq.4.64 and Eq.4.65.

Consider the ion-ion pure state generated by photon DTM. Before state correction, the ion-ion state is:

$$\Phi_{DTM} = D_1|1_A\tilde{0}_B\rangle + D_2|\tilde{0}_A 1_B\rangle \tag{4.66}$$

where:

$$\begin{aligned} D_1(t, t_H, t_V) &= D_V^A(t_V^A) D_H^B(t_H^B) \\ D_2(t, t_H, t_V) &= D_H^A(t_H^A) D_V^B(t_V^B) e^{i\phi} \end{aligned} \tag{4.67}$$

and

$$\begin{aligned} |\tilde{0}\rangle_B :=& |0\rangle_B + \frac{D_n^B(t_H - t_B - L/c)}{D_H^B(t_H - t_B - L/c)} e^{i[(\omega_2^B - \omega_0^B)t + (\omega_n^B - \omega_H^B)(t_H - L/c)]} |2_B\rangle \\ =& |0\rangle_B + \frac{D_n^B(t_H^B)}{D_H^B(t_H^B)} e^{i\theta_3} |2_B\rangle \\ |\tilde{0}\rangle_A :=& |0\rangle_A + \frac{D_n^A(t_H - t_H - (L+\Delta x)/c)}{D_H^A(t_H - t_H - (L+\Delta x)/c)} e^{i[(\omega_2^A - \omega_0^A)t + (\omega_n^A - \omega_H^A)(t_H - (L+\Delta x)/c)]} |2_A\rangle \\ =& |0\rangle_A + \frac{D_n^A(t_H^A)}{D_H^A(t_H^A)} e^{i(\theta_4 - \phi)} |2_A\rangle \end{aligned} \tag{4.68}$$

where ϕ and θ_i have the same definitions as in Eq.4.29. Simplifying the equation by defining:

$$\begin{aligned} J_A &= \frac{D_n^A(t_H^A)}{D_H^A(t_H^A)} e^{i\theta_3} \\ J_B &= \frac{D_n^B(t_H^B)}{D_H^B(t_H^B)} e^{i(\theta_4 - \phi)}, \end{aligned} \tag{4.69}$$

we get the ion-ion state rewritten as:

$$\Phi_{DTM} = D_1|10\rangle + D_2|01\rangle + D_1 J_A|12\rangle + D_2 J_B|21\rangle. \tag{4.70}$$

This can be rotated to a clean state without population on loss channel $|2\rangle$ by applying the unitary transformation U_{DTM} shown as Eq.4.71:

$$U_{DTM} \begin{bmatrix} D_1 \\ D_2 \\ D_1 J_A \\ D_2 J_B \end{bmatrix} = \begin{bmatrix} D_1\sqrt{1 + |J_A|^2} e^{i\phi} \\ D_2\sqrt{1 + |J_B|^2} \\ 0 \\ 0 \end{bmatrix} \tag{4.71}$$

The unitary transformation can be calculated numerically with the following procedure:

1. Find the unitary transformation ($3*3$ matrix) for X node ion that rotates $|\tilde{0}^X\rangle$ to $|0^X\rangle$:

$$U^X \begin{bmatrix} 1 \\ c_1 \\ J_X \end{bmatrix} = \begin{bmatrix} \sqrt{1+|J_X|^2} \\ c_1 \\ 0 \end{bmatrix} \tag{4.72}$$

where c_1 is arbitrary coefficient for ion level $|1^X\rangle$.

2. Construct the two-ion unitary transformation (9×9 matrix):

$$U = (U^A \otimes I^B).(I^A \otimes U^B) \tag{4.73}$$

3. Remove the rows and columns of U that does not show in the ion-ion entanglement subspace spanned by states $|01\rangle$, $|10\rangle$, $|21\rangle$ and $|12\rangle$. We are left with the 4*4 unitary matrix U_{DTM}.

At this point, the only difference between our state and the target Bell state is the qubit phase ϕ. However, this phase is only non-zero when the experiment parameters are different between Alice and Bob as suggested in Eq.4.8, and in practice, we would want to minimise this phase by stabilizing the two notes rather than correcting it afterwards.

We then have the corrected density matrix after each herald event to be:

$$\tilde{\rho}^{sd}_{ion-ion} = U_{DTM} \rho^{sd}_{ion-ion} U^{+}_{DTM} \tag{4.74}$$

We should point out that the unitary transformation consists of two steps.

(1). Rotate between the loss channel $|2\rangle$ and the qubit $|0\rangle$, through this rotation, $|\tilde{0}\rangle_X \rightarrow |0\rangle_X$ (state defined in Eq.4.68).

(2). Add a relative phase between two qubits state $|0\rangle$ and $|1\rangle$ by ϕ. This phase is the same for pure states and mixed states and is calculated in Eq.4.8. This phase is determined by the difference between Alice and Bob

We will discuss about how easy or difficult it is to implement these corrections in the section 4.5.

4.3.4 Entanglement rate and fidelity

The performance of the ion-ion entanglement is characterised by two figures of merit: the generation rate and state fidelity.

The state generation probability is straightforward:

$$P_{ion-ion} = \int_{\tau}^{\tau+T_d} \int_{\tau}^{\tau+T_d} (\rho_{11}^{sd} + \rho_{22}^{sd} + \rho_{33}^{sd} + \rho_{44}^{sd}) \mathrm{d}t_H \mathrm{d}t_V \tag{4.75}$$

where $\tau = \min\{t_H + (L + \Delta x)/c, t_B + L/c\}$ is the earliest possible detection time. T_d is the detector exposure window. ρ_{ii}^{sd} are the diagonal terms of the non-normalised density matrix defined in Eq.4.28.

Apart from detection, the entanglement protocol also requires state preparation with time T_p and state correction with time T_c (the state correction is only implemented when a heralded event happens). So the remote entanglement (RE) generation rate is:

$$\mathcal{R}_{re} = \frac{4P_{ion-ion}}{T_d + T_P + 4P_{ion-ion} \cdot T_c} \tag{4.76}$$

The factor of four assumes that the four heralding events: (1) $'a'$ arm detects $'H'$, $'b'$ arm detects $'V'$; (2) $'a'$ arm detects $'V'$, $'b'$ arm detects $'H'$; (3) $'a'$ arm detects both $'H'$ and $'V'$; (4) $'b'$ arm detects both $'H'$ and $'V'$; have the same probability. In reality one needs to calculate the four events separately and sum them up. The model is simplified here because the calculations for the other three heralding events are exactly the same.

To calculate the fidelity, we need to calculate the density matrix after state correction.

With the state corrected, there should be minimal population left in loss channel $|2\rangle$ and any phases $\{\phi, \theta_3, \theta_4\}$ introduced by different detection times t_H and t_V are eliminated.

The single detection fidelity times its probability is :

$$P(t_H, t_V) \times \mathcal{F}(t_H, t_V) = \frac{1}{M} (\mathrm{Tr}[\sqrt{\sqrt{\sigma} \tilde{\rho}_{ion-ion}^{sd}(t_H, t_V) \sqrt{\sigma}}])^2 \tag{4.77}$$

where $\sigma = (|01\rangle - |10\rangle)(\langle 01| - \langle 10|)/2$ is the density matrix of the Bell state, M is the normalisation factor, which is the total probability of such heralding events.

$$M = \int_{\tau}^{\tau+T_d} \int_{\tau}^{\tau+T_d} \mathrm{Tr}[\tilde{\rho}_{ion-ion}^{sd}(t_H, t_V)] \mathrm{d}t_H \mathrm{d}t_V \tag{4.78}$$

The final ion-ion entanglement fidelity is the time integral of single detection fidelity:

$$\mathcal{F} = \frac{1}{M} \int_{\tau}^{\tau+T_d} \int_{\tau}^{\tau+T_d} P(t_H, t_V) \times \mathcal{F}(t_H, t_V) \mathrm{d}t_H \mathrm{d}t_V \tag{4.79}$$

4.4 Scheme comparison

We have built the mathematical framework necessary to describe the Raman scheme entanglement dynamics, given the cavity parameters g and K. However, in a real experiment, the control over g and K is limited by fabrication techniques and they usually have an interplay relation. This inter-play will lead to a trade-off between entanglement generation rate and entanglement fidelity. Apart from the fabrication limits, some other parameters will also play a role in the trade-off, but can be freely chosen (within certain limits), for example, Raman driving field intensity, cavity concentricity, and detection exposure time. These parameters can be used to optimise the entanglement performance. Furthermore, all these dynamics are intrinsically determined by the ion species and scheme levels. Some level choices are better than others in some parameter regimes. In this section, I will numerically optimise and compare these level choices considering real-life fabrication errors, and give guidelines for a real experiment.

4.4.1 Real-life errors

In real experiment, multiple technical issues can lead to a degradation of the ion-ion entanglement performance. Some of the factors are independent of the excitation scheme, for example: magnetic field fluctuation, detection time resolution, the asymmetry of the beamsplitter and the misalignment of the PBS. We have already discussed these in Chapter 4.1.2.

There are also other scheme-independent errors, for example, excitation time difference, light path fluctuation, laser noise, detector dark counts and photon dispersion. These factors are usually minor in lab scale experiments and their physics are not the focus of this thesis. I will ignore them for now and focus on another type of error which is introduced by the cavity-enhanced Raman scheme:

(1). *Cavity misalignment*: For a cavity mode with wavelength λ. If an ion with transition linewidth γ is located at the center, the cavity coupling constant g_0 is related to the mode waist by (see Appendix C):

$$g_0 = \sqrt{\frac{3\lambda^2 c\gamma}{4\pi V_m}} = \sqrt{\frac{3\lambda^2 c\gamma}{\pi^2 w_0^2 L}} \tag{4.80}$$

where L is the cavity length along the mode axis. Mode waist w_0 is determined by the radius of curvature (ROC) of the cavity mirror R and

cavity length.

$$w_0 = \sqrt{\frac{\lambda}{2\pi}}(L(2R-L))^{1/4}, \quad (2R > L) \tag{4.81}$$

In order to achieve high g_0, one should try to minimise the mode volume by increasing the cavity length, pushing the cavity towards a concentric configuration ($L = 2R$). However, a near-concentric cavity is very sensitive to mirror alignment. If the transverse alignment between two mirrors is ϵ_t, the mode axis is tilted by:

$$\theta_{\text{tilt}} = \frac{\epsilon_t}{2R-L} \tag{4.82}$$

The divergence angle of the cavity mode is:

$$\theta_{\text{div}} = \frac{\lambda}{\pi\omega_0}, \tag{4.83}$$

assuming the misalignment is small so that the change of cavity length is negligible. For a misaligned cavity, the furthest 'edge' (as we will call the region where the intensity drops to e^{-2} of its peak value) of the optical mode on the mirror is offset from the mirror centre by $L(\theta_{\text{tilt}}+\theta_{\text{div}})/2$. We can see that both θ_{tilt} and θ_{div} increase with cavity length L. So the optical mode on the mirror is more likely to have significant amplitude beyond the radial extent of the mirror when we push cavity towards concentric. This kind of loss is called the "clipping loss" of the cavity. A clipping loss is part of total cavity loss K. Therefore there is a trade-off between g_0 and K given certain cavity misalignment and mirror diameter.

There has been great effort in the cavity community to achieve better alignment and stability. However, these alignment and stabilizing systems are very complicated and hard to scale [121, 84].

(2). *Mirror intrinsic loss*: The cavity loss K has three main components: the transmission of the cavity where photon is retrieved from the cavity mode, the clipping loss due to the finite size of the mirror, and the intrinsic loss which is a mirror fabrication issue.

Clipping loss can be improved by using better alignment technology or simply a larger mirror diameter, while intrinsic loss is set by the fabrication and coating processes themselves. The intrinsic loss l_{intr} limits the retrieval

of the generated cavity photon by its ratio to the mirror transmission T. The retrieval efficiency is simply:

$$\eta_R = \frac{T}{T + l_{\text{intr}}} \tag{4.84}$$

To have a high retrieval efficiency, the transmission should be large compared with intrinsic loss. However, a large transmission increases the cavity loss K. So the intrinsic loss sets a limit to the trade off between η_R and K and, consequently, the trade-off between ion-ion entanglement fidelity and rate.

The intrinsic loss is caused by mirror surface scattering or absorption by the mirror coating material. The mirror surface scattering is due to the mirror substrate roughness σ_{sc}. The scattering loss can be estimated by [10]:

$$\mathcal{S} \approx (\frac{4\pi\sigma_{\text{sc}}}{\lambda})^2 \tag{4.85}$$

where λ is the light wavelength. We can see that it's preferable to have a long wavelength cavity for low scattering loss. There has been extraordinary effort and progress made in aiming to reduce the roughness of cavity mirror surface. A roughness of angstrom to nanometer level is achievable for both macro-mirrors or micro-mirrors. For a wavelength of 397nm ($^{40}\text{Ca}^+ 4P_{1/2} \rightarrow 4S_{1/2}$), this corresponds to 10 ppm to 100 ppm (parts per million) loss. For a wavelength of 1033nm ($^{88}\text{Sr}^+ 5P_{3/2} \rightarrow 4D_{5/2}$), the scattering loss is 1.5 ppm to 15 ppm. Another factor contributing to the intrinsic loss is the absorption within the coating materials. This loss is highly controlled by commercial coating technology to a typical level of several ppm [60].

(3). *cavity-induced polarisation oscillation* I have discussed in Chapter 4.1.2 how polarisation oscillation can degrade the fidelity of the entanglement. The introduction of a non-ideal optical cavity can lead to different resonant frequencies for different polarisations [145]. The frequency splitting of the two eigenmodes of an elliptical cavity mirror is:

$$\Delta\nu = \frac{\nu_{\text{FSR}}}{2\pi k}\frac{R_1 - R_2}{R_1 R_2} \tag{4.86}$$

where ν_{FSR} is the free spectral range, k is the wavevector of the cavity mode, and R_1, R_2 are the ROC along the two principle axes of the elliptical

mirror. When the polarisation of the photon generated by the ion is not well-aligned with the cavity eigenmode, the cavity will impose polarisation oscillations on to the retrieved photon [7]. We built an analytical model for this effect and we propose to introduce deliberate ellipticity on mirror to suppress the random birefringence. This scheme will not be discussed further in this chapter, but is detailed for reference in Appendix D and Appendix E.

The first two fabrication limits (misalignment and intrinsic loss) themselves do not directly determine the entanglement fidelity and rate. The trade-off between them are adjusted by other easy-to-adjust experimental parameters (excitation field, detection window, etc.)

4.4.2 Scheme parameters

As has been discussed at the end of previous section, cavity misalignment and intrinsic loss are cavity-introduced errors that limit the performance of the ion-ion entanglement. Some other easy-to-adjust parameters determine the trade-off between entanglement fidelity and generation rate. We need to optimise these parameters in the presence of cavity misalignment and intrinsic loss. These easy-to-adjust parameters are:

(1). *Concentricity.* Concentricity is defined as

$$M := 2R - L \tag{4.87}$$

to describe how close the cavity is to concentric. If M is too small, the cavity is sensitive to mirror misalignment, increasing the cavity loss κ. If M is too large, the cavity mode volume will increase, resulting in a small cavity coupling constant g_0.

(2). *Mirror transmission* A larger mirror transmission will increase the photon retrieval efficiency, increasing the entanglement generation rate. However, this increase in the cavity loss κ leads to a drop of cooperativity, and temporal mixing effects will increase, decreasing the fidelity. Varying this parameter can therefore directly trade off the fidelity and generation rate.

(3). *Detection window.* A longer detection window will increase the probability of photon extraction, but temporal impurities due to spontaneous scattering are associated with the later part of the photon. Having a shorter detection window is therefore preferable for a more temporally pure photon. This parameter will directly trade off the fidelity and generation rate. However, the difference it makes to photon

extraction probability can potentially be largely compensated by using different driving parameters(potentially higher Raman laser intensity with optimised pulse shape). We will see this effect in the simulation results later in this section.

(4). *Driving pulse.* The question of what form of driving pulse is optimal, given all other parameters, is not a trival one, since the pulse cannot necessarily be described by a single parameter. However, this problem can be simplified considering that the exact pulse shape used only weakly contributes to the fidelity-rate trade-off. In another words, a driving pulse that is optimal for entanglement rate should also be close to optimal for entanglement fidelity. The driving pulse is found by optimising the pure photon (i.e. a photon produced without any spontaneous decays to the initial state) extraction rate. To justify this, reference [62] shows that in a system where driving field is the only variable, the ratio between the output cavity photon (including mirror loss) and the spontaneously emitted photon remain constant regardless of the driving field. In the regime where the majority of the ion population is transferred to the storage state at the end of the Raman process, the "good" photon, the "bad" photon and the "spontaneous emitted" photon add up to near constant 1. Therefore, the more pure photon it generates, the less "bad" photon (photon generated after spontaneous decay to the initial state) it produces and the higher fidelity the entanglement is. At the same time, since the probability of pure photon is optimal, the entanglement generation rate is also maximized. This is not strictly true, because firstly, the orthogonality of the "bad" photon wavepacket with respect to the DTM will change with the form of the driving pulse. But in the regime where the pure photon dominates the photon retrieval, this approximation is valid. Secondly, the assumption that the majority of the ion population is transferred to the storage states is not valid when the detection window is too short and become comparable with the cavity decay time $1/K$.

Since we assume the pulse shape doesn't contribute to the entanglement fidelity-rate trade-off, we can decouple the optimization of the driving field from the optimization of other parameters (1) $\rightarrow$ (3).

The optimization of the driving pulse has been conducted by William Hughes, and the details of the optimization algorithm is in reference [62]. For the rest of the optimisation simulations presented in this Chapter, optimal driving is used unless otherwise noted. To gain some understanding of what the photon and the driving field look like, we calculate the optimal photon and its corresponding driving field with two different system settings. One of them is in the small Zeeman splitting

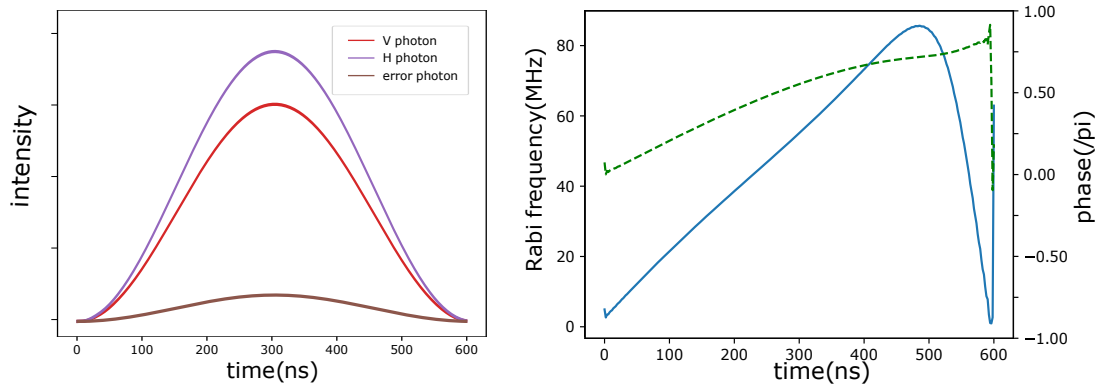

Figure 4.12: Optimal photon output and its driving. The parameters for this simulation is: $^{88}Sr^{+}$, $4D_{3/2} \rightarrow 5P_{3/2} \rightarrow 4D_{5/2}$, $\delta_H : 2\pi * 16\text{MHz}$, $\delta_V : 2\pi * 17.6\text{MHz}$, $\delta_n : 2\pi * 18.2\text{MHz}$, $g : 2\pi * 16\text{MHz}$ and $K : 2\pi * 24\text{MHz}$. The driving is optimised over a detection window of 0.6μs. The Zeeman splitting is small compared with K or g. The driving is shown in the rotating frame of the H polarised photon.

regime, where we would expect the driving to be a single frequency with a laser-cavity Raman resonance set somewhere between the level splitting. The other is in the large Zeeman splitting regime where the optimal driving should be bi-chromatic (or tri-chromatic) to drive each Raman transition separately.

Figure 4.12 shows the small splitting regime, where we indeed require a driving field that is close to single-frequency. We observe a sudden rise of the drive magnitude at the end of the window time. This is presumably because of the algorithm trying to transfer the last bit of population into photon without worrying about breaking the adiabaticity. We can see from the photon shape that at this time the photon wavepacket is already negligible so in real-life. we don't need to implement this sudden change of drive.

Figure 4.13 shows the other regime where the Zeeman splitting is relatively larger than κ or g. This means that a single driving cannot be simultaneously resonant with all cavity transitions so a bi-chromatic driving field is preferable. The sudden change of phase in the bottom right figure is just a periodical change from π to $-\pi$.

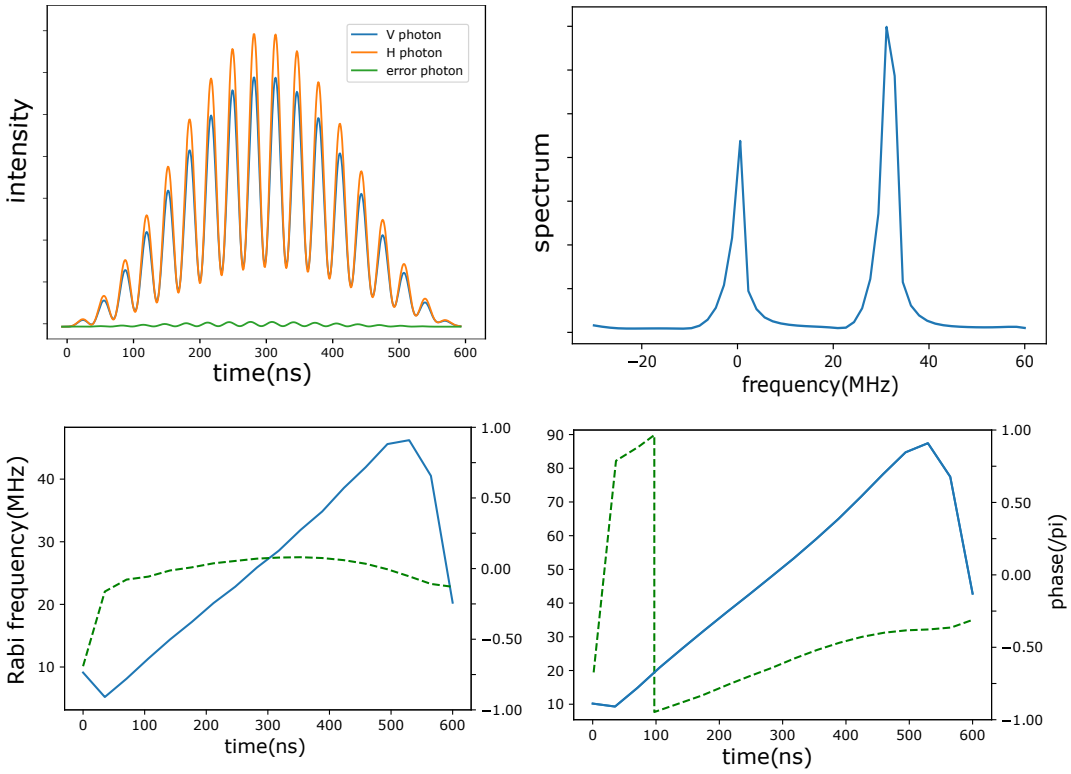

Figure 4.13: Optimal photon output and its associated driving field. The parameters for this simulation are the same as Fig.4.12 but with different detunings: δ_H : 0MHz, δ_V : $2\pi * 32$MHz, δ_n : $2\pi * 64$MHz. The detuning difference matches with the Zeeman splitting, which is larger than K or g.Top right plot is the spectrum of the optimal driving, indicating a bi-chromatic driving should be applied. The two bottom plots show the two driving fields respectively.

4.4.3 Scheme optimisation and scheme choice

4.4.3.1 Parameter optimisation for different level schemes

For a vacuum-stimulated Raman transition scheme producing an infrared optical cavity photon, there are limited species and level choices. In this thesis, we take $^{88}Sr^{+}$ as an example to analyse two different potential level schemes. Very similar conclusions apply to other ion species.

The first scheme is $^{88}Sr^{+} : 5S_{1/2} \rightarrow \{5P_{1/2}, mJ = 1/2\} \rightarrow \{4D_{3/2}, m_J = 3/2, 1/2\}$. This scheme has a wavelength of 422nm on the driving transition and 1092nm for the cavity (photon) transition. We call this scheme a "Blue-red scheme".

Another is $^{88}Sr^{+} : 4D_{3/2} \rightarrow \{5P_{3/2}, mJ = 3/2\} \rightarrow \{4D_{5/2}, m_J = 5/2, 3/2\}$. This scheme has a wavelength of 1004nm on the driving transition and 1033nm for the cavity transition. We call this scheme a "red-red scheme".

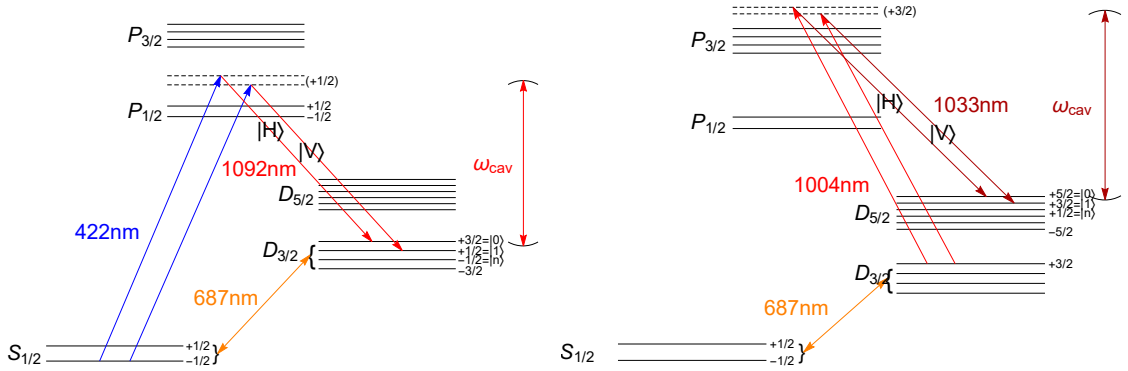

Figure 4.14: level scheme of the vacuum-stimulated Raman transitions. The left diagram is the "blue-red scheme", while the right one is the "red-red scheme".

The advantage of the "blue-red" scheme is that the driving transition has a large dipole moment so the driving field does not require large power, and state preparation into the S state is easy. The advantage of the "red-red" scheme is that the majority of spontaneous decay of the excited state is to the S state instead of the initial $4D_{3/2}$ state and so the production of post-spontaneous-decay cavity-Raman photons is unlikely to occur. It can therefore potentially avoid temporal mixing with modest cavity parameters. Another advantage of the "red-red" scheme is that both the Raman laser and cavity transitions are separated from the ion cooling transition.

We now present the trade-off between ion entanglement fidelity and generation rate as a function of each of the experimental parameters mentioned in the previous section (concentricity, transmission, detection window). We always use the optimised driving pulse as we assume it plays a minor role in the trade-off. We consider realistic parameters for the simulations. We take other losses into consideration, the fibre coupling right after the cavity is 90% because the output mode is a nice Gaussian mode. The fibre transmission in lab scale is negligible because the photon is infrared, the free space optics (BS,PBS,...) has a total loss of 10%, photon coupling to the detector fibre is also 90%, the detection efficiency is 90%. All these add up to 70% of the photon extracted from the cavity on each site. Other parameters are listed in Table. 4.1.

Fig. 4.15 shows the result of the simulation for the "blue-red" scheme. Three optimisation parameters are presented. For concentricity, we can see that both entanglement rate and fidelity go down when the cavity is either too concentric or too confocal, this is because of the increase of clipping loss and the decrease of cavity coupling constant g_0 respectively. There is a small regime (40-60μm) where both the

B field	cavity length	mirror diameter	T_p
10G	400μm	100μm	0.5μs

T_c	loss(intr.)	misalignment	other loss
2μs	30ppm	2μm	30%

Table 4.1: Simulation parameters for Raman scheme ion remote entanglement

entanglement rate and fidelity are close to optimal, however they are not optimised at the same point. This leads to a trade-off between them.

A similar trade-off is more obvious for the mirror transmission. The entanglement fidelity is better with smaller transmission. As has been explained previously, this is because a drop of cavity loss leads to an increase in cooperativity, therefore, higher pure photon is generated in the cavity with less temporal mode mixing. However, entanglement rate favors larger transmission because of the higher extraction efficiency that can be achieved. One should also notice that the required driving power shoots up with smaller mirror transmission. This is because a lower cavity loss leads to slower photon generation. In order to keep as much of the wavepacket as possible within the detection window, driving field with higher intensity has to be applied.

The detection window, however, does not play much of a role in the entanglement performance. Both the entanglement rate and fidelity stay more or less the same with different detection window. This is slightly counter-intuitive because one would expect a smaller photon extraction probability with shorter detection window. But this is not a big issue because an optimal driving field will compensate with a higher power. It is still true that there is a limit of such compensation. If we keep shortening the window further, we should expect a more dramatic drop of entanglement rate. Furthermore, with an even shorter detection window, optimal driving will not be able to transfer all the population to the storage states, so our assumption that the driving field is decoupled for the fidelity-rate trade-off becomes invalid.

All the noise in the plots are purely numerical. In fact, I have applied a rolling average to some of the results, each data point is the average of the three neighbouring data points. The numeric errors come from the calculation of the optimal driving field. A near-zero term is removed during the calculation to ensure numeric convergence and this removed term will cause inaccuracy of the final result. This computation can be time consuming because a very fine time resolution is required to solve the non-linear differential equations.

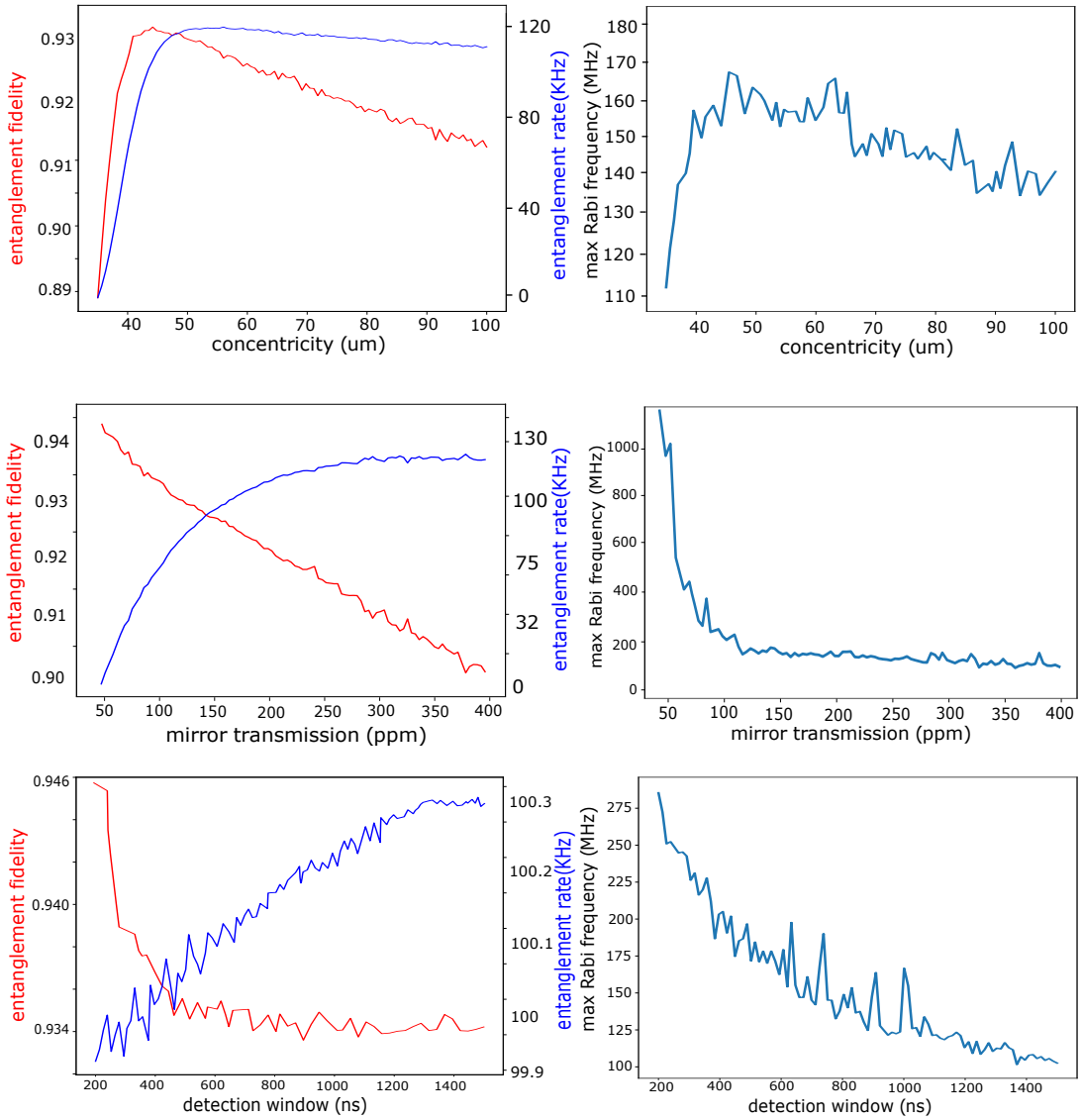

Figure 4.15: "Blue-red" trade-off between ion entanglement fidelity and entanglement rate. System parameters are in table 4.1. For concentricity scanning, the settings for mirror transmission and detection windows are: 200ppm and 1 μs; for mirror transmission scanning, the settings for concentricity and detection windows are: 45μm and 1 μs; for detection window scanning, the concentricity and mirror transmission are 45 μm and 200ppm. The unstable fluctuation comes solely from numerical errors

The "blue-red" scheme result is not very promising because the entanglement fidelity is relatively low even with optimised parameters. This is mainly because of the substantial temporal mixing due to spontaneous scattering back to the initial state during the Raman transfer. We can push the fidelity higher by producing very concentric, high finesse cavities, but this leads to even tighter limits on cavity mirror misalignment and intrinsic losses, and so it is very technically challenging. On the other hand, the "red-red" scheme is almost free from temporal mixing, and thus relaxes the requirement for cavity fabrication.

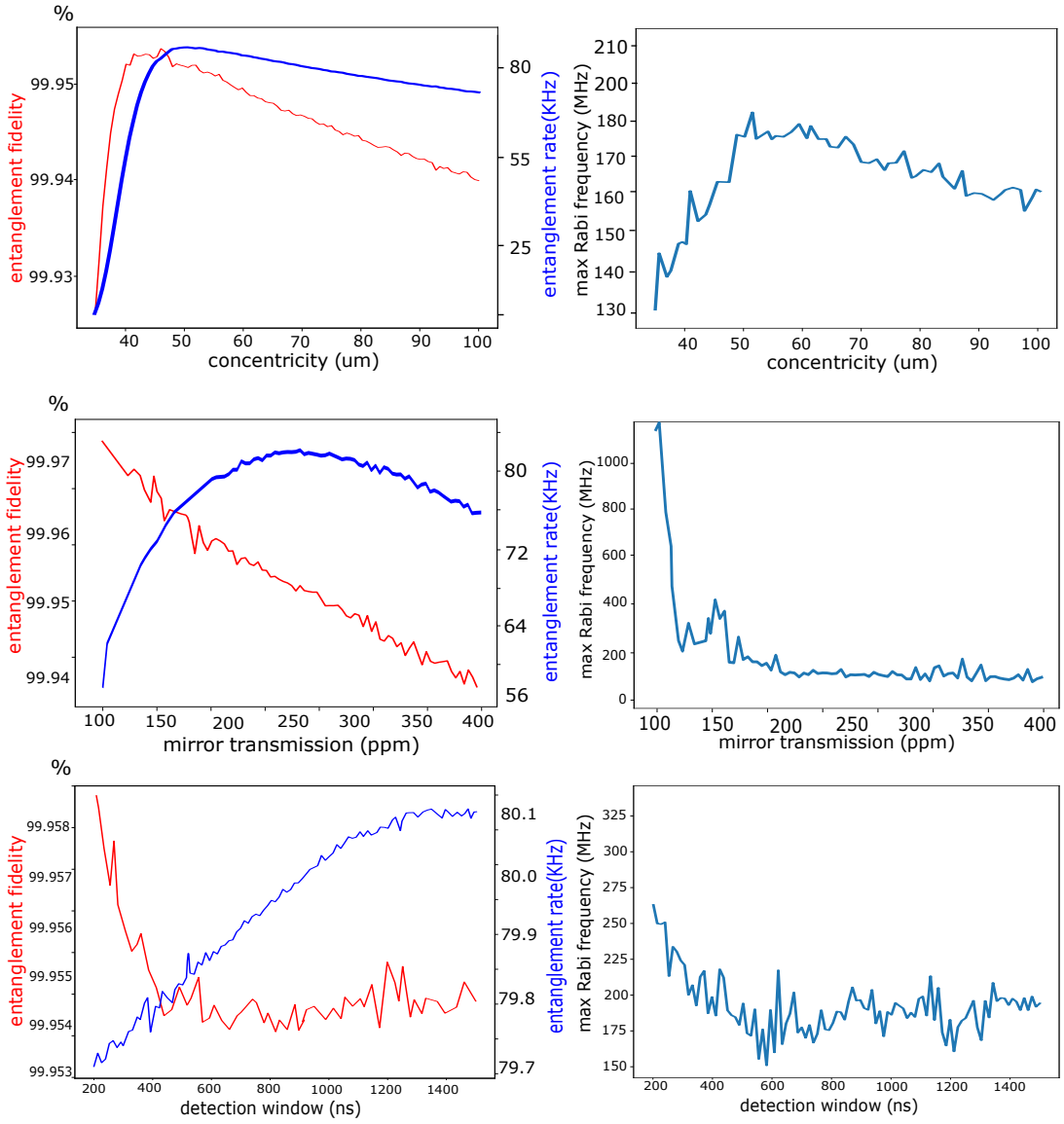

Figure 4.16: "Red-red" trade-off between ion entanglement fidelity and entanglement rate. System parameters are in table 4.1. For concentricity scanning, the settings for mirror transmission and detection windows are: 200ppm and 1 μs; for mirror transmission scanning, the settings for concentricity and detection windows are: 45μm and 1 μs; for detection window scanning, the concentricity and mirror transmission are 45 μm and 200ppm.The unstable fluctuation comes solely from numerical errors

Fig.4.16 shows the results for the "red-red" scheme. Compared with the "blue-red" scheme, the "red-red" scheme has the same trend when scanning the experimental parameters. The entanglement generation rate is a bit smaller because the population doesn't decay back to the initial $D_{3/2}$ state for photon regeneration. The entanglement fidelity is much higher than for the "blue-red" scheme and is so close to 1 that the infidelity can almost be neglected. The "red-red" scheme has a small loss in rate

but avoids a much more problematic reduction of fidelity. However, the required driving field is higher in power than the "blue-red" scheme because the dipole moment is smaller for the driving transition. A Rabi frequency of 200MHz corresponds to $\sim 60\mu W$ of laser power when the beam is focused down to a waist of $20\mu m$, compared with $\sim 4\mu W$ for "blue-red". With this being said, the "red-red" scheme is still probably a better choice because of the near-unit fidelity.

4.4.3.2 Fabrication requirements for the "red-red" scheme

The "red-red" scheme is free from temporal mixing so it is a natural choice for ion-ion remote entanglement. For a given set of fabrication tolerances (cavity misalignment, intrinsic loss), we can optimise the experimental parameters in the previous section to adjust the trade-off between entanglement rate and fidelity. However, the infidelity of the "red-red" scheme attributable to temporal mixing errors is so small compared to the variety of other likely error sources in the photonic entanglement protocol [137] that we can safely ignore it. Therefore, the trade-off problem is simplified as an optimisation-for-rate problem. We can simplify the optimisation problem further by the approximation that the effect of detection window can be compensated by adjustment of the optimal driving field. This is to say:

For a given set of fabrication tolerances, we can find an optimal entanglement rate for the "red-red" scheme by optimising over two experimental parameters: concentricity and mirror transmission, while maintaining a high entanglement fidelity.

Figure 4.17 shows the optimal entanglement rate for different fabrication tolerances as well as the corresponding Raman drive Rabi frequency, concentricity and mirror transmission. The detection window is set to be 0.5μs. This highlights the performance of the cavity-enhanced Raman scheme for ion-ion remote entanglement. We can expect 100kHz of entanglement rate with relatively modest fabrication tolerance. This is almost three orders of magnitude higher than the state of art ion-ion RE.

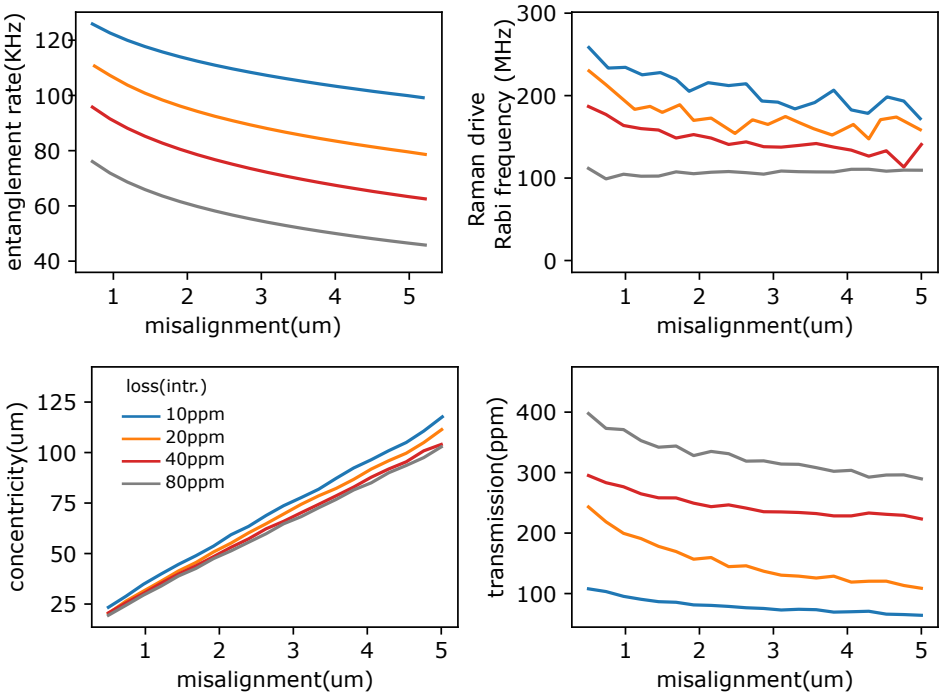

Figure 4.17: Entanglement performance with fabrication tolerance. The four lines are different mirror intrinsic loss. The system parameters are in Table.4.1 but varying intrinsic loss and misalignment. The detection time is set to be 0.5 μs.

Another fabrication related constraint, which we have not discussed so far, is the size of the mirror. In all the simulation above we use 100μm, which is close to the limit of some mirror profile fabrication technologies (e.g.focused ion beam (FIB)[143]). A smaller size will introduce more clipping loss, while a much larger mirror will increase the FIB milling time, and potentially the roughness of the surface at the steeper edges of the mirror, as well as introducing more stray electric deformation to the trap potential. Nevertheless, a small change of mirror size could have a impact on the cavity performance largely independent of many of the considerations discussed so far. In Fig. 4.18 and Fig. 4.19, I present the entanglement performance with the same system settings but with a larger (120μm) and smaller (80μm) mirror. We can see that with a larger mirror, the entanglement rate is only slightly increased, while it is more affected by smaller mirror size. This suggests that with a 100μm mirror diameter, the clipping loss is small compared to the compared with intrinsic loss. However, with mirror diameters smaller than this, clipping loss starts to play an important role. Of course, this conclusion is based on a cavity length of 400 μm, although it is unlikely this can be greatly decreased for the same reason we want to avoid much larger mirrors.

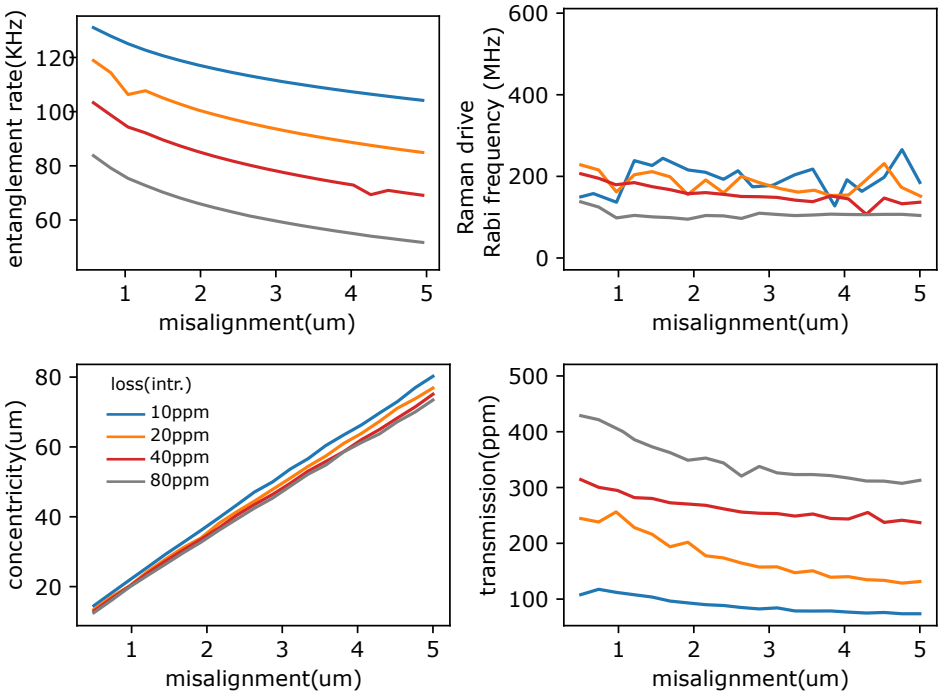

Figure 4.18: Entanglement performance with fabrication tolerance with cavity mirror diameter 120μm. The four lines are different mirror intrinsic loss. The system parameters are in Table.4.1 , with the simulations optimising performance for varying intrinsic loss and misalignment. The detection time is set to be 0.5 μs.

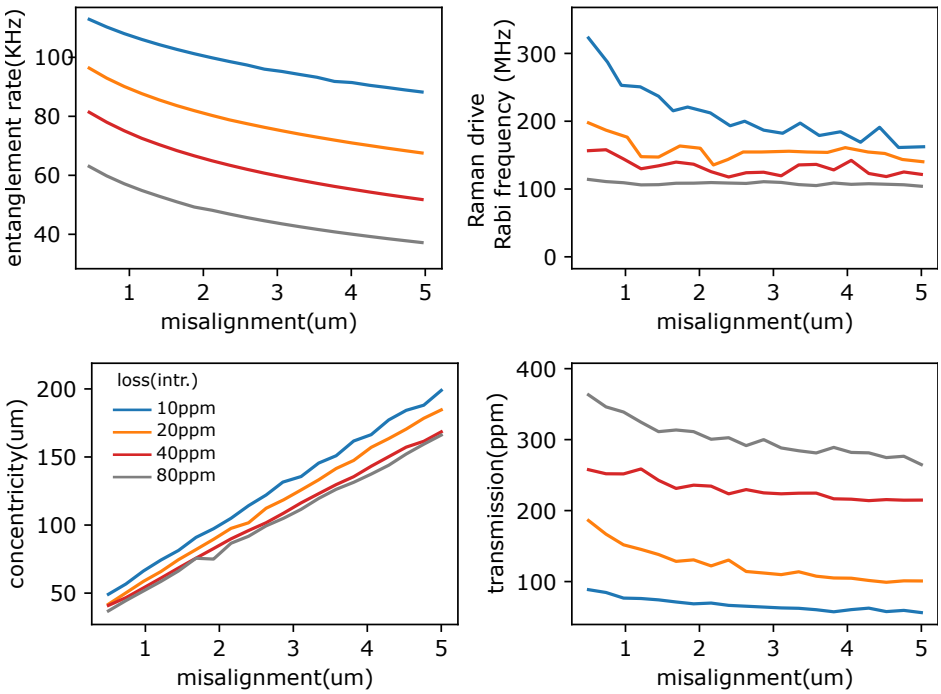

Figure 4.19: Entanglement performance with fabrication tolerance with cavity mirror diameter 80μm. The four lines are different mirror intrinsic loss. The system parameters are in Table.4.1 , with the simulations optimising performance for varying intrinsic loss and misalignment. The detection time is set to be 0.5 μs.

4.5 Discussion

4.5.1 Analytical approximation

We have built a full theory to describe the temporal mixing effects observed in the photons emitted via a Raman transfer process susceptible to spontaneous scattering to the initial state during the transfer. However, there is no simple analytical solution to the system. In fact, the simulation is fairly computationally complex for several reasons:

1. To retain numeric stability, the time resolution should be much finer than the fastest dynamics of the system. For Sr, the $5P$ state has a spontaneous decay rate of more than $10^8 s^{-1}$. To achieve high ion-cavity interaction, the coupling constant is also high (usually more than 2π*15MHz). The Zeeman splitting with large magnetic field is also typically a couple of hundred MHz. All of these factors require a numeric time resolution of less than a nanosecond.

2. Quantum regression theory requires a time regression calculation for each time step. This will make the computational complexity scale quadratically with the number of time steps.

3. The calculation of the optimal driving pulse parameters is a non-linear problem which requires even finer time resolution to maintain convergence.

It is very useful to have an analytical approximation of the fidelity without intense computational cost. We start with a recap of our previous claim:

There exists a set of discrete infinite orthogonal temporal modes

$$\{[\mathcal{E}_H^{Z(i)}(t), \mathcal{E}_V^{Z(i)}, \mathcal{E}_n^{Z(i)}(t)]\},$$

which gives the same ion-ion entanglement density matrix as the set of continuous photon emission temporal modes

$$\{[f_H^{Z(i)}(t), f_V^{Z(i)}(t), f_n^{Z(i)}(t)]\}.$$

These orthogonal temporal modes are the eigenmodes of the field two-time correlation functions (Eq.4.51) re-normalised to the corresponding eigenvalue:

$$\int \mathcal{E}_X^{Z(i)}(t)\mathcal{E}_X^{Z(i)*}(t)dt = \lambda_X^{Z(i)}.$$

Assuming Alice and Bob are the same, when both Alice and Bob generates the same temporal mode $\{[\mathcal{E}_H^{A(i)}(t), \mathcal{E}_V^{A(i)}(t), \mathcal{E}_n^{A(i)}(t)]\} = \{[\mathcal{E}_H^{B(i)}(t), \mathcal{E}_V^{B(i)}(t), \mathcal{E}_n^{B(i)}(t)]\}$ labeled by index (i), the ion-ion entanglement has unit fidelity.

We will now make several approximations. The first is that when Alice and Bob generate different temporal modes $i \neq j$, the ion-ion entanglement is random so the fidelity is approximately 1/2. The probability of having unit fidelity is:

$$\begin{aligned} P(\mathcal{F}=1) =& \sum_i ((\lambda_H^A(i) + \lambda_n^A(i)) * \lambda_V^B(i) + \lambda_V^A(i) * (\lambda_H^B(i) + \lambda_n^B(i))) \\ =& 2\sum_i (\lambda_H^i + \lambda_n^i) * \lambda_V^i \approx 2(\lambda_H^0 + \lambda_n^0)\lambda_V^0 \end{aligned} \tag{4.88}$$

The second approximation we make is that the dominant, lowest order eigenvalue is much larger than the higher order eigenvalues. The probability of having 1/2 fidelity is the total heralding probability minus the unit fidelity probability:

$$P(\mathcal{F}=1/2) = P_{herald} - P(\mathcal{F}=1) \tag{4.89}$$

where:

$$P_{herald} = \frac{(\sum_i(\lambda_H^i + \lambda_n^i + \lambda_V^i))^2}{2} \tag{4.90}$$

The factor of 1/2 here means that only half of the configurations (a H and a V polarised photon are detected) heralds events.

The total fidelity is:

$$\mathcal{F} = \frac{P(\mathcal{F}=1) \times 1 + P(\mathcal{F}=1/2) \times \frac{1}{2}}{P_{herald}} \tag{4.91}$$

In order to have the best entanglement generation rate, one would try to make:

$$\lambda_H^i + \lambda_n^i \approx \lambda_V^i \tag{4.92}$$

If we take this as the third approximation. and define:

$$\lambda^i := \frac{\lambda_H^i + \lambda_n^i + \lambda_V^i}{\sum_i(\lambda_H^i + \lambda_n^i + \lambda_V^i)} \tag{4.93}$$

We then have total fidelity Eq.4.91 to be:

$$\begin{aligned} \mathcal{F} =& (\lambda^0)^2 + \frac{1}{2}(1 - (\lambda^0)^2) \\ =& (1-\epsilon_F)^2 + \frac{1}{2}(1 - (1-\epsilon_F)^2) \\ \approx& 1 - \epsilon_F = \lambda^0 \end{aligned} \tag{4.94}$$

where we use and extend the second approximation such that $\epsilon_F << 1$.

λ^0 has very clear physical meaning. It is the probability that the ion generated cavity photon is in its dominant temporal mode (DTM), re-normalised by the probability of generating a cavity photon. Fig. 4.20 shows that λ^0 agrees very well with the simulated ion-ion entanglement fidelity, especially when the coupling constant is large, which is when the dominant mode is much larger than other modes. So λ^0 is a good approximation of the ion-ion remote entanglement fidelity. The analytic orange line will be explained later.

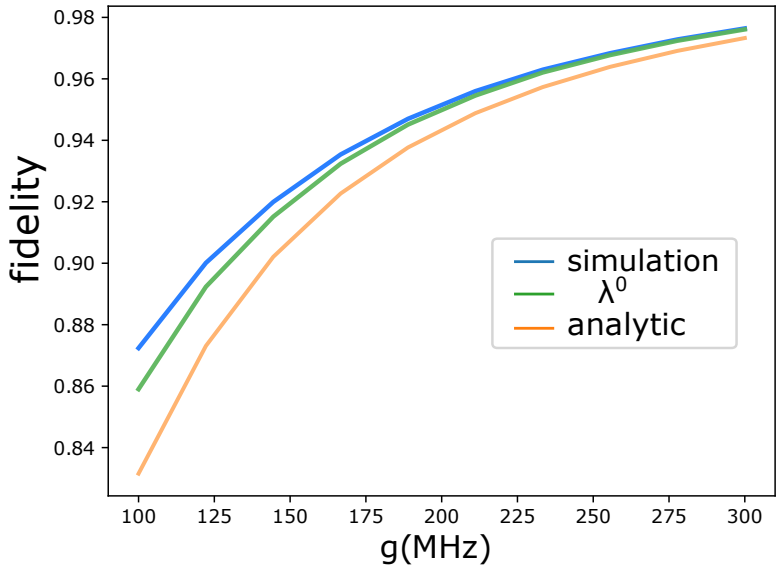

Figure 4.20: Approximation for ion-ion fidelity for "blue-red" scheme is being presented. The simulation uses a B field of 10G, $K = 2\pi * 24MHz$ and optimal driving with a detection window of 1μs.

Regardless of its clear link to the underlying physics, λ^0 cannot be analytically calculated. Nonetheless, its underlying physics allows us to have an analytical approximation of it. Before we move on, it is convenient to define a simple terminology to describe the process of generating a Raman cavity photon after spontaneous decay. We call this process the *repumping* process. The corresponding photon is called the *repumping photon*, which contributes to the temporal noise.

We now start to estimate λ^0 analytically. Firstly, we can easily estimate it to be lower bounded by $2C/(2C+1)$ because this is the probability the ion-cavity system generates a pure photon without any "repumping". In another word, this is the photon generation probability when we consider all spontaneous processes lead to population loss. Therefore, this is an estimation of λ^0 if we assume that all the spontaneous decayed photons are repumped and becomes temporal noise of the cavity photon mode. But this is not always true. In most cases, only a fraction of the spontaneous decay repopulate the initial state, trigger the repumping. This process happens for infinite cycles and for each cycle, the proportion of these "repumping" photons to the total spontaneous emitted photons is the branching ratio between the "repumping" decay rate to the total decay rate of the excited state. If we take "blue-red" scheme as an example. The "repumping" decay is $P_{1/2} \rightarrow S_{1/2}, m_J = 1/2$. One

should note that the cooperativity C here includes all different Raman channels:

$$\begin{aligned} C =& C_H + C_V + C_n, \\ C_X =& \frac{2g_X^2}{K\Gamma}. \end{aligned} \tag{4.95}$$

So we can now have a better lower bound of the ion-ion entanglement fidelity ($p_C = \frac{2C}{2C+1}$):

$$\begin{aligned} \mathcal{F} \approx& \lambda^0 \\ \approx& \frac{p_C}{p_C + (1-p_C)\cdot R_\gamma \cdot p_C + ((1-p_C)\cdot R_\gamma)^2 \cdot p_C + ...} \\ =& 1 - (1-p_C)\cdot R_\gamma \\ =& 1 - \frac{R_\gamma}{2C+1} \end{aligned} \tag{4.96}$$

where R_γ is the branching ratio of the "repumping" decay to the total excited state decay.

We have mentioned before that these repumping photons as temporal noise are not temporally orthogonal to the "no-repumping" photon. We don't know exactly the orthogonality of these photons and how different they are from the dominant temporal mode. But we can estimate a certain portion of it which can project to the dominant temporal mode. This would be our fourth approximation that this portion is 1/2. This estimation takes the intuition that the repumping photons are very random in temporal mode so they should be in the middle of parallel and orthogonal to the dominant mode. Furthermore, in the regime where the majority of the photon is the "pure" photon (cavity photon before spontaneous decay), the "pure" photon should be temporally close enough to the DTM such that its fidelity to the DTM is 1. These numbers, in principle, vary slightly with different driving field shapes and can be tested by the Quantum Monte Carlo method.

We now have a much better analytical approximation of the ion-ion fidelity:

$$\begin{aligned} \mathcal{F} \approx& 1 \times \left(1 - \frac{R_\gamma}{2C+1}\right) + \frac{1}{2} \times \frac{R_\gamma}{2C+1} \\ =& 1 - \frac{R_\gamma}{2(2C+1)} \end{aligned} \tag{4.97}$$

We can see in Fig.4.20 that Eq.4.97 agrees well with the simulation.

There is, however, another approximation. We assume the "no-repumping" pure photon has a probability of $2C/(2C+1)$, but this is only for the case when we drive the system adiabatically. In real life, the Raman driving field is optimised to maximize the photon extraction probability within the detection window. A short detection window will break the adiabaticity of the Raman process.

4.5.2 State correction operation

We have mathematically described how to correct the ion-ion state by optimally rotating the noise channel to $|0\rangle$ channel with unitary operation U_{DTM} Eq.4.71. It is important to have a more careful examination of this operation and investigate whether it is experimentally realistic or not.

The rotation applied on each node is defined in Eq.4.72. The rotation vector on Bloch sphere is:

$$\overrightarrow{\omega}_{\text{correction}} = 2\tan^{-1}[J_Z] * [\cos\frac{J_Z}{|J_Z|}, \sin\frac{J_Z}{|J_Z|}, 0], \quad (Z = \{A, B\}) \tag{4.98}$$

We can see that this correction is a Pauli X rotation with a detection time related phase. The phase evolution has two parts, the constant oscillation defined in Eq.4.8 as θ_i and the slow extra phase modulation from the DTM. If we take Bob as an example, its oscillation phase correction is defined by θ_3:

$$\theta_3 = (\omega_2^B - \omega_0^B)t + (\omega_n^B - \omega_H^B)(t_H - L/c) \tag{4.99}$$

The first term means that the phase will continue evolving regardless of detection event. In experiment, this term can be kept track of and cancelled by a laser phase locked with the Raman driving field. In our simulation, we are in the rotating frame of the atomic transition so this term is intrinsically 0. The second term is detection-time dependent and is the main phase error to be corrected.

Fig.4.21 shows the correction rotation required for a small Zeeman splitting of $2\pi * 1.6$MHz.

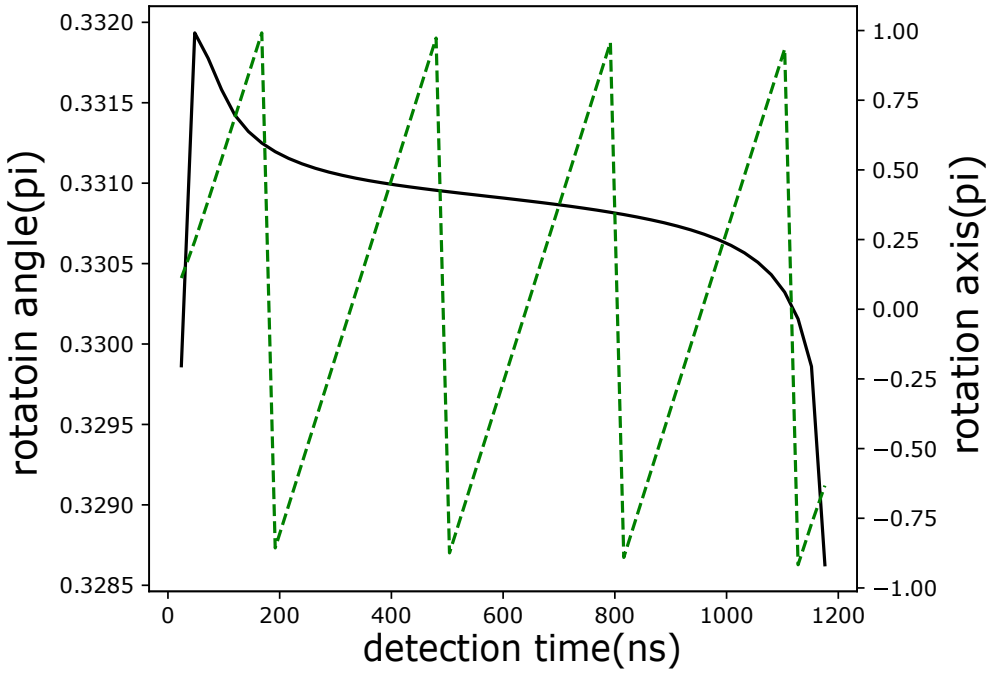

Figure 4.21: State correction operation. The solid black line is the rotation angle of the state correction operation and the green dashed line is the angle between the X axis and the rotation axis on the Bloch sphere equator. System parameters are: g $= K = 2\pi$*16MHz, Zeeman splitting $= 2\pi * 1.6$ MHz, and the optimal driving field turns out to be single frequency.

We can see that the rotation angle is almost constant. This is because the rotation angle is determined by the amplitude ratio between the n photon and the H polarised photon, The ratio is almost constant with small energy splitting and single frequency driving. The rotation axis is rotating on the Bloch sphere equator with a certain frequency $\sim 2\pi * 3.2$MHz, which indicates that the optimal driving is single frequency, on resonance with the H polarised cavity photon transition. Since the correction rotation angle is near constant and the rotation phase is simple, this state correction should be easy to implement experimentally.

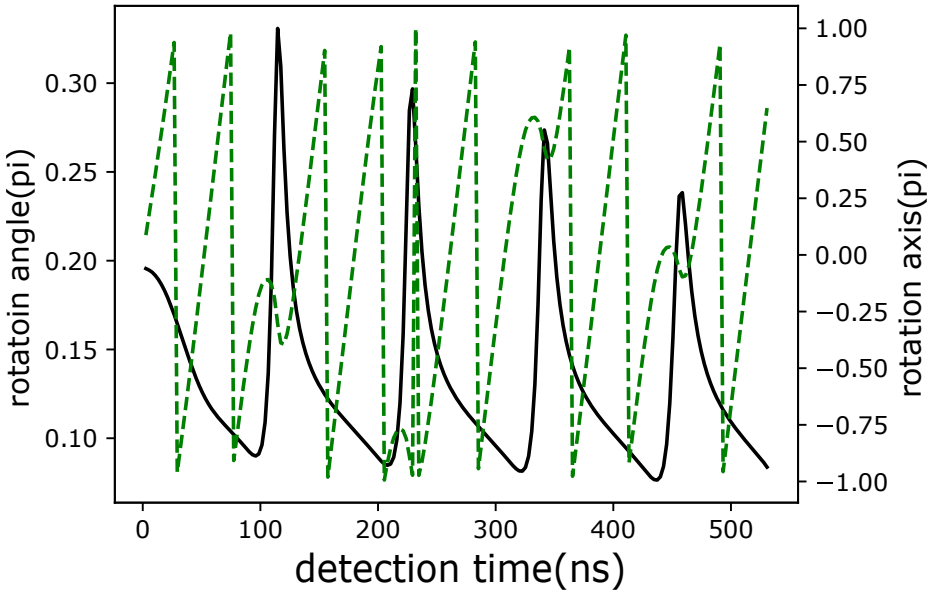

Figure 4.22: State correction operation. The solid black line is the rotation angle of the state correction operation and the green dashed line is the angle between the X axis and the rotation axis on the Bloch sphere equator. System parameters are: g $= K = 2\pi$*16MHz, Zeeman splitting $= 2\pi * 12$ MHz, and the optimal driving field turns out to two frequency components.

The correction operation is more complicated when bi-chromatic Raman driving field is applied for large Zeeman splitting with $2\pi * 12$MHz (Fig.4.22). Both the correction rotation angle and the phase are much more challenging to be performed than with small Zeeman splitting. However, one could choose to use single frequency Raman driving field, with the sacrifice of photon extraction probability, to make the state correction more experimentally feasible.

4.5.3 Summary and outlook

In this chapter, we have constructed a full description of cavity-enhanced Raman transition for ion-ion entanglement generation, considering two type of errors: temporal mixing and loss channel. We then employed this analysis to calculate ion-ion entanglement with real experiment parameters. Three types of fabrication errors are discussed: cavity misalignment, mirror intrinsic loss and cavity-induced polarisation oscillation. Among these errors, cavity-induced polarisation oscillation is uncoupled with other errors and are discussed separately. The system is optimised to have the highest entanglement generation rate without losing much fidelity. The optimisation is achieved by three easy-to-adjust experiment settings: Raman driving field,

concentricity and mirror transmission. We then present the optimised entanglement with respect to different fabrication tolerances, which gives a guideline for cavity fabrication requirement. With these simulations, we compare two ion level schemes. The "red-red" scheme is an overall better level choice to achieve high fidelity ion-ion entanglement. Last but not least, we develop an analytical solution to predict the ion-ion entanglement fidelity, which gives a strong physics insight of the system.

Using cross correlation functions for temporal mixing treatment is a novel angle of view to the system. It is also the foundation for all the simulations works and the analytical solution. This approach has two physical highlight:

1. The "repumping" process induced by spontaneous decay is a continuous and random dynamics. However, its effect on the ion-ion entanglement is determined by its statistical properties, which is tidied up into Cross Correlation Functions. Instead of simulating the spontaneous process individually using Monte Carlo simulation, one can directly calculate its statistical function through master equations. This will make the result more accurate statistically.

2. The continuous "repumping" process produces temporal modes incoherently. The new approach finds a new set of temporal modes that are equivalent to these "repumping" modes but discrete and orthogonal. The new sets of temporal modes tells us what is the "dominant" pure part of the modes mixture and helps us easily estimate the entanglement fidelity analytically.

Even though the theory is already fairly complete, there are still some details that require more investigations.

Firstly, the theory assumes the ion can be stably trapped at the center of the cavity mode, in which case, the coupling constant is a real number. However, in real experiment, in order to increase the coupling strength, the waist of the cavity mode is usually as small as several micrometer, the micro motion of the ion can become a factor to consider. In this case, the coupling constant is a complex number. It is still unknown how much this will degrade the entanglement.

Secondly, the state correction, though predictable, is not experimentally straightforward to implement. The correction rotation is determined by driving frequency and pulse shape. It is worth investigating whether there is a way to simplify the correction operation by sacrificing some photon extraction efficiency.

Thirdly, the calculation of clipping loss is assuming the clipping does not change the cavity transverse mode. However, this is not strictly true. A lot of work has been done to calculate the cavity mode with deformed mirror [114]. But the calculation is

relatively time consuming. We are working on a quick algorithm for such calculation [63], which will be integrated into the ion-ion entanglement simulation in the future.

Finally, we should improve the numeric stability of the simulation, especially the optimal driving calculation. The program tends to diverge in some specific parameter regimes.

Chapter 5

Conclusion and outlook

Conclusion

How exactly to build a scalable quantum computer is highly dependent on the computational model and the physical platform. One big challenge for a pure photonic quantum network is how to generate multiple single photons at the same time. To do this, a single-photon source with high brightness and high indistinguishability is required. We proposed the use of an atomic ensemble system, an ORCA buffer, to optimally clean the temporal mode of a solid state single-photon source to improve the temporal purity, and thus the indistinguishability, of the photon. More importantly, an ORCA buffer can change the temporal mode of the photons almost arbitrarily. So distinctive photons from different single-photon sources can be unified to generate multi single-photons in the same temporal mode. Simulation showed that the ORCA system can outperform any intensity filtering. It can also unify different single-photon sources and increase the indistinguishability from the current state-of-the-art of 60%, to as high as 96%. We also did a proof of principle experiment to demonstrate a 10% buffer efficiency and to verify that the noise of our system is below detector dark count. The ORCA buffer, if fully demonstrated experimentally, can be a powerful tool to improve the the performance of multi-single-photon sources without improving the sources themselves.

Another promising physical platform for quantum computing is trapped ions. Entangling ions from multiple traps by photonic interconnection is a promising approach to scale the physical qubit number of such platform. A systematic analysis was constructed to describe the dynamics of the entanglement generation. The Cross Correlation Function (CCF) was defined and validated for the purposes of calculating the photon temporal mixing driven by spontaneous Rayleigh scattering processes in

the Raman system during entanglement generation. We proposed a new entanglement scheme: the "red-red" scheme which offers a near-unit temporal fidelity, due to the greatly reduced probability of spontaneous decay back to the initial state. Using this scheme, an entanglement generation rate of more than 100kHz (taking into account transmission losses) is possible with negligible temporal mixing induced infidelity. Our simulations also offer a set of guidelines for cavity parameter optimization and cavity fabrication requirements. The simulations showed that the "red-red" level scheme also eases the fabrication requirement by significantly. Our theory work is useful when trying to design future practical systems and make predictions of their performance that takes into account most major experimental imperfections.

It is still too early to say which physical platform definitively outperforms the others. Both of these approaches, if experimentally accomplished, will constitute major building blocks towards large-scale quantum networking.

Outlook

A. Improving the singlemodeness of the ORCA

Although it has been shown that singlemodeness of the ORCA buffer is not necessary to achieve SPS mode selectivity, according to Eq.3.69, the mode selectivity is a combination of singlemodeness and buffer-SPS mode-overlap. However, without singlemodeness of the buffer, the overlap has to be intricately designed to optimise the indistinguishability, in which case the dominant mode of the SPS will very likely not maximally overlap with the dominant mode of the buffer, resulting in a reduction of the buffer efficiency. Meanwhile, without singlemodeness of the ORCA buffer, the output can never be truly single mode. It is always better to have a single-mode buffer to begin with so that we don't need to carefully configure the overlapping c_{ki}.

It is not easy to make the ORCA buffer single-mode while keeping high efficiency. However, we proved that it is theoretically possible [110]. The single-mode ORCA buffer with unit efficiency is achieved with a very strong and short square-shaped control field for a sinc^2 signal. This suggests that for other shape of single-photon, it is also possible to achieve single-mode unit efficiency ORCA buffer by a different control pulse shape. This has not yet been verified but will be investigated in the future.

B. Experimental realisation of ORCA as a quantum buffer

The biggest experimental problem of using the ORCA as a quantum buffer is the low efficiency. A known easy improvement is to increase the cell length and the control field power. A more complicated improvement would be optimising the control pulse shape. The integration of an ORCA system and a SPS system is also realistic in the near future.

C. Scalable ion trap design and fabrication

Traditional ion trap systems have macroscopic designs. They use bulk optics and wires for laser and electronic delivery. Trap components are assembled by bolts and rods. Ultrahigh vacuum systems are constructed from large, off-the-shelf components, bolted together. These are fine for a proof of principle experiment. However, from the point of view of scalability, the macroscopic architecture is not ideal, not just because it takes up too much space but also because it adds unnecessary random errors such as vibrational fluctuations. For some cavity-atom coupling experiments researches, it is favourable to achieve the strong coupling regime ($g \gg \kappa, \gamma$). $g \gg \gamma$ requires a small cavity volume and $g \gg \kappa$ requires a high reflectivity coating. However, in the context of increasing the photon collection rate, it is not obvious why it is beneficial to have a smaller cavity. In fact, the cooperativity is independent of cavity length:

$$C = \frac{g_0^2}{K\gamma} = \frac{2d^2\omega}{\pi\epsilon_0\hbar w_0^2 cT\gamma} \tag{5.1}$$

where w_0 is the cavity mode waist, T is the mirror transmission (including other losses), and other parameters are atomic constants and physical constants. This shows that a big cavity can achieve a cooperativity the same as a small cavity. However, we will show now that a big cavity is more sensitive to misalignment than a small cavity when they offer the same cooperativity.

When the mirror transmission is fixed, the cooperativity is determined by the cavity mode waist:

$$w_0 = \sqrt{\frac{\lambda L}{\pi}}\left(1 - \frac{L}{2R}\right)^{1/4} \tag{5.2}$$

where L is the cavity length, R is the RoC of the mirrors, λ is the wavelength of the cavity mode. When there is a perpendicular offset between the mirrors, the cavity mode will be tilted and leads to more clipping loss. If we assume the mirror diameter scales in the same way as the cavity length (to keep the same numeric aperture), the

mode tilting angle is then directly associated when the clipping loss. The mode tilt angle can thus be used to characterise the sensitivity to mirror misalignment:

$$\Theta_{\text{tilt}} = \frac{\Delta_{\perp}}{2R - L} \tag{5.3}$$

where $\Delta_{\perp}$ is the perpendicular misalignment of the cavity mirrors. Putting Eq.5.2 into Eq. 5.3, and we get:

$$\Theta_{\text{tilt}} = \left(\frac{\lambda^2}{w_0^4 \pi^2} L - \frac{1}{L} \right) \Delta_{\perp}, \quad (L > \frac{w_0^2 \pi}{\lambda}). \tag{5.4}$$

We can see that for a given waist, and thus cooperativity, the larger the cavity length is, the more sensitive it is to misalignment. This provides a strong motivation for building small traps for ion-ion remote entanglement. However, when traps are made very small, there will be more small scale structures too complex for traditional mechanical fabrication. Consequently, microfabrication technology should be utilized for future trap design.

Micro-fabrication technology has already been used for building surface trap for many years and remains a promising option for scalable ion traps. But surface traps have relatively small trapping depth, and the trapping field produced is more easily perturbed by the presence of the cavity mirror dielectrics than with a 3D trap geometry. A promising way forward is to use microfabrication technology to build a 3D trap with a integrated high finesse optical microcavity. Other trap components should also be miniaturized when possible.

When considering how we might integrate an optical cavity with an ion trap, it currently seems impossible to avoid fabricating the two mirrors separately and reassembling them after high reflectivity mirror coating deposition. The mirror fabrication is traditionally done by using high-power laser ablation to produce concave profiles on the fibre tips and the cavity is formed by aligning the fibre tips with translation stages. However, translation stages themselves are bulky devices. Even if they can be made small, stability remains a problem. Active alignment of fibre cavities is making great progress but the complicated structures [84] make it difficult to scale up to thousands to millions of modules. We propose to use passive alignment technology which relies on Lego-like pre-aligned parts. Once they are reassembled, they are in the right position within the required tolerance. Although difficult to fabricate, once they are in the vacuum chamber, they will be stable and only simple, if any, active control is required.

Traditional mirror fabrication technology and traditional lithography are not capable of such a task. However, other new fabrication technologies have begun to

make this proposal realistic. Focused ion beam (FIB) milling uses accelerated electrons to remove material surface and makes tiny structures on surface with precision in the nanometer scale. This makes FIB milling the perfect technology for mirror fabrication. Compared with the traditional laser ablation approach, FIB milling has the potential for much better placement accuracy, which is important for passive alignment. Lithography has very good precision but the 3D structures that can be produced involve many fabrication steps and are limited in scope. 3D laser-writing technology uses high-intensity femtosecond laser, focused inside transparent materials (e.g. glass and fused silica), to modify the refractive index, micro-structure, and other local features. Complicated 3D structures can be fabricated when additional chemical etching is applied to the laser-processed material. Companies like FEMTOPRINT® can make the printing precision in sub-micrometer scale, making it possible to fabricate the entire micro trap from a single monolithic piece of fused silica. Passive cavity alignment maybe possible by designing some alignment features and fiducial marks on the trap substrates and the cavity mirror holders. Other options for passive alignment includes liquid surface tension alignment which requires a reliable hydrophobic coating and precise hydrophilic channel etching on silica surface. This technique is also under development.

Appendix A

Adiabatic Following Approximation

A.1 Non-adiabatic equations of motion

The non-adiabatic equations of motion for modified ORCA system are:

$$\begin{aligned} \partial_t P_{12} &= i\Omega_c^* \sqrt{n} - \Gamma_1 P_{12}, \\ \partial_t P_{23} &= i\Omega_c B - \Gamma_2 P_{23}, \\ \partial_t B &= i\Omega_c^* P_{23} - \frac{g_s}{\hbar} d_{23}^* A P_{12}, \end{aligned} \tag{A.1}$$

where Ω_c is the Rabi frequency of the control pulse, $\Gamma_i = \gamma_i - i\Delta_i$, γ_i are the spontaneous decay rate associated with the intermediate state ($i = 1$) and excited state ($i = 2$), Δ_i are the detuning of the driving ($i = 1$) and the signal ($i = 2$). For ORCA protocol, $\Delta_1 = \Delta_2 = \Delta$ to fulfil the two-photon resonance condition. P and B are the annihilation operators for macroscopic polarization and spin wave:

$$\begin{aligned} P_{23} &= \frac{1}{\sqrt{n}\delta V} \sum_\beta \tilde{\sigma}_{23}^\beta, \\ P_{12} &= \frac{1}{\sqrt{n}\delta V} \sum_\beta \tilde{\sigma}_{12}^\beta, \\ B &= \frac{1}{\sqrt{n}\delta V} \sum_\beta \tilde{\sigma}_{13}^\beta, \end{aligned} \tag{A.2}$$

where n is the number density of atomic vapor δV is the macroscopic volume and β refers to every atom in volume δV.

A.2 Adiabatic following

The adiabatic following approximation usually takes the form $\partial_t P_{12} = \partial_t P_{23} = 0$. It is not clear why and what condition it requires. This appendix is to address these questions.

From the equations (A.1), we can tell that the polarizations are driven by two mechanisms: the external field Ω_c and the detuning Γ. $\Omega_c(t)$ is the slowly varying envelop of the driving field, while Γ leads to a relatively fast oscillation when the detuning is large. So we would guess that maybe the polarization can be separated into a slow term $P^{(o)}$ and a fast term P' : $P = P^{(o)} + P'$. The strategy here is to define $P^{(o)}$ as the slow varying term that we care about and then derive the form of P' to show under what condition this term is negligible.

We start with P_{12}. $P_{12}^{(o)}$ is defined such that: $0 = i\Omega_c^*\sqrt{n} - \Gamma_1 P_{12}^{(o)}$. So (assuming Ω_c is real):

$$P_{12}^{(o)} = \frac{\Omega_c\sqrt{n}}{\Delta} \tag{A.3}$$

Put this into the first equation in (A.1), we will get:

$$\frac{\partial P_{12}^{(o)}}{\partial t} + \frac{\partial P'_{12}}{\partial t} = i\Delta P'_{12} \tag{A.4}$$

To make the effect of P'_{12} negligible, we want P'_{12} to "oscillate" around zero fast enough such that in the time scale where $P_{12}^{(o)}$ remains almost constant, P'_{12} averages to zero. Mathematically:

$$\left| \int_t^{t+\frac{N}{\Delta}} P'_{12}(t')dt' \right| \ll \left| P_{12}^{(o)}(t) * \frac{N}{\Delta} \right| \tag{A.5}$$

where $\frac{N}{\Delta}$ is the time scale required. We already know that the fast varying term P'_{12} is changing in the time scale of $1/\Delta$, and the slow varying term $P_{12}^{(o)}$ follows $\Omega_c(t)$, so we have:

$$W \ll \Delta. \tag{A.6}$$

where W is the bandwidth of the drive field. With this condition, N can be a number larger than 1.

Define $\mathcal{A}$ as maximal mode magnitude of P'_{12}. We take the integral from the two

sides and then get the modulus:

$$\begin{aligned}\left|\int_t^{t+\frac{N}{\Delta}} \frac{\partial P_{12}^{(o)}(t')}{\partial t'}dt' + \int_t^{t+\frac{N}{\Delta}} \frac{\partial P'_{12}(t')}{\partial t'}dt'\right| = \left|i\Delta \int_t^{t+\frac{N}{\Delta}} P'_{12}(t')dt'\right| &\ll \left|iNP_{12}^{(o)}(t)\right|, \\ \left|P_{12}^{(o)}(t+\frac{N}{\Delta}) - P_{12}^{(o)}(t) + P'_{12}(t+\frac{N}{\Delta}) - P'_{12}(t)\right| &\ll |iNP_{12}^{(o)}(t)|, \\ 0 + 2\mathcal{A} &\ll N|P_{12}^{(o)}|, \\ \mathcal{A} &\ll |P_{12}^{(o)}|\end{aligned} \tag{A.7}$$

To fulfill this condition, we would have to estimate the upper bound of $\mathcal{A}$.

Let's go back to equation (A.4). Since $P_{12}^{(o)}$ is a slowly varying term, $\frac{\partial P_{12}^{(o)}}{\partial t}$ will vary much slower than $\frac{\partial P'_{12}}{\partial t}$. So we can take a time scale ϵ, during which $f(t) = \frac{\partial P_{12}^{(o)}}{\partial t}$ stays constant and $\frac{\partial P'_{12}}{\partial t}$ changes with t. We denote $y = P'_{12}$, equation (A.4) in the time interval $[N\epsilon, (N+1)\epsilon]$ becomes a simple form:

$$\begin{aligned}f(N\epsilon) + y' &= i\Delta y, \\ y(t_0) &= y(N\epsilon).\end{aligned} \tag{A.8}$$

The analytic solution of this differential equation is:

$$y(t) = \frac{f(N\epsilon)}{i\Delta}(1 - e^{i\Delta t}) + y(N\epsilon)e^{i\Delta t}, \qquad (t \in [0, \epsilon]) \tag{A.9}$$

$y(N\epsilon)$ can be expressed by the solution of the previous interval:

$$y(N\epsilon) = \frac{f((N-1)\epsilon)}{i\Delta}(1 - e^{i\Delta\epsilon}) + y((N-1)\epsilon)e^{i\Delta\epsilon}; \tag{A.10}$$

put $y(N\epsilon)$ into $y(t)$, tidy things up and we get:

$$y(t) = \frac{f(N\epsilon)}{i\Delta}(1 - e^{i\Delta t}) + \frac{f((N-1)\epsilon)}{i\Delta}e^{i\Delta t}(1 - e^{i\Delta\epsilon}) + y((N-1)\epsilon)e^{i\Delta(\epsilon+t)}. \tag{A.11}$$

We repeat this multiple times until we reach $y(0) = 0$:

$$y(t) = \frac{f(N\epsilon)}{i\Delta}(1-e^{i\Delta t}) + \sum_{j=1}^{N} \frac{f((N-j)\epsilon)}{i\Delta}e^{i\Delta((j-1)\epsilon+t)}(1-e^{i\Delta\epsilon}) + y(0)e^{i\Delta(N\epsilon+t)}. \tag{A.12}$$

We then make $\epsilon \to 0$ and find:

$$\begin{aligned}y(t) &= \int_{-\infty}^{t} \frac{f(t')}{i\Delta}e^{i\Delta(t-t')}(1 - e^{i\Delta(dt')}) + y(0)e^{i\Delta t}, \\ &= -\int_{-\infty}^{t} f(t')e^{i\Delta(t-t')}dt'.\end{aligned} \tag{A.13}$$

We have already assumed that $f(t)$ varies much slower than $e^{i\Delta t}$. So we can see that this integral cancel with itself for most of the integral interval, except for the last period of $e^{i\Delta t}$. Therefore we can estimate the upper bound of P'_{12}:

$$\mathcal{A} \approx |\int_{-\infty}^{t} f(t')e^{i\Delta(t-t')}dt'| < \frac{2|f(t)|}{\Delta} = \frac{2\sqrt{n}}{\Delta^2}\frac{\partial\Omega_c}{\partial t} \approx \frac{2\sqrt{n}}{\Delta^2}\Omega_c W \tag{A.14}$$

where W is the bandwidth of control pulse Ω_c. $\frac{2\sqrt{n}}{\Delta^2}\Omega_c W$ is then the upper bond of $\mathcal{A}$. In order to fulfill condition A.7, we just need to make this upper bound to be smaller than $|P_{12}^{(o)}|$. We then get:

$$W \ll \Delta \tag{A.15}$$

This is the same requirement as in equation (A.6). This means that there is no extra requirement to neglect fast oscillation term P'_{12}.

Now if we do the same trick for the second equation in A.1. we will arrive at:

$$\mathcal{A} \ll |\frac{\Omega_c B}{\Delta}| \tag{A.16}$$

as the adiabatic condition and we get the upper bound for the magnitude of $|P'_{23}|$:

$$\mathcal{A} < \frac{2}{\Delta^2}|\frac{\partial(\Omega_c B)}{\partial t}| \tag{A.17}$$

Note that both Ω_c and B are time dependent, so put (A.17) into (A.16). we will get:

$$\begin{aligned} \frac{2}{\Delta}|B\frac{\partial\Omega_c}{\partial t} + \Omega_c\frac{\partial B}{\partial t}| \ll |\Omega_c B|, \\ \frac{2}{\Delta}(W + |\frac{\partial B}{\partial t}/B|) \ll 1, \end{aligned} \tag{A.18}$$

Now let's examine the second term $|\frac{\partial B}{\partial t}/B|$. From the initial equations A.1, under the condition (A.15), defining signal Rabi frequency $\Omega_s = \frac{g_s}{\hbar}d_{23}^*\langle A\rangle$, we have:

$$\begin{aligned} \frac{\partial B}{\partial t} &= i\Omega_c(P_{23}^{(o)} + P'_{23}) - \frac{i\Omega_s\Omega_c\sqrt{n}}{\Delta}, \\ \frac{\partial B}{\partial t}/B &= \frac{i\Omega_c^2}{\Delta} + i\Omega_c P'_{23}/B - \frac{i\Omega_s\Omega_c\sqrt{n}}{\Delta B}, \end{aligned} \tag{A.19}$$

We then take the modulus and consider the upper bound of $|P'_{23}|$ in A.17 and that $\partial\Omega_c\partial t \approx \Omega_c W$:

$$\begin{aligned} |\frac{\partial B}{\partial t}/B| < \frac{\Omega_c^2}{\Delta} + \frac{2\Omega_c}{\Delta^2}|\frac{\Omega_c\partial B/\partial t + B\partial\Omega_c/\partial t}{B}| + \frac{\Omega_c\sqrt{n}}{\Delta}|\frac{\Omega_s}{B}|, \\ (1 - \frac{2\Omega_c^2}{\Delta^2})|\frac{\partial B}{\partial t}/B| < \frac{\Omega_c^2}{\Delta} + \frac{2\Omega_c^2 W}{\Delta^2} + \frac{\Omega_c\sqrt{n}}{\Delta}|\frac{\Omega_s}{B}| \end{aligned} \tag{A.20}$$

considering the condition $W \ll \Delta$. We get:

$$|\frac{\partial B}{\partial t}/B| < \frac{\Delta\Omega_c^2}{\Delta^2 - 2\Omega_c^2} + \frac{\Omega_c\Delta\sqrt{n}}{\Delta^2 - 2\Omega_c^2}|\frac{\Omega_s}{B}| \tag{A.21}$$

To satisfy the adiabatic constraint Eq. A.18, we would hope $|\frac{\partial B}{\partial t}/B| \ll \Delta$, meaning both term in Eq. A.21 need to be smaller than Δ. The first term will lead to:

$$3\Omega_c^2 \ll \Delta^2 \tag{A.22}$$

In this case, the second term becomes $\frac{\Omega_c\sqrt{n}}{\Delta^2}|\frac{\Omega_s}{B}| \ll 1$. B is the amplitude density of spin wave, so we could estimate $B^2 \approx A^2/V$, where V is the interaction region area. Considering Ω_s is the Rabi frequency of a single photon with energy $\hbar\omega$, we can come to:

$$\begin{aligned} \frac{\Omega_c}{\Delta}\sqrt{\frac{2nd^2\omega}{\Delta^2\epsilon_0\hbar}} &\ll 1, \\ \frac{\Omega_c}{\Delta}\frac{5.7 * 10^{10} rad \cdot s^{-1}}{\Delta} &\ll 1 \qquad (T \approx 340K) \end{aligned} \tag{A.23}$$

We can now wrap up the adiabatic following conditions for cesium modified ORCA memory (340K):

$$\begin{aligned} W &\ll \Delta, \\ \Omega_c &\ll \Delta, \\ \frac{\Omega_c}{\Delta}\frac{5.7 * 10^{10} rad \cdot s^{-1}}{\Delta} &\ll 1. \end{aligned} \tag{A.24}$$

The first two requirements mean that detuning is large compared with the bandwidth and the Rabi frequency of the drive. The third requirement sets the upper bound for the number density.

Appendix B

Optical Cavity

B.1 Hermite Gaussian beam

Hermite Gaussian (H-G) modes are a set of solutions of Maxwell's equations, which have spatially constrained distribution of electric magnetic field with a fixed direction of propagation. They are usually generated by a (or several) optical cavity with a gain media. The generated optical field is called laser which is widely used in different areas of science and technologies. The general form of a Hermite-Gaussian beam propagating along the z axis with a certain polarisation is:

$$E(\mathbf{r},t) = \frac{A}{\sqrt{1+z^2/z_R^2}} H_m(\sqrt{2}\frac{x}{w}) H_n(\sqrt{2}\frac{y}{w}) e^{i(kz-\omega t)} e^{-\rho^2/w^2} e^{ik\rho^2/2R} e^{-i(n+m+1)\phi} \quad \text{(B.1)}$$

where A is the amplitude, $H_{m/n}$ is the m/nth order Hermite function, $w = w(z)$ is the beam waist at position z. Waist is defined as the distance from the beam center to where the field drops to $1/e$ of the central value.

$$w(z) = w_0 \sqrt{1 + \left(\frac{z}{z_R}\right)^2} \quad \text{(B.2)}$$

$w_0 = w(0)$ is the waist size of the beam. k is the wave vector of the field, ω is the frequency. $\rho = \sqrt{x^2+y^2}$ is the transverse distance to the beam centre. z_R is the Rayleigh range:

$$z_R = \frac{\pi w_0^2}{\lambda}, \quad \text{(B.3)}$$

$R = R(z)$ is the radius of curvature at position z along the propagation axis:

$$R(z) = z\sqrt{1 + \left(\frac{z_R}{z}\right)^2}. \quad \text{(B.4)}$$

$\phi = \phi(z)$ is the Gouy phase which result from the wave momentum change due to geometric convergence:

$$\phi(z) = \tan^{-1}\left(\frac{z}{z_R}\right). \tag{B.5}$$

It is also helpful to note the asymptotic beam divergence angle is:

$$\Theta \approx \frac{\lambda}{\pi w_0}. \tag{B.6}$$

The transverse electromagnetic field of a certain order of the H-G mode with fixed wavelength can be fully characterised by the z position of interest and the Rayleigh range z_R. If we define a q parameter:

$$q = z + iz_R, \tag{B.7}$$

it can be used to specify the field in the H-G beam.

One should be aware that this solution is under paraxial approximation which is valid when the angle between the wave vector k and the optical axis is small.

B.2 Cavity modes and resonance frequency

An optical cavity is a cavity bounded by mirrors. An electromagnetic field is confined in the cavity, forming a stable distribution of it. This distribution is referred to as a "mode". Mathematically, such modes are the eigenfunctions of wave equations with boundary condition of two mirrors.

The most common modes in an optical cavity are the Hermite-Gaussian (H-G) modes. If a certain H-G mode is the eigenmode of the optical cavity electromagnetic field, its q parameter (Eq.B.7) must be unchanged after one round trip of the cavity. This constraint leads to the q parameter on one of the cavity mirror (position defined to be z_1):

$$q(z_1) = \frac{(A-D) \pm \sqrt{(A+D)^2 - 4}}{2C} \tag{B.8}$$

where

$$\begin{aligned} A =& 1 - \frac{2L}{R_2} \\ C =& -\frac{2}{R_1} - \frac{2}{R_2} + \frac{4L}{R_1 R_2} \\ D =& 1 - \frac{2L}{R_2} - \frac{4L}{R_1} + \frac{4L^2}{R_1 R_2}. \end{aligned} \tag{B.9}$$

where L is the cavity length, $R_{1,2}$ is the radius of curvature of the two mirrors.

The fact that $z_R \neq 0$ gives a constraint of stable cavity geometry:

$$0 < g_1 g_2 < 1. \tag{B.10}$$

where

$$g_1 = 1 - \frac{L}{R_1}, \quad g_2 = 1 - \frac{L}{R_2} \tag{B.11}$$

When $R_1 = R_2$, from Eq.B.8 we get the waist size

$$w_0 = \sqrt{\frac{\lambda L}{\pi}}(1 - \frac{L}{2R})^{1/4}. \tag{B.12}$$

Another constraint of having a stable field within the cavity is that the phase change after one round trip should be some integer multiple of 2π. The phase of the field on the axis is:

$$\theta(z) = kz - (n + m + 1)\phi, \tag{B.13}$$

where ϕ is the Gouy phase. We then have constraint of the field frequency:

$$f_{p,m,n} = \frac{c}{2L}\left(p + \frac{n + m + 1}{\pi}\cos^{-1}(\pm\sqrt{g_1 g_2})\right) \tag{B.14}$$

The cavity geometry can usually be cataloged into three types depending of the relation between cavity length L and mirror radius of curvature (ROC) $R_{1,2}$.

(1) Near planar cavity: This is when the mirror ROC is much larger than cavity length. The cavity mode is almost collimated. The frequencies for all orders of H-G mode degenerate and are only specified by p. The frequencies of these modes are separated by free spectrum range (FSR) $\frac{c}{2L}$.

(2) Confocal cavity: This is when the ROC and the cavity length are the same, $g_1 g_2 = 0$. The position of the mirror is Rayleigh range away from the waist. The even and odd orders of H-G modes are separated by half the FSR.

(3) Near concentric cavity: This is when the mirror ROC is close to half of cavity length. The beam waist can be arbitrarily small, the divergence angle is approaching $\pi/2$. Different orders of H-G modes are separated by the FSR. This cavity configuration offers very strong confinement of the field.

The field in a cavity will always leak out by various reasons. It will lead to a non-zero cavity resonance linewidth. The derivation follows the transmission of a Fabry-Perot etalon treatment, which I will not go through here but only highlight the result. The cavity intensity spectrum is:

$$I(\delta) = \frac{1}{1 + \frac{4\mathcal{F}^2}{\pi^2}\sin^2(\delta/2)}, \tag{B.15}$$

where δ is the round trip phase difference from $2\pi N$, where N is a integer. $\mathcal{F}$ is the cavity finesse:

$$\mathcal{F} = \frac{\pi\sqrt{R}}{1-R} \tag{B.16}$$

where R is the reflectivity of each mirror. We can see that the spectrum is a Lorentz function with full width half maximum (FWHM) $\delta_{FWHM} = \frac{2\pi}{\mathcal{F}}$. $\mathcal{F}$ thus has a physical meaning of the ratio between FSR and transmission linewidth.

$$\mathcal{F} = \frac{\text{FSR}}{\text{FWHM}} \tag{B.17}$$

The cavity intensity loss κ is $\kappa = \frac{c}{L}(1-R)$. So the we have the cavity frequency FWHM is:

$$\Delta\nu \approx \frac{\kappa}{2\pi} \tag{B.18}$$

Appendix C

Light-atom interaction

Light matter Hamiltonian can be written in any rotating frame. In Eq.4.25 in the main text, I wrote the Hamiltonian in the rotating frame of the atom transition.

The driving-atom interaction is:

$$H_{da} = -\mathbf{E} \cdot \hat{\mathbf{d}} \tag{C.1}$$

where $\mathbf{E}$ is the electric field of the driving pulse, $\hat{\mathbf{d}}$ is the electron dipole moment operator.

$$\begin{aligned} \mathbf{E} &= \mathbf{v}\frac{E}{2}e^{-i\omega_d t} + c.c. \\ \hat{\mathbf{d}} &= \mathbf{d}\sigma_{eg} + h.c. \end{aligned} \tag{C.2}$$

where $\sigma_{eg} = |e\rangle\langle g|$ is the transition operator which oscillates with positive frequency $e^{i\omega_{eg}t}$. According to the Rotation Wave Approximation (RWA), fast oscillation terms in the Hamiltonian are neglected, so we have the laser-atom interaction Hamiltonian:

$$H_{da} = -\frac{(\mathbf{v} * \mathbf{d})E}{2}\sigma_{eg}e^{-i\omega_d t} - h.c. = -\frac{\hbar\Omega}{2}\sigma_{eg}e^{-i\omega_d t} - h.c. \tag{C.3}$$

where Ω is the Rabi frequency which characterizes the coupling strength between the driving and the atom.

The interaction between the cavity and the atom is very similar with laser-atom interaction. The only difference is the description of the electric field. The single photon electric field in the cavity mode has a spatial distribution of $\mathbf{f}(\mathbf{r})$ which is determined by the cavity geometry. Electric field operator is then:

$$\mathbf{E}(\mathbf{r}, t) = -(\sqrt{\frac{\hbar\omega}{2\epsilon_0}}\mathbf{f}(\mathbf{r})a(t) + h.c.) \tag{C.4}$$

If we define:

$$\hbar g(\mathbf{r}) := \sqrt{\frac{\hbar\omega}{2\epsilon_0}}\mathbf{d} \cdot \mathbf{f}(\mathbf{r}) \tag{C.5}$$

and using the RWA, we have the cavity-atom Hamiltonian:

$$H_{ca} = -\hbar g \sigma_{ge} a^{+}(t) - h.c. \tag{C.6}$$

where we have assumed the atom is stable in the cavity field so that we can keep $g(\mathbf{r})$ to be constant g as a real positive number. Note that the field spatial distribution $\mathbf{f}(\mathbf{r})$ is normalized:

$$\int \mathrm{d}^3 r |\mathbf{f}(\mathbf{r})|^2 = 1 \tag{C.7}$$

We then have $|f(\mathbf{r})| = 1/\sqrt{V}$. V is the volume in which the cavity photon is in if we assume the field is uniform in the cavity. So the g is:

$$g = \mathbf{v} \cdot \mathbf{d} \sqrt{\frac{\omega}{2\epsilon_0 \hbar V}} \tag{C.8}$$

Usually, we are interested in the cavity coupling constant g at the waist of the cavity mode, so $V = \frac{\pi}{4} w_0^2 L$, where w_0 is the waist **radius**, L is the cavity length, $\pi/4$ is a geometric factor. We can have the coupling constant at the waist:

$$g_0 = \mathbf{v} \cdot \mathbf{d} \sqrt{\frac{2\omega}{\pi \epsilon_0 \hbar w_0^2 L}} \tag{C.9}$$

We now have the cavity-atom interaction Hamiltonian:

$$H_{ca} = -\hbar g_0 \sigma_{ge} a^{+} e^{i\omega_c t} - h.c. \tag{C.10}$$

The atom Hamiltonian is:

$$H_{atom} = \Sigma_s \hbar \omega_s \sigma_{ss} \tag{C.11}$$

where s is the index of all relevant atomic levels in the system. The field Hamiltonian is:

$$H_{field} = \Sigma_s \hbar \omega_s (a_s^{+} a_s + \frac{1}{2}) \tag{C.12}$$

where s is the index of all optical modes in the cavity.

In our system, there are three cavity modes $(\sigma^{+}, \pi, \sigma^{-})$ and five atomic levels (excited state, three metastable final states and initial state). However, this can be simplified because given the initial condition to be in the initial state, only a few of the field-atom level combinations are possible. We have discussed about this in the main text in chapter 4.2.3. There are eleven cavity-atom states, five of them are involved in the coherence dynamics: $|1\rangle$ which is the initial state, $|2\rangle$ which is the excited state without cavity photon. $|3\rangle$ generates a σ^{-} photon the cavity, $|5\rangle$

generates a π photon in the cavity, $|7\rangle$ generates a σ^+ photon in the cavity. So the atom and field Hamiltonian is then:

$$H_{af} = \hbar\omega_u\sigma_{11} + \hbar\omega_e\sigma_{22} + \hbar(\omega_0 + \omega_{\sigma^-})\sigma_{33} + \hbar(\omega_1 + \omega_\pi)\sigma_{55} + \hbar(\omega_2 + \omega_{\sigma^+})\sigma_{77} \quad \text{(C.13)}$$

Four of these five states are involved in the cavity-atom interaction: $|2\rangle$, $|3\rangle$, $|5\rangle$ and $|7\rangle$. Two of the five states are involved in the driving-atom interaction: $|1\rangle$ and $|2\rangle$. Following Eq.C.10 and Eq.C.3, we then have the interaction Hamiltonian for our system:

$$H_{int} = (\hbar g_{\sigma^-}\sigma_{32} + \hbar g_\pi\sigma_{52} + \hbar g_{\sigma^+}\sigma_{72} + h.c.) - (\frac{\Omega}{2}\sigma_{21}e^{-i\omega_d t} + h.c.) \quad \text{(C.14)}$$

where $g_{\sigma^+,\pi,\sigma^-}$ is the coupling constant (previously defined as g_0) for each corresponding transition.

The total Hamiltonian is $H = H_{af} + H_{int}$.

It is helpful to express the Hamiltonian in a rotating frame. It adds a fast oscillation term to the coherence between two levels, compensating the intrinsic fast oscillation due to the energy difference between the two levels. Physically, it shifts the energy of the system level by a certain amount. One common way of choosing the rotating frame is in the frame of the field. This means shifting the three initial levels up by $\hbar\omega_d$. We then define the excited state $|2\rangle$ to have 0 energy, then the Hamiltonian is:

$$\begin{aligned} H = &- \hbar\Delta_d\sigma_{11} - \hbar\Delta_{\sigma^-}\sigma_{33} - \hbar\Delta_\pi\sigma_{55} - \hbar\Delta_{\sigma^+}\sigma_{77} \\ &- (\hbar g_{\sigma^-}\sigma_{32} + \hbar g_\pi\sigma_{52} + \hbar g_{\sigma^+}\sigma_{72} + h.c.) \\ &- (\frac{\hbar\Omega}{2}\sigma_{21} + h.c.) \end{aligned} \quad \text{(C.15)}$$

There can be other choices of rotating frame. In the main text, I choose the "cavity-atom transition" rotating frame where I force all system states to have 0 energy. This will introduce oscillations to the transition operator:

$$\begin{aligned} H = &- (\hbar g_{\sigma^-}\sigma_{32}e^{i\Delta_{\sigma^-}t} + \hbar g_\pi\sigma_{52}e^{i\Delta_\pi t} + \hbar g_{\sigma^+}\sigma_{72}e^{i\Delta_{\sigma^+}t} + h.c.) \\ &- (\frac{\hbar\Omega e^{i\Delta_d t}}{2}\sigma_{21} + h.c.) \end{aligned} \quad \text{(C.16)}$$

For bi-chromatic driving, we have:

$$\Omega e^{i\Delta_d t} = \Omega_1 e^{i\Delta_1} + \Omega_2 e^{i\Delta_2} \quad \text{(C.17)}$$

We then come to the system Hamiltonian Eq.4.25 in the main text.

Appendix D

Cavity-induced polarization oscillation

Assume the ion emission's H/V polarised photon is misaligned with the principal axis of the cavity by α. A H/V photon generated into the cavity at time t_0 is rotated as a result. The time evolution of the polarisation states in the cavity bases A_1, A_2 are:

$$\begin{aligned} |H\rangle &\rightarrow \eta_H^1 \cos\alpha |A_1\rangle + \eta_H^2 \sin\alpha e^{i2\pi\Delta\nu t}|A_2\rangle \\ |V\rangle &\rightarrow \eta_V^1 \sin\alpha e^{i2\pi\Delta\nu t}|A_1\rangle - \eta_V^2 \cos\alpha |A_2\rangle \end{aligned} \tag{D.1}$$

where $\eta_{H,V}^{1,2}$ is the coupling efficiency of H, V photon coupled to A_1, A_2 cavity eigenmode. In real life, these coupling efficiencies are not the same because the frequency of H/V photon are detuned from the A_1, A_2 cavity resonance. The worst case is when all the coupling are the same such that the photon has the largest projection on the unwanted principal axis. We consider this situation for conservative result. We assume $\eta_H^1 = \eta_H^2 = \eta_V^1 = \eta_V^2 = 1$.

We now make a model for polarization oscillation in a birefringent cavity. The cavity photon amplitude without birefringence can be written as:

$$f_{H/V}(t) = \int_0^t \Lambda_{H/V}(t_0) e^{-\kappa(t-t_0)} \mathrm{d}t_0 \tag{D.2}$$

where $\kappa = K/2$ is the coherence decay rate, $\Lambda_{H/V}(t_0)$ is a *photon generation function*. It is the probability amplitude of generating a H/V photon at time t_0. This model takes into account the photon-atom coupling since the photon generation function is determined by cavity-atom interaction. Even for the strong coupling regime where an emitted photon can couple back to atom, this model remain valid because the photon generation function $\Lambda_{H/V}(t)$ is a complex function. A negative value of the real part describes the re-absorption of cavity photon by the atom.

For a birefringent cavity, $\Lambda_{H/V}$ is manipulated after time t_0. Here we take H polarised photon as an example and express it in A_1, A_2 basis:

$$\Lambda_H(t_0) \rightarrow \begin{bmatrix} \cos\alpha \\ \sin\alpha e^{i2\pi\Delta\nu(t-t_0)} \end{bmatrix}_{A_1A_2} \Lambda_H(t_0) \tag{D.3}$$

Rotating back to HV basis, we have:

$$\Lambda_H(t,t_0) \rightarrow \begin{bmatrix} \cos^2\alpha + \sin^2\alpha e^{i2\pi\Delta\nu(t-t_0)} \\ -\sin\alpha\sin\alpha + \sin\alpha\sin\alpha e^{i2\pi\Delta\nu(t-t_0)} \end{bmatrix}_{HV} \Lambda_H(t_0) \tag{D.4}$$

substituting Eq.D.4 into Eq.D.2, we get:

$$\begin{aligned} f_H(t) \rightarrow f'_H(t) &= \begin{bmatrix} H_H(t) \\ V_H(t) \end{bmatrix} \\ &= \begin{bmatrix} \cos^2\alpha f_H(t) + \sin^2\alpha \int_0^t \Lambda_H(t_0) e^{i2\pi\Delta\nu(t-t_0)} e^{-\kappa(t-t_0)} \mathrm{d}t_0 \\ -\sin\alpha\cos\alpha f_H(t) + \sin\alpha\cos\alpha \int_0^t \Lambda_H(t_0) e^{i2\pi\Delta\nu(t-t_0)} e^{-\kappa(t-t_0)} \mathrm{d}t_0 \end{bmatrix} \end{aligned} \tag{D.5}$$

A Fourier transform of Eq.D.5:

$$\begin{aligned} \tilde{H}_H(\omega) =& \cos^2\alpha \tilde{f}_H(\omega) + \sin^2\alpha \tilde{\Lambda}_H(\omega)\mathcal{L}^\kappa(\omega - 2\pi\Delta\nu) \\ \tilde{V}_H(\omega) =& -\sin\alpha\cos\alpha \tilde{f}_H(\omega) + \sin\alpha\cos\alpha \tilde{\Lambda}_H(\omega)\mathcal{L}^\kappa(\omega - 2\pi\Delta\nu) \end{aligned} \tag{D.6}$$

where $\mathcal{L}^\kappa(\omega)$ is the Fourier Transform of single sided exponential decay function, which is a non-normalised Lorentz function with line width 2κ:

$$\mathcal{L}^\kappa(\omega) = \frac{1}{\kappa + i\omega} \tag{D.7}$$

We can now calculate the polarization fidelity of the photon.

$$\begin{aligned} \mathcal{F}_H =& \frac{\left| \int_{-\infty}^{\infty} \begin{bmatrix} \tilde{f}_H^*(\omega) & 0 \end{bmatrix} \begin{bmatrix} \tilde{H}_H(\omega) \\ \tilde{V}_H(\omega) \end{bmatrix} \mathrm{d}\omega \right|^2}{\int_{-\infty}^{\infty} |\tilde{f}_H(\omega)|^2 \mathrm{d}\omega \int_{-\infty}^{\infty} (|\tilde{H}_H(\omega)|^2 + |\tilde{V}_H(\omega)|^2) \mathrm{d}\omega} \\ =& \frac{\left| \int_{-\infty}^{\infty} \tilde{f}_H^*(\omega) \tilde{H}_H(\omega) \mathrm{d}\omega \right|^2}{\int_{-\infty}^{\infty} |\tilde{f}_H(\omega)|^2 \mathrm{d}\omega \int_{-\infty}^{\infty} (|\tilde{H}_H(\omega)|^2 + |\tilde{V}_H(\omega)|^2) \mathrm{d}\omega} \\ =& \frac{\left| \cos^2\alpha P_H + \sin^2\alpha \int_{-\infty}^{\infty} |\tilde{\Lambda}_H(\omega)|^2 \mathcal{L}^{\kappa *}(\omega) \mathcal{L}^\kappa(\omega - 2\pi\Delta\nu) \mathrm{d}\omega \right|^2}{P_H(\cos^2\alpha P_H + \sin^2\alpha \int_{-\infty}^{\infty} |\tilde{\Lambda}_H(\omega)|^2 |\mathcal{L}^\kappa(\omega - 2\pi\Delta\nu)|^2 \mathrm{d}\omega)} \end{aligned} \tag{D.8}$$

where $P_H = \int_{-\infty}^{\infty} |\tilde{f}_H(\omega)|^2 \mathrm{d}\omega$ is the probability of generating a H polarised photon in the absence of birefringence. Eq.D.8 is an easy formula to estimate the photon polarisation fidelity with a given birefringence $\Delta\nu$ and an ideal photon temporal

mode $f_{H/V}$. If the polarization misalignment between H/V and A_1, A_2 is random, a conservative estimation is to assume $\alpha = \pi/4$.

We can see from Eq.D.8 that the fidelity is dependent on the photon temporal modes. Our goal now is to give some reasonable examples of temporal modes to estimate the photon polarisation fidelity. The fidelity is determined by the mode square of the spectrum of the photon generation function $|\Lambda(\omega)|^2$. We can get a lot of information by analyzing how each single frequency in the spectrum is contributing to the fidelity. To do this, we explore $|\Lambda(\omega)|^2$ begin a Dirac Delta function with different frequency shift ω': $|\Lambda(\omega)|^2 = A\delta(\omega - \omega')$. It should be pointed out before we move on that this doesn't give the whole story of any spectrum $|\Lambda(\omega)|^2$ because the dependence of fidelity to it is not linear. When the spectrum is spread across a wide range of frequency, there might be cross-talk effects, leading to local extrema:

$$\begin{aligned} &\mathcal{F}_H(\frac{|\Lambda(\omega)|_1^2 + |\Lambda(\omega)|_2^2}{M}) > \max\{\mathcal{F}_H(|\Lambda(\omega)|_1^2), \mathcal{F}_H(|\Lambda(\omega)|_2^2)\} \\ &\qquad\qquad \text{or} \\ &\mathcal{F}_H(\frac{|\Lambda(\omega)|_1^2 + |\Lambda(\omega)|_2^2}{M}) < \min\{\mathcal{F}_H(|\Lambda(\omega)|_1^2), \mathcal{F}_H(|\Lambda(\omega)|_2^2)\} \end{aligned} \tag{D.9}$$

However, in real experiments, for Raman transition scheme, the spectrum width is usually much smaller than κ. So the photon generation function $|\Lambda(\omega)|^2$ is not too far from a Dirac Delta function. So a study of Dirac Delta spectrum can give a general estimation of the ion entanglement fidelity.

With $|\Lambda(\omega)|^2 = A\delta(\omega - \omega')$, we calculate the coefficient:

$$A = P_H(\kappa^2 + \omega'^2) \tag{D.10}$$

by the probability constraint:

$$\int |\Lambda(\omega)|^2 |\mathcal{L}^\kappa(\omega)|^2 = P_H \tag{D.11}$$

We can then get photon polarisation fidelity spectrum:

$$\begin{aligned} \mathcal{F}_H(\omega') =& \frac{|\cos^2\alpha + \sin^2\alpha \frac{\kappa + i\omega'}{\kappa + i(\omega' - \Delta_\omega)}|^2}{\cos^2\alpha + \sin^2\alpha \frac{\kappa^2 + \omega'^2}{\kappa^2 + (\omega' - \Delta_\omega)^2}} \\ =& \frac{\frac{4\cos^4\alpha}{m^2} + 1 - 2\frac{2\cos^2\alpha}{m}\frac{\omega'}{\kappa} + (\frac{\omega'}{\kappa})^2}{1 + \frac{2\cos^2\alpha}{m}(\frac{2}{m} - 2\frac{\omega'}{\kappa}) + (\frac{\omega'}{\kappa})^2} \end{aligned} \tag{D.12}$$

where $\Delta_\omega = 2\pi\Delta\nu$ and

$$m := \frac{2\kappa}{\Delta_\omega} = \frac{2k\kappa}{V_{\text{FSR}} 2\Delta_\xi} = \frac{2\pi k}{finesse \Delta_\xi} \tag{D.13}$$

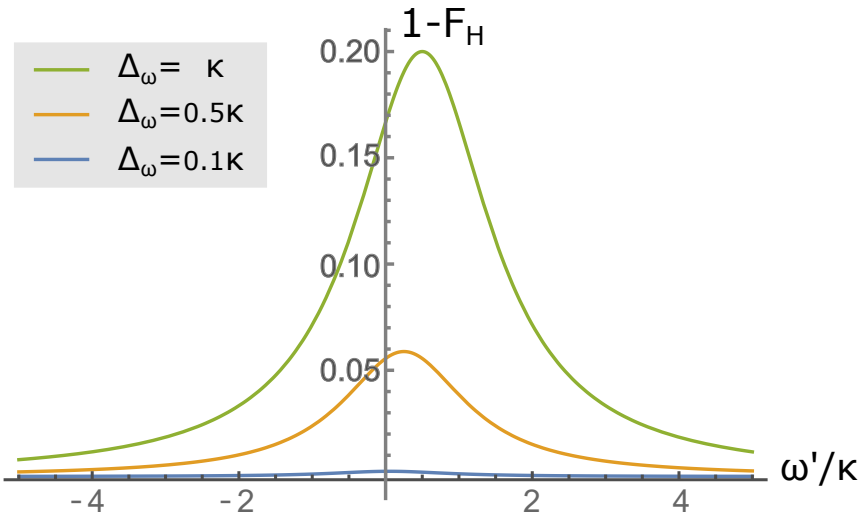

Figure D.1: Photon polarisation infidelity spectrum. Infidelity is plotted as function of the photon generation function frequency ω' scaled by cavity coherence loss rate κ. The angle of axis misalignment is $\alpha = \pi/4$ for conservative estimation.

where Δ_ξ is defined as half of the random curvature difference between the two mirror principal axes:

$$\Delta_\xi = \frac{1}{2}\left|\frac{1}{R_1} - \frac{1}{R_2}\right| \tag{D.14}$$

If we take the conservative axis alignment $\alpha = \pi/4$, we get the frequency response of the photon polarisation fidelity $\mathcal{F}_H(\omega')$ in Fig.D.1.

We can see that the fidelity can get better or worse if we tune the photon frequency away from resonance. One can get fidelity infinitely close to 1 by far-detuning the frequency, however in experiment this would be a huge hit on entanglement generation rate. If we don't impose any photon frequency shift ($\omega' = 0$), with $\alpha = \pi/4$, we get a simple fidelity dependence on birefringence:

$$\mathcal{F}_H(\omega' = 0) = 1 - \frac{1}{2 + m^2} \tag{D.15}$$

It is easy to prove that $\mathcal{F}_H(\omega')$ is minimised when

$$\omega' = \cos^2\alpha\Delta_\omega \tag{D.16}$$

with $\alpha = \pi/4$, the minimum of the photon polarisation fidelity with single-frequency photon generation function is then::

$$\mathcal{F}_H^{\min} = 1 - \frac{1}{1 + m^2} \tag{D.17}$$

We now try to see how polarisation oscillation affects ion-ion entanglement fidelity. To give an example, we consider birefringence on only one of the two sites. The

entanglement scheme we use is introduced in the main text in Chapter 4.1.1. For the case when two detectors (one for H, one for V) on the same port of the beamsplitter click at time t_H and t_V respectively, the ion-ion state is projected to a non-separable state [71]:

$$|\Psi'\rangle = (f_H(t_H)V_H(t_V)|00\rangle + f_H(t_H)V_V(t_V)|01\rangle + f_V(t_V)H_H(t_H)|10\rangle + f_V(t_V)H_V(t_H)|11\rangle) \tag{D.18}$$

The notation here is different from the notation in reference [71]. To clarify, here I recap the definition of the waveform functions:

$f_{H/V}$ is the waveform without birefringence for H/V polarised photon,

H_H, V_H is the waveform of H/V polarised photon originated from H polarised photon in the case of birefringence,

H_V, V_V is the waveform of H/V polarised photon originated from V polarised photon in the case of birefringence.

The fidelity of the ion-ion state is:

$$\begin{aligned}\mathcal{F}_{\text{ion}} =& \int\int \frac{|\langle\Psi^+|\Psi'\rangle|^2}{\langle\Psi'|\Psi'\rangle} \frac{\langle\Psi'|\Psi'\rangle}{\int\int\langle\Psi'|\Psi'\rangle \mathrm{d}t'_H \mathrm{d}t'_V} \mathrm{d}t_H \mathrm{d}t_V \\ =& \frac{\int\int |\langle\Psi^+|\Psi'\rangle|^2 \mathrm{d}t_H \mathrm{d}t_V}{\int\int\langle\Psi'|\Psi'\rangle \mathrm{d}t_H \mathrm{d}t_V}\end{aligned} \tag{D.19}$$

where $|\Psi^+\rangle = (|01\rangle + |10\rangle)/\sqrt{2}$ is the desired Bell state. Note that $|\psi'\rangle$ is not normalised.

Using Eq.D.18, we get ion entanglement fidelity:

$$\begin{aligned}\mathcal{F}_{\text{ion}} =& \frac{1}{2\int\int\langle\Psi'|\Psi'\rangle \mathrm{d}t_H \mathrm{d}t_V} \int\int |f_H(t_H)V_V(t_V) + f_V(t_V)H_H(t_H)|^2 \mathrm{d}t_H \mathrm{d}t_V \\ =& \frac{1}{2\int\int\langle\Psi'|\Psi'\rangle \mathrm{d}t_H \mathrm{d}t_V} [\int |f_H(t_H)|^2 \mathrm{d}t_H \int |V_V(t_V)|^2 \mathrm{d}t_V \\ &+ \int |f_V(t_V)|^2 \mathrm{d}t_V \int |H_H(t_H)|^2 \mathrm{d}t_H \\ &+ 2\mathrm{Re}[\int f_H(t_H) H_H^*(t_H) \mathrm{d}t_H \int f_V^*(t_V) V_V(t_V) \mathrm{d}t_V]] \\ =& \frac{1}{2\int\int\langle\Psi'|\Psi'\rangle \mathrm{d}t_H \mathrm{d}t_V} [P_H P_{V\to V} + P_V P_{H\to H} \\ &+ 2\mathrm{Re}[\int f_H(t_H) H_H^*(t_H) \mathrm{d}t_H \int f_V^*(t_V) V_V(t_V) \mathrm{d}t_V]]\end{aligned} \tag{D.20}$$

where $P_{H/V}$ has been defined as the probability of generating a H/V polarised photon without birefringence, $P_{H/V\to H/V}$ is the probability of an originally H/V polarised

photon remaining H/V polarisation. $P_{H/V\to V/H}$ is the probability of an originally H/V polarised photon rotate to V/H polarisation. They are:

$$\begin{aligned} P_{H/V} &= \int |f_{H/V}(t_{H/V})|^2 \mathrm{d}t_{H/V} \\ P_{H\to H} &= \int |H_H(t_H)|^2 \mathrm{d}t_H \\ P_{V\to V} &= \int |V_V(t_V)|^2 \mathrm{d}t_V \\ P_{V\to H} &= \int |H_V(t_H)|^2 \mathrm{d}t_H \\ P_{H\to V} &= \int |V_H(t_V)|^2 \mathrm{d}t_V \end{aligned} \tag{D.21}$$

To further simplify the formula, We only consider the most conservative misalignment angle $\alpha = \pi/4$ and assume symmetric dynamics between H photon and V photon. We then get equality:

$$f_H = f_V, \;\; H_H = V_V, \;\; H_V = -V_H. \tag{D.22}$$

With this assumption. we get:

$$\begin{aligned} \int\int \langle \Psi' | \Psi' \rangle \mathrm{d}t_H \mathrm{d}t_V =& 2P_H(P_{H\to V} + P_{H\to H}) \\ \int f_H(t_H) H_H^*(t_H) \mathrm{d}t_H \int f_V^*(t_V) V_V(t_V) \mathrm{d}t_V =& |\int f_H(t_H) H_H^*(t_H) \mathrm{d}t_H|^2 \end{aligned} \tag{D.23}$$

Another equality we use to simplify Eq.D.20 comes from the definition ofthr photon polarisation fidelity Eq.D.8. We have:

$$|\int f_H(t_H) H_H^*(t_H) \mathrm{d}t_H|^2 = \mathcal{F}_H P_H (P_{H\to V} + P_{H\to H}) \tag{D.24}$$

With Eq.D.22, Eq.D.23 and Eq.D.24. The ion-ion entanglement fidelity can be simplified as:

$$\begin{aligned} \mathcal{F}_{\text{ion}} =& \frac{1}{2}\left(\frac{P_{H\to H}}{P_{H\to H} + P_{H\to V}} + \mathcal{F}_H\right) \\ =& \mathcal{F}_H|_{\alpha=\pi/4} \end{aligned} \tag{D.25}$$

We have shown that mirror ellipticity can be a problem for photon polarisation fidelity and ion entanglement fidelity. There are different ways to tackle this problem:

(1). The most straight forward way to tackle this problem is to align the cavity principal axis along with the ion polarisation direction. Since the principal axis is random due to fabrication error, one will have to actively rotate the each cavity mirror

for alignment. This requires a complicated well-controlled mechanical system for the cavity mirrors. This is very challenging and one would need to do it for every mirror in a large scale quantum network system. Furthermore, this might not be an option for a monolithic system where the cavity mirror orientation is predetermined before mirror fabrication.

(2). If alignment is not an option, one can improve the ion entanglement fidelity by carefully characterising the polarization oscillation of each site and implementing a local operation on the ion-ion system after heralding detections [71]. However, this approach can not fully recover the entanglement and the operations are very sensitive to heralding time. Its dependence on the random fabrication error on each different site makes it difficult to scale.

(3). As we can see from Fig.D.1, the fidelity can be increased by driving the photon off resonance to the cavity. This is relatively easy to implement in experiment but it will decrease the generation rate. This approach cannot fully recover the fidelity either because of the photon generation function will never be a true Dirac Delta function.

(4). There could also be another approach of introducing a deliberate ellipticity during mirror fabrication to tackle this problem. The idea is that since it is actively introduced, the principal axis is well defined and if the deliberate ellipticity is much larger than random ellipticity, the principal axis' direction is robust against random fabrication error. However, with a large birefringence, the energy splitting is also increased. It isn't obvious which dynamic will be dominant. We now calculate how ion entanglement fidelity is dependent on deliberate ellipticity.

Assuming a random ellipticity $Z' = \Delta_\xi X'^2$ is added on a designed elliptical mirror. At the centre of the mirror, the mirror profile can be described by the elliptic formula $Z = \xi_1 X^2 + \xi_2 Y^2$, where we define X and Y are the axis and X' is along the random axis rotated with angle δ from X. Δ_ξ should be much smaller than ξ_1 and ξ_2. From definition, we can easily see that $\xi_{1,2}$ is half of the curvature along X or Y axis:

$$\xi_1 = \frac{1}{2R_X}, \;\; \xi_1 = \frac{1}{2R_Y}. \tag{D.26}$$

Rewriting them in cylindrical coordinate $Z = Z(r, \theta)$, we have:

$$\begin{aligned} Z &= r^2(\xi_1 \cos^2\theta + \xi_2 \sin^2\theta) \\ Z' &= r^2 \Delta_\xi \cos^2(\theta + \delta). \end{aligned} \tag{D.27}$$

We want to describe $Z + Z'$ in a elliptic formula with new axis which is deviated from X and Y by angle δ:

$$Z + Z' = r^2[A\cos^2(\theta + \alpha) + B\sin^2(\theta + \alpha)] \tag{D.28}$$

Eq.D.27 and Eq.D.28 give the equations for the new ellipse.

$$\begin{aligned} A\cos^2\alpha + B\sin^2\alpha =& \xi_1 + \Delta_\xi \cos^2\delta \\ A\sin^2\alpha + B\cos^2\alpha =& \xi_2 + \Delta_\xi \sin^2\delta \\ (A-B)\sin\alpha\cos\alpha =& \Delta_\xi \cos\delta\sin\delta \end{aligned} \tag{D.29}$$

To make a conservative conclusion, we take the mismatch between X and X' to be the largest, hence assuming $\delta = \pi/4$. The controlled ellipticity should be compared with the random ellipticity, so we define:

$$s = \frac{|\xi_2 - \xi_1|}{\Delta_\xi} \tag{D.30}$$

. We then get the solution for the new principal axis deviation:

$$\cos^2\alpha = \frac{1}{2}(1 + \sqrt{1 - \frac{1}{1+s^2}}) \tag{D.31}$$

A deliberate ellipticity will increase the birefringence splitting from m to m':

$$\begin{aligned} m' :=& \frac{2\kappa}{\Delta'_\omega} \\ =& (2\kappa) / \left(\frac{\nu_{\mathrm{FSR}}}{k} \frac{R_1 - R_2}{R_1 R_2} \right) \\ =& (2\kappa) / \left(\frac{2\nu_{\mathrm{FSR}}}{k} (A - B) \right) \\ =& (2\kappa) / \left(\frac{2\nu_{\mathrm{FSR}}}{k} \frac{\Delta_\xi \cos\delta\sin\delta}{\cos\alpha\sin\alpha} \right) \\ =& 2m\cos\alpha\sin\alpha \end{aligned} \tag{D.32}$$

where we have used $\delta = \pi/4$ and equality "$(A-B)\cos\alpha\sin\alpha = \Delta_\xi\cos\delta\sin\delta$" from Eq.D.29. Using Eq.D.32, and Eq.D.12, we rewrite ion entanglement fidelity Eq.D.25 as a function of photon generation function frequency ω' and axis misalignment angle α:

$$\begin{aligned} \mathcal{F}_{\mathrm{ion}}(\omega', \alpha) =& \frac{\frac{\cos^2\alpha}{m^2\sin^2\alpha} + 1 - 2\frac{\cos\alpha}{m\sin\alpha}\frac{\omega'}{\kappa} + (\frac{\omega'}{\kappa})^2}{1 + \frac{\cos\alpha}{m\sin\alpha}(\frac{1}{m\cos\alpha\sin\alpha} - 2\frac{\omega'}{\kappa}) + (\frac{\omega'}{\kappa})^2} \\ =& \frac{\frac{4\cos^4(\pi/4)}{m^2} + 1 - 2\frac{2\cos^2(\pi/4)}{m}\frac{\omega'-\delta\omega'}{\kappa} + (\frac{\omega'-\delta\omega'}{\kappa})^2}{1 + \frac{2\cos^2(\pi/4)}{m}(\frac{2}{m} - 2\frac{\omega'-\delta\omega'}{\kappa}) + (\frac{\omega'-\delta\omega'}{\kappa})^2} \\ =& \mathcal{F}_{\mathrm{ion}}(\omega' - \delta\omega', \alpha = \pi/4) \end{aligned} \tag{D.33}$$

where:

$$\delta\omega' = \frac{1}{m}(\frac{\cos\alpha}{\sin\alpha} - 1) \tag{D.34}$$

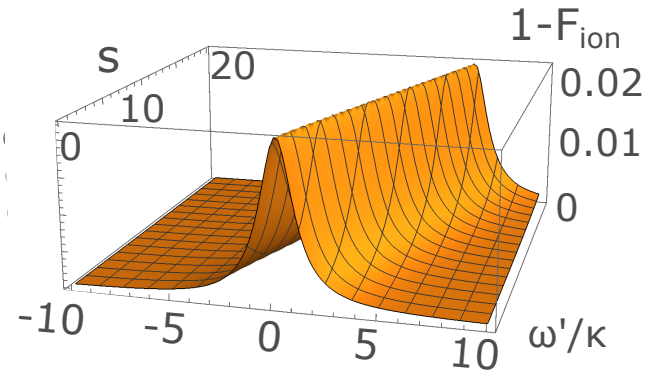

Figure D.2: Ion entanglement fidelity spectrum with deliberate birefringence. This is Eq.D.33 with an example of $m = 3$. The ion entanglement fidelity spectrum is just a shift when increasing deliberate birefringence.

However, one should be aware that Eq.D.33 is not strictly valid because $F_{\text{ion}} = F_H$ is only strictly valid when $\alpha = \pi/4$. We also assume that the output field H and V are automatically tuned to the frequency shifts due to deliberate birefringence, and that they share the same spectrum variable $\omega'_H = -\omega'_V = \omega'$. In Appendix E, we give a full description removing all the estimations and assumptions. We show that Eq.D.33 is a good estimation when $m > 1$ (small stray ellipticity) and $s > 1$ (large deliberate birefringence).

Eq.D.33 shows that a deliberate ellipticity s does is nothing more than just shift the ion entanglement fidelity spectrum by $\delta\omega'$. Fig.D.2 shows an example with $m = 3$.

So the minimum of the fidelity spectrum cannot be improved by introducing deliberate ellipticity. However, since the position of the minimum is shifted, for any certain photon temporal mode, deliberate ellipticity will change the ion entanglement fidelity. Particularly, for a photon generation function constraint narrowly around 0, the ion entanglement fidelity becomes:

$$\mathcal{F}_{\text{ion}}(\omega' = 0, s) = 1 - \frac{s - \sqrt{1+s^2}}{m^2 s - \sqrt{1+s^2}(2+m^2)} \tag{D.35}$$

Recall from Eq.D.13 that m is a solely mirror fabrication parameter, same as s in Eq.D.30. Fig.D.3 (a) shows the infidelity in Log scale. Fig.D.3 (a) is the cross section with some proposed ion entanglement fidelity. Usually, one would want to build a cavity with low loss to increase the cooperativity. This will lead to a small m. We can see that one can achieve fidelity $> 99.9\%$ by $s > 20$ even with very small m. In fact,

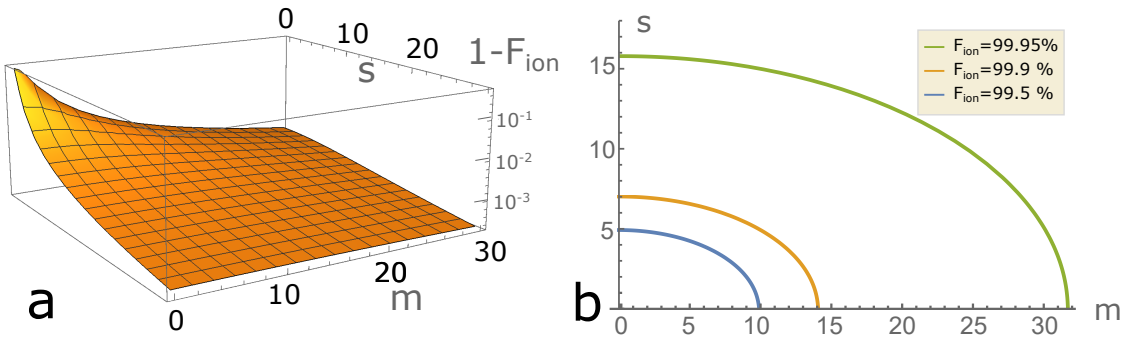

Figure D.3: Infidelity with deliberate ellipticity.

there is a critical s for every proposed fidelity $\mathcal{F}_{\text{ion}}$ when m can be arbitrary small:

$$S = \frac{2\mathcal{F}_{\text{ion}} - 1}{2\sqrt{\mathcal{F}_{\text{ion}}(1 - \mathcal{F}_{\text{ion}})}} \tag{D.36}$$

It is important to notice the validity of this formula. When s gets large, the splitting between the detunings of the two Raman paths (H and V) gets large too, which changes the dynamics of photon generation thus changing the photon generation function $\Lambda_H(t)$ in Eq.D.4. This will result in a deviation of fidelity calculation of any arbitrary photon shape.

Appendix E

Deliberate birefringence

In appendix D, I give a simple estimation of the ion entanglement fidelity with deliberate birefringence. There are several approximations and assumptions involved. Here I will present a full description of the theory and compare it with the formality in the main text.

Following Eq.D.20, we have:

$$\begin{aligned}\mathcal{F}_{\text{ion}} =& \frac{1}{2\int\int\langle\Psi'|\Psi'\rangle \mathrm{d}t_H \mathrm{d}t_V}[P_H P_{V\to V} + P_V P_{H\to H} \\ &+ 2\mathrm{Re}[\int f_H(t_H) H_H^*(t_H)\mathrm{d}t_H \int f_V^*(t_V) V_V(t_V)\mathrm{d}t_V]]\end{aligned} \tag{E.1}$$

The preset H/V photon frequency is $\omega_{H/V}$, the resonance frequencies of the two cavity principal axis are ω_{A1} and ω_{A2}. To get the spectrum, we make photon generation functions to be delta functions normalised to photon extraction probability $P_{H/V}$ with the spectrum variables $\omega'_{H/V}$:

$$|\Lambda_H|^2 = P_H(\kappa^2 + \omega_H'^2)\delta(\omega - \omega_H - \omega'_H);\ \ |\Lambda_V|^2 = P_V(\kappa^2 + \omega_V'^2)\delta(\omega - \omega_V - \omega'_V) \tag{E.2}$$

We now calculate several probabilities that will be used to calculate ion entanglement

fidelity.

$$
\begin{aligned}
P_{H\to H} =& P_H(\kappa^2+\omega_H'^2)\Bigg(\frac{\cos^4\alpha}{\kappa^2+(\omega_H+\omega_H'-\omega_{A1})^2}+\frac{\sin^4\alpha}{\kappa^2+(\omega_H+\omega_H'-\omega_{A2})^2}\\
&+\mathrm{Re}\left[\frac{2\cos^2\alpha\sin^2\alpha}{(\kappa+i(\omega_H+\omega_H'-\omega_{A1}))(\kappa+i(\omega_H+\omega_H'-\omega_{A2}))}\right]\Bigg)\\
P_{V\to V} =& P_V(\kappa^2+\omega_V'^2)\Bigg(\frac{\cos^4\alpha}{\kappa^2+(\omega_V+\omega_V'-\omega_{A2})^2}+\frac{\sin^4\alpha}{\kappa^2+(\omega_V+\omega_V'-\omega_{A1})^2}\\
&+\mathrm{Re}\left[\frac{2\cos^2\alpha\sin^2\alpha}{(\kappa+i(\omega_V+\omega_V'-\omega_{A2}))(\kappa+i(\omega_V+\omega_V'-\omega_{A1}))}\right]\Bigg)\\
P_{V\to V}+P_{V\to H} =& P_V(\kappa^2+\omega_V'^2)\left(\frac{\cos^2\alpha}{\kappa^2+(\omega_V+\omega_V'-\omega_{A2})^2}+\frac{\sin^2\alpha}{\kappa^2+(\omega_V+\omega_V'-\omega_{A1})^2}\right)\\
P_{H\to H}+P_{H\to V} =& P_H(\kappa^2+\omega_H'^2)\left(\frac{\cos^2\alpha}{\kappa^2+(\omega_H+\omega_H'-\omega_{A1})^2}+\frac{\sin^2\alpha}{\kappa^2+(\omega_H+\omega_H'-\omega_{A2})^2}\right)\\
\langle f_V|V_V\rangle =& P_V(\kappa+i\omega_V')\left(\frac{\cos^2\alpha}{\kappa+i(\omega_V+\omega_V'-\omega_{A2})}+\frac{\sin^2\alpha}{\kappa+i(\omega_V+\omega_V'-\omega_{A1})}\right)\\
\langle H_H|f_H\rangle =& P_H(\kappa+i\omega_H')\left(\frac{\cos^2\alpha}{\kappa+i(\omega_H+\omega_H'-\omega_{A1})}+\frac{\sin^2\alpha}{\kappa+i(\omega_H+\omega_H'-\omega_{A2})}\right)
\end{aligned}
$$

If we assume symmetric dynamics between H and V dynamics, we have $P_H = P_V$. The ion entanglement fidelity in Eq.E.1 is then:

$$
\begin{aligned}
\mathcal{F}_{\text{ion}} =& \frac{P_HP_{V\to V}+P_VP_{H\to H}+2\mathrm{Re}[\langle H_H|f_H\rangle\langle f_V|V_V\rangle]}{2(P_H(P_{H\to V}+P_{V\to V})+P_V(P_{V\to H}+P_{H\to H}))}\\
=& \frac{P_{V\to V}+P_{H\to H}+2\mathrm{Re}[\langle H_H|f_H\rangle\langle f_V|V_V\rangle]/P_H}{2(P_{H\to V}+P_{V\to V}+P_{V\to H}+P_{H\to H})}
\end{aligned}
$$

The variables fulfill:

$$
\omega_H=\omega_V+2\frac{s}{m};\ \ \omega_{A1}=\omega_{A2}+\frac{1}{m\cos\alpha\sin\alpha} \tag{E.3}
$$

where m characterizing the random birefringence is defined in Eq.D.13 and s characterizing the deliberate birefringence is defined in Eq.D.30. Since the absolute frequency doesn't matter, we can set $\omega_V=\omega_{A2}=0$. Recall that:

$$
\cos^2\alpha=\frac{1}{2}\left(1+\sqrt{1-\frac{1}{1+s^2}}\right) \tag{E.4}
$$

We then have:

$$
\mathcal{F}_{\text{ion}}=\mathcal{F}_{\text{ion}}(\omega_H',\omega_V',s,m) \tag{E.5}
$$

In order to compare it with the estimation Eq.D.33, we set $\omega_H'=-\omega_V'=\omega'$. Fig.(E.1) shows the infidelity of the full model. From figure (a) we can see that with $m>1$,

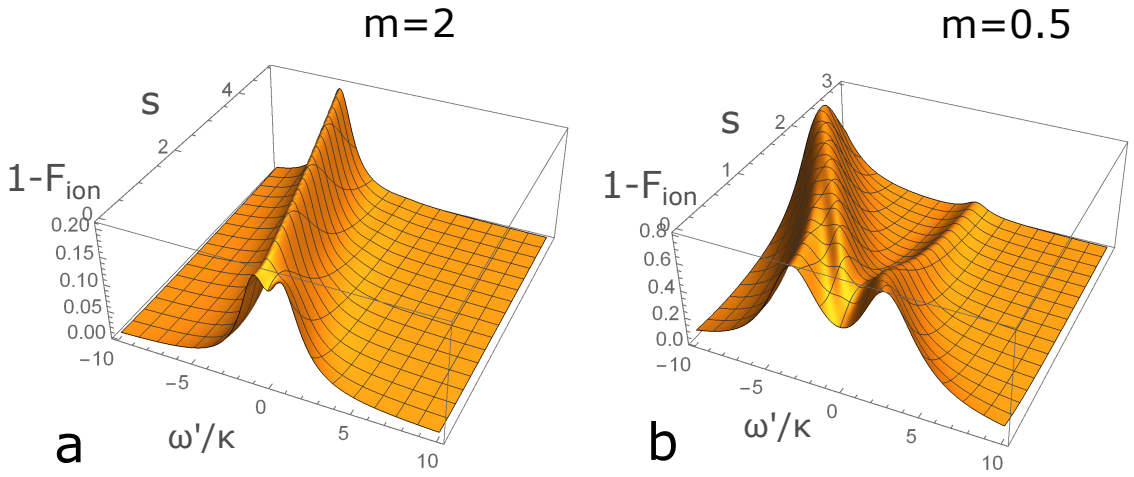

Figure E.1: Infidelity with full deliberate birefringence model.

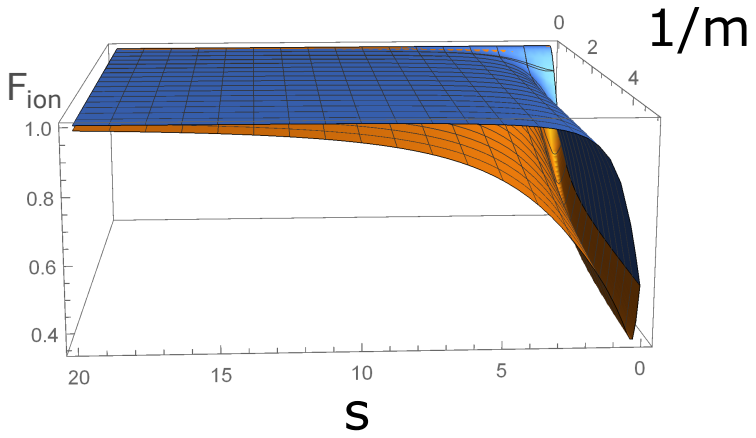

Figure E.2: Comparison with full model, orange surface is the full model while the blue surface is the simple model in the main text.

the approximate model is valid when $s > 1$; from figure (b) we can see that with $m < 1$, the approximate model is not valid any more.

To compare the result with the simple model in Eq.D.35, we make $\omega' = 0$ in Eq.E.5. Fig.E.2 shows the validity of the model Eq.D.35. We can see that the two models converge with large deliberate ellipticity and small stray birefringence.

Appendix F

Optimal driving

I will just briefly introduce the method here:

The ion-cavity state is described as a pure state:

$$|\phi\rangle = \alpha_u|u\rangle + \alpha_e|e\rangle + \alpha_0|0\rangle + \alpha_1|1\rangle + \alpha_2|2\rangle \tag{F.1}$$

where $|u\rangle$ is the initial system state, $|e\rangle$ is the excited atom state with no photon, $|0,1,2\rangle$ are the three storage states with the corresponding cavity photon. If we take all spontaneous decay as a system loss, meaning instead of the atom going back from excited state to the initial state, it decays into other irrelevant levels, the storage levels evolution is:

$$\begin{aligned}
\partial_t\alpha_0 &= -(\kappa + i\delta_0)\alpha_0 - g_H\alpha_e \\
\partial_t\alpha_1 &= -(\kappa + i\delta_1)\alpha_1 - g_V\alpha_e \\
\partial_t\alpha_2 &= -(\kappa + i\delta_2)\alpha_2 - g_b\alpha_e
\end{aligned} \tag{F.2}$$

where $\delta_{0,1,2}$ is the cavity detuning from transition between storage state $|0,1,2\rangle$ and the intermediate $|e\rangle$. $g_{H,V,b}$ is the cavity coupling constant between $|e\rangle$ and $|0,1,2\rangle$. Since we are only interested in the time evolution between time $t = 0$ and $t = T$, where T is the detection window. we can think of the photon wavefunction as a periodical function with its period $T_b > T$. A Fourier transform of the wavefunction re-express the $\alpha_0, \alpha_1, \alpha_2$ from the time domains to their frequency domains $\{C_n, D_n, E_n\}$, where $n = 0, 1, 2, 3, ...$ The time evolution function Eq. F.2 becomes:

$$\begin{aligned}
D_n &= \frac{g_V}{g_H}\frac{\kappa + i(\omega_n + \delta_0)}{\kappa + i(\omega_n + \delta_1)}C_n \\
E_n &= \frac{g_b}{g_H}\frac{\kappa + i(\omega_n + \delta_0)}{\kappa + i(\omega_n + \delta_2)}C_n \\
\omega_n &= \frac{2\pi n}{T_b}
\end{aligned} \tag{F.3}$$

We can see that the coefficient for storage state $|1,2\rangle$ is directly dependent on the coefficient for storage state $|0\rangle$. So what we need to do now is just to optimise in terms of C_n.

One important step of the method is to express the photon retrieval probabilities in the form of expectation values.

$$\begin{aligned} P_{RH} =& 2\kappa \int_0^T \alpha_0^*(t)\alpha_0(t)\mathrm{d}t \\ =& \sum_{n.n'} C_{n'}^*(2\kappa I_{n,n'})C_n := \langle\alpha_0|\hat{P}_{RH}|\alpha_0\rangle \end{aligned} \tag{F.4}$$

where $|\alpha_0\rangle$ is not normalised and:

$$I_{n,n'} = \int_0^T e^{i(\omega_n-\omega_{n'})t}\mathrm{d}t \tag{F.5}$$

For probability of V polarized photon retrieval, we get:

$$\begin{aligned} P_{RV} =& 2\kappa \int_0^T \alpha_1^*(t)\alpha_1(t)\mathrm{d}t \\ =& \sum_{n.n'} D_{n'}^*(2\kappa I_{n,n'})D_n \end{aligned} \tag{F.6}$$

Consider the transformation from $D_n \to C_n$ in Eq.F.3, we can write:

$$P_{RV} := \langle\alpha_0|\hat{P}_{RV}|\alpha_0\rangle \tag{F.7}$$

Same for b photon retrieval:

$$P_{Rb} = 2\kappa \int_0^T \alpha_2^*(t)\alpha_2(t)\mathrm{d}t := \langle\alpha_0|\hat{P}_{Rb}|\alpha_0\rangle \tag{F.8}$$

However, these forms of photon retrieval operator are very general. They are not constrained with particle-number conservation or the initial condition. A normalization and initial condition imposition on the retrieval operator and the state $|\alpha_0\rangle$ will transform $\hat{P}_{RH}, \hat{P}_{RV}, \hat{P}_{Rb}$ to $\hat{\rho}_H, \hat{\rho}_V, \hat{\rho}_b$, and $|\alpha_0\rangle$ to $|\bar{\alpha}_0\rangle$.

To get entanglement generation rate, consider two identical system that emit H, V, b photons with probability ρ_H, ρ_V, ρ_b. The entanglement is heralded when one system emit H or b (since b heralding can be corrected) while the other system emit V. The success probability is given by $P_S = \rho_V(\rho_H + \rho_b)$, which is what we want to maximize.

If we express these probabilities in the form of expectation values:

$$P_S = \langle\bar{\alpha_0}|\hat{\rho}_V|\bar{\alpha_0}\rangle\langle\bar{\alpha_0}|(\hat{\rho}_H + \hat{\rho}_b)|\bar{\alpha_0}\rangle \tag{F.9}$$

What we need to do left is finding the $|\bar{\alpha}_0\rangle$ that maximizes P_S. This is a standard algorithm for this kind of optimization which I would not go into details. With this method we can numerically find the "normalised coefficient" $|\bar{\alpha}_0\rangle$, transforming $|\bar{\alpha}_0\rangle$ back to $|\alpha_0\rangle$ gives us $\{C_n\}$, which is the Fourier coefficient of $\alpha_0(t)$ in Eq.F.2. $\alpha_1(t)$ and $\alpha_2(t)$ is straightforward from relation Eq.F.3.

With this optimal photon mode (described by α_0, α_1 and α_2), we can then use system equations of motion retrace the required driving field, with α_0, α_1 and α_2 being known function, the system equations of motion can be written as:

$$\begin{aligned}
\partial_t\alpha_u =& -i\Delta_u\alpha_u - \frac{\Omega^*}{2}\alpha_e \\
\partial_t\alpha_e =& -\tilde{\gamma}\alpha_e + \frac{\Omega}{2}\alpha_u + g\alpha_{eff} \\
\partial_t\alpha_0 =& -\tilde{\kappa}\alpha_0 - g_H\alpha_e \\
\partial_t\Omega(g_H g\alpha_{eff} + \tilde{\kappa}\tilde{\gamma}\alpha_0 + (\tilde{\kappa}+\tilde{\gamma})\partial_t\alpha_0 + \partial_t^2\alpha_0) =& \\
\Omega(i\Delta_u g_H g\alpha_{eff} + i\Delta_u\tilde{\kappa}\tilde{\gamma}\alpha_0 + g_H\partial_t g\alpha_{eff} + \tilde{\kappa}\tilde{\gamma} + i\Delta_u(\tilde{\kappa}+\tilde{\gamma})\partial_t\alpha_0& \\
+(\tilde{\kappa}+\tilde{\gamma}+i\Delta_u)\partial_t^2\alpha_0 + \partial_t^3\alpha_0) + \frac{|\Omega|^2}{4}\Omega(\frac{\kappa}{2}\alpha_0 + \partial_t\alpha_0)&
\end{aligned}$$

where:

$$\begin{aligned}
g\alpha_{eff} :=& g_H\alpha_0 + g_V\alpha_1 + g_b\alpha_2 \\
\tilde{\gamma} :=& \gamma + i\Delta_e \\
\tilde{\kappa} :=& \kappa + i\delta_0
\end{aligned}$$

We can see that this is a system of non-linear partial differential equations. So one should be very careful about the convergence of the solution.

References

[1] Igor Aharonovich, Dirk Englund, and Milos Toth. Solid-state single-photon emitters. *Nature Photonics*, 10(10):631–641, Oct 2016.

[2] Vahid Ansari, John M. Donohue, Benjamin Brecht, and Christine Silberhorn. Tailoring nonlinear processes for quantum optics with pulsed temporal-mode encodings. *Optica*, 5(5):534–550, May 2018.

[3] Takao Aoki, A. S. Parkins, D. J. Alton, C. A. Regal, Barak Dayan, E. Ostby, K. J. Vahala, and H. J. Kimble. Efficient routing of single photons by one atom and a microtoroidal cavity. *Phys. Rev. Lett.*, 102:083601, Feb 2009.

[4] M. Arcari, I. Söllner, A. Javadi, S. Lindskov Hansen, S. Mahmoodian, J. Liu, H. Thyrrestrup, E. H. Lee, J. D. Song, S. Stobbe, and P. Lodahl. Near-unity coupling efficiency of a quantum emitter to a photonic crystal waveguide. *Phys. Rev. Lett.*, 113:093603, Aug 2014.

[5] Frank Arute, Kunal Arya, Ryan Babbush, et al. Quantum supremacy using a programmable superconducting processor. *Nature*, 574(7779):505–510, Oct 2019.

[6] T. G. Ballance, J. F. Goodwin, B. Nichol, L. J. Stephenson, C. J. Ballance, and D. M. Lucas. A short response time atomic source for trapped ion experiments. *Review of Scientific Instruments*, 89(5):053102, 2018.

[7] Thomas D. Barrett, Oliver Barter, Dustin Stuart, Ben Yuen, and Axel Kuhn. Polarization oscillations in birefringent emitter-cavity systems. *Phys. Rev. Lett.*, 122:083602, Mar 2019.

[8] H G Barros, A Stute, T E Northup, C Russo, P O Schmidt, and R Blatt. Deterministic single-photon source from a single ion. *New Journal of Physics*, 11(10):103004, oct 2009.

[9] Jan Benhelm, Gerhard Kirchmair, Christian F. Roos, and Rainer Blatt. Towards fault-tolerant quantum computing with trapped ions. *Nature Physics*, 4(6):463–466, Jun 2008.

[10] J M Bennett. Recent developments in surface roughness characterization. *Measurement Science and Technology*, 3(12):1119–1127, dec 1992.

[11] J. C. Bergquist, Randall G. Hulet, Wayne M. Itano, and D. J. Wineland. Observation of quantum jumps in a single atom. *Phys. Rev. Lett.*, 57:1699–1702, Oct 1986.

[12] L. Besombes, K. Kheng, L. Marsal, and H. Mariette. Acoustic phonon broadening mechanism in single quantum dot emission. *Phys. Rev. B*, 63:155307, Mar 2001.

[13] R. Bowler, J. Gaebler, Y. Lin, T. R. Tan, D. Hanneke, J. D. Jost, J. P. Home, D. Leibfried, and D. J. Wineland. Coherent diabatic ion transport and separation in a multizone trap array. *Phys. Rev. Lett.*, 109:080502, Aug 2012.

[14] B. Brecht, Dileep V. Reddy, C. Silberhorn, and M. G. Raymer. Photon temporal modes: A complete framework for quantum information science. *Phys. Rev. X*, 5:041017, Oct 2015.

[15] K. R. Brown, A. C. Wilson, Y. Colombe, C. Ospelkaus, A. M. Meier, E. Knill, D. Leibfried, and D. J. Wineland. Single-qubit-gate error below $\mathbf{10^{-4}}$ in a trapped ion. *Phys. Rev. A*, 84:030303, Sep 2011.

[16] Daniel E. Browne and Terry Rudolph. Resource-efficient linear optical quantum computation. *Phys. Rev. Lett.*, 95:010501, Jun 2005.

[17] Christian Brunel, Brahim Lounis, Philippe Tamarat, and Michel Orrit. Triggered source of single photons based on controlled single molecule fluorescence. *Phys. Rev. Lett.*, 83:2722–2725, Oct 1999.

[18] C. Bruzewicz, J. Chiaverini, R. Mcconnell, and J. Sage. Trapped-ion quantum computing: Progress and challenges. *Applied physics reviews*, 6:021314, 2019.

[19] P. I. Bunyk, E. M. Hoskinson, M. W. Johnson, E. Tolkacheva, F. Altomare, A. J. Berkley, R. Harris, J. P. Hilton, T. Lanting, A. J. Przybysz, and J. Whittaker. Architectural considerations in the design of a superconducting quantum

annealing processor. *IEEE Transactions on Applied Superconductivity*, 24(4):1–10, 2014.

[20] Jerry M. Chow, Jay M. Gambetta, A. D. Córcoles, Seth T. Merkel, John A. Smolin, Chad Rigetti, S. Poletto, George A. Keefe, Mary B. Rothwell, J. R. Rozen, Mark B. Ketchen, and M. Steffen. Universal quantum gate set approaching fault-tolerant thresholds with superconducting qubits. *Phys. Rev. Lett.*, 109:060501, Aug 2012.

[21] Andreas Christ and Christine Silberhorn. Limits on the deterministic creation of pure single-photon states using parametric down-conversion. *Phys. Rev. A*, 85:023829, Feb 2012.

[22] J. I. Cirac and P. Zoller. Quantum computations with cold trapped ions. *Phys. Rev. Lett.*, 74:4091–4094, May 1995.

[23] C.J.Foot. *Atomic Physics*. Oxford Master Series in Physics. OUP Oxford, 2005.

[24] Julien Claudon, Joël Bleuse, Nitin Singh Malik, Maela Bazin, Périne Jaffrennou, Niels Gregersen, Christophe Sauvan, Philippe Lalanne, and Jean-Michel Gérard. A highly efficient single-photon source based on a quantum dot in a photonic nanowire. *Nature Photonics*, 4(3):174–177, Mar 2010.

[25] C. Couteau, S. Moehl, F. Tinjod, J. M. Gérard, K. Kheng, H. Mariette, J. A. Gaj, R. Romestain, and J. P. Poizat. Correlated photon emission from a single ii–vi quantum dot. *Applied Physics Letters*, 85(25):6251–6253, 2004.

[26] Christophe Couteau. Spontaneous parametric down-conversion. *Contemporary Physics*, 59(3):291–304, 2018.

[27] Arnab Das and Bikas K. Chakrabarti. Colloquium: Quantum annealing and analog quantum computation. *Rev. Mod. Phys.*, 80:1061–1081, Sep 2008.

[28] Barak Dayan, A. S. Parkins, Takao Aoki, E. P. Ostby, K. J. Vahala, and H. J. Kimble. A photon turnstile dynamically regulated by one atom. *Science*, 319(5866):1062–1065, 2008.

[29] David Deutsch and Richard Jozsa. Rapid solution of problems by quantum computation. *Proc. R. Soc. Lond. A*, 439:553–558, Dec 1992.

[30] A. M. Dibos, M. Raha, C. M. Phenicie, and J. D. Thompson. Atomic source of single photons in the telecom band. *Phys. Rev. Lett.*, 120:243601, Jun 2018.

[31] Xing Ding, Yu He, Z.-C. Duan, Niels Gregersen, M.-C. Chen, S. Unsleber, S. Maier, Christian Schneider, Martin Kamp, Sven Höfling, Chao-Yang Lu, and Jian-Wei Pan. On-demand single photons with high extraction efficiency and near-unity indistinguishability from a resonantly driven quantum dot in a micropillar. *Phys. Rev. Lett.*, 116:020401, Jan 2016.

[32] L.-M. Duan, E. Demler, and M. D. Lukin. Controlling spin exchange interactions of ultracold atoms in optical lattices. *Phys. Rev. Lett.*, 91:090402, Aug 2003.

[33] Andreas Eckstein, Benjamin Brecht, and Christine Silberhorn. A quantum pulse gate based on spectrally engineered sum frequency generation. *Opt. Express*, 19(15):13770–13778, Jul 2011.

[34] M. D. Eisaman, J. Fan, A. Migdall, and S. V. Polyakov. Invited review article: Single-photon sources and detectors. *Review of Scientific Instruments*, 82(7):071101, 2011.

[35] S. Fafard, D. Leonard, J. L. Merz, and P. M. Petroff. Selective excitation of the photoluminescence and the energy levels of ultrasmall ingaas/gaas quantum dots. *Applied Physics Letters*, 65(11):1388–1390, 1994.

[36] J. Fan, A. Migdall, and L. J. Wang. Efficient generation of correlated photon pairs in a microstructure fiber. *Opt. Lett.*, 30(24):3368–3370, Dec 2005.

[37] I. Favero, G. Cassabois, R. Ferreira, D. Darson, C. Voisin, J. Tignon, C. Delalande, G. Bastard, Ph. Roussignol, and J. M. Gérard. Acoustic phonon sidebands in the emission line of single inas/gaas quantum dots. *Phys. Rev. B*, 68:233301, Dec 2003.

[38] Kevin A Fischer, Kai Müller, Konstantinos G Lagoudakis, and Jelena Vučković. Dynamical modeling of pulsed two-photon interference. *New Journal of Physics*, 18(11):113053, nov 2016.

[39] Edward B. Flagg, Sergey V. Polyakov, Tim Thomay, and Glenn S. Solomon. Dynamics of nonclassical light from a single solid-state quantum emitter. *Phys. Rev. Lett.*, 109:163601, Oct 2012.

[40] Nicolai Friis, Oliver Marty, Christine Maier, Cornelius Hempel, Milan Holzäpfel, Petar Jurcevic, Martin B. Plenio, Marcus Huber, Christian Roos, Rainer Blatt, and Ben Lanyon. Observation of entangled states of a fully controlled 20-qubit system. *Phys. Rev. X*, 8:021012, Apr 2018.

[41] Edward S. Fry. Two-photon correlations in atomic transitions. *Phys. Rev. A*, 8:1219–1232, Sep 1973.

[42] D. Gammon, E. S. Snow, B. V. Shanabrook, D. S. Katzer, and D. Park. Homogeneous linewidths in the optical spectrum of a single gallium arsenide quantum dot. *Science*, 273(5271):87–90, 1996.

[43] S. Gao, W. Hughes, D.M. Lucas, T. G. Ballance, and J. F. Goodwin. An optically-heated atomic source for compact ion trap vacuum systems. *in preparation*, 2020.

[44] S. Gao, O. Lazo-Arjona, B. Brecht, K. T. Kaczmarek, S. E. Thomas, J. Nunn, P. M. Ledingham, D. J. Saunders, and I. A. Walmsley. Optimal coherent filtering for single noisy photons. *Phys. Rev. Lett.*, 123:213604, Nov 2019.

[45] Bryan T. Gard, Keith R. Motes, Jonathan P. Olson, Peter P. Rohde, and Jonathan P. Dowling. An introduction to boson-sampling. *From Atomic to Mesoscale*, page 167–192, Jun 2015.

[46] U. Gaubatz, P. Rudecki, M. Becker, S. Schiemann, M. Külz, and K. Bergmann. Population switching between vibrational levels in molecular beams. *Chemical Physics Letters*, 149(5):463 – 468, 1988.

[47] I.M. Georgescu, S. Ashhab, and Franco Nori. Quantum simulation. *Reviews of Modern Physics*, 86(1):153–185, Mar 2014.

[48] Stefan Gerhardt, Jake Iles-Smith, Dara P. S. McCutcheon, Yu-Ming He, Sebastian Unsleber, Simon Betzold, Niels Gregersen, Jesper Mørk, Sven Höfling, and Christian Schneider. Intrinsic and environmental effects on the interference properties of a high-performance quantum dot single-photon source. *Phys. Rev. B*, 97:195432, May 2018.

[49] Craig Gidney and Martin Ekerå. How to factor 2048 bit RSA integers in 8 hours using 20 million noisy qubits. May 2019. arXiv:1905.09749.

[50] Elizabeth A. Goldschmidt, Fabrizio Piacentini, Ivano Ruo Berchera, Sergey V. Polyakov, Silke Peters, Stefan Kück, Giorgio Brida, Ivo P. Degiovanni, Alan Migdall, and Marco Genovese. Mode reconstruction of a light field by multi-photon statistics. *Phys. Rev. A*, 88:013822, Jul 2013.

[51] Hayato Goto, Shota Mizukami, Yuuki Tokunaga, and Takao Aoki. Figure of merit for single-photon generation based on cavity quantum electrodynamics. *Phys. Rev. A*, 99:053843, May 2019.

[52] Daniel Gottesman. Theory of fault-tolerant quantum computation. *Phys. Rev. A*, 57:127–137, Jan 1998.

[53] Daniel Gottesman and Isaac L. Chuang. Demonstrating the viability of universal quantum computation using teleportation and single-qubit operations. *Nature*, 402(6760):390–393, Nov 1999.

[54] Lov K. Grover. A fast quantum mechanical algorithm for database search. *arXiv e-prints*, pages quant–ph/9605043, May 1996.

[55] R. Hanbury Brown and R. Q. Twiss. A test of a new type of stellar interferometer on sirius. *Nature*, 178:1046–1048, 1956.

[56] T. P. Harty, D. T. C. Allcock, C. J. Ballance, L. Guidoni, H. A. Janacek, N. M. Linke, D. N. Stacey, and D. M. Lucas. High-fidelity preparation, gates, memory, and readout of a trapped-ion quantum bit. *Phys. Rev. Lett.*, 113:220501, Nov 2014.

[57] Yu-Ming He, Genevieve Clark, John R. Schaibley, Yu He, Ming-Cheng Chen, Yu-Jia Wei, Xing Ding, Qiang Zhang, Wang Yao, Xiaodong Xu, Chao-Yang Lu, and Jian-Wei Pan. Single quantum emitters in monolayer semiconductors. *Nature Nanotechnology*, 10(6):497–502, Jun 2015.

[58] Yu-Ming He, Yu He, Yu-Jia Wei, Dian Wu, Mete Atatüre, Christian Schneider, Sven Höfling, Martin Kamp, Chao-Yang Lu, and Jian-Wei Pan. On-demand semiconductor single-photon source with near-unity indistinguishability. *Nature Nanotechnology*, 8(3):213–217, Mar 2013.

[59] Mark J. Holmes, Kihyun Choi, Satoshi Kako, Munetaka Arita, and Yasuhiko Arakawa. Room-temperature triggered single photon emission from a iii-nitride site-controlled nanowire quantum dot. *Nano Letters*, 14(2):982–986, Feb 2014.

[60] Christina J. Hood, H. J. Kimble, and Jun Ye. Characterization of high-finesse mirrors: Loss, phase shifts, and mode structure in an optical cavity. *Phys. Rev. A*, 64:033804, Aug 2001.

[61] D. Hucul, I. V. Inlek, G. Vittorini, C. Crocker, S. Debnath, S. M. Clark, and C. Monroe. Modular entanglement of atomic qubits using photons and phonons. *Nature Physics*, 11(1):37–42, Jan 2015.

[62] William Hughes et al. in preparation.

[63] William Hughes et al. in preparation.

[64] M. Żukowski, A. Zeilinger, M. A. Horne, and A. K. Ekert. Event-ready-detectors Bell experiment via entanglement swapping. *Phys. Rev. Lett.*, 71:4287–4290, Dec 1993.

[65] Jake Iles-Smith, Dara P. S. McCutcheon, Jesper Mørk, and Ahsan Nazir. Limits to coherent scattering and photon coalescence from solid-state quantum emitters. *Phys. Rev. B*, 95:201305, May 2017.

[66] Jake Iles-Smith, Dara P. S. McCutcheon, Ahsan Nazir, and Jesper Mørk. Phonon scattering inhibits simultaneous near-unity efficiency and indistinguishability in semiconductor single-photon sources. *Nature Photonics*, 11(8):521–526, Aug 2017.

[67] D.F.V. James. Quantum computation with hot and cold ions: An assessment of proposed schemes. *Fortschritte der Physik*, 48(9-11):823–837, 2000.

[68] A. Jeantet, Y. Chassagneux, C. Raynaud, Ph. Roussignol, J. S. Lauret, B. Besga, J. Estève, J. Reichel, and C. Voisin. Widely tunable single-photon source from a carbon nanotube in the purcell regime. *Phys. Rev. Lett.*, 116:247402, Jun 2016.

[69] K. T. Kaczmarek, P. M. Ledingham, B. Brecht, S. E. Thomas, G. S. Thekkadath, O. Lazo-Arjona, J. H. D. Munns, E. Poem, A. Feizpour, D. J. Saunders, J. Nunn, and I. A. Walmsley. High-speed noise-free optical quantum memory. *Phys. Rev. A*, 97:042316, Apr 2018.

[70] P. Kaer and J. Mørk. Decoherence in semiconductor cavity qed systems due to phonon couplings. *Phys. Rev. B*, 90:035312, Jul 2014.

[71] Ezra Kassa, William Hughes, Shaobo Gao, and Joseph F Goodwin. Effects of cavity birefringence on remote entanglement generation, 2020. arXiv: 2008.11712.

[72] Ivan Kassal, Stephen P. Jordan, Peter J. Love, Masoud Mohseni, and Alán Aspuru-Guzik. Polynomial-time quantum algorithm for the simulation of chemical dynamics. *Proceedings of the National Academy of Sciences*, 105(48):18681–18686, 2008.

[73] Mohammadsadegh Khazali, Hon Wai Lau, Adam Humeniuk, and Christoph Simon. Large energy superpositions via Rydberg dressing. *Phys. Rev. A*, 94:023408, Aug 2016.

[74] D. Kielpinski, C. Monroe, and D. J. Wineland. Architecture for a large-scale ion-trap quantum computer. *Nature*, 417(6890):709–711, Jun 2002.

[75] Andrew D. King, Juan Carrasquilla, Jack Raymond, et al. Observation of topological phenomena in a programmable lattice of 1,800 qubits. *Nature*, 560(7719):456–460, Aug 2018.

[76] A. Kiraz, M. Ehrl, Th. Hellerer, Ö. E. Müstecaplıoğlu, C. Bräuchle, and A. Zumbusch. Indistinguishable photons from a single molecule. *Phys. Rev. Lett.*, 94:223602, Jun 2005.

[77] S. C. Kitson, P. Jonsson, J. G. Rarity, and P. R. Tapster. Intensity fluctuation spectroscopy of small numbers of dye molecules in a microcavity. *Phys. Rev. A*, 58:620–627, Jul 1998.

[78] E. Knill, R. Laflamme, and G. J. Milburn. A scheme for efficient quantum computation with linear optics. *Nature*, 409(6816):46–52, Jan 2001.

[79] Boris Korzh, Qing-Yuan Zhao, Jason P. Allmaras, et al. Demonstration of sub-3 ps temporal resolution with a superconducting nanowire single-photon detector. *Nature Photonics*, 14(4):250–255, Apr 2020.

[80] Andreas V. Kuhlmann, Julien Houel, Arne Ludwig, Lukas Greuter, Dirk Reuter, Andreas D. Wieck, Martino Poggio, and Richard J. Warburton. Charge noise and spin noise in a semiconductor quantum device. *Nature Physics*, 9(9):570–575, Sep 2013.

[81] Takashi Kuroda, Takaaki Mano, Neul Ha, Hideaki Nakajima, Hidekazu Kumano, Bernhard Urbaszek, Masafumi Jo, Marco Abbarchi, Yoshiki Sakuma, Kazuaki Sakoda, Ikuo Suemune, Xavier Marie, and Thierry Amand. Symmetric quantum dots as efficient sources of highly entangled photons: Violation of bell's inequality without spectral and temporal filtering. *Phys. Rev. B*, 88:041306, Jul 2013.

[82] Melvin Lax. Quantum noise. x. density-matrix treatment of field and population-difference fluctuations. *Phys. Rev.*, 157:213–231, May 1967.

[83] Regina Lechner, Christine Maier, Cornelius Hempel, Petar Jurcevic, Ben P. Lanyon, Thomas Monz, Michael Brownnutt, Rainer Blatt, and Christian F. Roos. Electromagnetically-induced-transparency ground-state cooling of long ion strings. *Phys. Rev. A*, 93:053401, May 2016.

[84] Moonjoo Lee, Minjae Lee, Seokjun Hong, Klemens Schüppert, Yeong-Dae Kwon, Taehyun Kim, Yves Colombe, Tracy E. Northup, Dong-Il "Dan" Cho, and Rainer Blatt. Microelectromechanical-system-based design of a high-finesse fiber cavity integrated with an ion trap. *Phys. Rev. Applied*, 12:044052, Oct 2019.

[85] D. Leibfried, R. Blatt, C. Monroe, and D. Wineland. Quantum dynamics of single trapped ions. *Rev. Mod. Phys.*, 75:281–324, Mar 2003.

[86] V Y F Leung, D R M Pijn, H Schlatter, L Torralbo-Campo, AL La Rooij, GB Mulder, J Naber, ML Soudijn, A Tauschinsky, C Abarbanel, B Hadad, E Golan, R Folman, and R J C Spreeuw. Magnetic-film atom chip with 10 µm period lattices of microtraps for quantum information science with rydberg atoms. *The Review of scientific instruments*, 85(5):053102, May 2014.

[87] Harry Levine, Alexander Keesling, Ahmed Omran, Hannes Bernien, Sylvain Schwartz, Alexander S. Zibrov, Manuel Endres, Markus Greiner, Vladan Vuletić, and Mikhail D. Lukin. High-fidelity control and entanglement of rydberg-atom qubits. *Phys. Rev. Lett.*, 121:123603, Sep 2018.

[88] Xiaoying Li, Paul L. Voss, Jay E. Sharping, and Prem Kumar. Optical-fiber source of polarization-entangled photons in the 1550 nm telecom band. *Phys. Rev. Lett.*, 94:053601, Feb 2005.

[89] Norbert M. Linke, Dmitri Maslov, Martin Roetteler, Shantanu Debnath, Caroline Figgatt, Kevin A. Landsman, Kenneth Wright, and Christopher Monroe. Experimental comparison of two quantum computing architectures. *Proceedings of the National Academy of Sciences*, 114(13):3305–3310, 2017.

[90] Juan C. Loredo, Nor A. Zakaria, Niccolo Somaschi, Carlos Anton, Lorenzo de Santis, Valerian Giesz, Thomas Grange, Matthew A. Broome, Olivier Gazzano, Guillaume Coppola, Isabelle Sagnes, Aristide Lemaitre, Alexia Auffeves, Pascale Senellart, Marcelo P. Almeida, and Andrew G. White. Scalable performance in solid-state single-photon sources. *Optica*, 3(4):433–440, Apr 2016.

[91] B. Lounis and W. E. Moerner. Single photons on demand from a single molecule at room temperature. *Nature*, 407:491–493, Sep 2000.

[92] Chao-Yang Lu, Daniel E. Browne, Tao Yang, and Jian-Wei Pan. Demonstration of a compiled version of shor's quantum factoring algorithm using photonic qubits. *Phys. Rev. Lett.*, 99:250504, Dec 2007.

[93] D. M. Lucas, A. Ramos, J. P. Home, M. J. McDonnell, S. Nakayama, J.-P. Stacey, S. C. Webster, D. N. Stacey, and A. M. Steane. Isotope-selective photoionization for calcium ion trapping. *Phys. Rev. A*, 69:012711, Jan 2004.

[94] M. D. Lukin, M. Fleischhauer, R. Cote, L. M. Duan, D. Jaksch, J. I. Cirac, and P. Zoller. Dipole blockade and quantum information processing in mesoscopic atomic ensembles. *Phys. Rev. Lett.*, 87:037901, Jun 2001.

[95] J. McKeever, J. R. Buck, A. D. Boozer, and H. J. Kimble. Determination of the number of atoms trapped in an optical cavity. *Phys. Rev. Lett.*, 93:143601, Sep 2004.

[96] P. Michler, A. Kiraz, C. Becher, W. V. Schoenfeld, P. M. Petroff, Lidong Zhang, E. Hu, and A. Imamoglu. A quantum dot single-photon turnstile device. *Science*, 290(5500):2282–2285, 2000.

[97] J. Miszczak. Models of quantum computation and quantum programming languages. *Bulletin of the Polish Academy of Sciences: Technical Sciences*, 59(No 3):305–324, 2011.

[98] D. L. Moehring, P. Maunz, S. Olmschenk, K. C. Younge, D. N. Matsukevich, L.-M. Duan, and C. Monroe. Entanglement of single-atom quantum bits at a distance. *Nature*, 449(7158):68–71, Sep 2007.

[99] C. Monroe, D. M. Meekhof, B. E. King, S. R. Jefferts, W. M. Itano, D. J. Wineland, and P. Gould. Resolved-sideband raman cooling of a bound atom to the 3d zero-point energy. *Phys. Rev. Lett.*, 75:4011–4014, Nov 1995.

[100] C. Monroe, R. Raussendorf, A. Ruthven, K. R. Brown, P. Maunz, L.-M. Duan, and J. Kim. Large-scale modular quantum-computer architecture with atomic memory and photonic interconnects. *Phys. Rev. A*, 89:022317, Feb 2014.

[101] Ashley Montanaro. Quantum algorithms: an overview. *npj Quantum Information*, 2(1):15023, Jan 2016.

[102] Peter J. Mosley, Jeff S. Lundeen, Brian J. Smith, Piotr Wasylczyk, Alfred B. U'Ren, Christine Silberhorn, and Ian A. Walmsley. Heralded generation of ultrafast single photons in pure quantum states. *Phys. Rev. Lett.*, 100:133601, Apr 2008.

[103] J. H. D. Munns, S. E. Thomas, K. T. Kaczmarek, P. M. Ledingham, D. J. Saunders, J. Nunn, B. Brecht, and I. A. Walmsley. Temporal-mode selection with a raman quantum memory. In *Frontiers in Optics 2017*, page JW4A.16. Optical Society of America, 2017.

[104] A. H. Myerson, D. J. Szwer, S. C. Webster, D. T. C. Allcock, M. J. Curtis, G. Imreh, J. A. Sherman, D. N. Stacey, A. M. Steane, and D. M. Lucas. High-fidelity readout of trapped-ion qubits. *Phys. Rev. Lett.*, 100:200502, May 2008.

[105] Warren Nagourney, Jon Sandberg, and Hans Dehmelt. Shelved optical electron amplifier: Observation of quantum jumps. *Phys. Rev. Lett.*, 56:2797–2799, Jun 1986.

[106] Chetan Nayak, Steven H. Simon, Ady Stern, Michael Freedman, and Sankar Das Sarma. Non-abelian anyons and topological quantum computation. *Rev. Mod. Phys.*, 80:1083–1159, Sep 2008.

[107] Michael A. Nielsen and Isaac L. Chuang. *Quantum Computation and Quantum Information: 10th Anniversary Edition*. Cambridge University Press, 2010.

[108] J. Nunn. *Quantum memory in atomic ensemble*. PhD thesis, Oxford University, 2008.

[109] J. Nunn, N. K. Langford, W. S. Kolthammer, T. F. M. Champion, M. R. Sprague, P. S. Michelberger, X.-M. Jin, D. G. England, and I. A. Walmsley. Enhancing multiphoton rates with quantum memories. *Phys. Rev. Lett.*, 110:133601, Mar 2013.

[110] Lazo Oscar et al. in preparation.

[111] Mark Oxborrow and Alastair G Sinclair. Single-photon sources. *Contemporary Physics*, 46(3):173–206, 2005.

[112] E. Peter, J. Hours, P. Senellart, A. Vasanelli, A. Cavanna, J. Bloch, and J. M. Gérard. Phonon sidebands in exciton and biexciton emission from single gaas quantum dots. *Phys. Rev. B*, 69:041307, Jan 2004.

[113] Nina Podoliak, Hiroki Takahashi, Matthias Keller, and Peter Horak. Comparative numerical studies of ion traps with integrated optical cavities. *Phys. Rev. Applied*, 6:044008, Oct 2016.

[114] Nina Podoliak, Hiroki Takahashi, Matthias Keller, and Peter Horak. Harnessing the mode mixing in optical fiber-tip cavities. *Journal of Physics B: Atomic, Molecular and Optical Physics*, 50(8):085503, mar 2017.

[115] John Preskill. Quantum computing and the entanglement frontier, 2012.

[116] Young-Sik Ra, Clément Jacquard, Adrien Dufour, Claude Fabre, and Nicolas Treps. Tomography of a mode-tunable coherent single-photon subtractor. *Phys. Rev. X*, 7:031012, Jul 2017.

[117] Georg Raithel and Natalya Morrow. Atom manipulation in optical lattices. volume 53 of *Advances In Atomic, Molecular, and Optical Physics*, pages 187 – 225. Academic Press, 2006.

[118] Dileep V. Reddy and Michael G. Raymer. High-selectivity quantum pulse gating of photonic temporal modes using all-optical ramsey interferometry. *Optica*, 5(4):423–428, Apr 2018.

[119] Markus Reiher, Nathan Wiebe, Krysta M Svore, Dave Wecker, and Matthias Troyer. Elucidating reaction mechanisms on quantum computers. *Proceedings of the National Academy of Sciences of the United States of America*, 114(29):7555—7560, July 2017.

[120] T. Ruster, C. T. Schmiegelow, H. Kaufmann, C. Warschburger, F. Schmidt-Kaler, and U. G. Poschinger. A long-lived zeeman trapped-ion qubit. *Applied Physics B*, 122(10):254, Sep 2016.

[121] Andre Van Rynbach, George Schwartz, Robert F. Spivey, James Joseph, Geert Vrijsen, and Jungsang Kim. Design and characterization of an integrated surface ion trap and micromirror optical cavity. *Appl. Opt.*, 56(23):6511–6519, Aug 2017.

[122] M Saffman. Quantum computing with atomic qubits and rydberg interactions: progress and challenges. *Journal of Physics B: Atomic, Molecular and Optical Physics*, 49(20):202001, oct 2016.

[123] S. Scheel. Permanents in linear optical networks. *Acta Phys. Slovaca*, 58:675, 2004.

[124] Lucas Schweickert, Klaus D. Jöns, Katharina D. Zeuner, Saimon Filipe Covre da Silva, Huiying Huang, Thomas Lettner, Marcus Reindl, Julien Zichi, Rinaldo Trotta, Armando Rastelli, and Val Zwiller. On-demand generation of background-free single photons from a solid-state source. *Applied Physics Letters*, 112(9):093106, 2018.

[125] P. Senellart, G. Solomon, and A. White. High-performance semiconductor quantum-dot single-photon sources. *Nature Nanotechnology*, 12:1026–1039, dec 2017.

[126] M. A. Sepiol, A. C. Hughes, J. E. Tarlton, D. P. Nadlinger, T. G. Ballance, C. J. Ballance, T. P. Harty, A. M. Steane, J. F. Goodwin, and D. M. Lucas. Probing qubit memory errors at the part-per-million level. *Phys. Rev. Lett.*, 123:110503, Sep 2019.

[127] Amin Shahverdi, Yong Meng Sua, Lubna Tumeh, and Yu-Ping Huang. Quantum parametric mode sorting: Beating the time-frequency filtering. *Scientific Reports*, 7(1):6495, Jul 2017.

[128] K. Sheridan, W. Lange, and M. Keller. All-optical ion generation for ion trap loading. *Applied Physics B*, 104(4):755, May 2011.

[129] Peter W. Shor. Polynomial-time algorithms for prime factorization and discrete logarithms on a quantum computer. *SIAM Review*, 41(2):303–332, 1999.

[130] N Simon, R; Mukunda. Minimal three-component su(2) gadget for polarization optics. *Physics letters. A*, 1990.

[131] A. Sipahigil, M. L. Goldman, E. Togan, Y. Chu, M. Markham, D. J. Twitchen, A. S. Zibrov, A. Kubanek, and M. D. Lukin. Quantum interference of single photons from remote nitrogen-vacancy centers in diamond. *Phys. Rev. Lett.*, 108:143601, Apr 2012.

[132] A. Sipahigil, K. D. Jahnke, L. J. Rogers, T. Teraji, J. Isoya, A. S. Zibrov, F. Jelezko, and M. D. Lukin. Indistinguishable photons from separated silicon-vacancy centers in diamond. *Phys. Rev. Lett.*, 113:113602, Sep 2014.

[133] G. S. Solomon, J. A. Trezza, and J. S. Harris. Effects of monolayer coverage, flux ratio, and growth rate on the island density of inas islands on gaas. *Applied Physics Letters*, 66(23):3161–3163, 1995.

[134] N. Somaschi, V. Giesz, L. De Santis, J. C. Loredo, M. P. Almeida, G. Hornecker, S. L. Portalupi, T. Grange, C. Antón, J. Demory, C. Gómez, I. Sagnes, N. D. Lanzillotti-Kimura, A. Lemaítre, A. Auffeves, A. G. White, L. Lanco, and P. Senellart. Near-optimal single-photon sources in the solid state. *Nature Photonics*, 10(5):340–345, May 2016.

[135] D.A. Steck. *Quantum and Atom Optics*. 2007.

[136] Mathias Steiner, Achim Hartschuh, Rafał Korlacki, and Alfred J. Meixner. Highly efficient, tunable single photon source based on single molecules. *Applied Physics Letters*, 90(18):183122, 2007.

[137] L. J. Stephenson, D. P. Nadlinger, B. C. Nichol, S. An, P. Drmota, T. G. Ballance, K. Thirumalai, J. F. Goodwin, D. M. Lucas, and C. J. Ballance. High-rate, high-fidelity entanglement of qubits across an elementary quantum network. *Phys. Rev. Lett.*, 124:110501, Mar 2020.

[138] A. Stute, B. Casabone, P. Schindler, T. Monz, P. O. Schmidt, B. Brandstätter, T. E. Northup, and R. Blatt. Tunable ion–photon entanglement in an optical cavity. *Nature*, 485(7399):482–485, May 2012.

[139] R. A. Sunyaev, Ya. B.and Zeldovich. The interaction of matter and radiation in the hot model of the Universe, II. *Astrophysics and Space Science*, 7:20–30, April 1970.

[140] Hiroki Takahashi, Ezra Kassa, Costas Christoforou, and Matthias Keller. Strong coupling of a single ion to an optical cavity. *Phys. Rev. Lett.*, 124:013602, Jan 2020.

[141] S. E. Thomas, T. M. Hird, J. H. D. Munns, B. Brecht, D. J. Saunders, J. Nunn, I. A. Walmsley, and P. M. Ledingham. Raman quantum memory with built-in suppression of four-wave-mixing noise. *Phys. Rev. A*, 100:033801, Sep 2019.

[142] Toan Trong Tran, Kerem Bray, Michael J. Ford, Milos Toth, and Igor Aharonovich. Quantum emission from hexagonal boron nitride monolayers. *Nature Nanotechnology*, 11(1):37–41, Jan 2016.

[143] A A P Trichet, P R Dolan, and J M Smith. Strong coupling between 0d and 2d modes in optical open microcavities. *Journal of Optics*, 20(3):035402, feb 2018.

[144] Sebastian Unsleber, Yu-Ming He, Stefan Gerhardt, Sebastian Maier, Chao-Yang Lu, Jian-Wei Pan, Niels Gregersen, Martin Kamp, Christian Schneider, and Sven Höfling. Highly indistinguishable on-demand resonance fluorescence photons from a deterministic quantum dot micropillar device with 74% extraction efficiency. *Opt. Express*, 24(8):8539–8546, Apr 2016.

[145] Manuel Uphoff, Manuel Brekenfeld, Gerhard Rempe, and Stephan Ritter. Frequency splitting of polarization eigenmodes in microscopic fabry–perot cavities. *New Journal of Physics*, 17(1):013053, jan 2015.

[146] Thomas Walker, Samir Vartabi Kashanian, Travers Ward, and Matthias Keller. Improving the indistinguishability of single photons from an ion-cavity system. *Phys. Rev. A*, 102:032616, Sep 2020.

[147] Pengfei Wang, Chun-Yang Luan, Mu Qiao, Mark Um, Junhua Zhang, Ye Wang, Xiao Yuan, Mile Gu, Jingning Zhang, and Kihwan Kim. Single ion-qubit exceeding one hour coherence time, 2020. arXiv: 2008.00251.

[148] Yang Wang, Aishwarya Kumar, Tsung-Yao Wu, and David S. Weiss. Single-qubit gates based on targeted phase shifts in a 3d neutral atom array. *Science*, 352(6293):1562–1565, 2016.

[149] Katsuyuki Watanabe, Nobuyuki Koguchi, and Yoshihiko Gotoh. Fabrication of GaAs quantum dots by modified droplet epitaxy. *Japanese Journal of Applied Physics*, 39(Part 2, No. 2A):L79–L81, feb 2000.

[150] Yu-Jia Wei, Yu-Ming He, Ming-Cheng Chen, Yi-Nan Hu, Yu He, Dian Wu, Christian Schneider, Martin Kamp, Sven Höfling, Chao-Yang Lu, and Jian-Wei Pan. Deterministic and robust generation of single photons from a single quantum dot with 99.5% indistinguishability using adiabatic rapid passage. *Nano Letters*, 14(11):6515–6519, Nov 2014.

[151] D. J. Wineland, C. Monroe, W. M. Itano, D. Leibfried, B. E. King, and D. M. Meekhof. Experimental issues in coherent quantum-state manipulation of trapped atomic ions. *Journal of research of the National Institute of Standards and Technology*, 103(3):259–328, 1998. 28009379[pmid].

[152] Ya. B. Zeldovich and R. A. Sunyaev. The Interaction of Matter and Radiation in a Hot-Model Universe. *Astrophysics and Space Science*, 4(3):301–316, July 1969.

[153] J. Zhang, G. Pagano, P. W. Hess, A. Kyprianidis, P. Becker, H. Kaplan, A. V. Gorshkov, Z.-X. Gong, and C. Monroe. Observation of a many-body dynamical phase transition with a 53-qubit quantum simulator. *Nature*, 551(7682):601–604, Nov 2017.

[154] Bo Zhao, Yu-Ao Chen, Xiao-Hui Bao, Thorsten Strassel, Chih-Sung Chuu, Xian-Min Jin, Jörg Schmiedmayer, Zhen-Sheng Yuan, Shuai Chen, and Jian-Wei Pan. A millisecond quantum memory for scalable quantum networks. *Nature Physics*, 5(2):95–99, dec 2008.